MECHANISMS IN SINGLE MOLECULE FLUORESCENCE IMAGING: FROM PHOTOPHYSICS TO BIOLOGICAL APPLICATIONS

By Yasser Gidi

A Thesis submitted to McGill University in partial fulfilment

of the requirements for the degree of

Doctor of Philosophy

Department of Chemistry

McGill University

Montreal, Quebec, Canada

March 2020

Mechanisms in Single Molecule Fluorescence Imaging: from Photophysics to Biological Applications

"A society that puts equality before freedom will get neither. A society that puts freedom before equality will get a high degree of both."

–Milton Friedman

***I** dedicate this thesis*

***T**o my Family: My parents Ricardo and Isabel,*

and my siblings Alejandra, Ricardo, and Marian

ABSTRACT

Single molecule fluorescence (SMF) microscopy techniques have profoundly changed the way we can study the dynamics and structure of the microscopic and nanoscopic world. SMF methods, including cutting-edge super resolution microscopy, allow unprecedented spatiotemporal resolution and are particularly powerful for the study of heterogeneous and unsynchronized systems.

In order to unravel the full potential of SMF techniques, many challenges remain to be addressed, including surface passivation and a thorough mechanistic photochemical and photophysical understanding of fluorescent dyes and their associated SMF techniques.

The research presented in this thesis aims to address many of the current challenges plaguing SMF studies by providing key insights behind SMF data analysis related to single molecule Förster resonance energy transfer (FRET) studies and associated protein induced fluorescent enhancement (PIFE) studies. Our work provides a mechanistic underpinning for the photochemical and photophysical behavior of cyanine dyes, of relevance to photostabilization and photoswitching towards super resolution. These results also provide a framework for sample preparation in terms of enhanced surface quality for specific substrate immobilization. Armed with these technical improvements, we next tackled key biophysical aspects related to the mechanism and dynamics of the viral replication machinery of the Hepatitis C virus (HCV). The non-structural 5B (NS5B) polymerase of HCV has the remarkable ability to initiate synthesis *de novo* through a primer independent mechanism. Through our single molecule work, we report on NS5B binding, sliding, and searching for the 3’ of its single stranded RNA substrate.

Overall, our work provides new insights on critical aspects of SMF techniques such as sample preparation, fluorescence signal control, and data analysis. Moreover, it provides an example of the power of SMS to study relevant biomolecular mechanisms such as the replication machinery of viruses.

RÉSUMÉ

Les techniques de microscopie de fluorescence de molécules individuelles (FMI) ont profondément changé la façon dont nous pouvons mener les études dynamiques et structurelles aux échelles microscopiques et nanoscopiques. Les méthodes de FMI, y compris la microscopie à super résolution de pointe, permettent une résolution spatio-temporelle sans précédence et sont particulièrement puissantes pour l'étude des systèmes hétérogènes et non synchronisés.

Afin d'exploiter tout le potentiel des techniques FMI, de nombreux problèmes restent à résoudre. Ces défis incluent la passivation de surface et une compréhension mécanistique approfondie des propriétés photochimiques et photophysiques des marqueurs fluorescents et de leurs techniques FMI associées.

La recherche présentée dans cette thèse vise à aborder un grand nombre de défis actuels qui affligent les études FMI, tout en fournissant des informations clés sur l'analyse des données FMI liées aux études de transfert d'énergie par résonance de type Förster (FRET) et aux études associées à augmentation de la fluorescence induite par les protéines (PIFE). Elle fournit un fondement mécaniste au comportement photochimique et photophysique des marqueurs à base de cyanine, ce qui est important pour la photostabilisation et la photo-commutation afin d'atteindre la super résolution. Elle fournit également un cadre pour la préparation des échantillons en termes d'amélioration de la qualité de surface pour une immobilisation spécifique du substrat. En ayant établi ces améliorations techniques, nous avons ensuite abordé les aspects principaux de la pertinence biophysique liés au mécanisme et à la dynamique de la machinerie de réplication virale du virus de l'hépatite C (VHC). L'ARN polymérase du VHC, la protéine NS5B, possède la capacité remarquable d'initier la synthèse *de novo* par un mécanisme indépendant de l'amorce. Grâce à notre travail utilisant la microscopie de fluorescence de molécules individuelles, nous rapportons ici des études sur la liaison et le glissement de la protéine NS5B ainsi que sa capacité à identifier l'extrémité 3' de son substrat d'ARN à brin simple.

Collectivement, nos travaux fournissent de nouvelles informations sur les aspects principaux des techniques FMI telles que la préparation des échantillons, le contrôle du signal de fluorescence et l'analyse des données. De plus, ils fournissent un exemple de la puissance des méthodologies de

FMI pour étudier des mécanismes biomoléculaires pertinents tels que le mécanisme de réplication des virus.

ACKNOWLEDGEMENTS

I am deeply grateful to my supervisor Prof. Gonzalo Cosa for allowing me to be part of his research group, for our stimulating discussions, and for his encouragement throughout my graduate studies. His knowledge, enthusiasm, and research skills have always been an inspiration. Thank you for being always there when I needed advice, support, and feedback, especially when deadlines were quickly approaching.

I would like to thank my supervisory committee members, Prof. Anthony Mittermaier and Prof. Hanadi Sleiman for the excellent advice and guidance they provided in moving these projects forward. Further thanks to our collaborators: Dr. Matthias Götte, Dr. Amy Blum, Dr. Paul Wiseman, and Dr. Martin Schnermann for allowing me to extend my knowledge and skills through interdisciplinary research.

Many thanks to all the past and present members of the Cosa lab for providing such a great working environment. Hsiao-Wei Liu, Andres Durantini, Mayra Martinez, Kasia Jodko-Piórecka, Sol Martinez, John Hardwick, Robert Godin, Mei-Ni Belzile, Amani Hariri, Christina Calver, Lana Greene, Viktorija Glembockyte, Richard Lincoln, Casey Platnich, Aya Sakaya, Julia McCain, Semanti Mukherjee, Wenzhou (Kevin) Zhang, Anthony Van Kessel, Jorge Eduardo Ramos-Sánchez, Serge Hirka, Andy Yin, Florencia Fungo, Alexander Al-Feghali, and all visiting and summer students. Each of you, in your particular way, made my stay in the lab an unforgettable experience. I truly believe Cosa group is a great team and it will continue to be.

Thanks to all the Mittermaier group members, in particular Robert Harkness and Justin Di Trani for providing extra fun to the Cosa-Mittermaier area.

Many thanks to Kevin, Julia, and Anthony for carefully proofreading some of the chapters of this thesis. In particular, thanks to Casey and Aya for proofreading not only almost every single chapter of this thesis, but also most of my applications.

I want to thank all the friends I made inside and outside the Cosa lab, I will never forget all those memorable times we spent together in Montreal. Also, thanks to all of those old unconditional friends from Chile that never stopped asking “When are you finishing?”.

To my wonderful girlfriend Lauralicia Sacre who has made the last two years, an incredible experience. Thank you for all the special joy and unlimited support you have added to my life, specially at the end of this wonderful challenge called PhD.

Finally, I wish to express my gratitude to those who have been with me not only during the thesis period, but also through my entire life: my parents Ricardo and Isabel who are behind everything I have achieved so far. Also, to my siblings Alejandra, Ricardo, and Marian, for their continuous support and for providing me the great experience of being the uncle of Martin and Tomas.

AUTHOR CONTRIBUTIONS

This thesis consists of six Chapters. **Chapter 2** has been published in *Journal of Physical Chemistry B*. **Chapters 3** has been recently submitted. **Chapter 4** has been published in *ACS Applied Materials & Interfaces*. **Chapter 5** is based on a manuscript that is currently in preparation. **Chapter 6** includes final remarks and an outlook as well as suggestions for future work. All papers presented in **chapters 2 to 5** were co-authored with the research advisor Prof. Dr. Gonzalo Cosa (Department of Chemistry, McGill University) who guided and coordinated the studies, participated in project designs as well as manuscript writing and editing in all cases.

- **Chapter 2:** Gidi, Y.; Götte, M.; Cosa, G., Conformational Changes Spanning Angstroms to Nanometers via a Combined Protein-Induced Fluorescence Enhancement–Förster Resonance Energy Transfer Method. *J. Phys. Chem. B* **2017**, *121*, 2039

Yasser Gidi contributed to project design and acquisition of fluorescence single-molecule data. Contributions also include the analysis and interpretation of data in addition to manuscript writing and editing.

Prof. Dr. Matthias Götte contributed to project design as well as manuscript editing.

- **Chapter 3:** Gidi, Y.; Payne, L.; Glembockyte, V.; Schnermann, M. J.; Cosa G.; Unifying mechanism for thiol induced photoswitching and photostability of cyanine dyes. *Submitted.*

Yasser Gidi contributed to project design, performed fluorescence single-molecule and laser flash photolysis experiments. Contributions also include DFT calculations as well as analysis and interpretation of data, in addition to manuscript writing and editing.

Liam Payne contributed to experimental design and acquisition of laser flash photolysis data. Contributions also include the analysis and interpretation of data in addition to manuscript writing and editing.

Dr. Viktorija Glembockyte contributed to project design, and acquisition of fluorescence ensemble and laser flash photolysis data. Contributions also include the analysis and interpretation of data in addition to manuscript editing.

Dr. Megan Michie contributed with the synthesis of Cy5B.

Prof. Dr. Martin Shnermann contributed to project design, guided and coordinated the study as well as manuscript editing.

- **Chapter 4:** Gidi, Y.; Bayram, S.; Ablenas, C.J.; Blum, A. S.; Cosa, G., Efficient One-Step PEG-Silane Passivation of Glass Surfaces for Single-Molecule Fluorescence Studies. *ACS Appl. Mater. Interfaces* **2018**, *10*, 39505

Yasser Gidi contributed to project design and performed fluorescence single-molecule experiments as well as coverslip preparation. Contributions also include the analysis and interpretation of data in addition to manuscript writing and editing.

Dr. Serene Bayram contributed to protein expression, purification, and labeling as well as acquisition of AFM images and manuscript editing.

Dr. Christopher J Ablenas contributed to protein expression, purification, and labeling as well as manuscript editing.

Prof. Dr. Amy Szuchmacher Blum contributed to project design as well as guided and coordinated the study.

- **Chapter 5:** Gidi, Y.; Robert, A.; Tordo, A.; Götte, M.; Cosa G.; Binding and Sliding Dynamics Preceding de novo RNA Replication by the Hepatitis C Virus Polymerase: hunting the 3'. *To be submitted.*

Yasser Gidi contributed to project design and performed fluorescence single-molecule experiments as well as analysis and interpretation of data in addition to manuscript writing and editing.

Anais Robert contributed to acquisition, analysis, and interpretation of single-molecule fluorescence data. Contributions also include manuscript editing.

Alix Tordo contributed to acquisition, analysis, and interpretation of single-molecule fluorescence data. Contributions also include manuscript editing.

Prof. Dr. Matthias Götte contributed to project design as well as guided and coordinated the study jointly with Prof. Cosa.

TABLE OF CONTENTS

LIST OF TABLES

LIST OF FIGURES

LIST OF ABBREVIATIONS AND ACRONYMS

α	half the aperture angle of the objective
β	FRET correction factor due to leakage
β-ME	β-mercaptoethanol
γ	FRET correction factor due to fluorescence quantum yield and detector efficiencies
ΔE_{00}	electronic excitation energy of the fluorophore
ΔG^{o}_{PeT}	Gibbs free energy for photoinduced electron transfer
$\Delta G^{\neq}_{PeT}$	Gibbs free energy of activation for photoinduced electron transfer
ΔOD	difference in optical density (absorbance)
ε	dielectric constant of the solvent
ε_0	permittivity of the vacuum
ε_{max}	extinction coefficient at the absorption peak
h	Planck's constant
θ_c	critical angle
κ^2	geometric factor accounting for the relative donor-acceptor dipole orientation
λ	reorganization energy
λ_0	wavelength of the incident light in vacuum
λ^{abs}_{max}	maximum absorption wavelength
λ^{em}_{max}	maximum emission wavelength
υ	excitation frequency
υ_N	frequency for nuclear motion along the reaction coordinate
σ_p	absorption cross section

τ_f, τ_d	fluorescence lifetime
Φ_f	fluorescence quantum yield
a	size of the camera pixel edge length
A	beam excitation area
AA	ascorbic acid
AFM	atomic force microscopy
APTES	(3-Aminopropyl)triethoxysilane
ATP	adenosine triphosphate
b	background noise
B*e*T	back-electron transfer
BODIPY	boron-dipyrromethene
BSA	bovine serum albumin
CAT	catalase
C	Coulombic term
CCD	charge-coupled device
C_b	background count rate per watt of excitation power
Cy	Cyanine dye
D	instrument-dependent collection factor
d	penetration depth of evanescent field
DiD	1,1'-Dioctadecyl-3,3,3',3'-Tetramethylindodicarbocyanine
DNA	deoxyribonucleic acid
e	elementary charge
E	FRET efficiency

$\mathbf{E_{pr}}$	proximity ratio
EA	electron afinity
$\mathbf{E^{o}_{A}}$	standard one-electron reduction potential of the acceptor
$\mathbf{E^{o}_{D}}$	standard one-electron reduction potential of the donor
EMCCD	electron multiplying charge-coupled device
F	fluorophore
$\mathbf{F^{\bullet -}}$	fluorophore radical anion
$\mathbf{F^{\bullet +}}$	fluorophore radical cation
FRET	Förster resonance energy transfer
GFP	green fluorescent protein
GOD	glucose oxidase
GRP	geminate radical pair
h	Planck's constant
HCV	hepatitis C virus
HIV	human immunodeficiency virus
HOMO	highest occupied molecular orbital
HPLC	high-performance liquid chromatography
IC	internal conversion
IP	ionization potential
ISC	intersystem crossing
$\mathbf{I_z}$	intensity of evanescent field at perpendicular distance z
$\mathbf{I_0}$	intensity of evanescent field at glass-water interface
$\boldsymbol{J(\lambda)}$	spectral overlap integral between donor and acceptor dyes

$\mathbf{k_{dec}}$	decay rate constant of singlet excited state
$\mathbf{k_{IC}}$	rate constant of internal conversion
$\mathbf{k_{fl}}$, $\mathbf{k_r}$	rate constant of fluorescence or radiative rate constant
$\mathbf{k_{esc}}$	rate constant of escape from a solvent cage
$\mathbf{k_{ex}}$	rate constant of excitation
$\mathbf{k_{ISC}}$	rate constant of intersystem crossing
$\boldsymbol{k_{Nt}}$, $\boldsymbol{k_{tN}}$	rates of interconversion between the *N* and *t* forms of Cyanines
$\mathbf{k_{nr}}$	nonradiative rate constant
$\mathbf{k_p}$	rate constant of phosphorescence
$\mathbf{k_{PeT}}$	rate constant of photoinduced electron transfer
$\mathbf{k_q}$	rate constant of quenching
$\mathbf{k_T}$	rate of energy transfer
$\boldsymbol{k_{tP}}$, $\boldsymbol{k_{Pt}}$	rates of interconversion between the *t*, and *P* forms of Cyanines
$\mathbf{k_{vr}}$	rate constant of vibrational relaxation
$\mathbf{K_{SV}}$	Stern-Volmer constant
LFP	laser flash photolysis
LUMO	lowest unoccupied molecular orbital
MV	methyl viologen
$\boldsymbol{n}$	refractive index of the medium
$\boldsymbol{N}$	normal *trans* isomer, also number of photons
$\mathbf{N_A}$	Avogadro's number
NA	numerical aperture of the objective
$\mathbf{N_d}$	dark count rate

NHS	*N*-hydroxysuccinimide
NS3h	non-structural 3 helicase
NS5B	non-structural 5B
NSOM	near-field scanning optical microscopy
***n*-PG**	*n*-propyl gallate
Ox	oxidizing agent
P	*cis* photoisomer
P_0	excitation irradiance at the sample
PAINT	Points Accumulation for Imaging in Nanoscale Topography
PALM	photoactivated localization microscopy
PBS	phosphate-buffered saline
PCA	protocatechuic acid
PCD	protocatechuate-3,4-dioxygenase
PEG	polyethelyne glycol
PES	potential energy surface
P*e*T	photoinduced electron transfer
PIFE	protein-induced fluorescence enhancement
PMT	photomultiplier tube
POC	pyranose oxidase
PSF	point spread function
Q	quencher
r	distance
R_0	Förster radius

Red	reducing agent
RdRp	RNA dependent RNA polymerase
RNA	ribonucleic acid
ROXS	reducing-oxidizing system(s)
RT	reverse transcriptase
s	standard deviation of the PSF
S_0	singlet ground state
S_n	singlet excited state
sCMOS	scientific complementary metal oxide semiconductor
SMF	single-molecule fluorescence
SMLM	single molecule localization microscopy
SMS	single-molecule spectroscopy
SNR	signal-to-noise ratio
STORM	stochastic optical reconstruction microscopy
SR	super resolution
SVA	succinimidyl valerate
t	twisted intermediate
T	detector counting interval (binning time)
T_n	triplet excited state
TIR	total internal reflection
TIRFM	total internal reflection fluorescence microscope/microscopy
Tris	trisaminomethane
TX	Trolox

T20	Tween 20
UV	ultraviolet
VR	vibrational relaxation
z	perpendicular distance from glass-water interface

1 Introduction

In this introductory chapter, we discuss the most important aspects related to single molecule fluorescence (SMF) imaging techniques. First, in **section 1.1**, we introduce the fundamentals of the many processes that occur to a fluorophore upon absorption of a photon and ensuing excitation, including fluorescence. We follow, in **section 1.2**, with a brief theoretical description of the underlying photophysical and photochemical processes associated with single molecule techniques. Next, in **section 1.3**, we familiarize the reader with the main SMF techniques utilized in this thesis work and provide some examples where these techniques have been used to study molecular machines. Finally, in **section 1.4** we discuss relevant chemical aspects associated with the visualization of single molecules via fluorescence, highlighting some of the challenges of SMF techniques.

1.1 Electronic Excitation, Decay via Fluorescence, and Competing Pathways; the Fundamentals

Irradiation of molecules with photons of suitable energy can promote, upon a photon absorption, an electron from an occupied molecular orbital (OMO) to a higher energy unoccupied molecular orbital (UMO), where typically the highest (HOMO) and the lowest (LUMO), respectively, are at play (**see Figure 1.1**). In the excited state, depending on the adopted spin configuration of the two electrons in different orbitals, singlet (S_1) (spin antiparallel) and triplet (T_1) (spin parallel) are possible.

Photon absorption, occurring on the femtosecond timescale (10^{-15} s), changes the molecular electronic configuration from the initial ground state to the electronically excited state. The absorption of a photon and the multiple pathways a molecule can follow to return to its ground

state (including fluorescence) is well described by the Perrin-Jablonski diagram (**see Figure 1.2**).[1-3]

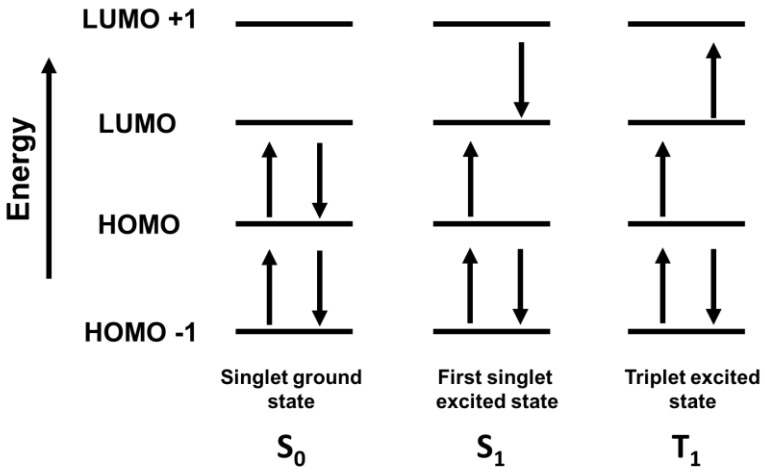

Figure 1.1 Molecular orbitals of typical ground (S_0), excited singlet (S_1) and excited triplet (T_1) states in terms of occupied (OMO) and unoccupied (UMO) molecular. Typical electronic transitions (as shown) occur from the highest OMO (HOMO) to the lowest UMO (LUMO), however other transitions can involve HOMO-n and LUMO+n levels.

At room temperature the electronic configuration of most organic molecules is that of the singlet ground state (S_0), where all electrons are spin paired. Due to selection rules, electronic transitions must conserve the spin multiplicity.[4] Absorption of a photon leads to a transition from S_0 to one of the vibrational levels of an excited singlet state S_n (**Figure 1.2, green arrows**). Molecules in higher vibrational levels quickly (10^{-12}-10^{-10} s) reach the lowest vibrational level, in a given electronic excited state, through vibrational relaxation (VR) (**Figure 1.2, blue arrows**). Molecules in an electronic states S_n where n>1 (for example n=2) undergo internal conversion (IC) (**Figure 1.2, pink arrows**) to a high vibrational energy level of the n-1 level, followed by vibrational relaxation until the first vibrational level of the first singlet excited state is reached $S_{1,v=1}$.

Relaxation to the singlet ground state S_0 occurs from the $S_{1,v=1}$ state through several physical competing pathways. A photon can be emitted via fluorescence (**Figure 1.2, orange arrows**) to one of the vibrational levels of the S_0 state. The energy lost through vibrational relaxation results in emitted photons having energy equal or lesser than the photons that caused the excitation. This is experimentally reflected by a red-shifted emission spectrum as compared to the absorption spectrum; the Stokes shift.[5] Relaxation to vibrational fundamental state of S_0 can also occur non-radiatively via internal conversion, followed by vibrational relaxation.

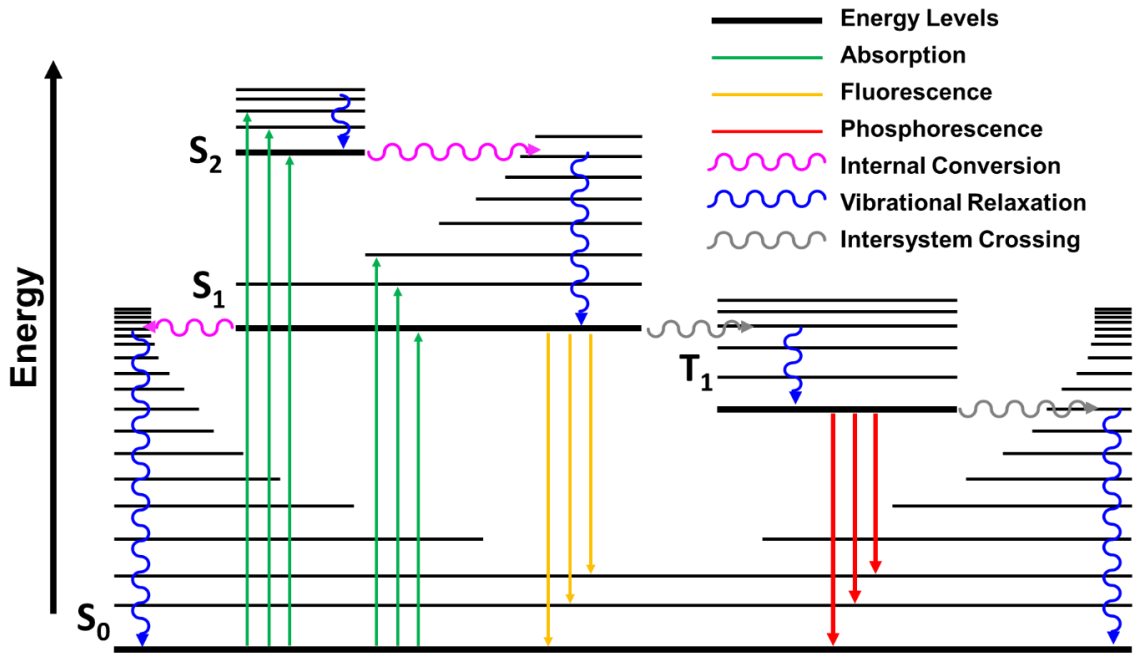

Figure 1.2 State energy (Perrin-Jablonski) diagram of Singlet and triplet states.[6]

Alternatively, a molecule in $S_{1,v=1}$ can undergo spin conversion to reach a triplet excited state T_n such as T_1 (**see Figure 1.1**), a process named intersystem crossing (ISC) (**Figure 1.2, grey arrows**). This is a spin forbidden transition, and as such its rate constant is usually significantly smaller when compared to competing processes such as fluorescence or internal conversion (**Table 1.1**). While ISC is usually very inefficient, significant overlap of vibrational energy levels between the states involved (e.g. $S_{1,v=1}$ and $T_{1,v=n}$) can favour this process. Additionally, the presence of heavy atoms can increase k_{ISC} via the so-called "heavy atom effect".[7]

Once the first triplet excited state (T_1) is populated through IC and VR from S_n, the molecule can undergo ISC to a high vibrational level of S_0 followed by VR to reach the lowest vibrational level. Alternatively, and typically at low temperature or in high viscosity media, relaxation occurs with emission of light, termed phosphorescence. Given that ISC is a spin forbidden process, triplet state relaxation to the ground singlet state via either ISC or phosphorescence is a slow process (several orders of magnitude slower) when compared to the $S_1 \rightarrow S_0$ transition. Therefore, triplet states represent a bottleneck in the decay process and provide a longer-lived target for irreversible

photochemical reactions to take place. These reactions ultimately can lead to dramatic changes in the molecular absorption and emission capabilities (photobleaching).

Singlet and triplet excited states are extremely important in single molecule fluorescence microscopy. While singlets are the states that provide the necessary photons to be detected, triplets are associated with undesired signal fluctuations and photobleaching. In **section 1.4.2**, we will revisit triplet states and discuss how extension of survival times as well as minimization of undesired fluctuations can be achieved through shortening the time molecules reside in this state.

Table 1.1. Typical timescale for the various processes described in the Perrin -Jablonski diagram.[4, 8]

Process	Transition involved	Rate constant abbreviation	Rate constant (s^{-1})
Absorption	$S_0 \rightarrow S_n$	k_{ex}	10^{15}
Internal conversion	$S_n \rightarrow S_1, T_n \rightarrow T_1$	k_{IC}	10^{10}-10^{14}
Vibrational relaxation	$S_{n,v=n} \rightarrow S_{n,v=1}$	k_{vr}	10^{10}-10^{12}
Fluorescence	$S_1 \rightarrow S_0$	k_r	10^{7}-10^{12}
Intersystem crossing	$S_1 \rightarrow T_1, S_n \rightarrow T_n, T_n \rightarrow S_n$	k_{ISC}	10^{5}-10^{10}
Internal conversion	$S_1 \rightarrow S_0$	k_{IC}	10^{6}-10^{9}
Phosphorescence	$T_1 \rightarrow S_0$	k_p	10^{-2}-10^{3}

1.2 Photophysical and Photochemical Processes Behind Single Molecule Fluorescence Techniques

Several photophysical and photochemical processes are key to single-molecule techniques. While these processes apply to all fluorophores, we will introduce them in the context of Cyanines as this is the main family of dyes utilized in this work. We will start with a brief introduction to *trans-cis* photoisomerization (key for single molecule protein induced fluorescence enhancement, smPIFE). Then, a description of Forster Resonance energy transfer (key for smFRET) will be provided. Importantly, smPIFE and smFRET have been widely utilized to study protein and DNA dynamics and interactions. Notably, smPIFE and smFRET are two "molecular rulers" that work on different length scales, making it desirable to combine smPIFE and smFRET into one single experiment. We next discuss the challenge of combining PIFE and FRET techniques as they are seemingly

incompatible. Finally, a theoretical description of Photoinduced electron transfer (P*e*T) (key to extend the survival time of fluorophores) will be presented.

1.2.1 *Trans-cis* Photoisomerization

Cyanine (Cy) dyes such as Cy3 and Cy5 (**Figure 1.3, Panel a, top**) are the most popular dyes used in single molecule fluorescence spectroscopy. One of the most important characteristics of Cy3 and Cy5 is their ability to undergo isomerization around the C-C bonds of the polymethine chain. In the ground state, Cy3 and Cy5 dyes exist in the all-*trans* conformation. Upon absorption of light, Cy3 and Cy5 can isomerize to the *cis* form, which will next thermally reverse to the all-*trans* conformation.

As first proposed by Rulliere, the photoisomerization process of Cy dyes can be described by a potential energy surface (PES) diagram (**Figure 1.3, Panel b**).[9] Upon excitation (green arrow), the singlet excited state of the fluorophore (S_1) can relax through various competing pathways to recover the singlet ground state of the fluorophore (S_o). The most efficient processes are fluorescence (orange arrow), internal conversion (blue arrow), and via rotation of two carbons of the polymethine chain (red arrow).

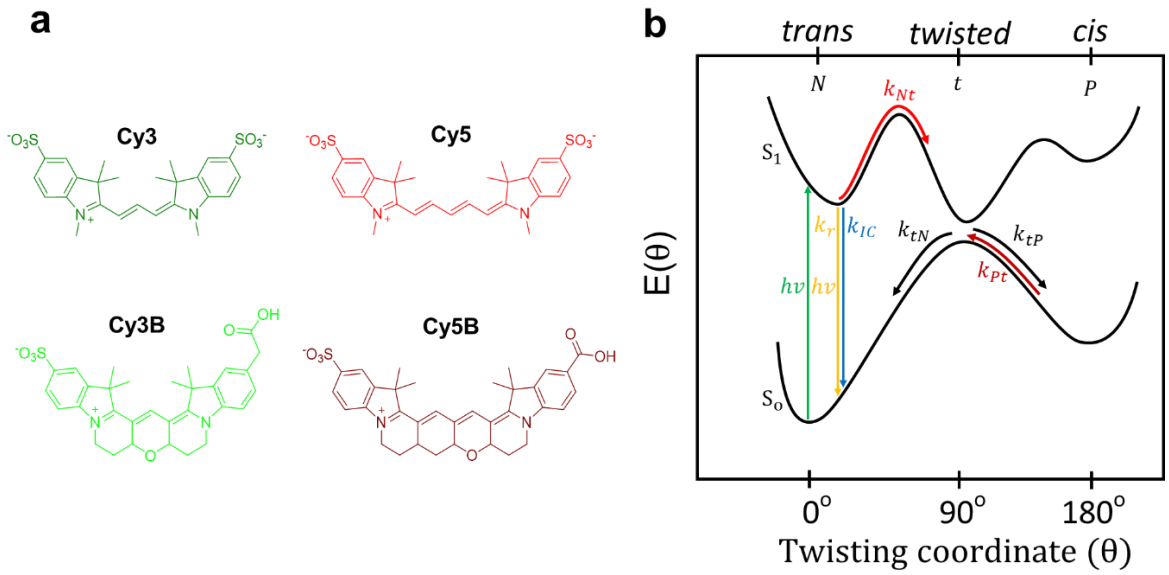

Figure 1.3. *trans-cis* photoisomerization of Cyanine dyes. a) Chemical structures of Cyanine dyes. b) PES diagram of energy vs torsion angle for the photoisomerization process. Ground (S_o) and excited (S_1) singlet states. *N* represents the normal (*trans* isomer) form, *t* the 90° twisted

intermediate, and *P* the *cis* photoisomer. $\boldsymbol{k_r}$ and $\boldsymbol{k_{IC}}$ are the radiative and the internal conversion rate constants, respectively. Additionally, $\boldsymbol{k_{Nt}}$, $\boldsymbol{k_{tN}}$, $\boldsymbol{k_{tP}}$, and $\boldsymbol{k_{Pt}}$ are the rates of interconversion between the *N*, *t*, and *P* forms of Cyanines. Adapted with permission from Levitus, M.; Ranjit, S., *Quarterly Reviews of Biophysics* **2011**, 44, 123. Copyright 2010 Cambridge University Press.

The photoisomer, proposed to have a mono *cis* conformation,[10-11] has a very low fluorescence quantum yield.[12-14] After formation, the *cis* photoisomer can be rapidly converted back to the *trans* isomer via a thermal back-isomerization. The back-isomerization process is a first order process and its rate depend strongly on the solvent viscosity.[10-11]

Due to efficient rotation taking place in the excited state, *N* → *t*, cyanine dyes, such as Cy3 and Cy5, are generally characterized by a low fluorescence quantum yield Φ_f (**see Table 1.1**). However, the Φ_f can be increased when rotation is sterically hindered by either an increase in the solvent viscosity,[15-16] or when in close proximity to biomolecules such as proteins[17-18] and oligonucleotides.[19-22] This has resulted in a new technique to conduct single molecule studies termed "Protein Induced Fluorescence Enhancement" (PIFE),[23-24] **see Section 1.3** below for more details. Additionally, the rotation can be structurally hindered via chemical modifications as shown for the locked analogs of Cy3 and Cy5, Cy3B and Cy5B, respectively (**see Figure 1.3, Panel a**).[25-26] Thus, Cy3B and Cy5B report increased fluorescence quantum yields compared to their unlocked counterparts Cy3 and Cy5, respectively (**see Table 1.1**).

Table 1.2. Spectroscopic Properties of Cy3, Cy3B, Cy5, and Cy5B in aqueous solutions

	Cy3	**Cy3B**	**Cy5**	**Cy5B**
$\boldsymbol{\lambda_{max}^{abs}}$ **(nm)**	550[27]	559[27]	649[27]	670[26]
$\boldsymbol{\varepsilon_{max}}$ **(M^{-1} cm^{-1})**	150,000[25]	130,000[25]	250,000[28]	199,000[26]
$\boldsymbol{\lambda_{max}^{em}}$**(nm)**	570[27]	570[27]	670[27]	683[26]
$\boldsymbol{\Phi_f}$	0.04[25], 0.09[29]	0.67[25], 0.85[29]	0.27[28]	0.55[26]

1.2.2 Förster Resonance Energy Transfer (FRET)

Förster Resonance Energy Transfer (FRET) theory describes the mechanism by which a donor fluorophore transfers energy to an acceptor fluorophore. In FRET, the energy is transferred in a nonradiative fashion via through-space dipole-dipole interactions in the 1-10 nm range. FRET is a distance dependent process which allows the assessment of the distance between the two

fluorophores. In 1948, Förster described the relationship between distance (r) and the rate of energy transfer (k_T) (**equations 1.1-1.3**).[30] In 1967, Stryer and Haugland coined the term "spectroscopic ruler" for FRET and confirmed experimentally Förster's predictions for the rate of energy transfer, based on a model arising from dipole-dipole coulombic interactions. This model shows that the rate of energy transfer scales with the inverse of the sixth power of the distance between fluorophores, consistent with the rate being proportional to the square of the interaction energy (Fermi's Golden Rule) which is in turn inversely proportional to the cube of the distance separating both fluorophores.[31]

The rate of energy transfer (k_T) (**equation 1.1**) is written in terms of several fundamental constants as well as experimentally available or assumable parameters, leaving the interfluorophore distance (r) as the only unknown variable. The rate of energy transfer is dependent on the fluorescence quantum yield (Φ_f^D) and lifetime (τ_d^D) of the donor in the absence of acceptor, and on the spectral overlap integral between donor and acceptor dyes $J(\lambda)$. It also includes the Avogadro's number (N_A), the refractive index of the medium (n), the geometric factor (κ^2) which accounts for the relative dipole orientation between the donor and acceptor, and the interfluorophore distance r.

$$k_T = \frac{\Phi_f^D \kappa^2}{\tau_d^D r^6}\left(\frac{9000(ln10)}{128\pi^5 N_A n^4}\right)J(\lambda) \tag{1.1}$$

The Förster radius (R_0) (**equation 1.2**), a most popular variable in bulk and single molecule FRET studies, can be defined as the interfluorophore distance (r) at which 50% of the energy is transferred to the acceptor. Then, **equation 1.1** can be simplified to **equation 1.3**.

$$R_0 = \left(\Phi_f^D \kappa^2 \left(\frac{9000(ln10)}{128\pi^5 N_A n^4}\right)J(\lambda)\right)^{1/6} \tag{1.2}$$

$$k_T = \frac{1}{\tau_d^D}\left(\frac{R_0}{r}\right)^6 \tag{1.3}$$

The efficiency of energy transfer is the fraction of energy of the donor that is transferred to the acceptor (quantum yield of energy transfer). It can be written in terms of the radiative (k_r) and non-radiative (k_{nr}) decay rate constants as well as k_T. Using **equation 1.3**, a direct relationship between distance and efficiency can be obtained **equation 1.4**.

$$E = \frac{k_T}{k_T + k_r + k_{nr}} = \frac{1}{1+\left(\frac{r}{R_0}\right)^6} \quad (1.4)$$

1.2.3 FRET in the presence of PIFE; the apparent incompatibility.

In **section 1.2.1**, we have shown that the PIFE technique relies on the decreased photoisomerization rate of Cy3. This decreased rate directly impacts the recorded intensity for this fluorophore in the form of an increased fluorescence quantum yield. In FRET experiments Cy3 is usually used as a donor dye. We have also shown in **section 1.2.2** that the efficiency of energy transfer can be directly related to the interfluorophore distance (**equation 1.4**). This relationship is only valid if the Forster radius (R_0) remains unchanged. Therefore, a change in the fluorescence quantum yield of the donor dye as in PIFE experiments will modify R_0. It follows that PIFE experiments would interfere with FRET experiments, making them apparently incompatible. In **chapter 2** we demonstrate theoretically and experimentally that PIFE and FRET are compatible techniques as we developed a strategy to measure FRET in the presence of PIFE associated fluctuations. Furthermore, we were able to extract the fluctuation in the fluorescence quantum yield of the donor when performing FRET experiments.

1.2.4 Fluorescence Quenching *via* Photoinduced electron transfer (P*e*T)

The first singlet excited state of a closed shell organic fluorophore (S_1), compared to its ground state (S_0), is simultaneously more prone to both accept and donate an electron. This becomes evident when examining the gas phase energetic diagram in **Figure 1.4**. Upon excitation, an electron is promoted from the HOMO to the LUMO. The new electronic configuration, with a semi occupied HOMO, causes an increase in the energy released when injecting an electron into the fluorophore (green arrows, electron affinity, EA), facilitating the acceptance of an electron. On the other hand, the semi occupied LUMO causes a decrease in the required energy to remove an electron from the fluorophore (blue arrows, ionization potential, IP), facilitating electron donation. Indeed, life as we know it relies on this paradigm to enable both the oxidation of water to oxygen and the reduction of CO_2 to sugars as porphyrins within the photosynthetic reaction center become photoexcited, providing the necessary driving force for these two redox reactions to take place, i.e., ensuring these reactions are thermodynamically feasible.

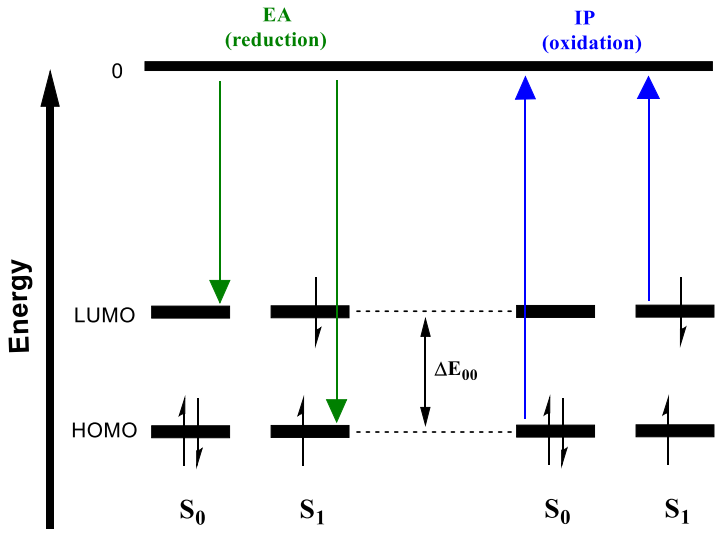

Figure 1.4. Comparison of the electron affinity (EA) and ionization potential (IP) of a molecule in the singlet ground state (S_0) and singlet excited state (S_1).[32]

1.2.4.1 Thermodynamics of P*e*T

A photoinduced electron transfer reaction can only occur if, upon fluorophore photoexcitation, it is thermodynamically favoured i.e. $\Delta G < 0$. HOMO and LUMO energy levels are key to anticipate the direction of the electron transfer. In the case of photoinduced reduction of the fluorophore (**Figure 1.5, left**), the excited fluorophore acts as the acceptor species, as its half-filled HOMO lies lower in energy than the HOMO of the donor. In the case of photoinduced oxidation of the fluorophore (**Figure 1.5, right**), the excited fluorophore acts as the donor species, as its half-filled LUMO lies higher in energy than the empty LUMO of the acceptor.

In gas phase, the free energy of the P*e*T reaction is given by **equation 1.5** and depends on the ionization potential $(IP)_D$, the electron affinity $(EA)_A$, and the electronic excitation energy of the fluorophore ΔE_{00}. This equation only provides a good representation of a gas system as it does not consider the solvation of the species at play.

$$\Delta G^{o}_{PeT} = (IP)_D - (EA)_A - \Delta E_{00} \qquad (1.5)$$

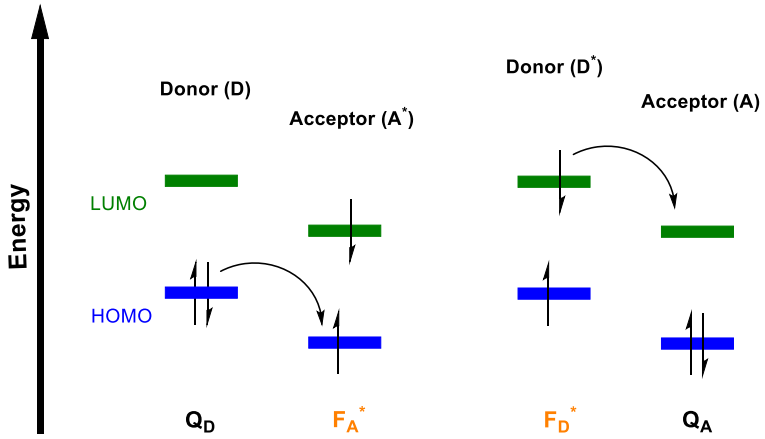

Figure 1.5. P*e*T between a photoexcited fluorophore F* and a quencher (Q). The photoexcited fluorophore (F^*) can act as an electron acceptor (A) (left) as well as an electron donor (D) (right).

In solution, the free energy of the P*e*T reaction is given by **equation 1.6**.[33-34] Here, $(IP)_D$ and $(EA)_A$ are replaced by the reduction potential of the donor ($E^o_{D^{*+}/D}$) and acceptor ($E^o_{A/A^{*-}}$), respectively. In the first term in **equation 1.6** n and F are the number of transferred electrons and the Faraday constant, respectively. The last term in **equation 1.6** accounts for the Coulombic energy released associated with bringing two particles of opposite charge close together. This correction term depends on the dielectric constant of the solvent (ε), and the distance between the two charges (r). It also includes the Avogadro's number (N_A), the charge of the electron (e), and the permittivity of the vacuum (ε_o).

$$\Delta G^o_{PeT} = \left(E^o_{D^{*+}/D} - E^o_{A/A^{*-}}\right) nF - \Delta E_{00} - N_A \frac{e^2}{4\pi\varepsilon_o \varepsilon r} \tag{1.6}$$

1.2.4.2 Rate constant of P*e*T

The rate constant of P*e*T can be estimated by the Marcus Theory of electron transfer.[35] In this approach, the free energy of the system is plotted as a function of the nuclear geometry along the reaction coordinate (**Figure 1.6**). Upon excitation, a fluorophore undergoes a vertical transition (Franck-Condon), followed by vibrational relaxation. Electron transfer occurs at the intersection (TS) of the excited-state and radical (ion when applicable) pair potential-energy curves.

Marcus derived an expression that relates the ensuing thermodynamics of electron transfer with the kinetic parameters (**equation 1.7**). Photoinduced electron transfer processes are a particular

case where his models can be applied. In Marcus theory, the activation Gibbs free energy of the electron transfer reaction ($\Delta G^{\neq}_{PeT}$) is expressed in terms the Gibbs free energy of the reaction (ΔG^{o}_{PeT}) and the reorganization energy (λ).

$$\Delta G^{\neq}_{PeT} = \frac{(\Delta G^{o}_{PeT}+\lambda)^2}{4\lambda} \quad (1.7)$$

The reorganization energy (λ) is the energy required to force the products (**Figure 1.6, top right**) to have the same nuclear configuration as the reactants (**Figure 1.6, top left**). It is essentially given by the energy difference in the harmonic corresponding to products, evaluated at the equilibrium position of the products and at the equilibrium position of reactants. λ can be separated into two contributions (**equation 1.8**).[32, 36-37] The first contribution (λ_{inner}) arises from the reorganization of the inner coordinates of reactants and products. The second contribution (λ_{outer}) arises from the reorganization of the solvent around the reactants and products.

$$\lambda = \lambda_{inner} + \lambda_{outer} \quad (1.8)$$

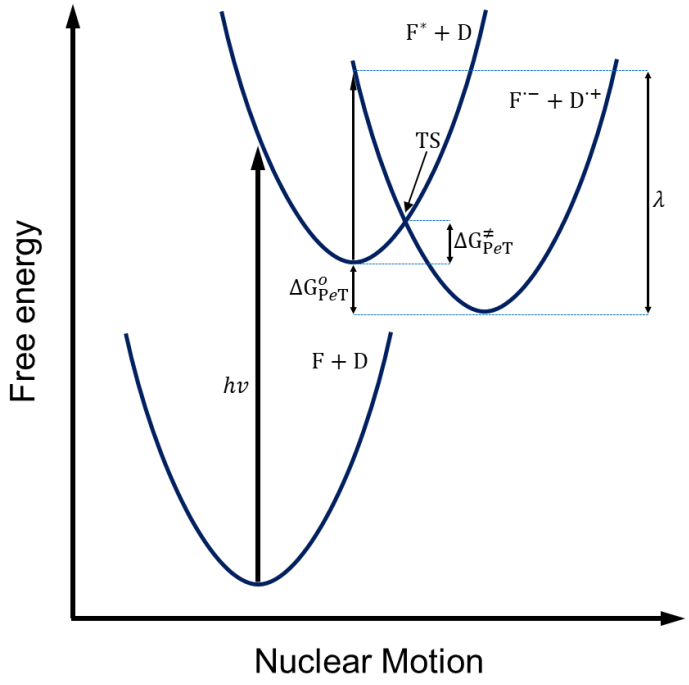

Figure 1.6. P*e*T visualized as the intersection of harmonic potential-energy curves.

In the context of transition state theory, the rate constant of P*e*T can be written as in **equation 1.9**. Here, in the adiabatic regime, ν_N is an effective frequency for nuclear motion along the reaction

coordinate and κ is the transmission coefficient (probability that reagents upon reaching the transition state, will proceed to the formation of products).[35, 38]

$$k_{PeT} = v_N \kappa e^{-\left(\frac{\Delta G^{\neq}_{PeT}}{RT}\right)} \quad (1.9)$$

As we will see in chapter 3, **equations 1.8 and 1.9** will be useful to calculate activation Gibbs free energies of the photoinduced electron transfer between β-mercaptoethanol and Cyanine dyes in the context of photostabilization and photoswitching. Additionally, activation Gibbs free energies can be correlated with rate constants of P*e*T (**equation 1.9**) to explain the different capacities of β-mercaptoethanol to quench triplet excited states of cyanine dyes.

1.3 Single Molecule Fluorescence Imaging Techniques

Fluorescence is an extremely sensitive technique: nowadays, using the appropriate instrumentation, even single emitters can be detected with nanometer precision and high temporal resolution for extended periods of time. These and many other unique properties of fluorescence and associated single molecule fluorescence (SMF) imaging techniques have allowed scientists to uncover a wealth of previously inaccessible information pertaining to the nanoworld.

In this section we will introduce the reader to single molecule techniques. In **section 1.3.1**, we will provide a brief historical overview of the early detection of single molecules. In **section 1.3.2**, we will discuss the importance of the single molecule approach. Next, in **sections 1.3.3-1.3.4**, we will introduce the reader to two powerful single molecule techniques: single molecule Förster resonance energy transfer (smFRET) and single molecule protein induced fluorescence enhancement (smPIFE). smFRET and smPIFE are the most utilized and powerful single molecule techniques to study the dynamics of proteins and oligonucleotides, as well as their interactions with one another. Finally, in **section 1.3.5**, we will familiarize the reader with super resolution (SR) techniques, with special emphasis on single molecule localization microscopy (SMLM) and the use of organic fluorophores.

1.3.1 Early Detection of Single Molecules

In 1952, Erwin Schrödinger wrote: "*[…] we never experiment with just one electron or atom or (small) molecule. In thought-experiments we sometimes assume that we do;*"[39] Within less than 40 years, this statement was proven to be wrong.

In 1989, Moerner and Kador detected, for the first time, the absorption of a single dye molecule (pentacene) embedded in organic crystals, at liquid helium temperatures.[40] Shortly after, in 1990, Orrit and Bernard, using the same molecular system and low temperatures, were able to detect for the first time a single dye molecule, however, now via a more sensitive method, fluorescence.[41] Soon after, single molecules were detected at room temperature via fluorescence, paving the way to study biomolecules in more suitable conditions such as room temperature and in aqueous solutions. In 1990, Keller and co-workers performed experiments at room temperature in aqueous solutions and achieved detection of single Rhodamine 6G (R6G) molecules passing through a small detection volume.[42] The next milestone was achieved in 1993, when near-field scanning optical microscopy (NSOM) was utilized by Betzig to image individual carbocyanines at room temperature.[43] In 1994, using NSOM, the first single molecule photobleaching, using Rhodamine 6G, was reported by Keller and colleagues.[44] Single molecule imaging was soon extended to far-field techniques such as total internal reflection fluorescence (TIRF) (1995),[45] widefield epifluorescence (1996),[46] and confocal microscopy (1996).[47] In order to maximize the amount of information of the system under study, many aspects associated with the emitted photons were analysed, including location, polarization, time dependence, and spectral content.[48] Since the first detection of single molecules, single molecule spectroscopy and microscopy has inspired numerous research approaches that brought the concept of single molecule observation to the realms of physics, chemistry, and biology.[49]

1.3.2 Single Molecule vs Ensemble Techniques

The most fascinating characteristic of single molecule methods, compared to ensemble techniques, is that for any given property under study, one will obtain the moments of the distribution, instead of only the mean value as available from bulk studies. Thus, a more complete description of the system as provided by the distribution of values will be attained. In this context, static and dynamic

heterogeneity can be directly accessed from individual molecules. This is particularly important when studying biomolecules as they are intrinsically heterogeneous.[50]

Static heterogeneity appears when an ensemble of (bio)molecules consists of stable subpopulations that are unable to interconvert during the observation time (**Figure 1.7, panel a**). Molecular subpopulations, within the species of interest, can reveal different conformations as well as affinities for the substrate. Additionally, visualization of static heterogeneity allows to focus on the species of interest, and judiciously remove subpopulations such as aggregates, single labeled, and free or inactive species.

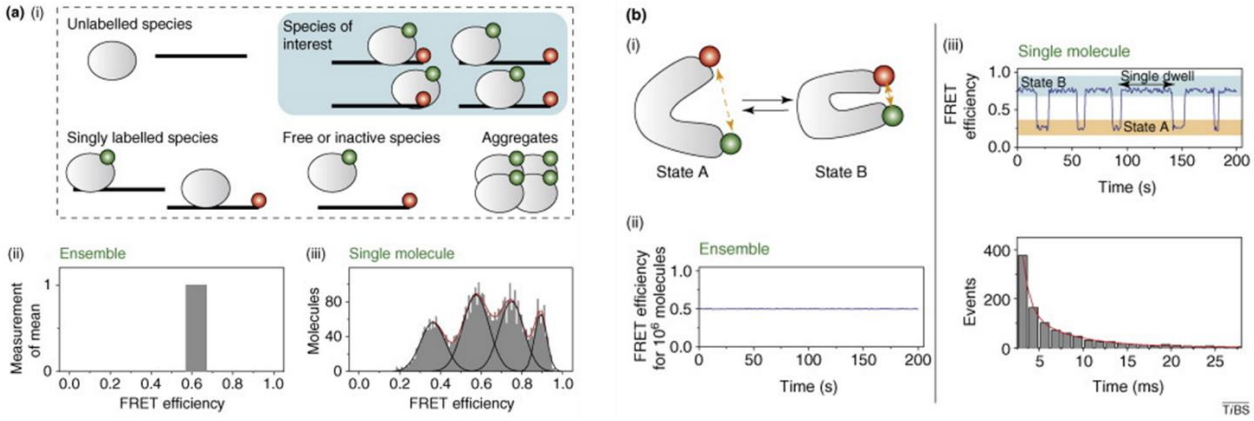

Figure 1.7 Comparison of ensemble and single molecule approaches in terms of static and dynamic heterogeneity.(a) Example of static heterogeneity utilizing a donor-acceptor labeling strategy to visualize the system via a FRET experiment. (i) labeled species can report on subpopulations such as free, inactive, unlabeled and aggregated components and doubly labeled species that constitute the species of interest (ii) an ensemble experiment of FRET efficiency reports a single value (iii) single molecule experiment allows to recover data that includes the subpopulations of interest (b) Example of dynamic heterogeneity where (i) an enzyme is double labeled to study the dynamic interchange of conformational states (ii) an ensemble experiment of FRET efficiency reports a single value over time (iii) single molecule trajectories of FRET efficiency allows to monitor a single enzyme over time providing a direct observation of the interconversion of conformational states. Here, statistical analysis of dwell times allows to obtain the average lifetime of each conformation. Adapted with permission from Kapanidis *et al*., *Trends Biochem. Sci.* **2009**, 34, 234. Copyright 2009 Elsevier.

In turn, dynamic heterogeneity is exhibited when an ensemble of (bio)molecules consist of subpopulations that are able to interconvert during the observation time (**Figure 1.7, panel b**). Considering an enzyme that can interconvert between two different conformations: provided that the interconversion is slow when compared to the temporal resolution of instrument,

interconversions between the states can be directly observed and quantified. The study of multi-step biomolecular systems with different kinetic rates associated to each step is extremely challenging, as even with all molecules starting simultaneously, the stochastic nature of the individual states will cause rapid desynchronization. When tracking single molecules, the problem of desynchronization disappears, allowing to extract the kinetic rates of the different processes.

An additional advantage of single molecule studies relies on the minute amounts of sample required to carry out experiments, where usually only few hundreds of molecules are required to perform a reliable statistical analysis. Given the power of the single molecule approach, single molecule fluorescence techniques have been utilized to answer an increasing number of fundamental questions. Our own research group has implemented their application to study the replication machinery of relevant viruses,[51-53] DNA nanostructures,[54-61] and optoelectronic materials.[62-64]

1.3.3 Single Molecule Imaging Setup: Total Internal Reflection Fluorescence Microscopy

Wide field microscopy is a powerful technique where a significantly large area (typically around 80^2 um^2) is illuminated allowing to image hundreds of single fluorescent molecules simultaneously. Here, fluorescence is collected, filtered, and directed to an array detector. The most utilized array detectors for widefield single molecule imaging are electron multiplying charge-coupled device EMCCD, and, recently, scientific complementary metal oxide semiconductor (sCMOS) cameras.[65]

One of the most widely used modes of widefield microscopy is epi-fluorescence microscopy. In this type of microscopy, the same lens (objective) is used to both illuminate and collect the emitted light from a sample, allowing to minimize the amount of excitation light entering the detector.

Two illumination modalities in SMFM can be described; standard and total internal reflection fluorescence (TIRF) microscopy (**Figure 1.8, left and middle panels**). In the standard mode, a collimated gaussian-shaped beam passes through the sample perpendicularly to the coverslip plane, maximizing the amount of illumination.[66] The standard mode is useful when imaging thick samples (over 10 μm deep). However, the intense illumination and excitation of molecules outside the focal plane can produce images with significant background from out of focus illumination,

lowering image contrast. This latter problem is addressed in TIRF microscopy, where only the thin layer of an evanescent wave is used for illumination, effectively removing background signal from out of focus illumination (**Figure 1.8, middle and right panels**).[67-69]

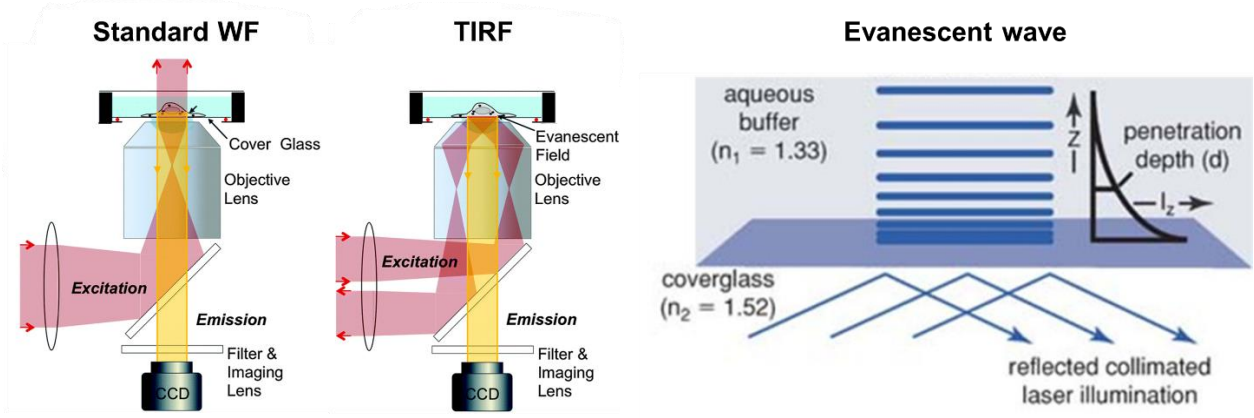

Figure 1.8 Widefield epi-fluorescence microscopy setup. a) Standard widefield illumination (b) total internal reflection fluorescence (TIRF) illumination. (c) The evanescent wave generated when the incident beam utilized is engaged at an angle higher than the critical angle. Adapted with permission from Park *et al*., *Chem. Soc. Rev.*, **2015**, 44, 1302. Copyright 2015 Royal Society of Chemistry.

In TIRF microscopy, the laser beam is focused off-axis at the back focal plane of the objective lens, causing the beam to approach the sample at an angle (**Figure 1.8, middle panel**). The light then exits the objective in the form of a collimated beam and passes through an immersion oil that matches the refractive index of the glass coverslip utilized to immobilize the fluorescent sample (n_{glass}~1.52). The excitation beam propagating through the coverslip then reaches the glass-water interphase causing a change in the direction of the beam (n_{water}~1.33). At angles of incidence higher than the critical angle (θ_c) the beam undergoes total internal reflection (TIR). Utilizing Snell's law (**equation 1.10**), the critical angle can be calculated. Here n_1 and n_2 are the refractive indices of the sample solution and the coverslip, respectively.[70]

$$\theta_c = sin^{-1}\left(\frac{n_1}{n_2}\right) \tag{1.10}$$

When the beam undergoes TIR, the excitation beam is reflected off the coverslip-water interface back into the cover slip. However, some of the incident energy penetrates through the interface, creating a standing wave called the evanescent field/wave.

The intensity of this evanescent wave (I_z) drops exponentially as a function of the distance from the glass-water interphase (z) (**equation 1.11**). Here, I_0 is the intensity of the evanescent field at $z = 0$ and d the penetration depth of the evanescent field as defined by (**equation 1.12**). The value of d depends on the wavelength of the incident light in vacuum λ_0, and the refractive indices of the two media ($n_1$and n_2).[71]

$$I_z = I_0 e^{-z/d} \tag{1.11}$$

$$d = \frac{\lambda_0}{4\pi}(n_2^2 \sin^2\theta - n_1)^{-1/2} \tag{1.12}$$

The main asset of the evanescent wave in TIRF illumination mode is that only fluorophores that are close to the coverslip-water interface are excited while those residing further out in the bulk are not, effectively minimizing the volume of sample producing interfering background. In a typical single molecule TIRF assay, fluorescently tagged molecules of interest are surface immobilized. As we will see in **section 1.4** and **chapter 4**, this poses challenges to the field of surface chemistry as nonspecific binding of fluorescent molecules can increase the fluorescence background, limiting signal to noise ratio.

1.3.4 Single Molecule Förster Resonance Energy Transfer (smFRET)

Förster Resonance Energy Transfer (FRET) is a unique phenomenon that results in fluorescence signals which are sensitive to fluorophore positional changes in the 1–10 nm range. This length scale is particularly important as it allows to study structures and dynamics of the nanoscopic world, where many macromolecules of biological relevance operate.

In 1996, the first detection of FRET at the single molecule level was achieved by the Weiss group.[72] Since then, smFRET has been utilized to study a variety of biomolecules and associated biological processes including replication, recombination, transcription, translation, RNA folding and catalysis, DNA dynamics, protein folding and conformational changes, several motor proteins, membrane fusion proteins, ion channels, and signal transduction.[73-79] This impressive number of problems that have been tackled via smFRET represents only but the tip the iceberg. As single molecule techniques become more prevalent, with ongoing improvements in data analysis, fluorophore photophysics and photostability, and surface passivation, one may only anticipate that

an ever increasing number of biological, chemical and physical problems will be tackled with smFRET and single molecule in general-based techniques.

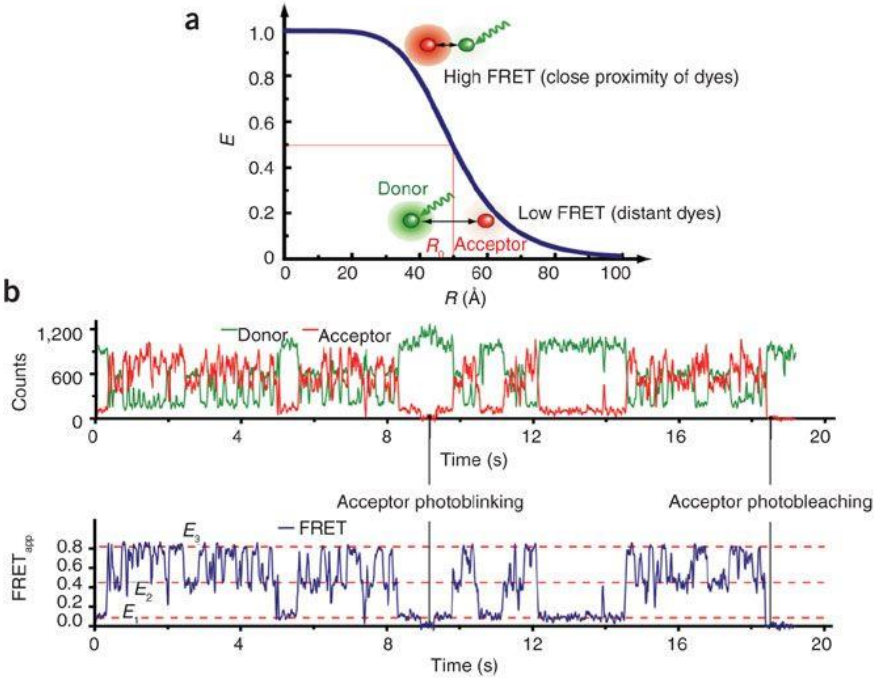

Figure 1.9 Illustration analytical prediction and experimental data of FRET. Efficiency of energy transfer vs inter-dye distance separation for a Förster radius $\boldsymbol{R_o}$= 5 nm. b) single molecule intensity-time trajectories for donor (green) and acceptor dye (red) and the calculated proximity ratio $\boldsymbol{E_{pr}}$ (blue). Reprinted with permission from Roy *et al*., *Nat. Meth.* 2008, *5*, 507. Copyright 2008 Nature Publishing group.

In a single pair FRET assay, a pair of fluorescent molecules, donor and acceptor, is attached to the biomolecule(s) to be studied. Energy transfer, via dipole-dipole interaction, leads to a decrease in the donor emission and simultaneously to an increase in the acceptor emission. The energy transfer efficiency E is given by $E = 1/(1 + (r/R_o)^6)$, where r is the donor-acceptor inter-dye distance and R_o the Förster radius at which $E = 0.5$ (**Figure 1.9, panel a**). The Förster radius R_o is commonly found to be 3 to 8 nm, making FRET sensitive to changes of a few nanometers in the donor-acceptor distance. Experimentally, E is typically approximated by the proximity ratio E_{pr} (or FRET apparent), defined as the ratio of acceptor intensity to total emission intensity $E_{pr} = I_A/(I_D + I_A)$. [80-82] At the single molecule level, intensity-time trajectories of anticorrelated signals

provide a measure of the intra- and intermolecular motion of biomolecules in real time (**Figure 1.9, panel b**). An important advantage of FRET is its ability to measure the internal distance of the donor-acceptor, independent of the center of mass movement of the molecular system, making it very insensitive to instrumental drift.

1.3.4.1 smFRET on Viral Replication Machinery

Many research laboratories, including ours, have successfully utilized smFRET to study key enzymes involved in the viral replication machinery of viruses.[83] Our research group, in collaboration with the Götte group, is particularly interested in blood-borne viruses affecting humans such as the human immunodeficiency virus (HIV)[52] and the hepatitis C virus (HCV).[51, 53, 84]

A great example to illustrate the power of smFRET for the study of viral polymerases has been reported by the Zhuang group. They have studied the reverse transcriptase, which is a multifunctional enzyme belonging to the HIV that contains polymerase (Pol) and ribonuclease H (RNase H) subunits. It transcribes the viral RNA into double-stranded DNA. In a first step, as the complementary DNA strand is synthesised, the template RNA is cleaved from the RNA/DNA hybrid by the RNase H subunit. smFRET studies involving reverse transcriptase labeling (with a green dye) and primer/template duplexes labeled (with a red dye) were used to interrogate the dynamics of enzyme substrate (**Figure 1.10, panel a**). Real time binding/unbinding events as well as orientational and translational dynamics were revealed. Reverse transcriptase was reported to slide on nucleic acid duplexes, rapidly shuttling between opposite duplex termini. Importantly, upon reaching the DNA 3’ terminus, reverse transcriptase can flip into a polymerization orientation.[85] In a related report, authors showed that the enzyme adopted opposite binding orientations, flipped by 180 degrees, on duplexes containing DNA or RNA primers, directing its DNA synthesis or RNA hydrolysis activity, respectively.[86]

In our own work, we have focused on the use of smFRET (and smPPIFE) to study the viral replication machinery of Hepatis C virus (HCV) a member of the *Flaviviridae* family. This family of viruses, including Dengue (DENV), Zika (ZIKV), and Bovine Viral Diarrhea (BVDV), represents a major health threat and economic challenge.

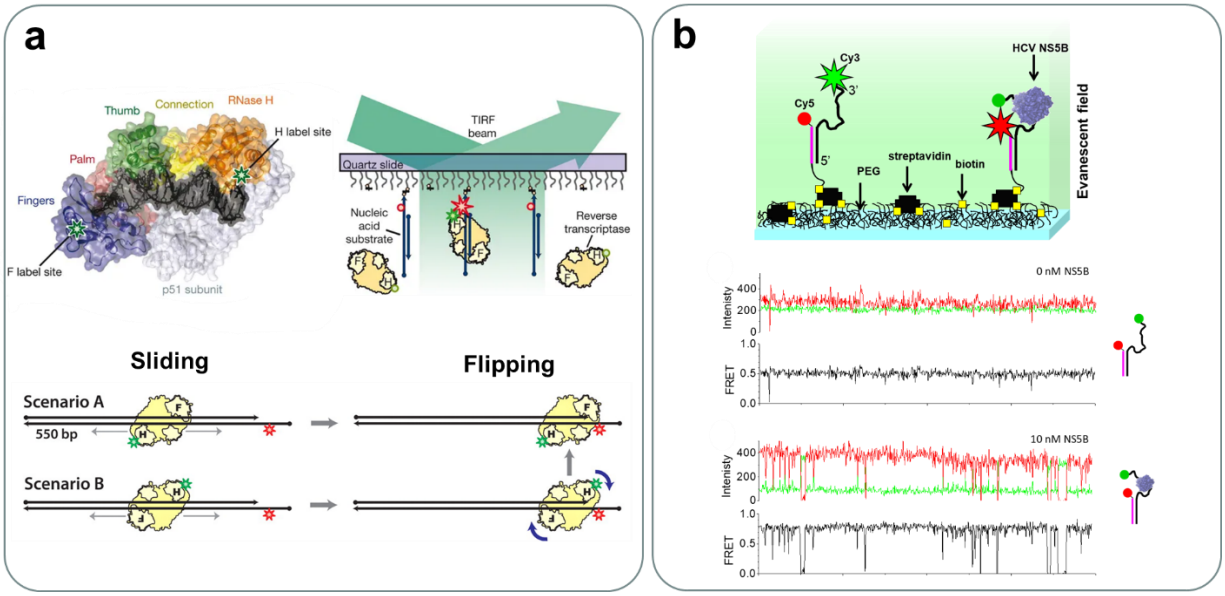

Figure 1.10 smFRET assays to study viral proteins of HIV and HCV a) smFRET experimental design to monitor the dynamics of reverse transcriptase. b) smFRET experimental design to monitor the dynamics of NS5B. Adapted from Liu *et al*. *Science* **2008**. 322, 1092; Abbondanzieri *et al*. *Nature*. **2008**. 453, 184; Karam *et al*. *J. Biol. Chem.* **2014**, 289, 14399. Copyright 2008 American Association for the Advancement of Science, 2008 Springer Nature, 2014 American Society for Biochemistry & Molecular Biology.

The non-structural 5B (NS5B) protein of HCV is an RNA dependent RNA polymerase (RdRp), essential for viral replication. NS5B catalyses the conversion of the (+) single-stranded RNA genome of HCV into double-stranded RNA. *In vitro* studies have shown that this task can be performed through both a primer-dependent and a remarkable primer-independent mechanism. [87-90] How these enzymes locate the 3′-terminus of the RNA template, however, remains an unsolved question. In a first approach to investigate NS5B dynamic behavior via single molecule methods, Karam *et al.* reported a smFRET assay to study NS5B-RNA binary complexes in real time (**Figure 1.10, panel b**).[51] An advantage of this platform is the ability to work with unlabeled enzymes, enabling rapid monitoring and screening of NS5B mutants with substitution at various different residues, including drug resistant forms.

Karam *et al.* reported that in the absence of NS5B, average FRET values derived from single molecule intensity-time trajectories were centered around 0.5. Upon NS5B (wild type) incubation, average FRET values increased to 0.75, indicating a bound enzyme to RNA. The data is consistent

with a stable binary complex that extend over prolonged periods of time. Additionally, mutations in close proximity to the template entrance, and in the center of the RNA binding channel, reduced the population of RNA-bound enzyme. Similar observations were reported with an allosteric nonnucleoside NS5B inhibitor.

The smFRET assay reported by Karam *et al.* is an extraordinarily simple and effective assay to study binding/unbinding dynamics of NS5B-RNA complexes. However, it does not provide precise information on NS5B dynamics once bound to RNA. This information is key to study mechanistic questions related to *de novo* initiation, a shared characteristic of several polymerases of viruses belonging the *Flaviviridae* family such as DENV, BVDV, and ZIKV.[91-93] Mechanistic knowledge on this process can be key to develop antiviral drugs with improved efficacy.

In **chapter 5**, inspired by this smFRET assay, we report a single molecule protein induced fluorescence enhancement (smPIFE) assay (**see section 1.3.5**). The smPIFE assay is a simpler yet more powerful assay to precisely study short scale (couple of nanometers) movements of NS5B once bound to its RNA substrate. Application of this technique has expanded our understanding of key mechanistic aspects of NS5B-RNA complexes preceding *de novo* initiation, including RNA binding/unbinding and sliding. It also has allowed us to study the effect of a divalent ion such as Mg^{2+} on the stability and dynamics of NS5B and its RNA substrate.

1.3.5 Single Molecule Protein Induced Fluorescence Enhancement (smPIFE)

Protein Induced fluorescence enhancement (PIFE) has emerged as a complementary technique to FRET to study conformational changes involving proteins and nucleic acids.[23-24] PIFE relies on the fluorescence enhancement of a fluorophore, typically Cy3, when a protein is located in close proximity. Upon excitation, Cy3 can undergo a rapid photoisomerization that can compete with fluorescence **(Figure 1.11, panel a)**. As a result, Cy3 bears a modest fluorescence quantum yield (0.04-0.09)[25, 29] in aqueous solution. A protein in close proximity however can increase the microenvironmental steric hindrance and/or viscosity, decreasing the rate at which Cy3 undergoes photoisomerization.[94] As a result, the fluorescence quantum yield/intensity of Cy3 increases as a function of protein-Cy3 distance, allowing to sense changes in distances below 4 nm. **(Figure 1.11, panel b)**.

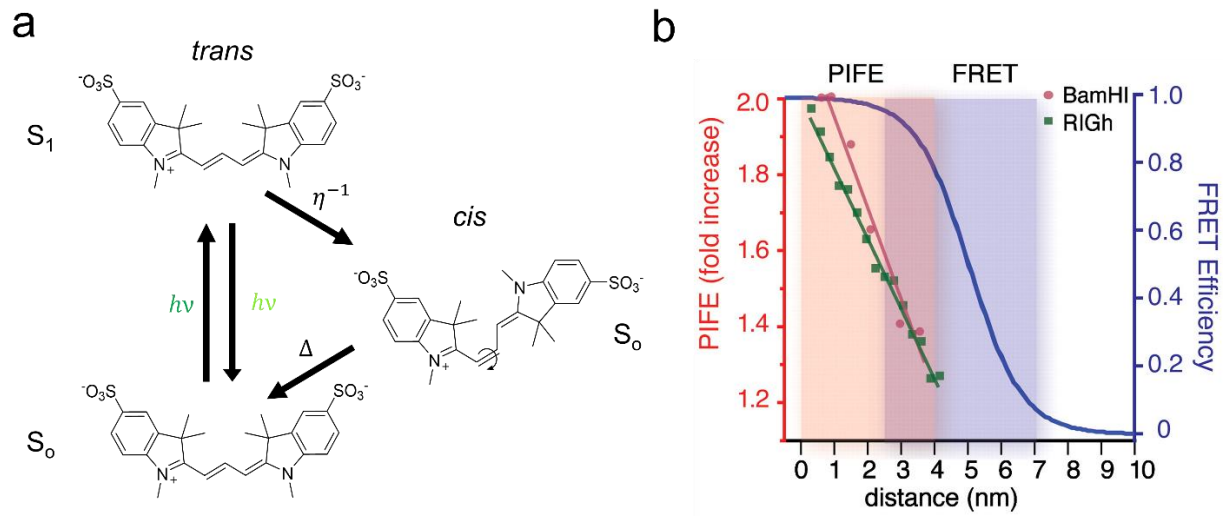

Figure 1.11 a) trans-cis photoisomerization of Cy3 competing with fluorescence. b) Comparison of distance sensitivity of PIFE and FRET. Adapted from Hwang *et al*. *Proc. Natl. Acad. Sci. U.S.A.* **2011** 108, 7414. Copyright 2011 National Academy of Sciences.

While FRET requires dual labelling of substrates (a donor and an acceptor), PIFE necessitates only a single fluorophore, which significantly simplifies experimental design. For example, to study protein-DNA systems, a FRET assay requires both the protein and the DNA to be labeled. While oligonucleotides are relatively simple to label, protein labeling is a complex task and it may alter the properties of the protein under study. Additionally, the elimination of the acceptor dye required for FRET, decreases the likelihood of signal artifacts due to the formation of transient dark species of the acceptor dye, as reported for the commonly used Cy5.[95-97]

Importantly, PIFE can also access a distance range difficult to asses using FRET assays (**Figure 1.11, panel b**). The main disadvantage of PIFE is that, unless previously calibrated,[23] it cannot provide quantitative information on the distance. Thus, the relative changes in intensity cannot be directly translated into changes in distance. However, a qualitative description of protein-dye distances is often sufficient to extract rich biophysical information. Overall, the simplicity and the working range of PIFE positions the technique as a powerful tool to study protein-DNA dynamics.

Many proteins, after binding, can slide on single and double stranded DNA and RNA. smPIFE was initially utilized to study the ATP dependent movement of the human antiviral protein, RIG-I (**Figure 1.12, panel a**).[98] Through an smPIFE assay, It was shown that RIG-I can translocate across a dsRNA repetitively, generating a single molecule trajectory with a sawtooth shape. In this

case, the need for only a single label was key to the experiment, as the authors reported that labelling of RIG-I was extremely challenging. Moreover, the high dissociation constant (>100 nM) required addition of high protein concentration. A labeled protein at ~100 nM would have generated a high intensity background via direct excitation of either the Dye-RIG-I in solution or the Dye-RIG-I non-specifically bound to the surface.

The working mechanism of Rep, an *E. coli* helicase involved in DNA recombination and repair, was initially studied via smFRET.[99] Authors reported FRET fluctuations and interpreted the data as Rep undergoing repetitive cycles of translocation of on ssDNA. Later, authors reported a smPIFE assay with data consistent with their previous findings (**Figure 1.12, panel b**).[98] The asymmetric peaks exhibited in the smPIFE trajectories arise from the 3' to 5' directed translocation followed by a fast snapping back of the protein.

The translocation of PcrA, a Rep homolog, was studied through smFRET and smPIFE assays.[100] PcrA was interrogated on a dsDNA bearing a ssDNA overhang (5' end) (**Figure 1.12, panel c**). The smFRET assays indicated that PcrA anchors to the duplex junction while it reels in 5' direction and is followed by release of the strand upon reaching the 5' end. smPIFE intensity-time trajectories confirmed the smFRET observation. Trajectories are characterized by asymmetric peaks showing a gradual increase, followed by a sudden drop in the Cy3 intensity (**Figure 1.12, panel c**). The pattern reflects that the sequential process of binding, reeling, and unbinding is continuously repeated.

Another example of oligonucleotide binding protein studies via smPIFE is the work on TAR RNA binding protein (TRBP), an enzyme implicated in antiviral signaling. TRBP exhibited an ATP-independent diffusion along dsRNA (**Figure 1.12, panel d**).[101] smPIFE trajectories are consistent with TRBP undergoing repetitive motion on a dsRNA. This behaviour was exclusive to dsRNA as TRBP was unable to bind on DNA:RNA hybrids or ssRNA strands.

In our lab smPIFE technique has been previously exploited to study the dynamics of binding and sliding of viral enzymes of important human pathogens such as the human immunodeficiency virus (HIV)[52] and hepatitis C Virus (HCV).[53]

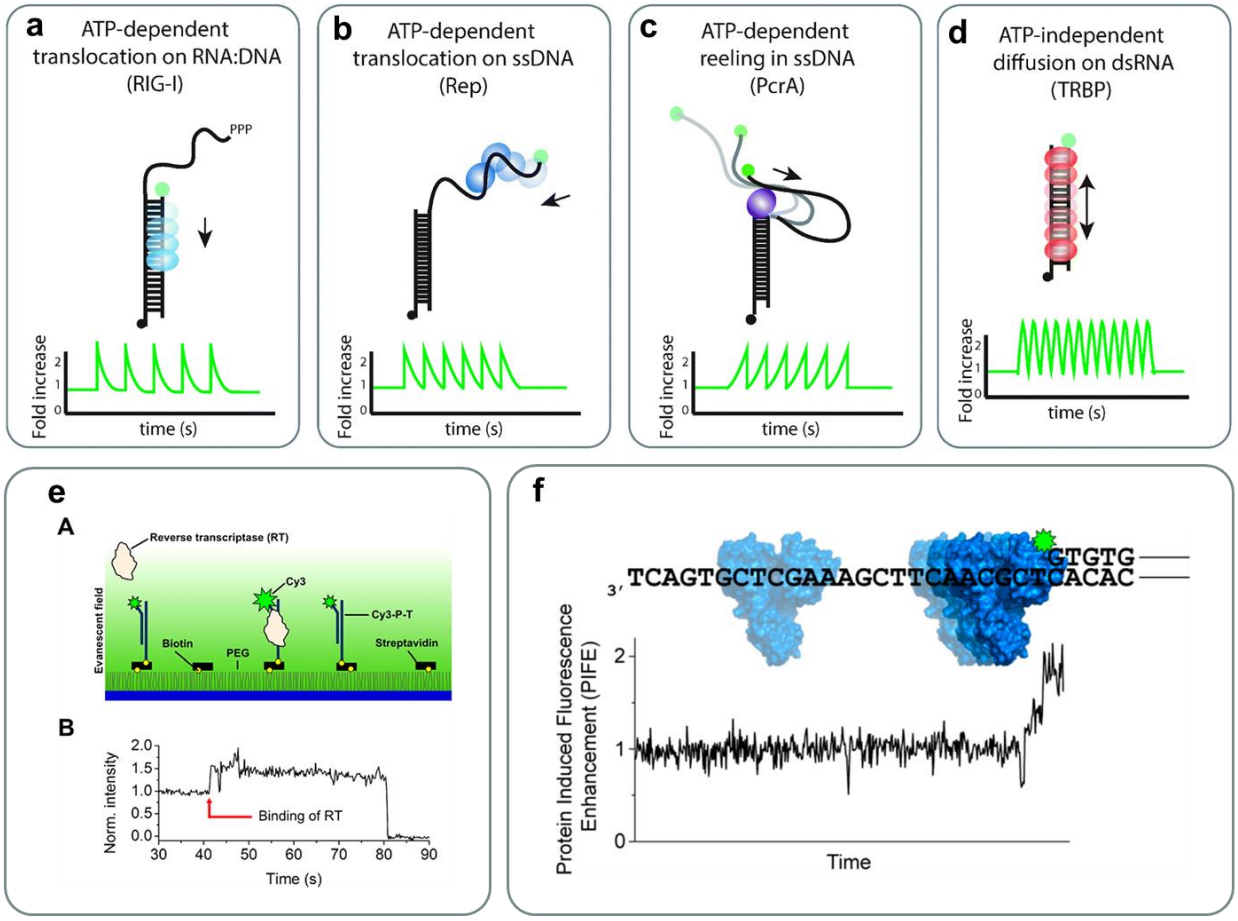

Figure 1.12 Examples of smPIFE assays to study motor proteins.smPIFE visualization of RIG-I translocation across dsRNA showing repetitive translocation. b) smPIFE measurements of Rep translocation is consistent with repetitive shuttling. c) smPIFE trace indicating a PcrA reeling in ssDNA in repetition. d) smPIFE trace reflects the rapid intensity fluctuations of the TRBP's diffusion along the dsRNA axis e) smPIFE binding trace reflects the rapid intensity fluctuations of the TRBP's diffusion along the dsRNA axis f) smPIFE trace reflects the rapid intensity fluctuations of the TRBP's diffusion along the dsRNA axis. Adapted from Hwang *et al. Chem. Soc. Rev.* **2014**, 43, 1221; Marko *et al. J. Phys. Chem. B.* **2013**, 117, 4560; Ablenas *et al. ACS Infect. Dis.* **2017**, 3, 99. Copyright 2014 Royal Society of Chemistry, 2013 American Chemical Society, 2017 American Chemical Society.

The reverse transcriptase (RT) of HIV plays a pivotal role in converting genomic RNA into proviral DNA. The biologically relevant form of RT is the p66–p51 heterodimer, however, two recombinant homodimer forms of RT, p66–p66 and p51–p51, are also catalytically active. smPIFE was previously utilized to investigate the binding of the three RT isoforms to a fluorescently labeled 19/50-nucleotide primer/template (P/T) DNA duplex (**Figure 1.12, panel e**).[52] Kinetic

analysis showed 50-100 times higher binding affinities of RTp66-p51 and RTp66-p66 by the P/T than the RTp51-p51.

The helicase domain of the non-structural 3 (NS3h) protein of (HCV) can unwind both dsRNA and dsDNA in an ATP-dependent manner. However, before unwinding, NS3h can bind and interact with oligonucleotides in an ATP-independent fashion. Ablenas in our group studied the binding and sliding dynamics of NS3h on a ssDNA overhang and its interaction with a ss/ds DNA junction (**Figure 1.12, panel f**).[102] smPIFE experiments revealed three enhancement levels that correspond to three discrete binding sites at adjacent bases to the ss/ds DNA junction. The enzyme is able to transition between binding sites in both directions without dissociating from the nucleic acid. Ablenas *et al*. proposed a dynamic model for NS3h that favors ATP-independent random binding and sliding by one and two nucleotides along the overhang of the single stranded loading region. In **chapter 5**, we extend our studies on viral enzymes and report a smPIFE assay to interrogate the binding and sliding dynamics of the non-structural 5B (NS5B) polymerase of the Hepatitis C Virus.

While most of the reported smPIFE studies have been carried out using Cy3, the PIFE effect has been also reported for other cyanine derivatives that are able to undergo photoisomerization such as DY547, Cy5 and Alexa dyes.[23, 98] Importantly, fluorescence enhancement is not limited to nearby proteins. When Cy3 (and related Cyanine fluorophores) are conjugated to nucleic acids, the quantum yield increases.[19-22] This phenomenon has been termed NAIFE, for nucleic acid induced fluorescence enhancement.[103]

1.3.6 Super-Resolution Microscopy

In 1873, Ernest Abbe postulated **equation 1.13**, expressing the best resolution achievable in optical microscopy.[104] Resolution in optical microscopy is the shortest distance between two point objects at which they can still be distinguished by the observer or camera system as separate entities. In Abbe's equation the resolution (Δx_{min}^{Abbe}) depends on the imaging wavelength (λ), the refractive index of the imaging medium (n), and half the aperture angle of the objective (α). In **equation 1.13,** ($n \sin \alpha$) is usually referred as the numerical aperture of the objective (NA).

$$\Delta x_{min}^{Abbe} = \frac{\lambda}{2n \sin \alpha} = \frac{\lambda}{2NA} \tag{1.13}$$

Abbe's equation takes into account the diffraction of light. This is a physical limitation that makes point emitters appear larger in size. The largest values of NA for state-of-the-art, highly corrected microscope objectives are in the range of about 1.3–1.6, with little room for improvement. Therefore, the spatial resolution of optical imaging has been limited to about ~200 nm for visible light of 600 nm wavelength. Given the purely physical basis underlying the resolution limit, it was thought to be impossible to overcome.

Working separately Eric Betzig, Stefan Hell, and William E. Moerner demonstrated that the diffraction-limited resolution can be circumvented to transform optical microscopy into nanoscopy. Their work ultimately led to them be jointly awarded the 2014 Nobel Prize in Chemistry "*for the development of super-resolved fluorescence microscopy*". Two different strategies were proposed; Hell's approach uses patterned illumination to spatially control the emission of excited fluorophores.[105-107] The second approach takes advantage of the detection of single molecules[40] and combines a strategy to achieve precise localization down to few nanometers with a strategy to achieve sequential localization of many single molecules.[108-109]

The super resolution single molecule-based approach consists of a combination of two key ideas. The first idea relies on the fact that a diffraction limited spot of a single emitter, which is around 200 nm in size, can be localized with a much higher precision (**Figure 1.13, a-d**). A diffraction limited spot or point spread function (PSF) can be described by an airy function (**Figure 1.13, a**). The detection of a PSF over many pixels (**Figure 1.13, b**) allows to fit a 2D function, where the airy function can be approximated by a Gaussian function to localize the centroid (**Figure 1.13, c**).[46, 110] The localization precision of a single emitter Δx is given by **equation 1.14**, where N is the number of detected photons, s is the standard deviation of the PSF, a is the size of the camera pixel edge length and b is background noise.[111] Utilizing **equation 1.13 and 1.14**, and assuming that $s \approx \Delta x_{min}^{Abbe}$, a new equation can be obtained to incorporate the improved localization precision (**equation 1.15**).

$$\langle(\Delta x)^2\rangle = \frac{s^2+a^2/12}{N} + \frac{4\sqrt{\pi}s^3b^2}{aN^2} \approx \frac{s^2}{N} \tag{1.14}$$

$$\Delta x \approx \frac{\lambda}{2NA\sqrt{N}} \tag{1.15}$$

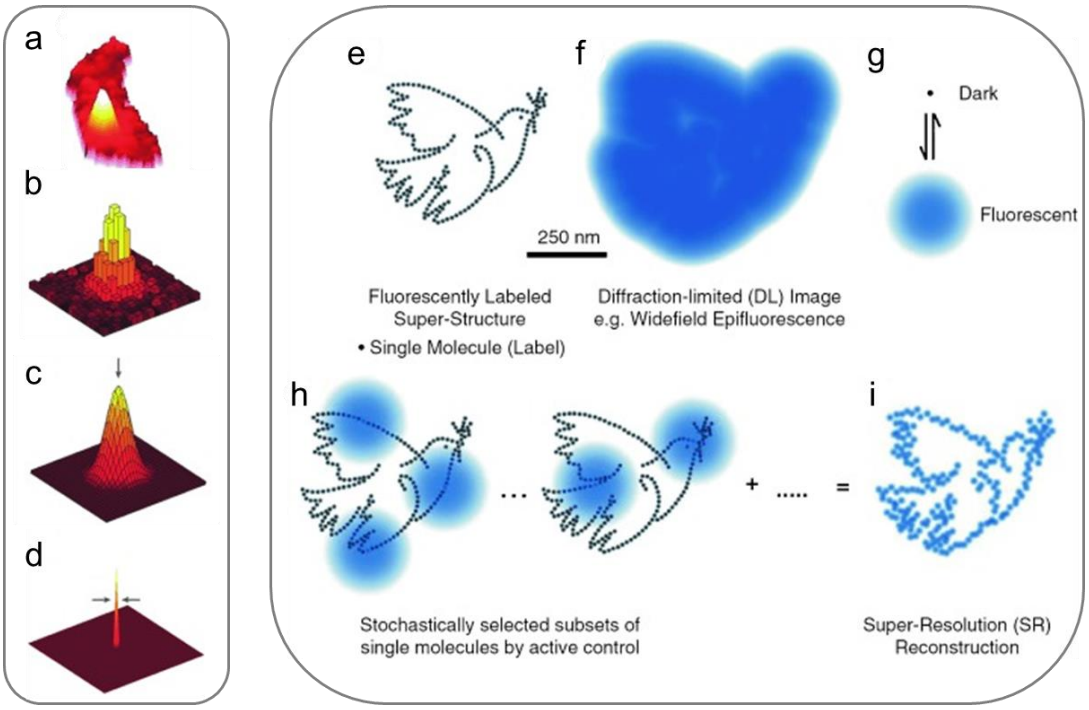

Figure 1.13 . Key ideas of single molecule based super resolution microscopy. a-d) Diffraction-limited spot and its centroid localization. e-i) active control of emitters and sequential localization.[112] Adapted with permission from Möckl *et al*., *Angew. Chem.* **2014,** *53,* 13972. Copyright 2014 John Wiley and Sons.

Importantly, **equation 1.15** predicts that with only 100 detected photons, the localization precision is enhanced by ten-fold (**Figure 1.13, d**). This allowed tracking single molecules with nanometer accuracy when they were sparsely distributed and separated by a distance greater than the diffraction limit. In 2003, Selvin and co-workers took advantage of this improvement to visualize Myosin V, a dimeric molecular motor that moves processively on actin filaments. The authors labeled myosin V with a single fluorophore at different positions and measured the step size with a standard deviation smaller than 1.5 nm. Their results strongly support a hand-over-hand model of motility, instead of an inchworm model, a matter of debate among scientists at that time.[113]

While localization precision is greatly enhanced for sparsely separated emitters fluorophores, this task becomes challenging for multiple fluorophores separated by distances below the diffraction limit (**Figure 1.13, e**). Here, signal overlap inhibits the precise localization of individual fluorophores (**Figure 1.13, f**).

The second key idea in the single molecule-based super resolution microscopy approach circumvents this problem by simply not allowing all the molecules to emit at the same time. As

such, a mechanism to actively control the concentration of emitting molecules at any given imaging cycle is required, allowing to maintain a very small number of active emitters such that the PSFs do not overlap (**Figure 1.13, g-h**). By having a random, small subset of the emitters in the "on" state at any given time, the localization of centroids of single emitters in one acquired image can be achieved. Molecules in the on state are then turned "off" or photobleached. Next, another subset is turned on and localized individually. Repeating this process several times allows for the computation of many localizations of the structure being imaged. The underlying image is then reconstructed in a pointillist manner to reveal details hidden on a diffraction limited image (**Figure 1.13, i**).

Eric Betzig was the first, in 1995,[108] to propose to isolate the emitters. He initially suggested to utilize some spectral property such as the inhomogeneity in the absorption wavelength to achieve this necessary isolation. However, this was later shown to be challenging.[114] In 2006, using photoswitchable fluorescent proteins (such as the photoactivatable (PA)GFP) as an active control mechanism, Betzig reported PALM (PhotoActivated Localization Microscopy) where he achieved ~20 nm resolution.[109] paGFP densely labeling the sample and initially in a dark state can be sequentially activated (with light of a proper wavelength), imaged, and photobleached to achieve active control and sequential localization.

Shortly after Betzig's initial publication, similar super-resolution techniques were reported. A nearly identical approach (fPALM, Fluorescence PhotoActivation Localization Microscopy) was published by Samuel Hess and co-workers.[115] Utilizing the same principles but taking advantage of the photoswitching properties of a small organic fluorophore Cy5[56] instead of fluorescent proteins, Xiaowei Zhuang and co-workers achieved super-resolution and presented their technique under the acronym STORM (STochastic Optical Reconstruction Microscopy).[95, 116] Many other related techniques quickly appeared, only differing on the mechanism to achieve active control. They include, PAINT (Points Accumulation for Imaging in Nanoscale Topography),[117-118] DNA-PAINT,[119] dSTORM (direct STORM),[97, 120] and GSDIM (Ground-State Depletion with Intermittent Return).[121]

One of the most reliable and popular methods for active control is the photoswitching of Cyanines dyes as initially utilized in STORM. STORM was first demonstrated utilizing the remarkable photoswitching properties of the red-absorbing (633/638 nm) carbocyanine dye Cy5.[116] Prior to

the development of STORM, two groups had shown that Cy5 can be reversibly switched on and off in a controlled manner.[95, 97] It was reported that the reversibility of the non-bleached dark state can be observed exclusively under efficient oxygen depletion conditions and in the presence of thiols. Additionally, it was reported that the on → off rate is linearly dependent on the red illumination power, allowing control of the on time by modulating the excitation intensity. On the other hand, three different strategies to control the off → on process were also reported. While Bates *et al*.[95] used the green-absorbing dye Cy3, positioned in a close proximity to Cy5, and a low-intensity 532 nm laser to facilitate the restoration of the fluorescent on state, Heilemann *et al*.[97] used direct high-intensity illumination in the range of 337-532 nm to restore the on state, allowing control of the off time. More recently, it was demonstrated that the fluorescent state can also be recovered thermally, providing an alternative pathway for the off → on transition.[96] The Cy3-facilitated restoration of the Cy5 on-state was later exploited for the development of STORM.[116, 122-123] In a similar manner, direct STORM (*d*STORM) takes advantage of the strategy based on the light-induced direct restoration of Cy5 on-state.[120, 124-125]

Similar photoswitching properties have been observed for dyes structurally related to Cy5, such as Cy5.5,[122] Cy7,[122] as well as Alexa Fluor 647[97, 120, 122, 126] and 750[126]. Though highly sought after, efficient photoswitching of the green-absorbing carbocyanines Cy3 and its rigid analog Cy3B have not been reported, revealing structure-dependent photoswitching behaviour. The Schnermann group has recently reported Cy5B, the structurally rigid analog of Cy5,[26] which exhibits an improved fluorescence quantum yield. This is a potential advantage for SMLM as the localization precision scales with the square root of the number of detected photons.[111] Unfortunately, under the same conditions utilized for Cy5 photoswitching, Cy5B is unable to photoswitch, and is further characterized by a relatively low photon budget.[26]

While the nature of the non-fluorescent states of Cy5 and Cy7 has been studied utilizing mass spectrometry and are proposed to be Cy-SR adducts (

Figure 1.14)**,**[96] little is known about the mechanistic underpinnings of this photochemical reaction allowing photoswitching. Utilizing principles of photoinduced electron transfer (P*e*T) (**section 1.2.4)**, we report in **chapter 3** the photoswitching mechanism of Cyanine dyes as well as the mechanistic relationship of photoswitching and photostability in the presence of thiols.

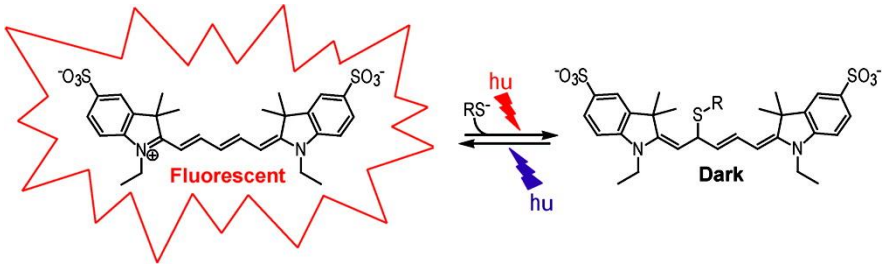

Figure 1.14 . Photoswiching of Cy5 in the presence of thiols. Reprinted with permission from Dempsey *et al*., *J. Am. Chem. Soc.* **2009**, *131* (51), 18192-18193. Copyright 2009 American Chemical Society.

1.4 Chemical Aspects and Challenges in Single Molecule Fluorescence Imaging

Single molecule fluorescence spectroscopy is in essence a multidisciplinary field. It requires concerted efforts and technological advances in areas related to chemistry (i.e., surface chemistry, photochemistry), biology (specimen preparation, genetic labeling), physics (i.e., optics, electronics) and software for data acquisition and data analysis. All technological advances work in a convergent manner to allow the revelation of the microscopic and nanoscopic world. In this section we will focus the discussion in some of the important chemical aspects required for SMF imaging and their relationship to the signal.

1.4.1 Signal Size, Noise, and Background

1.4.1.1 Signal to Noise Ratio (SNR)

The detection of an individual fluorescent molecule is usually performed in the presence of billions of other molecules, including solvent molecules. One of the most important aspects to successful single-molecule detection is the need to optimize the signal to noise ratio (SNR), which must be higher than one.[127] The SNR can be quantitatively expressed by **equation 1.16**.[128]

$$\mathrm{SNR} = \frac{D\Phi_f\left(\frac{\sigma_p}{A}\right)\left(\frac{P_0}{h\nu}\right)T}{\sqrt{D\Phi_f\left(\frac{\sigma_p}{A}\right)\left(\frac{P_0}{h\nu}\right)T + C_b P_0 T + N_d T}} \qquad (1.16)$$

Where Φ_f is the fluorescence quantum yield of the fluorophore, σ_p the absorption cross section (related to the extinction coefficient), T the detector counting interval, A the beam area, P_0/hv the number of incident photons per second, C_b the background count rate per watt of excitation power, and N_d the dark count rate. D is an instrument-dependent collection factor which depends on a collection factor, a transmission factor, and the detector quantum efficiency. **Equation 1.16** highlights the importance of maximizing the fluorophore brightness ($\Phi_f \sigma_p$) (**see section 1.4.1.2**) and minimizing the background (C_b) (**see section 1.4.1.3**).

1.4.1.2 Fluorophore Brightness

Fluorophores are the molecular beacons utilized in single molecule fluorescence techniques. Their utility is dictated by their specific chemical properties (e.g., reactivity, lipophilicity, pKa, stability) and photophysical properties (e.g.,λ_{max}^{ex}, λ_{max}^{em}, ε, Φ_f, τ).[129] As shown by **equation 1.16**, the signal to noise ratio scales with the brightness of a fluorophore. A fluorophore's brightness is defined by the product of two parameters: its fluorescence quantum yield (Φ_f) and its extinction coefficient (ε) (or absorption cross section (σ_p) when referring to a single molecule, **equation 1.17**). The extinction coefficient is a measure of the quantity of absorbed light at a given wavelength. Therefore, a high extinction coefficient will lead to a greater amount of light being absorbed. Quantum yield is the number of emitted photons relative to the number of absorbed photons.

$$Brightness = \Phi_f \varepsilon \tag{1.17}$$

In order to facilitate the unequivocal detection of individual fluorophores, emitters should exhibit brightness of at least ~1000 $cm^{-1}M^{-1}$ (ε> 10000 $cm^{-1}M^{-1}$) and (Φ_f>0.1) (**see Figure 1.15)**.[130] Cyanine dyes such as Cy3 and Cy5 are among the most utilized fluorophores in SMF techniques due to their high brightness, photostability, and versatility (**see Figure 1.15 and Table 1.2**).[131]

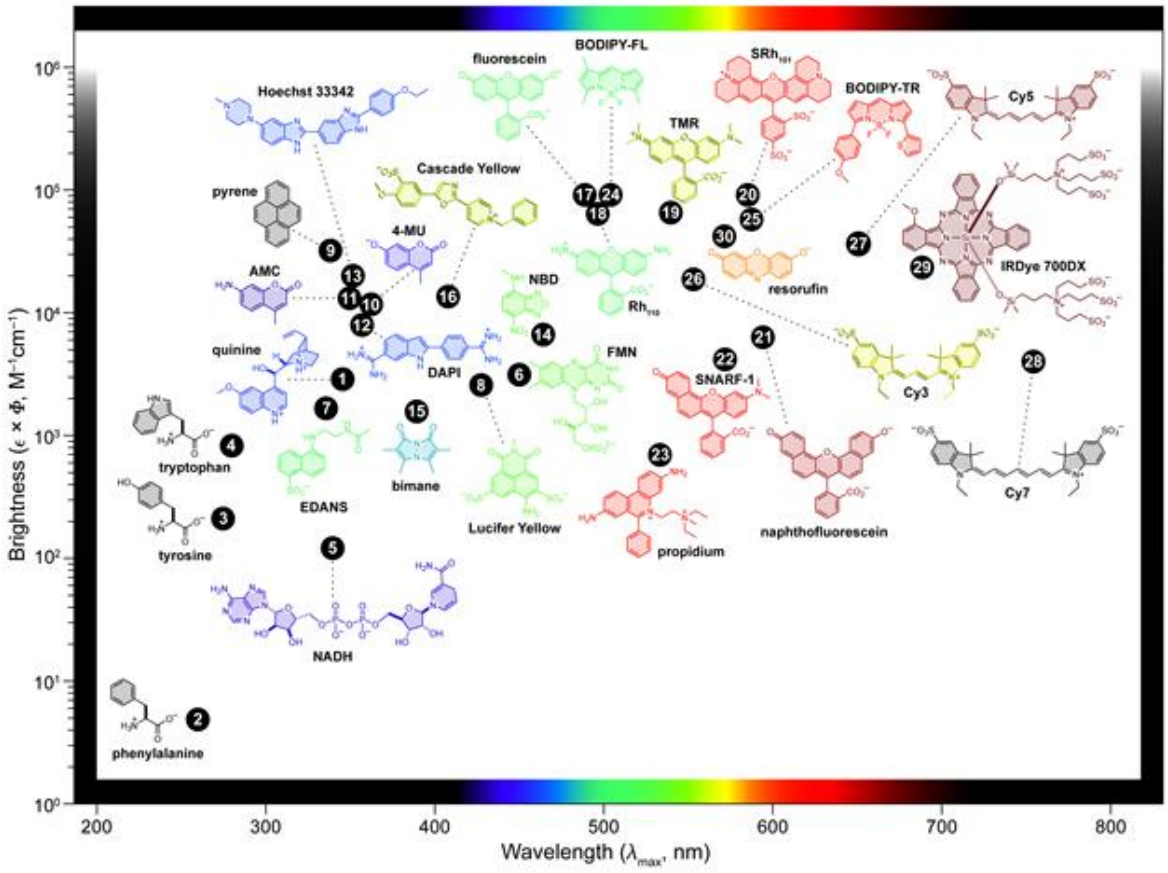

Figure 1.15. Plot of fluorophore brightness (Φ_f ε) as a function of the wavelength of maximum absorption (λ_{max}) for several classes of fluorophores. The color of the structure represents its maximum emission wavelength (λ_{em}). Reprinted with permission from Lavis, L. D.; Raines, R. T., *ACS Chem. Biol*. **2008**, 3, 142. Copyright 2008 American Chemical Society.

1.4.1.3 The importance of surfaces in SMF techniques

From **equation 1.16**, it follows that the signal to noise ratio decreases as the background signal (C_b) increases. The background can be reduced by minimizing the excitation or detection volume using various methods, including physical confinement of the sample, confocal detection, and total internal reflection fluorescence microscopy (TIRFM) (**see section 1.3.3**).[132] Many methods, including TIRFM, are capable of performing real time measurements of single-molecule behaviour and dynamics. These methods require the attachment of molecules under investigation to a solid support surface. The specific immobilization of molecules is commonly achieved by using biotin tethered to the surface via biotin-streptavidin interactions, in a bottom-up self-assembly scheme where streptavidin is initially immobilized over the surface followed by the flow of biotinylated

substrate. While this strategy allows to specifically attach fluorescent molecules to the surface, it does not prevent unwanted fluorescent molecules to be non-specifically attached to the surface. This is highly detrimental as it increases fluorescent background. Thus, surface passivation to avoid non-specific binding is of paramount importance to maximize SNR (**equation 1.16**).[133]

Initially, surface coating using bovine serum albumin (BSA) was effectively used as a blocking agent for hydrophobic and hydrophilic surfaces (**Figure 1.16, panel a**).[134] However, in some cases BSA failed as a passivation agent. A solution came in the form of covalent attachment of poly(ethylene glycol) (PEG) to the surface to provide an antifouling coating and thus to prevent non-specific binding to the surface (**Figure 1.16, panel b**).[135] In cases when cell-like environment is required for *in vitro* studies, supported lipid bilayers can be used as an alternative approach to mimic the natural environment of biomolecules in living cells.[136-137] Functionalization of lipid heads with biotin allows for compatibility with protein and nucleic acids (**Figure 1.16, panel c**). Lipid vesicles can also be used to encapsulate molecules of interest. The vesicles are then tethered to a surface via biotinylated lipids (**Figure 1.16, panel d**).[138-140] This approach allows to circumvent the concentration barrier of optical single-molecule detection as in a vesicle the effective observation volume is strongly reduced. Accordingly, high concentrations of e.g. labeled complementary substrates may be achieved with minimal total number in the excitation volume. For example, a single molecule trapped in a 100 nm size vesicle would have an effective concentration of ~4 μM. This concentration is well above the picomolar-nanomolar concentrations normally used for single-molecule spectroscopy in order to minimize background. Labeled molecules that bind a substrate of interest could be then employed at tens of micromolar, rather than pico-nanomolar, yet only having a total count of e.g. 10 fluorophores overall. The main challenge of using this encapsulation approach however lies in ensuring that only one molecule of interest is encapsulated per vesicle.[141]

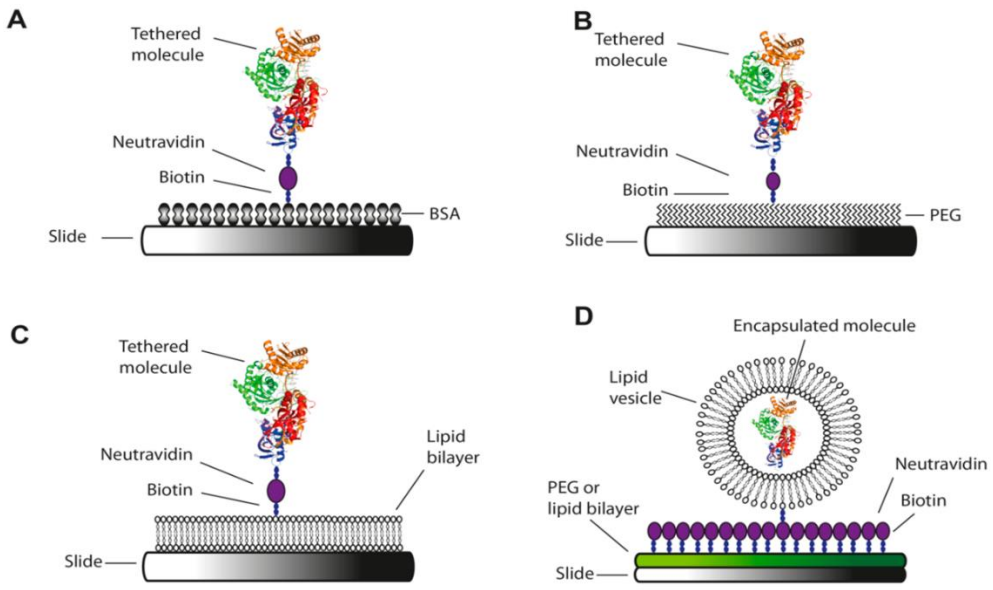

Figure 1.16. Immobilization and passivation strategies commonly utilized in single molecule measurements.. Surface passivation strategies of glass slides to prevent nonspecific binding typically uses a) bovine serum albumin, b) Polyethylene glycol (PEG) or lipids in the form of c) surface passivation and d) encapsulation. Adapted from Gust *et al.*, *Molecules*. **2014**, 19, 15824.

Surface passivation via PEG relying on a two-step process has been (until now) the most commonly used method in SMF studies.[81, 142] Here, the surface is functionalized with amine groups by attaching (3-aminopropyl)triethoxysilane (APTES) to the surface via silane chemistry in a first step. The second step involves grafting of a succinimidyl valerate PEG molecule (mPEG-SVA, typically 5000 Da) via NHS amino reaction. This protocol suffers from high variability from slide to slide and batch to batch. Several strategies to mitigate problems associated to surface quality have been proposed at the expenses of increasing the effective cost (reagents and time) of the passivation method. [143-146] Recently, Tween 20 (T20), a detergent, was used in hydrophobic quartz surfaces in combination with Biotinylated-BSA.[147] Treatment with T20 is highly effective and so far has shown the highest performance in terms of minimal background. However, fluorescent impurities and short ssDNA labeled with ATTO647N can bind and diffuse in T20 surfaces presumably due to incorporation into the surfactant layer. As such, T20 is expected to be unsuitable for lipophilic dyes such as nonsulfonated cyanines and membrane proteins that can potentially bind to a T20 surface. Additionally, the non-capped hydroxyl groups at the end of each polyethylene glycol chain in T20 can form a high-density layer of hydroxyl groups providing reactivity to the surface.

As an alternative to the conventional two-step surface passivation PEG, functionalization can be achieved by directly attaching PEG-Silane,[148-155] which is typically exploited in the optimization of surfaces used for nanoarrays. To the best of our knowledge, however, all reported protocols perform incubations lasting several hours and require the use of catalysts such as acetic acid or triethylamine in large amounts of organic solvents.

Current procedures using PEG suffer from poor surface passivation and/or are labor and time intensive. Additionally, they use considerable amounts of organic solvents. In **chapter 4**, we describe and efficient protocol (15 min) that provides a simple, cost-effective, and environmentally benign approach toward rendering glass surfaces for single-molecule studies with improved passivation.

1.4.2 Signal stability and enhanced survival time

Single molecule fluorescence techniques such as smPIFE and smFRET require fluorescence signals to be affected only by the process under study. Therefore, in the absence of the process of interest, stable fluorescence signals are key to avoid incorrect interpretation of data. The importance of stable fluorescence signals can be illustrated by smFRET trajectories (**Figure 1.17**).[156-157] Donor (green, Cy3) and acceptor (red, Cy5) trajectories shown in **Figure 1.17a** report FRET fluctuations as the Holliday junction undergoes conformational changes. In **Figure 1.17b** similar FRET fluctuations are shown in the sub second timescale. However, in the second case, where a double-stranded DNA has been labeled with ATTO647N as donor and ATTO680 as acceptor, the origin of the fluctuation is fundamentally different. Here, a one-electron reduction of the acceptor, yielding a transient radical anion that does not absorb in the visible range induces a low-FRET state. This example highlights the importance of understanding the photophysical and photochemical processes leading to signal fluctuations of fluorophores used in SMS techniques.

In addition to undesired intensity fluctuations, another important problem in single molecule biophysical studies is photobleaching, as the survival time of a fluorophore limits our observation period. These two problems are in some cases related, as long-lived triplet states cannot only cause signal fluctuations, but can also be intermediates of a photobleaching reaction.[158-159] In order to solve this problem triplet quenchers have been utilized to both, decrease signal fluctuations as well as to decrease photobleaching.

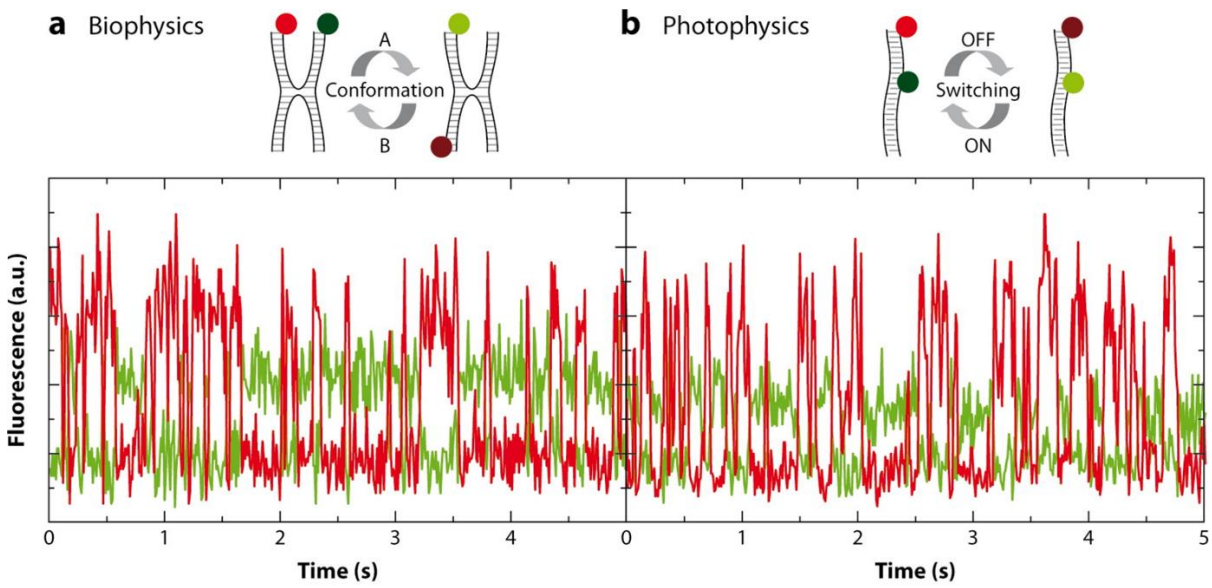

Figure 1.17. Biophysical and photochemical processes showing similar signal fluctuations in smFRET.. a) smFRET fluctuations due to conformational changes in the Holliday junction. b) smFRET fluctuations of donor-acceptor dyes due to a photochemical reaction where the acceptor dye forms a radical anion, which is unable to accept the energy from the donor. Reprinted with permission from Ha, T.; Tinnefeld, P., *Annu. Rev. Phys. Chem.* **2012**, 63, 595. Copyright 2012 Annual Reviews of Physical Chemistry.

1.4.2.1 Dual role of molecular Oxygen

Molecular oxygen can quench the triplet state (T_1) of many fluorophores in a diffusion-controlled fashion ($k_q \sim 10^{10}$ $M^{-1}s^{-1}$).[32] This rapid quenching eliminates the long-lived triplet and radical states intermediates that can affect the signal quality. However, upon T_1 quenching, singlet oxygen ($^1O_2$), a highly reactive species, is generated. Ground state fluorophores, including cyanines, can react with singlet oxygen, causing irreversible photobleaching.[160] As a consequence, in the presence of molecular oxygen, single molecule fluorescence trajectories show stable signals (triplet quenching by oxygen) yet with limited survival times (irreversible photobleaching typically arising from singlet oxygen), see **Figure 1.18, panel a**. Removal of oxygen can partly mitigate photobleaching by minimizing the sensitization of $^1O_2$, however, it allows for long lived triplets and radical states involved in signal fluctuations and photobleaching (**Figure 1.18, panel b**). In order to achieve both stable signals and longer survival times, removal of oxygen is accompanied by the addition of exogenous triplet quencher additives (**Figure 1.18, panel c**).

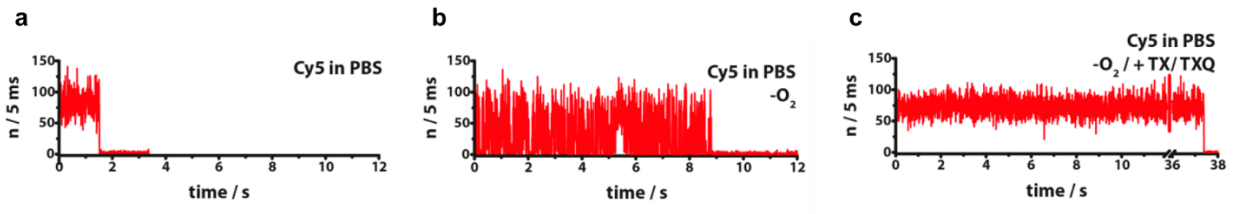

Figure 1.18. Signal intensity fluctuations and survival times of a single fluorophore in the presence and absence of molecular oxygen and triplet quenchers.. Intensity-time fluorescence trajectory of Cy5 in PBS buffer: a) in the presence of molecular oxygen, b) in the absence of oxygen, and c) in the absence of oxygen and in the presence triple quenchers additives. Adapted from Gust *et al.*, *Molecules*. **2014**, 19, 15824.

1.4.2.2 Enzymatic Oxygen removal

Given the difficulty of efficiently removing oxygen by physical methods, enzymatic oxygen scavenging systems are widely used. The most popular system (GODCAT) contains a combination of glucose, glucose oxidase (GOD), and catalase (CAT) (**Figure 1.19**).[161] In this scheme, GOD requires molecular oxygen to convert glucose into gluconic acid and hydrogen peroxide (H_2O_2). Catalase enzyme is added to deplete the formation of H_2O_2, partly regenerating oxygen. Therefore, two full enzymatic cycles are required to remove one molecule of oxygen. The main drawback of using the GODCAT system in pH sensitive environments is the acidification of the imaging solution due to the formation of gluconic acid.[162]

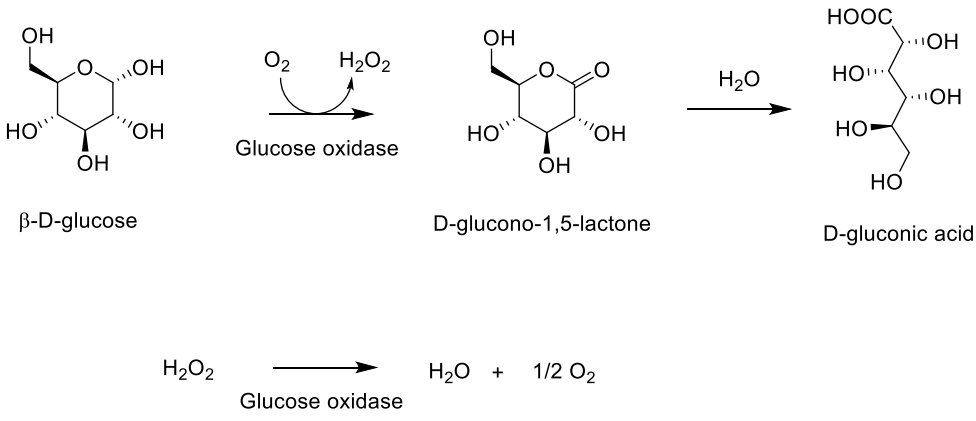

Figure 1.19. Standard enzymatic oxygen scavenger system (GODCAT) utilized in SMF imaging.

Alternatively, oxygen can be depleted using the protocatechuate-3,4-dioxygenase (PCD) enzyme and protocatechuic acid (PCA) as a substrate.[163-164] This system removes the need of using catalase, H_2O_2 is not produced as a sub-product. However, similarly to GODCAT it suffers from acidification of the sample over time.

A third system, addressing the acidification of the imaging buffer has been reported. In this strategy GOD is replaced by pyranose oxidase (POC). POC, like GOD uses glucose as a substrate, however, the oxidation product results on a ketone instead of a carboxylic acid, allowing to maintain the pH.[165]

1.4.2.3 Photochemical Triplet State Quenching:

Compared to the singlet ground state, a fluorophore in an excited electronic state is both a better electron donor and a better electron acceptor (**see section 1.2.4**). Then, triplet states of fluorophores can be effectively quenched photochemically via photoinduced electron transfer (P*e*T).The P*e*T between a reducing or oxidizing agent and a fluorophore in its triplet excited state results in the formation of a fluorophore radical anion ($F^{\bullet -}$) or radical cation ($F^{\bullet +}$), respectively (**Figure 1.20, panel a**). However, these radicals are undesired long-lived non-emissive states associated to signal fluctuations and photobleaching. The introduction of a second redox agent able to regenerate the singlet ground state of the fluorophore, can minimize the lifetime of radicals. A strategy, utilizing reducing and oxidizing systems (ROXS) has been successfully applied to effectively restore fluorophores to their ground state.[159]

In the ROXS scheme, two independent pathways can achieve rapid restoration of the singlet ground state of the fluorophore. The triplet state of a fluorophore (T_1) can be initially quenched via P*e*T with a reducing agent, generating a radical anion that can be further oxidized using an oxidizing agent. It is also possible that the T_1 is initially quenched via P*e*T with an oxidizing agent, followed by a reduction.

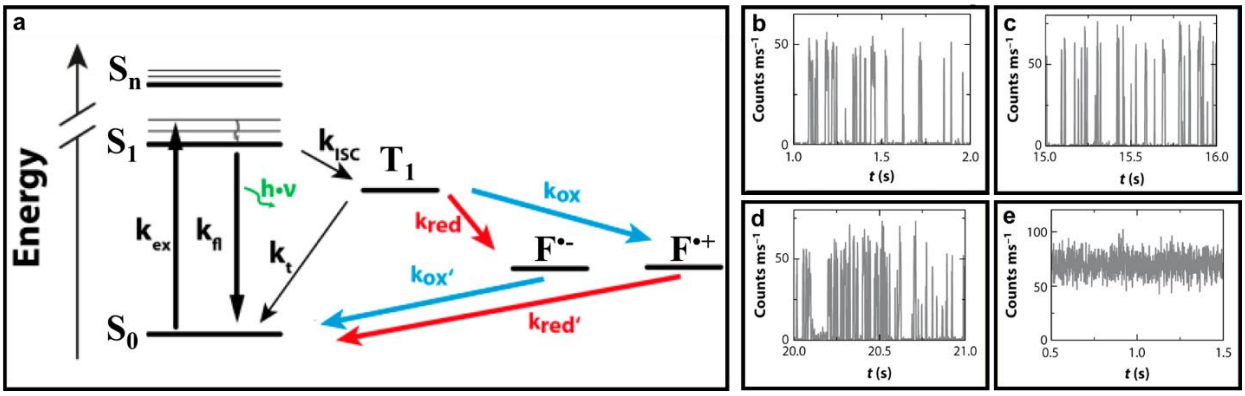

Figure 1.20. Reducing oxidizing system (ROXS). a) Energy state diagram illustrating the ROXS system. Single molecule trajectories of ATTO647N recorded under oxygen depleted conditions b) in the absence of redox agents c) in the presence of a reducing agent (AA) d) in the presence of an oxidizing agent (MV), and e) in the presence of both reducing (AA) and oxidizing (MV) agents. Adapted with permission from Ha, T.; Tinnefeld, P., *Annu. Rev. Phys. Chem.* **2012**, 6*3*, 595; Gust *et al.*, *Molecules*. **2014**, 19, 15824. Copyright 2012 Annual Reviews of Physical Chemistry.

Triplet state quenching studies of ATTO647N provide a useful example to illustrate the ROXS concept.[156, 159] Under oxygen depleted conditions, intensity-time single molecule trajectories of ATTO647N are characterized by signal instabilities (**see Figure 1.20, panel b**). Addition of a reducing agent such as ascorbic acid (AA) induces the formation of $F^{\bullet-}$ species as a result of the quenching of the fluorophore via P*e*T. While effectively eliminating triplet blinking, AA induces redox blinking (**see Figure 1.20, panel c**). Similarly, addition of the oxidizing agent such as methyl viologen (MV) induces the formation of $F^{\bullet+}$ (**see Figure 1.20, panel d**). However, simultaneous addition of reducing and oxidizing agents allows for the $F^{\bullet-}$ and $F^{\bullet+}$ formed to be quenched in a consecutive redox reaction with the complimentary redox reagent. Using this strategy, the lifetimes of triplets and radical intermediates are minimized, allowing to achieve a stable intensity-time single molecule fluorescence signal (**see Figure 1.20, panel e**).

1.4.2.4 Stand-alone Redox Triplet State Quenching; The Unusual Case of β-ME.

Among the reducing agents, thiols were initially recognized as photobleaching supressing agents[166] with enhanced performance when utilized under oxygen-depleted conditions.[161] Tinnefeld and coworkers have recently reported that β-mercaptoethanol (β-ME) can proceed as a stand-alone triplet quencher for dyes such as Alexa 568 (Rhodamine) and Atto647N (Carbopironine). They showed that reduction of triplet states *via* P*e*T by a thiolate generates a

geminate radical pair (GRP) in the solvent cage before radical escape occurs. The generated radical anion of the fluorophore can be rapidly reoxidized *via* back electron transfer (B*e*T) to restore the singlet ground state of the fluorophores (**see Figure 1.21**).[167] More recently, utilizing basic principles of photochemistry, our group has provided a more complete mechanistic framework accounting for this phenomenon.[168] Cosa and Glembockyte recognized that following P*e*T from a reducing agent, a geminate radical pair (GRP) in the triplet manifold is formed due to spin conservation rules. From this stage, while energetically favorable, a back-electron transfer (B*e*T) process is spin-forbidden and therefore radical escape from the solvent cage typically dominates. Then, intersystem crossing (ISC) in the GRP is a key requirement for B*e*T, a process competing with radical escape. Cosa and Glembockyte also reported that other widely used reducing agents such as Trolox (TX), n-propyl gallate (n-PG), and ascorbic acid (AA), when used with Cy3B, can participate in B*e*T to different extents, specifically >48%, >27%, and >13%, respectively.

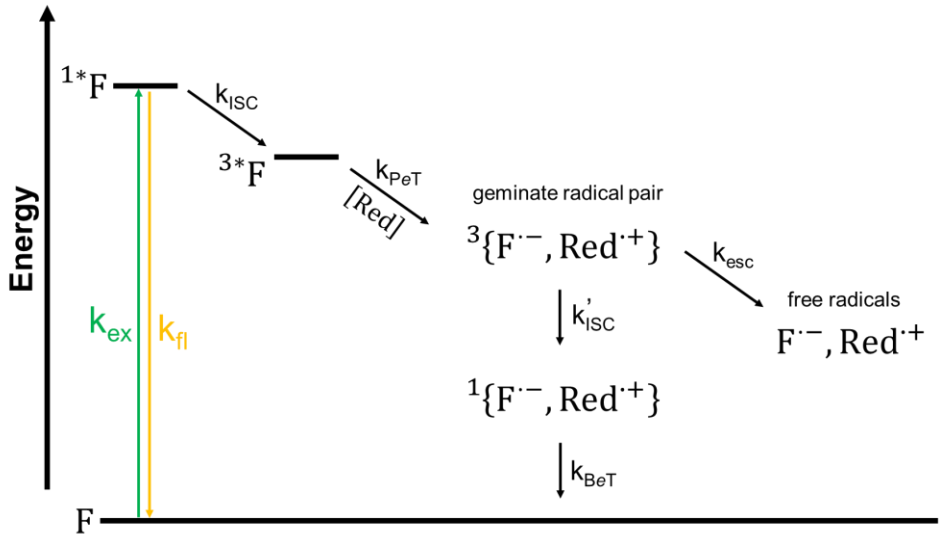

Figure 1.21. Photochemical pathways associated to the ground state recovery by β-ME. Triplet excited states can be quenched with a reducing (or oxidizing) agent leading to the formation of a geminate radical pair (GRP) in the triplet state. Triplet to singlet ISC in the GRP can compete with the typically dominant radical escape allowing for β-ME to be used as an efficient stand-alone triplet state quencher.

In **chapter 3**, in a unified mechanism, we highlight the connection between the excellent photostabilization and photoswitching properties of β-ME. Specifically, we show that the triplet to singlet ISC on the GRP is key to both photostability and photoswitching.

1.5 Context and Scope of this thesis

Single molecule fluorescence (SMF) techniques are uniquely positioned to study the biological microscopic and nanoscopic world with high spatiotemporal resolution. Although SMF techniques have profoundly changed the approach utilized to study the working mechanisms of many bionanomachines, several challenges remain to be addressed to exploit SMF full potential. Challenges include aspects related to sample preparation, fluorescence signal control, and data analysis.

The goals of this thesis are two: 1) To improve current single molecule methods in terms of enhancing the quality of passivated surfaces, extend our knowledge on principles related to controlling fluorescence signal and survival times, and deepening our understanding of the interplay of commonly used SMF techniques; 2) To apply single molecule methodologies to understand molecular machines involved in the replication of viruses such as the Hepatitis C. We approached all the chapters of this thesis in a mechanistic fashion. In some cases, we use known mechanisms to solve a particular problem, while in others, mechanisms are what we aim to learn from the system under study.

In SMF, PIFE and FRET are two powerful techniques working on complementary distance ranges. However, for many years PIFE and FRET techniques were believed to be inherently incompatible. In **chapter 2**, through a fundamental analysis, we challenge this idea and demonstrate that PIFE and FRET are compatible techniques. This is, distances in FRET can be reliable extracted in the presence of PIFE fluctuations. Furthermore, we next show that changes in the fluorescence quantum yield related to PIFE can be extracted from FRET data. This allows to expand the scope of these two techniques allowing to track distance changes spanning from angstrom to nanometers.

In the context of PIFE and FRET, Cyanines dyes such as Cy3 and Cy5 have been widely used as the molecular beacons of choice. β-ME, one of the most widely used triplet quenchers, however yields divergent results when used on Cy3 and Cy5. While for Cy3 stable signals and enhanced survival times are obtained, Cy5 reports repeated on-off fluctuations (photoswitching). Photoswitching has been effectively utilized on single molecule based super resolution techniques yet its full mechanism remains elusive. In **chapter 3** we report a unified mechanism accounting for cyanine dye photostability and photoswitching in the presence of β-ME. Following PeT and

geminate ISC, competing pathways from the newly formed singlet geminate radical pair intermediate are key to both photostability and photoswitching. We propose that the reported mechanism can lead to the rational design of photostabilizers and photoswitching agents with improved properties.

Most TIRF based SMF techniques require surface immobilization of the analytes on interest. Here, reducing non-specific binding through surface passivation is key to minimize background resulting from fluorophores nonspecifically bound to the surface. However, most of the reported protocols require extensive labor and suffer from high variability. In **chapter 4** we report a novel protocol aiming to mitigate the above-mentioned issues. Our protocol utilizes silanized PEG in DMSO as solvent and the reaction is carried out at high temperature (90 °C). This protocol improves the surface quality in terms of reduced nonspecific binding and surface variability. At the same time, it enabled reducing the number of steps, the total time, and the amount of organic solvents utilized.

In **chapter 5**, we have applied SMF techniques to study relevant biomolecular mechanisms related to the replication machinery of the Hepatitis C virus (HCV). In particular, we developed an smPIFE assay to study the non-structural 5B polymerase of HCV which has the ability to initiate synthesis *de novo* through a primer independent mechanism. Here, we report studies on NS5B binding, sliding, and searching for the 3’ of its single stranded RNA substrate. Our studies are centered in the dynamic processes allowing this protein to locate the 3’-terminus of the RNA template.

1.6 References

1. Perrin, F., La fluorescence des solutions. *Ann. Phys.* **1929,** *10* (12), 169-275.
2. Jablonski, A., Efficiency of Anti-Stokes Fluorescence in Dyes. *Nature* **1933,** *131* (3319), 839-840.
3. Jabłoński, A., Über den Mechanismus der Photolumineszenz von Farbstoffphosphoren. *Zeitschrift für Physik* **1935,** *94* (1), 38-46.
4. Valeur, B.; Berberan-Santos, M. r. N., Molecular Fluorescence : principles and applications. 2nd ed. ed.; Wiley-VCH: Weinheim, 2013.
5. Lakowicz, J. R., *Principles of Fluorescence Spectroscopy*. 3 ed.; Springer: 2006; Vol. 2, p 954.
6. Braslavsky, S. E., Glossary of terms used in photochemistry, 3rd edition (IUPAC Recommendations 2006). In *Pure and Applied Chemistry*, 2007; Vol. 79, p 293.
7. Widengren, J.; Schwille, P., Characterization of Photoinduced Isomerization and Back-Isomerization of the Cyanine Dye Cy5 by Fluorescence Correlation Spectroscopy. *The Journal of Physical Chemistry A* **2000,** *104* (27), 6416-6428.
8. Basic Principles of Fluorescence Spectroscopy. In *Handbook of Fluorescence Spectroscopy and Imaging*, pp 1-30.
9. Rullière, C., Laser action and photoisomerisation of 3,3′-diethyl oxadicarbocyanine iodide (DODCI): Influence of temperature and concentration. *Chemical Physics Letters* **1976,** *43* (2), 303-308.
10. Chibisov, A. K.; Zakharova, G. V.; Görner, H., Effects of substituents in the polymethine chain on the photoprocesses in indodicarbocyanine dyes. *Journal of the Chemical Society, Faraday Transactions* **1996,** *92* (24), 4917-4925.
11. Aramendia, P. F.; Negri, R. M.; Roman, E. S., Temperature Dependence of Fluorescence and Photoisomerization in Symmetric Carbocyanines.Influence of Medium Viscosity and Molecular Structure. *The Journal of Physical Chemistry* **1994,** *98* (12), 3165-3173.
12. Dempster, D. N.; Morrow, T.; Rankin, R.; Thompson, G. F., Photochemical characteristics of cyanine dyes. Part 1.—3,3′-diethyloxadicarbocyanine iodide and 3,3′-diethylthiadicarbocyanine iodide. *Journal of the Chemical Society, Faraday Transactions 2: Molecular and Chemical Physics* **1972,** *68* (0), 1479-1496.
13. Di Paolo, R. E.; Scaffardi, L. B.; Duchowicz, R.; Bilmes, G. M., Photoisomerization Dynamics and Spectroscopy of the Polymethine Dye DTCI. *The Journal of Physical Chemistry* **1995,** *99* (38), 13796-13799.
14. Duchowicz, R.; Scaffardi, L.; Tocho, J. O., Relaxation processes of singlet excited state of 3,3′-diethyloxadicarbocyanine iodide (DODCI) photoisomer. *Chemical Physics Letters* **1990,** *170* (5), 497-501.
15. Åkesson, E.; Sundström, V.; Gillbro, T., Solvent-dependent barrier heights of excited-state photoisomerization reactions. *Chemical Physics Letters* **1985,** *121* (6), 513-522.
16. Sundstroem, V.; Gillbro, T., Viscosity-dependent isomerization yields of some cyanine dyes. A picosecond laser spectroscopy study. *The Journal of Physical Chemistry* **1982,** *86* (10), 1788-1794.
17. Gruber, H. J.; Hahn, C. D.; Kada, G.; Riener, C. K.; Harms, G. S.; Ahrer, W.; Dax, T. G.; Knaus, H.-G., Anomalous Fluorescence Enhancement of Cy3 and Cy3.5 versus

Anomalous Fluorescence Loss of Cy5 and Cy7 upon Covalent Linking to IgG and Noncovalent Binding to Avidin. *Bioconjugate Chemistry* **2000,** *11* (5), 696-704.
18. Brismar, H.; Trepte, O.; Ulfhake, B., Spectra and fluorescence lifetimes of lissamine rhodamine, tetramethylrhodamine isothiocyanate, texas red, and cyanine 3.18 fluorophores: influences of some environmental factors recorded with a confocal laser scanning microscope. *Journal of Histochemistry & Cytochemistry* **1995,** *43* (7), 699-707.
19. Harvey, B.; Levitus, M., Nucleobase-Specific Enhancement of Cy3 Fluorescence. *Journal of Fluorescence* **2009,** *19*, 443-448.
20. Harvey, B. J.; Perez, C.; Levitus, M., DNA sequence-dependent enhancement of Cy3 fluorescence. *Photochemical & Photobiological Sciences* **2009,** *8* (8), 1105-1110.
21. Stennett, E. M. S.; Ma, N.; van der Vaart, A.; Levitus, M., Photophysical and Dynamical Properties of Doubly Linked Cy3–DNA Constructs. *Journal of Physical Chemistry B* **2014,** *118*, 152-163.
22. Sanborn, M. E.; Connolly, B. K.; Gurunathan, K.; Levitus, M., Fluorescence Properties and Photophysics of the Sulfoindocyanine Cy3 Linked Covalently to DNA. *The Journal of Physical Chemistry B* **2007,** *111* (37), 11064-11074.
23. Hwang, H.; Kim, H.; Myong, S., Protein induced fluorescence enhancement as a single molecule assay with short distance sensitivity. *Proceedings of the National Academy of Sciences* **2011,** *108* (18), 7414-7418.
24. Hwang, H.; Myong, S., Protein induced fluorescence enhancement (PIFE) for probing protein-nucleic acid interactions. *Chemical Society Reviews* **2014,** *43* (4), 1221-1229.
25. Cooper, M.; Ebner, A.; Briggs, M.; Burrows, M.; Gardner, N.; Richardson, R.; West, R., Cy3B™: Improving the Performance of Cyanine Dyes. *Journal of Fluorescence* **2004,** *14* (2), 145-150.
26. Michie, M. S.; Gotz, R.; Franke, C.; Bowler, M.; Kumari, N.; Magidson, V.; Levitus, M.; Loncarek, J.; Sauer, M.; Schnermann, M. J., Cyanine Conformational Restraint in the Far-Red Range. *J Am Chem Soc* **2017,** *139* (36), 12406-12409.
27. Dempsey, G. T.; Vaughan, J. C.; Chen, K. H.; Bates, M.; Zhuang, X., Evaluation of fluorophores for optimal performance in localization-based super-resolution imaging. *Nature methods* **2011,** *8* (12), 1027-36.
28. Mujumdar, R. B.; Ernst, L. A.; Mujumdar, S. R.; Lewis, C. J.; Waggoner, A. S., Cyanine dye labeling reagents: Sulfoindocyanine succinimidyl esters. *Bioconjugate Chemistry* **1993,** *4* (2), 105-111.
29. Sanborn, M. E.; Connolly, B. K.; Gurunathan, K.; Levitus, M., Fluorescence Properties and Photophysics of the Sulfoindocyanine Cy3 Linked Covalently to DNA. *Journal of Physical Chemistry B* **2007,** *111*, 11064-11074.
30. Förster, T., Zwischenmolekulare Energiewanderung und Fluoreszenz (Intermolecular Energy Migration and Fluorescence). *Annalen der Physik* **1948,** *437*, 55-75. Translated by RS Knox, Department of Physics and Astronomy, University of Rochester, Rochester, NY 14627.
31. Stryer, L.; Haugland, R. P., Energy Transfer: A Spectroscopic Ruler. *Proceedings of the National Academy of Sciences, USA* **1967,** *58*, 719-726.
32. Turro, N. J.; Ramamurthy, V.; Scaiano, J. C., *Modern molecular photochemistry of organic molecules*. University Science Books: Sausalito, Calif., 2010.
33. IUPAC. Compendium of Chemical Terminology, 2nd ed. (the "Gold Book"). Compiled by A. D. McNaught and A. Wilkinson. Blackwell Scientific Publications, Oxford (1997).

Online version (2019-) created by S. J. Chalk. ISBN 0-9678550-9-8. *https://doi.org/10.1351/goldbook.*

34. Rehm, D.; Weller, A., Kinetics of Fluorescence Quenching by Electron and H-Atom Transfer. *Israel Journal of Chemistry* **1970,** *8* (2), 259-271.
35. Marcus, R. A.; Sutin, N., Electron transfers in chemistry and biology. *Biochimica et Biophysica Acta (BBA) - Reviews on Bioenergetics* **1985,** *811* (3), 265-322.
36. Marcus, R. A., Electron transfer reactions in chemistry theory and experiment. *Journal of Electroanalytical Chemistry* **1997,** *438* (1), 251-259.
37. Mattay, J., Photoinduced Electron Transfer I. Springer Berlin Heidelberg: Berlin, Heidelberg, 1990.
38. Turro, N. J.; Ramamurthy, V.; Scaiano, J. C., *Principles of Molecular Photochemistry: An Introduction*. University science books: 2009.
39. SCHRÖDINGER, E., ARE THERE QUANTUM JUMPS ?: PART II*. *The British Journal for the Philosophy of Science* **1952,** *III* (11), 233-242.
40. Moerner, W. E.; Kador, L., Optical detection and spectroscopy of single molecules in a solid. *Physical Review Letters* **1989,** *62* (21), 2535-2538.
41. Orrit, M.; Bernard, J., Single pentacene molecules detected by fluorescence excitation in a p-terphenyl crystal. *Physical Review Letters* **1990,** *65* (21), 2716-2719.
42. Brooks Shera, E.; Seitzinger, N. K.; Davis, L. M.; Keller, R. A.; Soper, S. A., Detection of single fluorescent molecules. *Chemical Physics Letters* **1990,** *174* (6), 553-557.
43. Betzig, E.; Chichester, R. J., Single Molecules Observed by Near-Field Scanning Optical Microscopy. *Science* **1993,** *262* (5138), 1422-1425.
44. Ambrose, W. P.; Goodwin, P. M.; Martin, J. C.; Keller, R. A., Single molecule detection and photochemistry on a surface using near-field optical excitation. *Physical Review Letters* **1994,** *72* (1), 160-163.
45. Funatsu, T.; Harada, Y.; Tokunaga, M.; Saito, K.; Yanagida, T., Imaging of single fluorescent molecules and individual ATP turnovers by single myosin molecules in aqueous solution. *Nature* **1995,** *374* (6522), 555-559.
46. Schmidt, T.; Schütz, G. J.; Baumgartner, W.; Gruber, H. J.; Schindler, H., Imaging of single molecule diffusion. *Proceedings of the National Academy of Sciences* **1996,** *93* (7), 2926-2929.
47. Macklin, J. J.; Trautman, J. K.; Harris, T. D.; Brus, L. E., Imaging and Time-Resolved Spectroscopy of Single Molecules at an Interface. *Science* **1996,** *272* (5259), 255-258.
48. Moerner, W. E.; Orrit, M., Illuminating Single Molecules in Condensed Matter. *Science* **1999,** *283* (5408), 1670-1676.
49. Nobel, S.; Gräslund, A.; Rigler, R.; Widengren, J., Single molecule spectroscopy in chemistry, physics and biology : Nobel Symposium. Springer: Heidelburg [Germany] ;, 2010.
50. Lu, H. P.; Xun, L.; Xie, X. S., Single-Molecule Enzymatic Dynamics. *Science* **1998,** *282* (5395), 1877-1882.
51. Karam, P.; Powdrill, M. H.; Liu, H.-W.; Vasquez, C.; Mah, W.; Bernatchez, J.; Götte, M.; Cosa, G., Dynamics of Hepatitis C Virus (HCV) RNA-dependent RNA Polymerase NS5B in Complex with RNA. *Journal of Biological Chemistry* **2014,** *289* (20), 14399-14411.
52. Marko, R. A.; Liu, H.-W.; Ablenas, C. J.; Ehteshami, M.; Götte, M.; Cosa, G., Binding Kinetics and Affinities of Heterodimeric versus Homodimeric HIV-1 Reverse

Transcriptase on DNA–DNA Substrates at the Single-Molecule Level. *Journal of Physical Chemistry B* **2013,** *117*, 4560-4567.

53. Ablenas, C.; Liu, H.-W.; Shkriabai, N.; Kvaratskhelia, M.; Cosa, G.; Götte, M., Dynamic Interconversions of HCV Helicase Binding Modes on its Nucleic Acid Substrate. *ACS Infectious Diseases* **2016**.
54. Platnich, C. M.; Hariri, A. A.; Sleiman, H. F.; Cosa, G., Advancing Wireframe DNA Nanostructures Using Single-Molecule Fluorescence Microscopy Techniques. *Accounts of Chemical Research* **2019**.
55. Hariri, A. A.; Hamblin, G. D.; Gidi, Y.; Sleiman, H. F.; Cosa, G., Stepwise growth of surface-grafted DNA nanotubes visualized at the single-molecule level. *Nat Chem* **2015,** *7*, 295-300.
56. Hariri, A. A.; Hamblin, G. D.; Hardwick, J. S.; Godin, R.; Desjardins, J.-F.; Wiseman, P. W.; Sleiman, H. F.; Cosa, G., Stoichiometry and Dispersity of DNA Nanostructures Using Photobleaching Pair-Correlation Analysis. *Bioconjugate Chemistry* **2017,** *28* (9), 2340-2349.
57. Rahbani, J. F.; Hariri, A. A.; Cosa, G.; Sleiman, H. F., Dynamic DNA Nanotubes: Reversible Switching between Single and Double-Stranded Forms, and Effect of Base Deletions. *ACS Nano* **2015,** *9* (12), 11898-11908.
58. Rahbani, J. F.; Vengut-Climent, E.; Chidchob, P.; Gidi, Y.; Trinh, T.; Cosa, G.; Sleiman, H. F., DNA Nanotubes with Hydrophobic Environments: Toward New Platforms for Guest Encapsulation and Cellular Delivery. *Advanced Healthcare Materials* **2018,** *7* (6), 1701049.
59. Platnich, C. M.; Hariri, A. A.; Rahbani, J. F.; Gordon, J. B.; Sleiman, H. F.; Cosa, G., Kinetics of Strand Displacement and Hybridization on Wireframe DNA Nanostructures: Dissecting the Roles of Size, Morphology, and Rigidity. *ACS Nano* **2018,** *12* (12), 12836-12846.
60. Hamblin, G. D.; Hariri, A. A.; Carneiro, K. M. M.; Lau, K. L.; Cosa, G.; Sleiman, H. F., Simple Design for DNA Nanotubes from a Minimal Set of Unmodified Strands: Rapid, Room-Temperature Assembly and Readily Tunable Structure. *ACS Nano* **2013,** *7* (4), 3022-3028.
61. Lo, P. K.; Karam, P.; Aldaye, F. A.; McLaughlin, C. K.; Hamblin, G. D.; Cosa, G.; Sleiman, H. F., Loading and selective release of cargo in DNA nanotubes with longitudinal variation. *Nature Chemistry* **2010,** *2* (4), 319-328.
62. Godin, R.; Palacios, R. E.; Cosa, G., Heterogeneous Charge Mobility in Individual Conjugated Polyelectrolyte Nanoparticles Revealed by Two-Color Single Particle Spectroelectrochemistry Studies. *The Journal of Physical Chemistry C* **2015,** *119* (23), 12875-12886.
63. Godin, R.; Sherman, B. D.; Bergkamp, J. J.; Chesta, C. A.; Moore, A. L.; Moore, T. A.; Palacios, R. E.; Cosa, G., Charge-Transfer Dynamics of Fluorescent Dye-Sensitized Electrodes under Applied Biases. *The Journal of Physical Chemistry Letters* **2015,** *6* (14), 2688-2693.
64. Calver, C. F.; Liu, H.-W.; Cosa, G., Exploiting Conjugated Polyelectrolyte Photophysics toward Monitoring Real-Time Lipid Membrane-Surface Interaction Dynamics at the Single-Particle Level. *Langmuir* **2015,** *31* (43), 11842-11850.
65. Saurabh, S.; Maji, S.; Bruchez, M. P., Evaluation of sCMOS cameras for detection and localization of single Cy5 molecules. *Opt. Express* **2012,** *20* (7), 7338-7349.

66. Webb, D. J.; Brown, C. M., Epi-Fluorescence Microscopy. In *Cell Imaging Techniques: Methods and Protocols*, Taatjes, D. J.; Roth, J., Eds. Humana Press: Totowa, NJ, 2013; pp 29-59.
67. van den Wildenberg, S. M. J. L.; Prevo, B.; Peterman, E. J. G., A Brief Introduction to Single-Molecule Fluorescence Methods. In *Single Molecule Analysis: Methods and Protocols*, Peterman, E. J. G.; Wuite, G. J. L., Eds. Humana Press: Totowa, NJ, 2011; pp 81-99.
68. Park, Y. I.; Lee, K. T.; Suh, Y. D.; Hyeon, T., Upconverting nanoparticles: a versatile platform for wide-field two-photon microscopy and multi-modal in vivo imaging. *Chemical Society Reviews* **2015,** *44* (6), 1302-1317.
69. Fish, K. N., Total Internal Reflection Fluorescence (TIRF) Microscopy. *Current Protocols in Cytometry* **2009,** *50* (1), 12.18.1-12.18.13.
70. Mattheyses, A. L.; Simon, S. M.; Rappoport, J. Z., Imaging with total internal reflection fluorescence microscopy for the cell biologist. *Journal of Cell Science* **2010,** *123* (21), 3621-3628.
71. Martin-Fernandez, M. L.; Tynan, C. J.; Webb, S. E. D., A 'pocket guide' to total internal reflection fluorescence. *Journal of Microscopy* **2013,** *252* (1), 16-22.
72. Ha, T.; Enderle, T.; Ogletree, D. F.; Chemla, D. S.; Selvin, P. R.; Weiss, S., Probing the interaction between two single molecules: fluorescence resonance energy transfer between a single donor and a single acceptor. *Proceedings of the National Academy of Sciences* **1996,** *93* (13), 6264-6268.
73. Roy, R.; Hohng, S.; Ha, T., A practical guide to single-molecule FRET. *Nature Methods* **2008,** *5*, 507.
74. Mohapatra, S.; Lin, C.-T.; Feng, X. A.; Basu, A.; Ha, T., Single-Molecule Analysis and Engineering of DNA Motors. *Chemical Reviews* **2019**.
75. Kapanidis, A. N.; Laurence, T. A.; Lee, N. K.; Margeat, E.; Kong, X.; Weiss, S., Alternating-Laser Excitation of Single Molecules. *Accounts of Chemical Research* **2005,** *38* (7), 523-533.
76. Weiss, S., Fluorescence Spectroscopy of Single Biomolecules. *Science* **1999,** *283*, 1676-1683.
77. Michalet, X.; Weiss, S.; Jäger, M., Single-Molecule Fluorescence Studies of Protein Folding and Conformational Dynamics. *Chemical Reviews* **2006,** *106* (5), 1785-1813.
78. Smiley, R. D.; Hammes, G. G., Single Molecule Studies of Enzyme Mechanisms. *Chemical Reviews* **2006,** *106* (8), 3080-3094.
79. Zhuang, X., Single-Molecule RNA Science. *Annual Review of Biophysics and Biomolecular Structure* **2005,** *34* (1), 399-414.
80. Ha, T., Single-Molecule Fluorescence Resonance Energy Transfer. *Methods* **2001,** *25* (1), 78-86.
81. Roy, R.; Hohng, S.; Ha, T., A practical guide to single-molecule FRET. *Nat Meth* **2008,** *5* (6), 507-516.
82. Cosa, G.; Harbron, E. J.; Zeng, Y.; Liu, H.-W.; O'Connor, D. B.; Eta-Hosokawa, C.; Musier-Forsyth, K.; Barbara, P. F., Secondary Structure and Secondary Structure Dynamics of DNA Hairpins Complexed with HIV-1 NC Protein. *Biophysical Journal* **2004,** *87*, 2759-2767.

83. Lu, M.; Ma, X.; Mothes, W., Chapter Eight - Illuminating the virus life cycle with single-molecule FRET imaging. In *Advances in Virus Research*, Rey, F. A., Ed. Academic Press: 2019; Vol. 105, pp 239-273.
84. Ngure, M.; Issur, M.; Shkriabai, N.; Liu, H.-W.; Cosa, G.; Kvaratskhelia, M.; Götte, M., Interactions of the Disordered Domain II of Hepatitis C Virus NS5A with Cyclophilin A, NS5B, and Viral RNA Show Extensive Overlap. *ACS Infectious Diseases* **2016,** *2* (11), 839-851.
85. Liu, S.; Abbondanzieri, E. A.; Rausch, J. W.; Grice, S. F. J. L.; Zhuang, X., Slide into Action: Dynamic Shuttling of HIV Reverse Transcriptase on Nucleic Acid Substrates. *Science* **2008,** *322* (5904), 1092-1097.
86. Abbondanzieri, E. A.; Bokinsky, G.; Rausch, J. W.; Zhang, J. X.; Le Grice, S. F. J.; Zhuang, X., Dynamic binding orientations direct activity of HIV reverse transcriptase. *Nature* **2008,** *453* (7192), 184-189.
87. Luo, G.; Hamatake, R. K.; Mathis, D. M.; Racela, J.; Rigat, K. L.; Lemm, J.; Colonno, R. J., De Novo Initiation of RNA Synthesis by the RNA-Dependent RNA Polymerase (NS5B) of Hepatitis C Virus. *Journal of Virology* **2000,** *74* (2), 851-863.
88. Oh, J.-W.; Ito, T.; Lai, M. M. C., A Recombinant Hepatitis C Virus RNA-Dependent RNA Polymerase Capable of Copying the Full-Length Viral RNA. *Journal of Virology* **1999,** *73* (9), 7694-7702.
89. Zhong, W.; Uss, A. S.; Ferrari, E.; Lau, J. Y. N.; Hong, Z., De Novo Initiation of RNA Synthesis by Hepatitis C Virus Nonstructural Protein 5B Polymerase. *Journal of Virology* **2000,** *74* (4), 2017-2022.
90. Sun, X.-L.; Johnson, R. B.; Hockman, M. A.; Wang, Q. M., De Novo RNA Synthesis Catalyzed by HCV RNA-Dependent RNA Polymerase. *Biochemical and Biophysical Research Communications* **2000,** *268* (3), 798-803.
91. Ackermann, M.; Padmanabhan, R., De Novo Synthesis of RNA by the Dengue Virus RNA-dependent RNA Polymerase Exhibits Temperature Dependence at the Initiation but Not Elongation Phase. *Journal of Biological Chemistry* **2001,** *276* (43), 39926-39937.
92. Kao, C. C.; Del Vecchio, A. M.; Zhong, W., De NovoInitiation of RNA Synthesis by a Recombinant Flaviridae RNA-dependent RNA Polymerase. *Virology* **1999,** *253* (1), 1-7.
93. Calmels, C.; Ventura, M.; Aknin, C.; Métifiot, M.; Andreola, M.-L., De novo RNA synthesis catalyzed by the Zika Virus RNA polymerase domain. *Scientific Reports* **2017,** *7* (1), 2697.
94. Stennett, E. M. S.; Ciuba, M. A.; Lin, S.; Levitus, M., Demystifying PIFE: The Photophysics Behind the Protein-Induced Fluorescence Enhancement Phenomenon in Cy3. *The Journal of Physical Chemistry Letters* **2015,** *6* (10), 1819-1823.
95. Bates, M.; Blosser, T. R.; Zhuang, X., Short-range spectroscopic ruler based on a single-molecule optical switch. *Phys Rev Lett* **2005,** *94* (10), 108101.
96. Dempsey, G. T.; Bates, M.; Kowtoniuk, W. E.; Liu, D. R.; Tsien, R. Y.; Zhuang, X., Photoswitching Mechanism of Cyanine Dyes. *Journal of the American Chemical Society* **2009,** *131* (51), 18192-18193.
97. Heilemann, M.; Margeat, E.; Kasper, R.; Sauer, M.; Tinnefeld, P., Carbocyanine Dyes as Efficient Reversible Single-Molecule Optical Switch. *Journal of the American Chemical Society* **2005,** *127* (11), 3801-3806.

98. Myong, S.; Cui, S.; Cornish, P. V.; Kirchhofer, A.; Gack, M. U.; Jung, J. U.; Hopfner, K.-P.; Ha, T., Cytosolic Viral Sensor RIG-I Is a 5'-Triphosphate–Dependent Translocase on Double-Stranded RNA. *Science* **2009,** *323* (5917), 1070-1074.
99. Myong, S.; Rasnik, I.; Joo, C.; Lohman, T. M.; Ha, T., Repetitive shuttling of a motor protein on DNA. *Nature* **2005,** *437* (7063), 1321-1325.
100. Park, J.; Myong, S.; Niedziela-Majka, A.; Lee, K. S.; Yu, J.; Lohman, T. M.; Ha, T., PcrA Helicase Dismantles RecA Filaments by Reeling in DNA in Uniform Steps. *Cell* **2010,** *142* (4), 544-555.
101. Koh, H. R.; Kidwell, M. A.; Ragunathan, K.; Doudna, J. A.; Myong, S., ATP-independent diffusion of double-stranded RNA binding proteins. *Proceedings of the National Academy of Sciences* **2013,** *110* (1), 151-156.
102. Ablenas, C. J.; Liu, H.-W.; Shkriabai, N.; Kvaratskhelia, M.; Cosa, G.; Götte, M., Dynamic Interconversions of HCV Helicase Binding Modes on the Nucleic Acid Substrate. *ACS Infectious Diseases* **2017,** *3* (1), 99-109.
103. Steffen, F. D.; Sigel, R. K. O.; Börner, R., An atomistic view on carbocyanine photophysics in the realm of RNA. *Physical Chemistry Chemical Physics* **2016,** *18* (42), 29045-29055.
104. Abbe, E., Beiträge zur Theorie des Mikroskops und der mikroskopischen Wahrnehmung. *Archiv für Mikroskopische Anatomie* **1873,** *9* (1), 413-468.
105. Hell, S. W.; Wichmann, J., Breaking the diffraction resolution limit by stimulated emission: stimulated-emission-depletion fluorescence microscopy. *Opt. Lett.* **1994,** *19* (11), 780-782.
106. Hell, S. W.; Kroug, M., Ground-state-depletion fluorscence microscopy: A concept for breaking the diffraction resolution limit. *Applied Physics B* **1995,** *60* (5), 495-497.
107. Klar, T. A.; Jakobs, S.; Dyba, M.; Egner, A.; Hell, S. W., Fluorescence microscopy with diffraction resolution barrier broken by stimulated emission. *Proceedings of the National Academy of Sciences* **2000,** *97* (15), 8206-8210.
108. Betzig, E., Proposed method for molecular optical imaging. *Opt. Lett.* **1995,** *20* (3), 237-239.
109. Betzig, E.; Patterson, G. H.; Sougrat, R.; Lindwasser, O. W.; Olenych, S.; Bonifacino, J. S.; Davidson, M. W.; Lippincott-Schwartz, J.; Hess, H. F., Imaging Intracellular Fluorescent Proteins at Nanometer Resolution. *Science* **2006,** *313* (5793), 1642-1645.
110. Bobroff, N., Position measurement with a resolution and noise-limited instrument. *Review of Scientific Instruments* **1986,** *57* (6), 1152-1157.
111. Thompson, R. E.; Larson, D. R.; Webb, W. W., Precise Nanometer Localization Analysis for Individual Fluorescent Probes. *Biophysical Journal* **2002,** *82* (5), 2775-2783.
112. Möckl, L.; Lamb, D. C.; Bräuchle, C., Super-resolved Fluorescence Microscopy: Nobel Prize in Chemistry 2014 for Eric Betzig, Stefan Hell, and William E. Moerner. *Angewandte Chemie International Edition* **2014,** *53* (51), 13972-13977.
113. Yildiz, A.; Forkey, J. N.; McKinney, S. A.; Ha, T.; Goldman, Y. E.; Selvin, P. R., Myosin V Walks Hand-Over-Hand: Single Fluorophore Imaging with 1.5-nm Localization. *Science* **2003,** *300* (5628), 2061-2065.
114. van Oijen, A. M.; Köhler, J.; Schmidt, J.; Müller, M.; Brakenhoff, G. J., 3-Dimensional super-resolution by spectrally selective imaging. *Chemical Physics Letters* **1998,** *292* (1), 183-187.

115. Hess, S. T.; Girirajan, T. P. K.; Mason, M. D., Ultra-High Resolution Imaging by Fluorescence Photoactivation Localization Microscopy. *Biophysical Journal* **2006,** *91* (11), 4258-4272.
116. Rust, M. J.; Bates, M.; Zhuang, X., Sub-diffraction-limit imaging by stochastic optical reconstruction microscopy (STORM). *Nature Methods* **2006,** *3*, 793.
117. Mei, E.; Gao, F.; Hochstrasser, R. M., Controlled bimolecular collisions allow sub-diffraction limited microscopy of lipid vesicles. *Physical Chemistry Chemical Physics* **2006,** *8* (17), 2077-2082.
118. Sharonov, A.; Hochstrasser, R. M., Wide-field subdiffraction imaging by accumulated binding of diffusing probes. *Proceedings of the National Academy of Sciences* **2006,** *103* (50), 18911-18916.
119. Jungmann, R.; Steinhauer, C.; Scheible, M.; Kuzyk, A.; Tinnefeld, P.; Simmel, F. C., Single-Molecule Kinetics and Super-Resolution Microscopy by Fluorescence Imaging of Transient Binding on DNA Origami. *Nano Letters* **2010,** *10* (11), 4756-4761.
120. Heilemann, M.; van de Linde, S.; Schuttpelz, M.; Kasper, R.; Seefeldt, B.; Mukherjee, A.; Tinnefeld, P.; Sauer, M., Subdiffraction-resolution fluorescence imaging with conventional fluorescent probes. *Angewandte Chemie (International ed. in English)* **2008,** *47* (33), 6172-6.
121. Fölling, J.; Bossi, M.; Bock, H.; Medda, R.; Wurm, C. A.; Hein, B.; Jakobs, S.; Eggeling, C.; Hell, S. W., Fluorescence nanoscopy by ground-state depletion and single-molecule return. *Nature Methods* **2008,** *5* (11), 943-945.
122. Bates, M.; Huang, B.; Dempsey, G. T.; Zhuang, X., Multicolor Super-Resolution Imaging with Photo-Switchable Fluorescent Probes. *Science* **2007,** *317* (5845), 1749-1753.
123. Huang, B.; Wang, W.; Bates, M.; Zhuang, X., Three-Dimensional Super-Resolution Imaging by Stochastic Optical Reconstruction Microscopy. *Science* **2008,** *319* (5864), 810-813.
124. Heilemann, M.; van de Linde, S.; Mukherjee, A.; Sauer, M., Super-Resolution Imaging with Small Organic Fluorophores. *Angewandte Chemie International Edition* **2009,** *48* (37), 6903-6908.
125. van de Linde, S.; Löschberger, A.; Klein, T.; Heidbreder, M.; Wolter, S.; Heilemann, M.; Sauer, M., Direct stochastic optical reconstruction microscopy with standard fluorescent probes. *Nature Protocols* **2011,** *6*, 991.
126. Baddeley, D.; Crossman, D.; Rossberger, S.; Cheyne, J. E.; Montgomery, J. M.; Jayasinghe, I. D.; Cremer, C.; Cannell, M. B.; Soeller, C., 4D Super-Resolution Microscopy with Conventional Fluorophores and Single Wavelength Excitation in Optically Thick Cells and Tissues. *PLOS ONE* **2011,** *6* (5), e20645.
127. Moerner, W. E.; Fromm, D. P., Methods of single-molecule fluorescence spectroscopy and microscopy. *Review of Scientific Instruments* **2003,** *74* (8), 3597-3619.
128. Basché, T.; Ambrose, W. P.; Moerner, W. E., Optical spectra and kinetics of single impurity molecules in a polymer: spectral diffusion and persistent spectral hole burning. *J. Opt. Soc. Am. B* **1992,** *9* (5), 829-836.
129. Lavis, L. D.; Raines, R. T., Bright Ideas for Chemical Biology. *ACS Chemical Biology* **2008,** *3* (3), 142-155.
130. Fluorophore Selection for Single-Molecule Fluorescence Spectroscopy (SMFS) and Photobleaching Pathways. In *Handbook of Fluorescence Spectroscopy and Imaging*, pp 85-92.

131. Levitus, M.; Ranjit, S., Cyanine dyes in biophysical research: the photophysics of polymethine fluorescent dyes in biomolecular environments. *Quarterly Reviews of Biophysics* **2011,** *44* (1), 123-151.
132. Kim, H.; Ha, T., Single-molecule nanometry for biological physics. *Reports on Progress in Physics* **2012,** *76* (1), 016601.
133. Visnapuu, M.-L.; Duzdevich, D.; Greene, E. C., The importance of surfaces in single-molecule bioscience. *Molecular BioSystems* **2008,** *4* (5), 394-403.
134. Jeyachandran, Y. L.; Mielczarski, J. A.; Mielczarski, E.; Rai, B., Efficiency of blocking of non-specific interaction of different proteins by BSA adsorbed on hydrophobic and hydrophilic surfaces. *Journal of Colloid and Interface Science* **2010,** *341* (1), 136-142.
135. Rasnik, I.; Myong, S.; Cheng, W.; Lohman, T. M.; Ha, T., DNA-binding Orientation and Domain Conformation of the E. coli Rep Helicase Monomer Bound to a Partial Duplex Junction: Single-molecule Studies of Fluorescently Labeled Enzymes. *Journal of Molecular Biology* **2004,** *336* (2), 395-408.
136. Sackmann, E., Supported Membranes: Scientific and Practical Applications. *Science* **1996,** *271* (5245), 43-48.
137. Granéli, A.; Yeykal, C. C.; Prasad, T. K.; Greene, E. C., Organized Arrays of Individual DNA Molecules Tethered to Supported Lipid Bilayers. *Langmuir* **2006,** *22* (1), 292-299.
138. Rhoades, E.; Gussakovsky, E.; Haran, G., Watching proteins fold one molecule at a time. *Proceedings of the National Academy of Sciences* **2003,** *100* (6), 3197-3202.
139. Okumus, B.; Wilson, T. J.; Lilley, D. M. J.; Ha, T., Vesicle Encapsulation Studies Reveal that Single Molecule Ribozyme Heterogeneities Are Intrinsic. *Biophysical Journal* **2004,** *87* (4), 2798-2806.
140. Cisse, I.; Okumus, B.; Joo, C.; Ha, T., Fueling protein–DNA interactions inside porous nanocontainers. *Proceedings of the National Academy of Sciences* **2007,** *104* (31), 12646-12650.
141. Gust, A.; Zander, A.; Gietl, A.; Holzmeister, P.; Schulz, S.; Lalkens, B.; Tinnefeld, P.; Grohmann, D., A Starting Point for Fluorescence-Based Single-Molecule Measurements in Biomolecular Research. *Molecules* **2014,** *19* (10), 15824-15865.
142. Ha, T.; Rasnik, I.; Cheng, W.; Babcock, H. P.; Gauss, G. H.; Lohman, T. M.; Chu, S., Initiation and re-initiation of DNA unwinding by the Escherichia coli Rep helicase. *Nature* **2002,** *419* (6907), 638-641.
143. Chandradoss, S. D.; Haagsma, A. C.; Lee, Y. K.; Hwang, J.-H.; Nam, J.-M.; Joo, C., Surface Passivation for Single-molecule Protein Studies. *J. Vis. Exp.* **2014,** (86), e50549.
144. Zhang, Z.; Park, S. R.; Pertsinidis, A.; Revyakin, A., Cloud-point PEG Glass Surfaces for Imaging of Immobilized Single Molecules by Total-internal-reflection Microscopy. *Bio-protocol* **2016,** *6* (7).
145. Revyakin, A.; Zhang, Z.; Coleman, R. A.; Li, Y.; Inouye, C.; Lucas, J. K.; Park, S.-R.; Chu, S.; Tjian, R., Transcription initiation by human RNA polymerase II visualized at single-molecule resolution. *Genes & Development* **2012,** *26* (15), 1691-1702.
146. Hai, P.; Yifan, X.; Meng, Q.; Yi, C.; Wei, W., A simple procedure to improve the surface passivation for single molecule fluorescence studies. *Physical Biology* **2015,** *12* (4), 045006.
147. Hua, B.; Han, K. Y.; Zhou, R.; Kim, H.; Shi, X.; Abeysirigunawardena, S. C.; Jain, A.; Singh, D.; Aggarwal, V.; Woodson, S. A.; Ha, T., An improved surface passivation method for single-molecule studies. *Nat Meth* **2014,** *11* (12), 1233-1236.

148. Cai, H.; Depoil, D.; Palma, M.; Sheetz, M. P.; Dustin, M. L.; Wind, S. J., Bifunctional nanoarrays for probing the immune response at the single-molecule level. *Journal of Vacuum Science & Technology B, Nanotechnology and Microelectronics: Materials, Processing, Measurement, and Phenomena* **2013,** *31* (6), 06F902.
149. Cai, H.; Wolfenson, H.; Depoil, D.; Dustin, M. L.; Sheetz, M. P.; Wind, S. J., Molecular Occupancy of Nanodot Arrays. *ACS Nano* **2016,** *10* (4), 4173-4183.
150. Schvartzman, M.; Palma, M.; Sable, J.; Abramson, J.; Hu, X.; Sheetz, M. P.; Wind, S. J., Nanolithographic Control of the Spatial Organization of Cellular Adhesion Receptors at the Single-Molecule Level. *Nano Letters* **2011,** *11* (3), 1306-1312.
151. Palma, M.; Abramson, J. J.; Gorodetsky, A. A.; Penzo, E.; Gonzalez, R. L.; Sheetz, M. P.; Nuckolls, C.; Hone, J.; Wind, S. J., Selective Biomolecular Nanoarrays for Parallel Single-Molecule Investigations. *Journal of the American Chemical Society* **2011,** *133* (20), 7656-7659.
152. Blümmel, J.; Perschmann, N.; Aydin, D.; Drinjakovic, J.; Surrey, T.; Lopez-Garcia, M.; Kessler, H.; Spatz, J. P., Protein repellent properties of covalently attached PEG coatings on nanostructured SiO2-based interfaces. *Biomaterials* **2007,** *28* (32), 4739-4747.
153. Chai, J.; Wong, L. S.; Giam, L.; Mirkin, C. A., Single-molecule protein arrays enabled by scanning probe block copolymer lithography. *Proceedings of the National Academy of Sciences* **2011,** *108* (49), 19521-19525.
154. Palma, M.; Abramson, J. J.; Gorodetsky, A. A.; Nuckolls, C.; Sheetz, M. P.; Wind, S. J.; Hone, J., Controlled Confinement of DNA at the Nanoscale: Nanofabrication and Surface Bio-Functionalization. In *DNA Nanotechnology: Methods and Protocols*, Zuccheri, G.; Samorì, B., Eds. Humana Press: Totowa, NJ, 2011; pp 169-185.
155. Cai, H.; Wind, S. J., Improved Glass Surface Passivation for Single-Molecule Nanoarrays. *Langmuir* **2016,** *32* (39), 10034-10041.
156. Ha, T.; Tinnefeld, P., Photophysics of Fluorescent Probes for Single-Molecule Biophysics and Super-Resolution Imaging. *Annual Review of Physical Chemistry* **2012,** *63* (1), 595-617.
157. McKinney, S. A.; Déclais, A.-C.; Lilley, D. M. J.; Ha, T., Structural dynamics of individual Holliday junctions. *Nature Structural Biology* **2003,** *10* (2), 93-97.
158. Hoogenboom, J. P.; van Dijk, E. M. H. P.; Hernando, J.; van Hulst, N. F.; García-Parajó, M. F., Power-Law-Distributed Dark States are the Main Pathway for Photobleaching of Single Organic Molecules. *Physical Review Letters* **2005,** *95* (9), 097401.
159. Vogelsang, J.; Kasper, R.; Steinhauer, C.; Person, B.; Heilemann, M.; Sauer, M.; Tinnefeld, P., A Reducing and Oxidizing System Minimizes Photobleaching and Blinking of Fluorescent Dyes. *Angewandte Chemie International Edition* **2008,** *47* (29), 5465-5469.
160. Nani, R. R.; Kelley, J. A.; Ivanic, J.; Schnermann, M. J., Reactive species involved in the regioselective photooxidation of heptamethine cyanines. *Chemical Science* **2015,** *6* (11), 6556-6563.
161. Harada, Y.; Sakurada, K.; Aoki, T.; Thomas, D. D.; Yanagida, T., Mechanochemical coupling in actomyosin energy transduction studied by in vitro movement assay. *Journal of Molecular Biology* **1990,** *216* (1), 49-68.
162. Shi, X.; Lim, J.; Ha, T., Acidification of the Oxygen Scavenging System in Single-Molecule Fluorescence Studies: In Situ Sensing with a Ratiometric Dual-Emission Probe. *Analytical Chemistry* **2010,** *82* (14), 6132-6138.

163. Aitken, C. E.; Marshall, R. A.; Puglisi, J. D., An Oxygen Scavenging System for Improvement of Dye Stability in Single-Molecule Fluorescence Experiments. *Biophysical Journal* **2008,** *94* (5), 1826-1835.
164. Patil, P. V.; Ballou, D. P., The Use of Protocatechuate Dioxygenase for Maintaining Anaerobic Conditions in Biochemical Experiments. *Analytical Biochemistry* **2000,** *286* (2), 187-192.
165. Swoboda, M.; Henig, J.; Cheng, H.-M.; Brugger, D.; Haltrich, D.; Plumeré, N.; Schlierf, M., Enzymatic Oxygen Scavenging for Photostability without pH Drop in Single-Molecule Experiments. *ACS Nano* **2012,** *6* (7), 6364-6369.
166. Yanagida, T.; Nakase, M.; Nishiyama, K.; Oosawa, F., Direct observation of motion of single F-actin filaments in the presence of myosin. *Nature* **1984,** *307*, 58.
167. Holzmeister, P.; Gietl, A.; Tinnefeld, P., Geminate recombination as a photoprotection mechanism for fluorescent dyes. *Angewandte Chemie (International ed. in English)* **2014,** *53* (22), 5685-8.
168. Glembockyte, V.; Cosa, G., Redox-Based Photostabilizing Agents in Fluorescence Imaging: The Hidden Role of Intersystem Crossing in Geminate Radical Ion Pairs. *Journal of the American Chemical Society* **2017,** *139* (37), 13227-13233.

2 Conformational Changes Spanning Angstroms to Nanometers *via* a Combined Protein-Induced Fluorescence Enhancement–Förster Resonance Energy Transfer Method

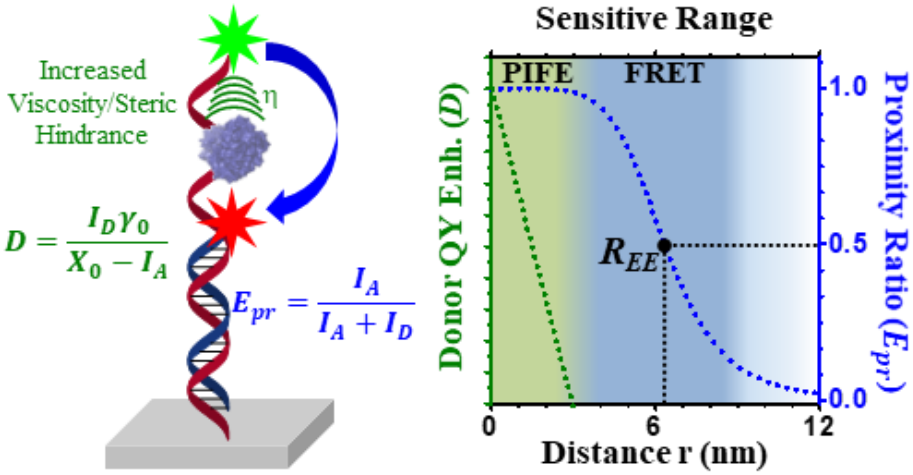

2.1 Preface

In **chapter 1**, we described the photophysical and photochemical processes underlying PIFE and FRET assays and provided several examples of smPIFE and smFRET to illustrate the importance of these two techniques. smPIFE and smFRET allow the monitoring of conformational changes in bionanomachines at different length scales. Therefore, a unified technique would enable an extended molecular ruler, spanning angstroms to nanometers. In order to make PIFE and FRET compatible, we need to establish a parameter permitting the measurement of FRET independent of the photophysical processes underlying PIFE. On the other hand, a parameter derived from donor/acceptor intensities that can account for the fluctuation in the donor quantum yield in the presence of energy transfer fluctuations is required. In **chapter 2** we merge smPIFE and smFRET into a unified intensity-FRET assay by demonstrating theoretically and experimentally that PIFE and FRET are compatible techniques. Here we develop a strategy to measure FRET in the presence of PIFE associated fluctuations. Furthermore, we are able to show how to extract fluctuations in the fluorescence quantum yield of the donor dye (associated to PIFE) when performing FRET experiments.

2.2 Abstract

Förster resonance energy transfer (FRET)-based single-molecule techniques have revolutionized our understanding of conformational dynamics in biomolecular systems. Recently, a new single-molecule technique based on protein-induced fluorescence enhancement (PIFE) has aided studies in which minimal (<3 nm) displacements occur. Concerns have been raised regarding whether donor fluorophore intensity (and correspondingly fluorescence quantum yield Φ_f) fluctuations, intrinsic to PIFE methods, may adversely affect FRET studies when retrieving the donor–acceptor dye distance. Here, we initially show through revisions of Förster's original equation that distances may be calculated in FRET experiments regardless of protein-induced intensity (and Φ_f) fluctuations occurring in the donor fluorophore. We additionally demonstrate by an analysis of the recorded emission intensity and competing decay pathways that PIFE and FRET methods may be conveniently combined, providing parallel complementary information in a single experiment. Single-molecule studies conducted with Cy3- and ATTO647N-labeled RNA structures and the HCV-NS5B polymerase protein undergoing binding dynamics along the RNA backbone provide a case study to validate the results. The analysis behind the proposed method enables for PIFE and FRET changes to be disentangled when both FRET and PIFE fluctuate over time following protein arrival and, for example, sliding. A new method, intensity-FRET, is thus proposed to monitor conformational changes spanning from angstroms to nanometers.

2.3 Introduction

Single-molecule fluorescence (SMF) studies based on Förster resonance energy transfer (FRET) have advanced our understanding of structural dynamics in proteins, nucleic acids (DNA and RNA), and their multimeric complexes, that is, binary, ternary, or larger structures encompassing either proteins, nucleic acids, or both.[1-5] The judicious choice of the donor and acceptor pair of fluorophores based on their spectral overlap has enabled exploring fluctuations ranging from 1.0 to 7.5 nm.[6-7] Among many available fluorophores, cyanine dyes Cy3 and Cy5 have been amply adopted to conduct smFRET studies due to their photochemical robustness.

Most recently, an SMF method based on protein-induced fluorescence enhancement (PIFE) has provided insights on structural changes spanning <3 nm.[8-13] The use of PIFE circumvents protein

labeling making the method amenable to, for example, enzymatic studies requiring multiple enzyme variants. PIFE relies on the increase in the emission intensity (and fluorescence quantum yield, Φ_f) of Cy3 when in close proximity to a protein. The increased steric hindrance/viscosity in the vicinity of the protein leads to a reduced probability for the first singlet excited state of Cy3 to relax into a configurational isomer upon 90° rotation along the Cy3 polymethine bridge. This intermediate is known to decay in a nonradiative manner to the twisted ground state and as such provides a nonemissive deactivation pathway for Cy3, leading to a drop in its Φ_f.[14-16] Importantly, deactivation to the twisted ground state may next regenerate the trans form of the dye, yet it may also result in the cis configuration of Cy3. The latter is a fairly unstable species that rapidly isomerizes to the trans form on timescales spanning microseconds to milliseconds.[14, 17] The cis-Cy3 is also characterized by an absorption spectrum that is red-shifted by 20 nm compared to that of the trans isomer.[17-19] cis-Cy3 in the first singlet excited state has further been reported to show negligible emission.[15, 19-20] All in all, rotation in the excited state and consequent nonradiative relaxation to the ground state result in a drop in emission from Cy3, a phenomenon that is mitigated in the presence of the increased steric hindrance/viscosity provided by a nearby protein, giving rise to the protein-dependent PIFE phenomenon.

The Cy3 intensity fluctuations that the PIFE method builds on, however, adversely affect SMF studies that are based on the estimation of the absolute efficiency, E, of energy transfer by the FRET mechanism. That is, processes that modulate the donor Cy3 fluorescence quantum yield, Φ_f^D, will render E an unreliable parameter to use to retrieve distance fluctuations between donor and acceptor dyes. It would thus appear that PIFE and FRET techniques are mutually exclusive, wherein what constitutes an ideal substrate for one method is highly detrimental to the other.

To reconcile the two techniques, a quantitative method capable of simultaneously and independently measuring PIFE and FRET changes is required. In this regard, a number of studies have utilized PIFE and FRET methods in a parallel set of experiments in ensemble[21-24] and/or at the single-molecule level.[25-27] Ongoing work from our group on the dynamics of the hepatitis C virus nonstructural protein 5B (HCV-NS5B)[28] and helicase (NS3)[29] and that of others provided for motivation into decoupling contributions from PIFE and FRET such that ultimately both techniques may be utilized simultaneously. That is, through a single set of experiments, one may

obtain information on both short-range dynamics, <3 nm, through PIFE and long-range dynamics, between 3 and 8 nm, through FRET.

To the best of our knowledge, two different research teams have tackled this problem. Initially, Penedo *et al.* reported on single-molecule studies of surface-immobilized substrates involving binding dynamics of a monomeric single-stranded binding protein to DNA.[30] They used the apparent FRET efficiency (intensities corrected for the background only) and the detected total intensity (donor plus acceptor intensities) as a marker of PIFE. Such a treatment would provide an indirect marker of increase in Φ_f^D, as long as the PIFE effect occurs without affecting FRET, that is, FRET remains constant throughout the visualization.[13] More recently, the groups of Weiss and Cordes reported the theoretical underpinning and methodological application of PIFE–FRET,[31-32] a method building on ALEX, originally reported by Weiss,[33] that enables disentangling PIFE from FRET, effectively providing two molecular rulers at different length scales. Working under the assumption that Cy3 emission is nonexistent for the 90° conformer, they developed a technique that is suitable for freely diffusing substrates. Their method requires for alternating excitation of the donor (Cy3) and the acceptor (e.g., ATTO647N) fluorophores. In addition, it requires a calibration to account for changes in the Förster radius of Cy3; this is effectively accomplished by conducting a parallel set of experiments with Cy3B-labeled substrates, the locked analogue of Cy3 unable to undergo rotation in the excited state.[34] In their work, Weiss, Cordes, and colleagues used stoichiometry value[31-32] S as an indirect marker of fluctuations in the fluorescence quantum yield of the donor, Φ_f^D, hence accounting for changes in PIFE. Caution was, however, expressed in interpreting changes in S when the efficiency of energy transfer changed during the experiment.

Our own rationalization of the problem led us to realize, through revision of Förster's initial theory on energy transfer, that donor–acceptor distances r may be reliably retrieved regardless of artifacts in FRET efficiency arising from changes in Φ_f^D. That is, even when PIFE or, for example, quenching through photoinduced electron transfer (P*e*T) may exist and as such may affect Φ_f^D, donor–acceptor distances may still be safely retrieved. This in turn would allow decoupling FRET from PIFE (vide infra).

In this work, we initially demonstrate that the proximity ratio (E_{pr}, **eq 2.1**), a parameter typically applied in smFRET studies[4-5, 35] and related to the donor, I_D, and acceptor, I_A, emission intensities

per unit time (corrected for background and cross-talk, but also, in the case of the acceptor dye, corrected for direct excitation), provides a suitable marker of interdye distances independently of fluctuations in Φ_f^D. In addition, a new parameter, R_{EE}, related to the distance parameter R_0 in the Förster's equation, is introduced, allowing to relate interdye distance r to the proximity ratio. By combining the use of E_{pr} and R_{EE}, we show that the former is the most suitable method to compute distance fluctuations from single-molecule donor–acceptor intensity–time trajectories even in the presence of fluctuations affecting Φ_f^D. Experiments conducted with surface-immobilized Cy3–Cy5-tagged RNA strands, differing both in the Cy3 attachment and concomitantly on Φ_f^D, are shown. Also shown are experiments in which Cy3 is replaced by Cy3B, the locked form of Cy3. These results validate the convenience of using jointly E_{pr} and R_{EE}. These results are of general validity provided only one species is emissive for the donor dye (see also **Figure 2.1**). Such a situation would be applicable for Cy3 under the hypothesis that the cis configurational isomer is nonemissive. This is a valid hypothesis given the negligible fluorescence quantum yield reported for the first singlet excited state of cis-Cy3 due to a very fast relaxation to the 90° intermediate.[15, 19-20] This relaxation is estimated to be 2 orders of magnitude faster at room temperature for cis- versus trans-Cy3 given the ~3.0 kcal/mol lower activation energy barrier for the former.[36] On the basis of the fluorescence quantum yields of Cy3 (Φ_f = 0.09) and Cy3B (Φ_f = 0.85),[14] one may further estimate that the relaxation rate constant for trans (and thus cis)-Cy3 is 1 (3) order(s) of magnitude larger than its radiative rate constant, under the assumption that the radiative rate constants for cis- and trans-Cy3 do not differ. It is then safe to estimate that at room temperature the fluorescence quantum yield of cis-Cy3 is <0.001.

$$E_{pr} = \frac{I_A}{I_A + I_D} \tag{2.1}$$

We next show in this work that for doubly labeled donor–acceptor systems, we may monitor distance fluctuations following FRET analysis (E_{pr}) while simultaneously retrieving PIFE information or in general fluctuations on Φ_f^D arising from environmental perturbations. The presence of the acceptor dye does not prevent the evaluation of PIFE; in fact, we use the intensity of the acceptor to determine changes in Φ_f^D. Our method enables decoupling PIFE from FRET for single surface-immobilized molecules, provided the signal may be monitored before and after protein arrival, a requirement that enables obtaining a reference point to compute the enhancement.

Our analysis requires excitation of the donor dye only, under the assumption that the acceptor dye does not undergo changes in its fluorescence quantum yield, that is, Φ_f^A is constant throughout the experiment.

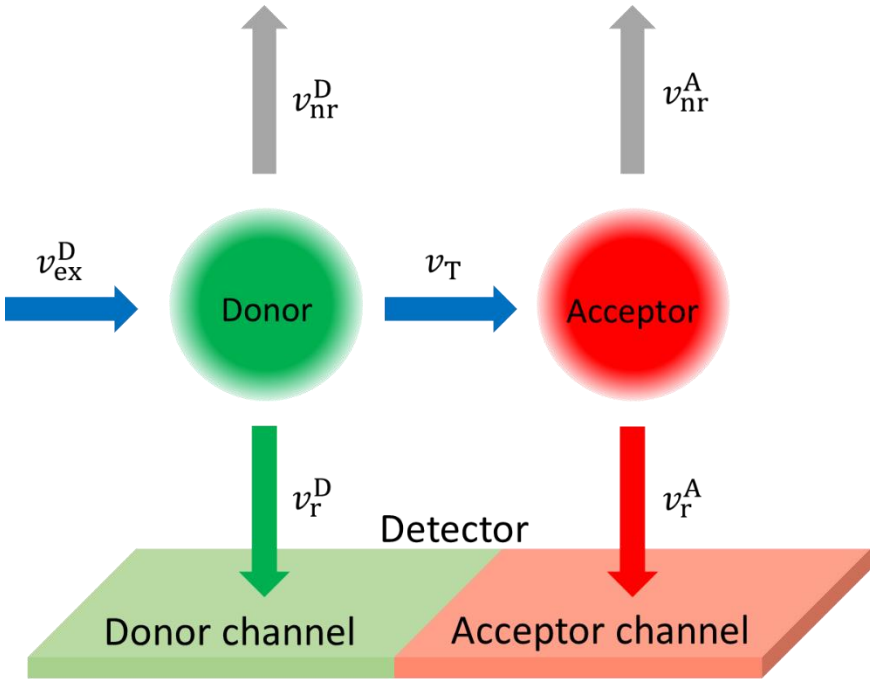

Figure 2.1. Flux diagram showing all processes that populate and depopulate the first singlet excited state of the donor and acceptor dyes. Here, $\boldsymbol{v_{ex}^D}$ is the donor excitation rate, $\boldsymbol{v_r^D}$ the donor emission rate, $\boldsymbol{v_{nr}^D}$ the donor nonradiative decay rate, $\boldsymbol{v_T}$ the energy transfer rate, $\boldsymbol{v_r^A}$ the acceptor emission rate, and $\boldsymbol{v_{nr}^A}$ the acceptor nonradiative decay rate. All rates are in s^{-1}. The figure is of general validity, provided only one species is emissive for the donor dye. An assumption that may be considered valid for Cy3 given the negligible fluorescence quantum yield reported for the first singlet excited state of cis-Cy3. [15, 19-20]

PIFE and FRET strategies may thus be conveniently combined through a simple analysis in experiments in which proteins are flowed in. A new method, intensity-FRET (I-FRET), is thus proposed to monitor conformational changes spanning from angstroms to nanometers. The analysis behind our method enables for PIFE and FRET changes to be disentangled when both FRET and PIFE fluctuate over time following protein arrival and, for example, sliding (i.e., there is sliding of the protein affecting the donor and acceptor mutual distances and also affecting the intrinsic (in the absence of the acceptor) fluorescence quantum yield of the donor). Studies at the single-molecule level with doubly labeled constructs in the presence of the HCV nonstructural protein NS5B[28] validate the I-FRET approach. The new technique offers the opportunity to

monitor a diverse range of dynamic biomolecular systems, wherein fluctuations in Φ_f^D (enhancement or drop) resulting from environmental changes may be uncoupled from FRET changes, providing parallel complementary information in a single experiment.

2.4 Materials and Methods

2.4.1 Reagents

d-(+)-Glucose, glucose oxidase type VII from *Aspergillus niger* (G2133), and β-mercaptoethanol were purchased from Sigma Aldrich. Tris–HCl buffer (1 M); 1 M HEPES buffer, pH 7.3; hydrogen peroxide; hydrochloric acid; and acetone (HPLC grade) were purchased from Fischer Scientific. NaCl stock solution (5 M) was purchased from Life Technologies (Ambion brand). Water (molecular biology grade) and sodium bicarbonate 7.5% solution were acquired from Thermo Scientific HyClone (South Logan, UT). Streptavidin protein was purchased from Life Technologies (Burlington, ON). Vectabond was purchased from Vector Laboratories (Burlington, ON). Poly(ethylene glycol) succinimidyl valerate, MW 5000 (mPEG-SVA), and biotin-PEG-SVA were purchased from Laysan Bio Inc. (Arab, AL). Sulfuric acid was purchased from Caledon Laboratories.

2.4.2 Fluorophores

8-Acetoxymethyl-2,6-diethyl-1,3,5,7-tetramethylpyrromethene fluoroborate (PM605) was purchased from Exciton, Inc. 1,1′-Dioctadecyl-3,3,3′,3′ tetramethylindodicarbocyanine perchlorate (DiD) was purchased from Invitrogen Canada (Burlington, ON). All materials were used without further purification.

2.4.3 Nucleic Acids

(Cy3 and Cy3B)-tagged RNA strands were purchased from Trilink Biotechnologies, and (Cy5 and ATTO647N)-biotin-tagged DNA strands were purchased from Integrated DNA Technologies IDT. Listed below in **Figure 2.2** are the sequences utilized in constructing the DNA/RNA duplexes in our study.

2.4.4 Preparation of RNA–DNA Duplexes

The RNA–DNA duplexes were annealed from biotinylated 18mers (ACC TCG CGA CCG TCG CCA-biotin, Cy5-ACC TCG CGA CCG TCG CCA-biotin, or ATTO647N-ACC TCG CGA CCG TCG CCA-biotin) and dye/R_n^X sequences (**see Figure 2.2**). Oligonucleotides were purified through HPLC by the provider. To enable surface immobilization of the DNA/RNA duplex, the 3′ end of the DNA strand was attached to a biotin moiety. The duplexes were annealed by mixing 2.5 μm of both DNA and RNA strands in an annealing buffer (50 mM Tris–HCl, 50 mM NaCl, pH ∼ 8.0) and then incubating the mixture in a thermal cycler at 95 °C for 2 min and gradually (2 °C/min) cooling it to 25 °C. The duplex formation was confirmed using 10% native polyacrylamide gel electrophoresis.

2.4.5 Steady-State Absorption and Fluorescence

Absorbances were recorded using a HITACHI U-2800 UV–vis spectrophotometer. Emission scans were recorded using a PTI QuantaMaster 400 spectrofluorometer and the provided software. The fluorescence spectra were recorded using a 2 nm bandwidth excitation and emission slits. Fluorescence was recorded every 1 nm using a 0.2 s integration time. Emission spectra were corrected for wavelength-dependent variations in the detector sensitivity. Room temperature fluorescence quantum yields of green dyes were determined using PM605 in acetonitrile (Φ_f^D = 0.72)[37]. For red dyes, DiD in methanol (Φ_f^D = 0.33)[38] was used as a reference. Absorption and emission spectra of the dyes of interest were measured in imaging buffer (10 mM in HEPES buffer pH 7.3 and 20 mM in NaCl) at different concentrations. The absorbance of all samples was kept below 0.05 at the excitation wavelength (514 nm (green) and 620 nm (red)). The integrated intensity versus absorbance were then plotted and fitted linearly. Relative fluorescence quantum yields for the unknown with respect to the standard were obtained according to well-established methods[39] by comparing the absorption and emission of the unknown and standard samples and correcting for the solvent refractive index of the solution of the unknown and standard.

2.4.6 Single-Molecule Sample Preparation and Surface Immobilization

Coverslips were soaked in piranha solution (25% H_2O_2 and 75% concentrated H_2SO_4) and sonicated for 1 h, followed by multiple water (molecular biology grade) and acetone (high-

performance liquid chromatography (HPLC) grade) rinsing cycles. Dry and clean coverslips were then treated with vectabond/acetone 2.5% v/v solution for 5 min and then rinsed with H_2O and left in a dried state until used. To prevent nonspecific adsorption of biomolecules onto the glass surface, coverslips were functionalized before use with a mixture of poly(ethylene glycol) succinimidyl valerate, MW 5000 (mPEG-SVA), and biotin-PEG-SVA at a ratio of 99/1 (w/w), in a 0.1 M sodium bicarbonate solution for 3 h. Excess PEG was rinsed with water, and the coverslips were dried under a N_2 stream. Imaging chambers (~8 μL) were constructed by pressing a polycarbonate film with an adhesive gasket onto a PEG-coated coverslip. Two silicone connectors were glued onto the predrilled holes of the film and served as inlet and outlet ports.

Before image acquisition, the surface was incubated with 15 μL of 0.2 mg/mL streptavidin solution for 10 min. The unbound streptavidin was washed away with the imaging buffer (20 mM NaCl, 10 mM HEPES buffer pH 7.3). After streptavidin incubation, the DNA/RNA hybrid was immobilized on PEG-coated glass coverslips through biotin–streptavidin interactions upon incubating a 200 pM solution of the annealed construct. Unbound duplexes were flushed out with additional imaging buffer.

2.4.7 Antifading Solution

To increase Cy3 and Cy5 photostability, all experiments were done under a constant flow of an oxygen scavenger solution consisting of 2-mercaptoethanol 1% v/v, d(+)glucose 0.8% w/v, and glucose oxidase 1.1 mg/mL (165 units/mL). Solutions were 10 mM in HEPES buffer pH 7.3 and 20 mM in NaCl with 100 nM NS5B when necessary. All experiments were conducted at room temperature (23 °C).

2.4.8 TIRF Microscopy and Image Analysis

Fluorescence single-molecule experiments were carried out using a TIRF microscope (TIRFM) as described previously.[28] The TIRFM setup consisted of an inverted microscope (IX71; Olympus) equipped with a laser-based TIRFM illumination module (IX2-RFAEVA-2; Olympus) coupled to a diode-pumped solid-state green laser (532 nm, CrystaLaser). The beam position was adjusted using the illuminator to attain total internal reflection through an oil-immersion objective (N.A. 1.45, Olympus PLAN APO N 60×). Fluorescence emission was collected through the objective, and images were captured with an EMCCD camera (CascadeII: 512B, Photometrics, Roper

Scientific). For imaging of Cy3, the laser beam was coupled into the microscope objective using a beam splitter (FF562-Di02 25 × 36, BrightLine, Semrock). The emission was then refocused by a lens with a focal length equal to 150 mm. Emission was chromatically separated using two dichroic mirrors (640dcxr; Chroma Technology) with the "green" and "red" emission filtered through band pass filters (HQ590/70M and HQ685/80M, respectively, Chroma Technology) before being captured each by one half of the EMCCD camera chip.

The camera was controlled using Micro-Manager Software (Micro-Manager 1.4.13, San Francisco, CA), capturing 8-bit 512 × 512 pixel images with an exposure time of 200 ms. Excitation was carried out at a full power setting (25 mW) with a power output of ~9.0 mW at the objective for the green (532 nm) laser. We observe typically ~200–300 spots over one field of view (35 μm × 70 μm). Fluorescence intensity–time trajectories of individual molecules were extracted from the videos using a self-written algorithm in IDL and Matlab defining a square region of 3 × 3 pixels around the centers of the spots captured.

2.5 Results and Discussion

2.5.1 Reformulating Förster Equation

In deriving an equation to account for the rate constant of energy transfer k_T as a function of distance r due to perturbations from coulombic dipole–dipole interactions, Förster sought to replace the square of the scalar product of the donor and acceptor transition dipole moments ($\overrightarrow{\mu_D}$ and $\overrightarrow{\mu_A}$, respectively, **eq 2.2**) by readily available experimental parameters related to the donor and acceptor dyes. [40-41] It is then that the extinction coefficient of the acceptor dye, ε_A, and the radiative rate constant of the donor dye, k_r^D, came into place in addition to other factors to render the Förster equation as we have known of it for the past ca. 70 years[39, 41-42] (**eq 2.3**, where we use 9000 rather than the frequently encountered 9 for unit considerations[39] (see also **Section 2.6.2** for a revision of the Förster theory)). Here, the extinction coefficient was incorporated into the integral term, $J(\lambda)$; in turn, k_r^D was replaced by the product of the decay rate constant of the donor in the absence of the acceptor, k_d^D (the reciprocal of the fluorescence lifetime, τ_d^D) and its fluorescence quantum yield, Φ_f^D.

$$k_T = \left(\frac{\overrightarrow{\mu_D}\cdot\overrightarrow{\mu_A}}{r^3}\right)^2 \tag{2.2}$$

$$k_T = \frac{k_r^D \kappa^2}{r^6}\left(\frac{9000(\ln 10)}{128\pi^5 N_A n^4}\right)J(\lambda) = \frac{\Phi_f^D k_d^D \kappa^2}{r^6}\left(\frac{9000(\ln 10)}{128\pi^5 N_A n^4}\right)J(\lambda) \tag{2.3}$$

The efficiency of energy transfer, E, defined as the ratio of probabilities of undergoing energy transfer versus decaying through all processes, and frequently encountered in any of the forms displayed in **eq 2.4**, has become the paradigm equation to follow changes in distance *r* between a donor and acceptor dye.[39, 42] The Förster radius, R_0, the distance at which energy transfer is 50% efficient ($k_T = k_d^D$), follows as a corollary of the energy transfer efficiency definition and **eq 2.3** (**see eq 2.5**).

$$E = \frac{k_T}{k_T + k_d^D} = \frac{1}{1+\left(\frac{r}{R_0}\right)^6} = 1 - \frac{\tau_d^{DA}}{\tau_d^D} \tag{2.4}$$

$$R_0 = \left(\Phi_f^D \kappa^2 \left(\frac{9000(ln10)}{128\pi^5 N_A n^4}\right)J(\lambda)\right)^{1/6} \tag{2.5}$$

A major caveat of working with energy transfer efficiency to determine *r* arises from the dependence of the former on Φ_f^D and thus on the effect the environment may exert in modulating the nonradiative decay rate constant of the donor dye, k_{nr}^D. Phenomena such as PIFE, or quenching following, for example, P*e*T by a peptide residue or nucleic acid base, upon changing the value of Φ_f^D may yield *E* an unreliable parameter to work with in determining *r*.

We reasoned that a more appropriate way to relate the single-molecule acceptor and donor emission intensities over time with *r* would be to compute the ratio of energy transfer to emission probabilities for the donor dye, given by **eq 2.6**. This ratio is only dependent on orientation κ^2 and distance *r* parameters but, and in contrast to *E*, not on Φ_f^D. That is, nonradiative transitions may deplete the energy jointly available for emission and energy transfer processes but do not affect their mutual relationship, which remains constant over time (see also the diagram in **Figure 2.1**). Importantly, the independence of the ratio of probabilities for energy transfer and emission is of general validity provided only one species is emissive for the donor dye. Such a situation would be applicable for Cy3 under the assumption that only the trans configurational isomer is emissive (vide supra). For a more complete analysis of Cy3 photophysics based on a Jablonski diagram, please see references 15 and 31.

It next follows that distance *r* at which the energy transfer and the emission probabilities for the donor dye are the same may be determined. The radius of emission-transfer equipartition (R_{ET}) may thus be defined, in analogy to the Förster radius (**eq 2.7**). The ratio k_T/k_r^D may then be calculated as a function of R_{ET} upon rearranging **eqs 2.6 and 2.7** (**see eq 2.8**). Note once again that this magnitude is devoid of artifacts associated with fluctuations in Φ_f^D.

Toward the ensuing discussion, a change of variables should be adopted where instead of utilizing rate constants or coefficients k, it is most suitable to next utilize rates v for a given process (see **Figure 2.1** and **eq 2.8**; see also **Section 2.6.3** for more details). This change of variables is required when discussing the rate of excitation of fluorophores, toward ultimately defining fluorescence quantum yields as the rate of emission over the rate of excitation.[43] This becomes most apparent in **eq 2.9** below, where the fluorescence quantum yield of the acceptor, Φ_f^A, is expressed in terms of its rate of emission, v_r^A, over its rate of excitation, v_T, which in turn is the rate of energy transfer from the donor (use of the rate constant of energy transfer, k_T, would have no physical meaning at this point).

$$\frac{k_T}{k_r^D} = \frac{\kappa^2}{r^6}\left(\frac{9000(\ln 10)}{128\pi^5 N_A n^4}\right)J(\lambda) \tag{2.6}$$

$$R_{ET} = \left(\kappa^2\left(\frac{9000(\ln 10)}{128\pi^5 N_A n^4}\right)J(\lambda)\right)^{\frac{1}{6}} \tag{2.7}$$

$$\frac{k_T}{k_r^D} = \frac{v_T}{v_r^D} = (R_{ET}/r)^6 \tag{2.8}$$

To directly relate the acceptor emission intensity and donor emission intensity with *r*, we may use the interdependence of the acceptor excitation rate through energy transfer to its rate of emission, as shown in **eq 2.9**. Combining **eqs 2.8 and 2.9**, a newly obtained expression (**eq 2.10**) renders the ratio of rates of emission for the acceptor over the donor, independently of nonradiative transitions (and Φ_f^D) of the donor dye. It next follows to replace these rates of photon emission by the rates of photon detection for both the acceptor, I_A, and the donor, I_D (**see eqs 2.11–2.12**, where η_A and η_D are the detection efficiencies for the acceptor and donor channel, respectively). Ultimately, we obtain the expression given by **eq 2.13**, relating distance *r* with the corrected emission intensities of the acceptor and the donor, yet independent of the value of Φ_f^D.

$$\Phi_f^A = \frac{v_r^A}{v_T} \tag{2.9}$$

$$\frac{v_r^A}{v_r^D} = \Phi_f^A \frac{\kappa^2}{r^6}\left(\frac{9000(\ln 10)}{128\pi^5 N_A n^4}\right) J(\lambda) = \Phi_f^A (R_{ET}/r)^6 \tag{2.10}$$

$$I_A = \eta_A v_r^A \tag{2.11}$$

$$I_D = \eta_D v_r^D \tag{2.12}$$

$$\frac{I_A}{I_D} = \frac{\eta_A}{\eta_D}\Phi_{\mathrm{f}}^{\mathrm{A}}\left(\frac{R_{ET}}{r}\right)^6 \tag{2.13}$$

The proximity ratio, E_{pr} (**eq 2.1**), typically applied in SMF studies to estimate an apparent FRET efficiency,[4-5, 35] may now be expressed in terms of R_{ET} upon combining **eqs 2.13 and 2.1** to yield a new equation, **eq 2.14**. Whereas both **eqs 2.13 and 2.14** show a dependence of distance r on the acceptor fluorescence quantum yield (and thus nonradiative transitions), the dependence of the environment on the donor dye is removed. The calculation of the absolute efficiency of energy transfer, E, in terms of the single-molecule emission intensity trajectories is shown for comparison in **eq 2.15**, which shows the additional appearance of the term $\Phi_{\mathrm{f}}^{\mathrm{D}}$ in the correction factor, γ (**see Sections 2.6.2 and 2.6.4** for more details about γ).

$$E_{pr} = \frac{I_A}{I_A + I_D} = \frac{1}{1+\frac{I_D}{I_A}} = \frac{1}{1+\frac{\eta_D}{\eta_A}\frac{1}{\Phi_{\mathrm{f}}^{\mathrm{A}}}\left(\frac{r}{R_{ET}}\right)^6} \tag{2.14}$$

$$E = \frac{I_A/\left(\eta_A\Phi_{\mathrm{f}}^{\mathrm{A}}\right)}{I_A/\left(\eta_A\Phi_{\mathrm{f}}^{\mathrm{A}}\right)+I_D/\left(\eta_D\Phi_{\mathrm{f}}^{\mathrm{D}}\right)} = \frac{1}{1+\left(\frac{\eta_A\Phi_{\mathrm{f}}^{\mathrm{A}}}{\eta_D\Phi_{\mathrm{f}}^{\mathrm{D}}}\right)\frac{I_D}{I_A}} = \frac{1}{1+(\gamma)\frac{I_D}{I_A}} = \frac{1}{1+\frac{1}{\Phi_{\mathrm{f}}^{\mathrm{D}}}\left(\frac{r}{R_{ET}}\right)^6} = \frac{1}{1+\left(\frac{r}{R_0}\right)^6} \tag{2.15}$$

To validate the convenience of using E_{pr} given its independence on fluctuations on nonradiative decay processes of the donor dye, we next recorded single-molecule intensity–time trajectories and calculated E_{pr} for three donor–acceptor-labeled RNA structures differing in the fluorescence quantum yield of the donor dye. To this end, we utilized a TIRFM setup[44] coupled to an electron multiplied CCD camera (see **Figure 2.2** for a cartoon and **section 2.6** for additional details). The structures utilized were prepared bearing the donor dye Cy3 (or its rigid analogue Cy3B) and the acceptor dye Cy5. The dyes were attached at similar positions in the three constructs (preserving

r and *J*(λ)), yet the structures differed in the anchoring chemistry utilized to tag the nucleic acid with Cy3, or in the actual structure of the chromophore, effectively affecting Φ_f^D (see Table 2.1). Specifically, DNA/RNA duplexes with 20 base overhangs were tagged with a Cy3 either through an internal amidite, where the dye becomes part of the RNA phosphate backbone minimizing its rotational freedom (Cy3/R_{20}^A), or through a succinimide linker to a nucleotide base, enabling ample rotational motion (Cy3/R_{20}^S). Alternatively, we used Cy3B, a rigid form of Cy3 unable to undergo configurational changes (trans–cis photoisomerization) upon photoexcitation (Cy3B/R_{20}^S).[34]

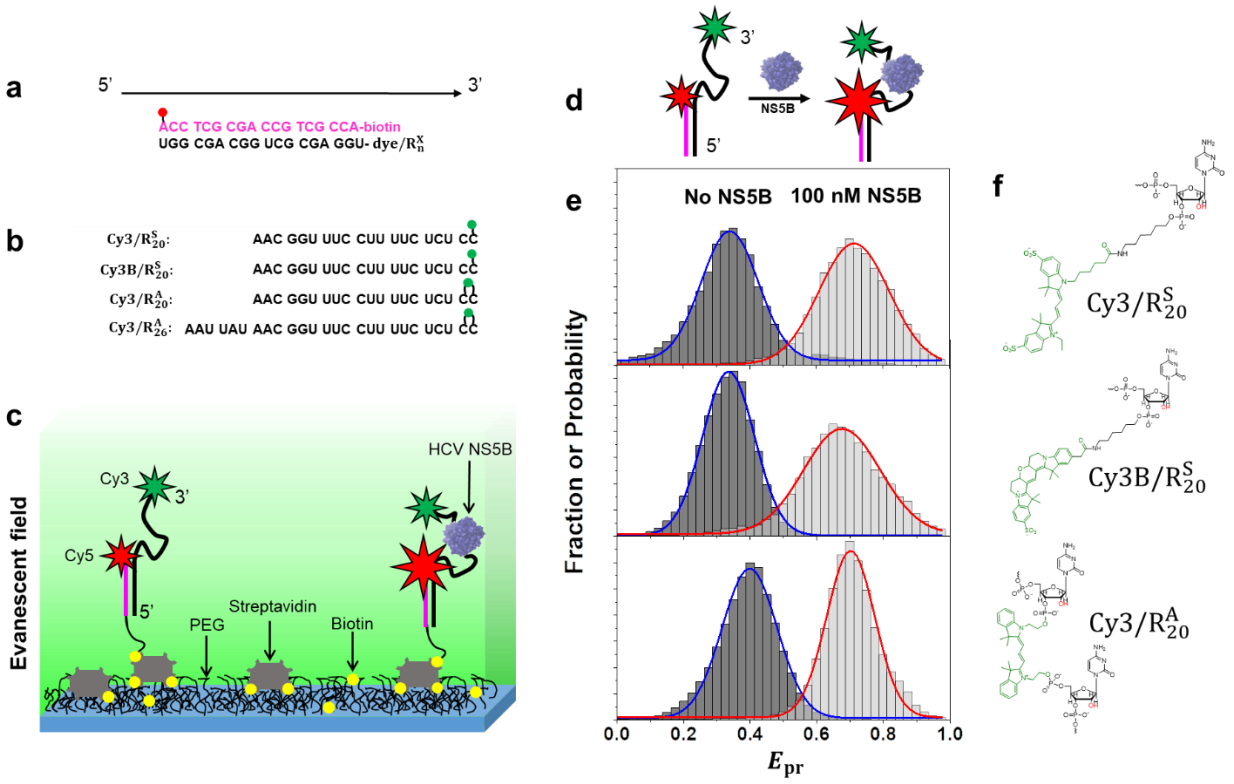

Figure 2.2. Experimental design and distribution of E_{pr} values recorded from smFRET total internal reflection fluorescence (TIRF) experiments. (a) Eighteen base pair DNA/RNA hybrid duplex region with 3′ RNA overhang (dye/R_n^X); DNA is shown in pink and RNA in black. (b) RNA template (3′ overhang, dye/R_n^X) sequences used in our studies, where n denotes the length of the 3′ overhang, and X specifies the dye functionalization strategy (A for amidite and S for succinimide); the Cy3 position is displayed as a hook when an internal Cy3 amidite is used and as a stem when a succinimide–C6 linker is used. Cy5 and ATTO647N in (a) are terminal amidites. (c) Schematic illustration of surface immobilization of oligonucleotides used in smFRET. (d) Cartoon illustrating a DNA/RNA duplex before (left) and after (right) HCV-NS5B binding. (e) Ensemble histograms of single-molecule E_{pr} values for DNA/RNA duplexes before (left) and after (right) HCV-NS5B binding (E_{pr} was corrected as detailed in **Sections 2.6.4-2.6.7**). (f) Chemical

structures of the linkers utilized to couple the donor (either Cy3 or Cy3B) in Cy3/R_{20}^{S}, Cy3B/R_{20}^{S}, and Cy3/R_{20}^{A}.

Consistent with our estimates, the three constructs displayed a similar ensemble distribution for E_{pr} regardless of the values of Φ_f^D characterizing the donor dye in each structure (**Figure 2.2e**). (These distributions were assembled from the single-molecule intensity–time trajectories recorded for the surface-immobilized constructs in a buffer solution in the presence of an antifading cocktail.) Specifically, upon Gaussian fittings, maximums of 0.34, 0.34, and 0.40 were found for Cy3/R_{20}^{S}, Cy3B/R_{20}^{S}, and Cy3/R_{20}^{A}, respectively, after correcting the trajectories for background, cross-talk, and direct excitation of the Cy5 dye (**see Sections 2.6.4-2.6.7**). The shift in the maximum for Cy3/R_{20}^{A}, compared to that for Cy3/R_{20}^{S}, and Cy3B/R_{20}^{S}, may be accounted for by the slightly closer position of Cy3 to Cy5 in the former structure. We may not rule out the contribution of κ^2 as the donor dye in Cy3/R_{20}^{A}, has a more restricted rotational movement.

Table 2.1. Photophysical and Energy Transfer Parameters for Cy3, Cy3B and Cy5 Attached to Oligonucleotides.

	Φ_f	$J(\lambda)$ ($M^{-1}cm^{-3}$)	R_0 (nm)	R_{ET} (nm)	R_{EE} (nm)
Cy3/R_{20}^{S} [a]	0.09	7.45×10^{-13}	4.81	7.19	6.36
Cy3/R_{20}^{A} [b]	0.15	7.90×10^{-13}	5.23	7.26	6.42
Cy3B/R_{20}^{S} [c]	0.98	9.07×10^{-13}	7.41	7.43	6.57
Cy5/D_{18} [d]	0.48	-	-	-	-

Superscript letters indicate the structures of the dyes as per **Figure 3.5**. All parameters were measured in imaging buffer. DiD was used as a standard in methanol for red dyes[38] (Φ_f = 0.33) and PM605 was used as standard for green dyes[37] (Φ_f = 0.72 in acetonitrile).

We next explored the effect on E_{pr} distributions upon the addition of a protein, the HCV nonstructural protein 5B (HCV-NS5B).[45-47] This is a polymerase protein that, on the basis of our previous studies, affects the absolute FRET efficiency in the construct Cy3/R_{20}^{A}, a result of bringing the donor and the acceptor dye closer in distance after the protein binding along the single-stranded RNA region.[28] HCV-NS5B additionally induces PIFE after binding to the Cy3/R_{20}^{A} structure (**Figure 2.9**).

The E_{pr} distributions obtained in the presence of HCV-NS5B were similar in each case and showed a marked shift toward higher E_{pr} values (closer donor–acceptor distance r) compared to those obtained with no protein (**Figure 2.2e**). In the presence of HCV-NS5B, maximums of 0.71, 0.68, and 0.70 were found for Cy3/R_{20}^{S}, Cy3B/R_{20}^{S}, and Cy3/R_{20}^{A}, respectively, after correcting the trajectories for background and cross-talk. This similarity is remarkable as the three constructs studied differed in their Φ_f^D and also in the magnitude of PIFE in the presence of HCV-NS5B.

Upon establishing the convenience of working with E_{pr}, a new magnitude, for which we coined the name radius of emission equipartition, R_{EE}, may be introduced highlighting the distance r at which the donor and acceptor emissions have the same probability per unit time, yielding E_{pr} = 0.5 (assuming (η_D/η_A) = 1). A direct comparison of **eqs 2.14 and 2.15** illustrates that R_{EE} may be defined as shown in **eq 2.16**, underscoring the dependence of R_{EE} on the fluorescence quantum yield of the acceptor dye (but not the donor), on R_{ET}, and on the donor/acceptor detection efficiency ratio, η_D/η_A, which can be either estimated or calculated experimentally. In turn, the relationship between E_{pr} and r as a function of R_{EE} is given by **eq 2.17**.

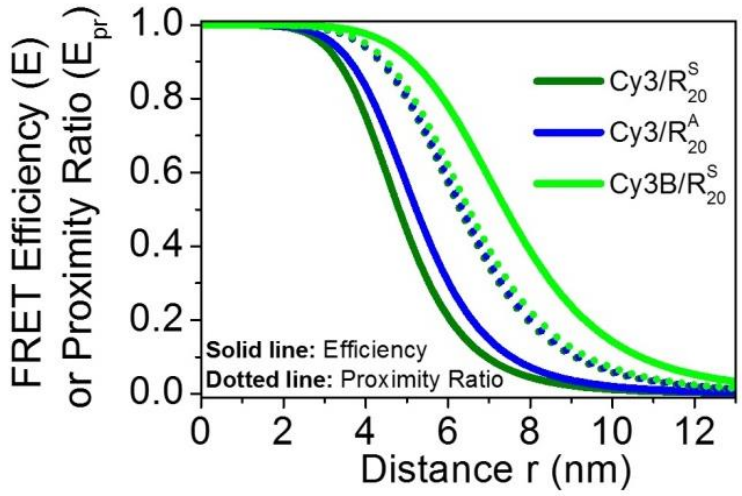

Figure 2.3. Theoretical Distance Dependence of FRET Efficiency *E* and Proximity Ratio E_{pr}. The theoretical curves were calculated utilizing equations in **Table 2.2** and the absorption and emission spectra of the dyes in the 3 constructs studied. Herein it has been assumed $\kappa^2 = 2/3$ and η_D/η_A=1. Solid and dotted lines represent FRET efficiency and proximity ratio respectively.

Changes in E_{pr} with distance r will be most sensitive in the proximity of R_{EE}, the inflection point of the curve of E_{pr} versus r provided that η_D/η_A = 1 (**Figure 2.3**). The magnitude R_{EE} may thus

provide a more suitable parameter to select a given donor–acceptor pair when performing SMF measurements on distance fluctuations, in analogy to the popular use of the Förster radius when working with the bulk absolute efficiency of energy transfer E. **Table 2.2** summarizes and compares the properties of E and E_{pr}.

$$R_{EE} = \left(\Phi_f^A\right)^{\frac{1}{6}} R_{ET} = \left(\Phi_f^A \kappa^2 \left(\frac{9000(ln10)}{128\pi^5 N_A n^4}\right) J(\lambda)\right)^{\frac{1}{6}} \tag{2.16}$$

$$E_{pr} = \frac{I_A}{I_A + I_D} = \frac{1}{1 + \frac{\eta_D}{\eta_A}\left(\frac{r}{R_{EE}}\right)^6} \tag{2.17}$$

Table 2.2. Properties of absolute efficiency of energy transfer and Proximity ratio.

	Absolute efficiency	**Proximity ratio**
Equation	$E = \frac{I_A}{I_A + \gamma I_D} = \frac{1}{1 + \left(\frac{r}{R_0}\right)^6}$	$E_{pr} = \frac{I_A}{I_A + I_D} = \frac{1}{1 + \frac{\eta_D}{\eta_A}\left(\frac{r}{R_{EE}}\right)^6}$
Sensitive range	$R_0^6 = \Phi_f^D R_{ET}^6 = \Phi_f^D \kappa^2 \left(\frac{9000(ln10)}{128\pi^5 N_A n^4}\right) J(\lambda)$	$R_{EE}^6 = \Phi_f^A R_{ET}^6 = \Phi_f^A \kappa^2 \left(\frac{9000(ln10)}{128\pi^5 N_A n^4}\right) J(\lambda)$
Φ_f^D **Dependence**	+	-
Φ_f^A **Dependence**	+	+

Consistent with the above discussion, **Figure 2.3** illustrates that E_{pr} curves vary minimally from construct to construct as R_{EE} is independent of Φ_f^D. The small variation observed is due to the spectral overlap integral difference for the different constructs studied (**Figure 2.6**). In turn, the E curves as a function of r show marked differences arising from the differing values of Φ_f^D for the three constructs studied.

2.5.2 Unifying FRET and PIFE Methods

Upon inspection of **Figure 2.1**, one may intuitively conclude that an increase/(decrease) in the donor intrinsic fluorescence quantum yield resulting from, for example, the PIFE phenomena will

translate to a potential—considering that the dye interdistance and κ are not affected—increase/(decrease) in the acceptor emission intensity, in as far as the environmental effects acting on the donor dye do not affect the emission properties of the acceptor chromophore. In other words, a drop/(enhancement) of the rate accounting for the nonradiative processes would be accompanied by a larger/(smaller) joint rate for donor emission and energy transfer to take place, without affecting their mutual relationship.

One may place the previous qualitative observation into a quantitative result and show that the PIFE technique, typically applied to Cy3-labeled substrates, may be extended to donor–acceptor-labeled constructs provided environmental effects only translate to changes in Φ_f^D but not Φ_f^A. A first step is to consider that the rate of excitation for the donor dye, v_{ex}^D, remains constant throughout the experiment, where the excitation rate equals the rate of decay through all processes including donor emission and—when the acceptor is in close proximity—donor energy transfer (**eq 2.33**). Realizing that the rate of excitation of the acceptor in turn is given by the rate of energy transfer from the donor (where direct acceptor excitation would be nonexistent or corrected for otherwise), an equation may be formulated relating the rate of energy transfer from the donor with an acceptor fluorescence quantum yield and the rate of emission from the acceptor (**eq 2.34**). The constant rate of excitation of the donor may be ultimately expressed in terms of rates of emission of the donor and the acceptor each normalized by their intrinsic fluorescence quantum yields (**eq 2.35**). Rates of emission may in turn be replaced by rates of photon detection, that is, donor and acceptor intensities (corrected for background and cross-talk), to yield an expression like **eq 2.18** below (**eq 2.36**).

$$v_{ex}^D = \frac{I_D}{\eta_D \Phi_f^D} + \frac{I_A}{\eta_A \Phi_f^A} \tag{2.18}$$

Provided the fluorescence quantum yield of the acceptor remains constant with time, fluctuations in the fluorescence quantum yield of the donor over time in **eq 2.18** must be compensated by changes in the donor and acceptor emission to keep the right term in **eq 2.18** constant. Considering that the fluorescence quantum yield of the donor can be written in terms of its initial value before protein arrival $\Phi_f^{D_0}$ and a factor D accounting for fluctuations in Φ_f^D over time (**eq 2.19** below), one may reorganize **eq 2.18** yielding **eq 2.20** below.

$$\Phi_f^D = D\Phi_f^{D_0} \tag{2.19}$$

$$v_{ex}^D = \frac{I_D(t)}{\eta_D D\Phi_f^{D_0}} + \frac{I_A(t)}{\eta_A \Phi_f^A} \tag{2.20}$$

Rearrangement of **eq 2.20** ultimately leads to **eq 2.21** below (**see also eqs 2.36-2.44**), where the left term is acquired before the arrival of a protein for every single molecule and is once again constant. The right term in turn shows that the donor intensity and acceptor intensities change over time, as does the term D, yet they compensate to yield the right term a constant.

$$\gamma_0 I_{D_0} + I_{A_0} = X_0 = \frac{\gamma_0}{D} I_D + I_A \tag{2.21}$$

In a final reorganization of **eq 2.21**, one may retrieve the fluorescence quantum yield enhancement factor, D, that would be observed for the donor in the absence of the acceptor, that is, the PIFE signal reflecting changes in the fluorescence quantum yield of the donor dye with time (**eq 2.22**). Here I_D and I_A are the intensities per unit time of the donor and the acceptor, respectively, at any time (corrected by background and cross-talk), γ_0 is the correction factor for fluorescence quantum yields and detection efficiencies for both donor and acceptor dyes in their channels[48-50] (**see also eq 2.15 and section 2.6**), evaluated at a reference time, before protein arrival/environmental change. The factor $X_0 = I_{D_0}\gamma_0 + I_{A_0}$ is given by the intensities of the donor and the acceptor, I_{D_0} and I_{A_0}, respectively, at the reference time (**see also Section 2.6.3 for a derivation of eq 2.22**). Importantly, the value of D is insensitive to changes in the rate of energy transfer associated to, for example, changes in the orientational factor or interdye distances. **Equation 2.22** applies both for a donor−acceptor-labeled structure where Φ_f^A remains constant and also for a donor-only-labeled construct, when I_{A_0} and I_A values are zero, and the expression simplifies to the standard (donor-only) PIFE version where D is given by the ratio $D = \frac{I_D}{I_{D_0}}$.

$$D = \frac{I_D \gamma_0}{X_0 - I_A} \tag{2.22}$$

It follows that unification of PIFE and FRET methods toward measuring distance fluctuations is thus possible as one may obtain readout values for PIFE when the structure bears an acceptor dye. PIFE and FRET may thus be conveniently combined providing parallel complementary

information in a single experiment. The analysis behind the proposed method enables for PIFE and FRET changes to be disentangled when FRET is not constant (i.e., there is sliding of the protein affecting the donor and acceptor mutual distances) and when the intrinsic (in the absence of the acceptor) fluorescence quantum yield of the donor dye is also not constant, as a result of protein binding and, for example, sliding.

A new method, I-FRET, is thus proposed to monitor conformational changes spanning from a few angstroms (protein-induced intensity fluctuations "I") to a few nanometers (FRET fluctuations). This is experimentally demonstrated by monitoring the donor and acceptor fluorescence intensity−time trajectories obtained for $Cy3/R_{26}^{A}$, following the addition of HCV-NS5B (**Figure 2.4a**), and then calculating both E_{pr} and D values for the same trajectory (**Figure 2.4b,c**, respectively). Importantly, to satisfy that Φ_f^A remains constant, we utilized ATTO647N rather than Cy5 as the latter has been shown to also undergo PIFE.[8] Further, the sequence was enlarged 6 bases to ensure working under a sensitive FRET range.

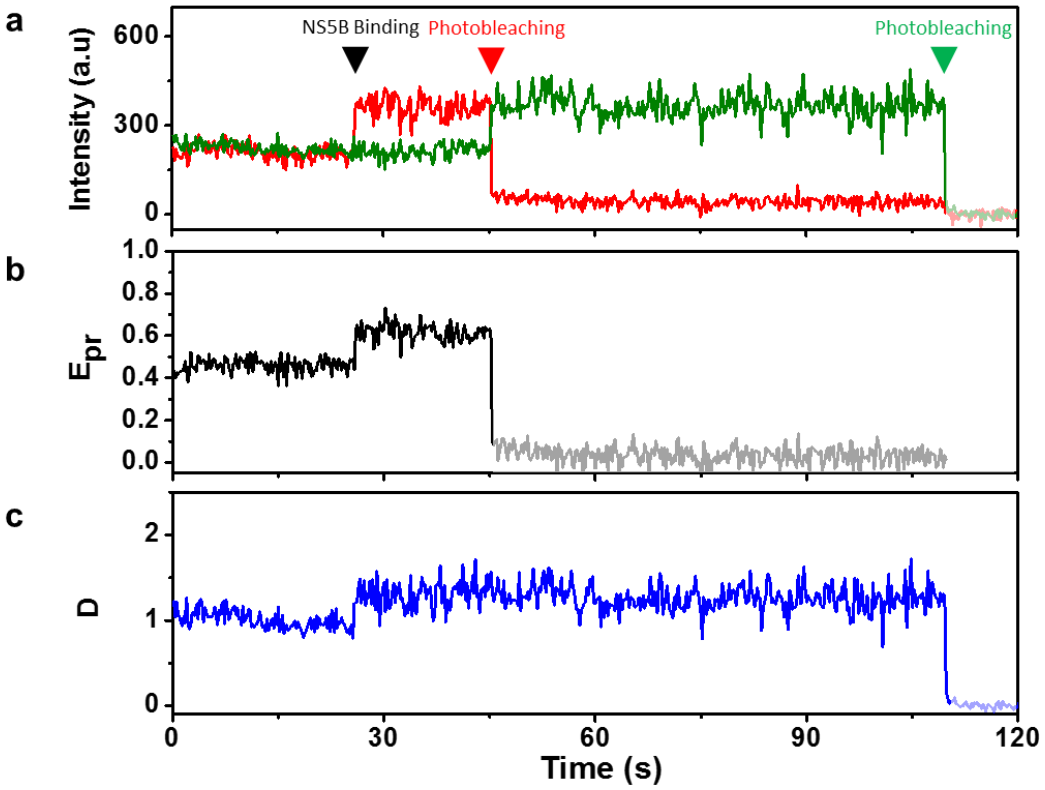

Figure 2.4. Deconvolution of PIFE and FRET Trajectories (I-FRET). Single molecule intensity-time trajectories and calculated PIFE and FRET trajectories are shown for doubly-labeled DNA(ATTO647N)/RNA ($\mathbf{Cy3/R_{26}^{A}}$) duplexes before and after flowing 100 nM of NS5B. (a) Representative donor (green) and acceptor (red) intensity-time trajectories for doubly-labeled DNA/RNA duplex. (b) Calculated proximity ratio $\boldsymbol{E_{pr}}$ from trajectories in (a). (c) Calculated *D* for doubly-labeled DNA/RNA duplex according to **equation 2.22.** Combining results from (b) and (c) one obtains I-FRET results. (Correction parameter used for $\boldsymbol{E_{pr}}$ and *D* analysis were $\boldsymbol{\gamma_0 = 2.6}$ and $\boldsymbol{\beta = 0.09}$, (**Figure 2.7**)).

Figure 2.4 illustrates that upon protein binding, the expected anticorrelated change in the donor and acceptor signals is not observed, rather the Cy3 intensity remains relatively constant while that of ATTO647N increases. The expected decrease in the donor signal as the protein brings to close proximity the acceptor and donor dyes is compensated here by the increase in the intrinsic (in the absence of the acceptor) fluorescence quantum yield of the donor, highlighting the outcome of the combined PIFE and FRET effects. Although anticorrelation is not observed, an increase in the total signal over time, and on *D* as given by **eq 2.22** (qualitatively and quantitatively reporting on PIFE, respectively) and a change in E_{pr} (reporting on FRET), may be observed.

Upon inspection of **Figure 2.4**, it may be additionally appreciated that after acceptor photobleaching, evaluation of E_{pr} serves no purpose, in turn the value of *D* may be recorded through all times, from the initiation of the experiment, before protein arrival, through the arrival of the protein, past the acceptor photobleaching, and till donor photobleaching. The PIFE time trajectory retrieved before and after acceptor photobleaching is unaffected, albeit there is a substantial increase in the donor emission after acceptor photobleaching.

2.6 Conclusions

Our work opens the door for single-molecule FRET studies to be conducted in the presence of either a donor emission enhancer (e.g., a protein when conducting experiments with Cy3) or an emission quencher (such as that observed upon P*e*T). Those perturbations, although affecting the intrinsic fluorescence quantum yield of the donor, do not prevent our ability to retrieve donor−acceptor interdye distances in SMF studies. Such a limitation is apparent when the analysis involves the absolute efficiency of energy transfer but not when the recorded magnitude is the ratio of acceptor intensity over total intensity. Restrictions still exist, however, requiring for no perturbations to apply to the acceptor fluorophore in a FRET pair. It is interesting to mention that

in the context of using E_{pr} as the parameter of choice in single-molecule FRET studies, a new convention should be chosen in selecting a donor− acceptor pair. Instead of utilizing the popular Förster radius, we propose adopting R_{ET} devoid of artifacts associated with fluctuations in the fluorescence quantum yields of either the donor or the acceptor dye.

An equally important outcome of our work is the realization that FRET and PIFE techniques may be unified enabling retrieving distance parameters from a few angstroms to nanometers in doubly labeled donor−acceptor pairs. Essentially, the acceptor becomes a surrogate reporter of fluctuations in the donor dye, where a drop in the rate of nonradiative decay increases the energy jointly available for either emission or energy transfer processes and where distance fluctuations determine how much of that energy is partitioned between both pathways.

2.7 Supplementary Information

2.7.1 Modifications to Oligonucleotides and Spectral Discrimination of Dyes

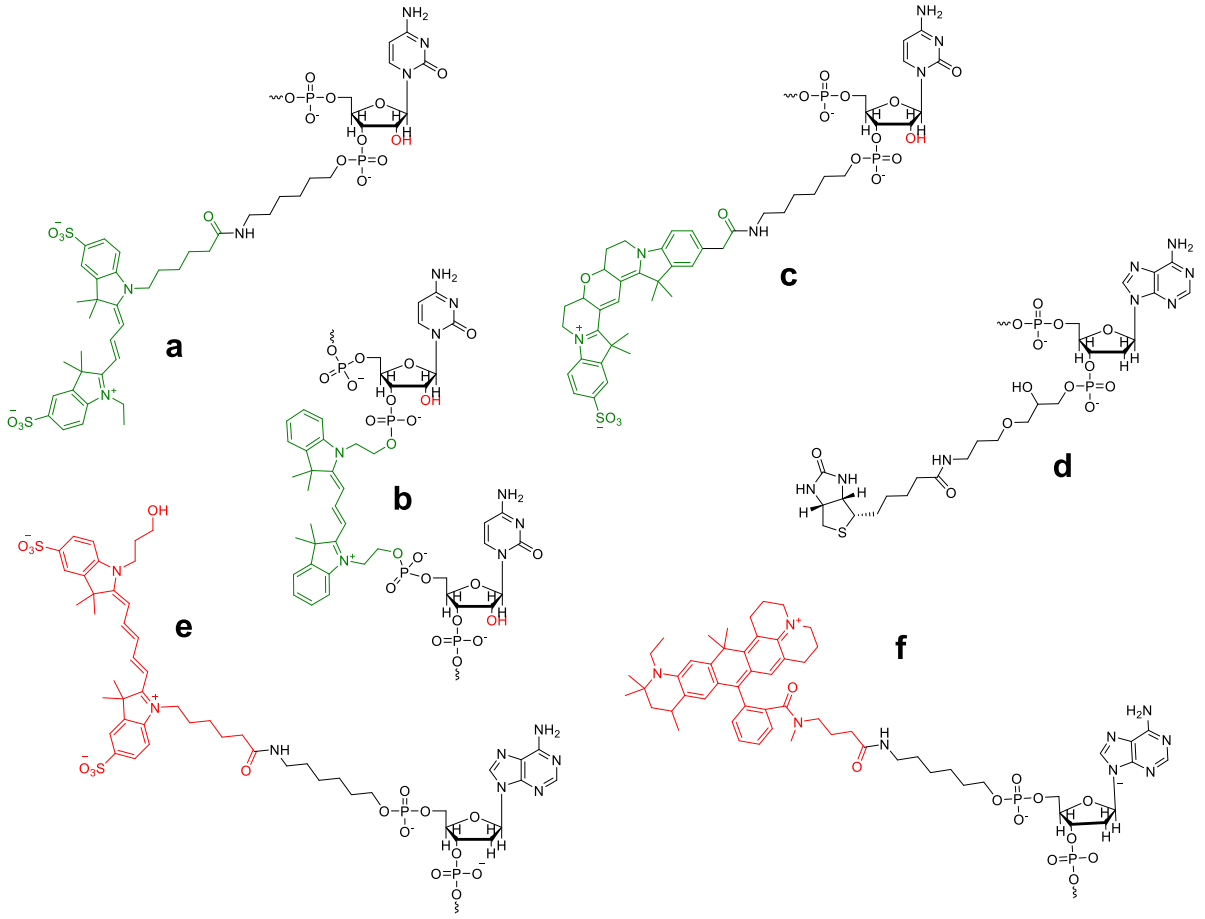

Figure 2.5. Dyes and Modifications Utilized: Chemical structure of the various dye conjugates utilized, Cy3 and Cy3B appear in green and Cy5 and ATTO647N in red. Conjugate (**a**) utilized in R_{20}^{S} is a cytidylate terminated 3' overhang with Cy3 tethered to the phosphate at position 3' of the ribose via a succinimide linker. Conjugate (**b**) utilized in R_{20}^{A} is an internal Cy3 tethered to the phosphate backbone (internal amidite). Conjugate (**c**) utilized in R_{20}^{S} is a cytidylate terminated 3' overhang with Cy3B tethered to the phosphate at position 3' of the ribose via a succinimide linker. Structure (**d**) shows the biotin conjugation at the 3' end of the DNA strand. (**e**) and (**f**) correspond to Cy5 and ATTO647N[51] conjugates at the 5' end of the DNA strand respectively.

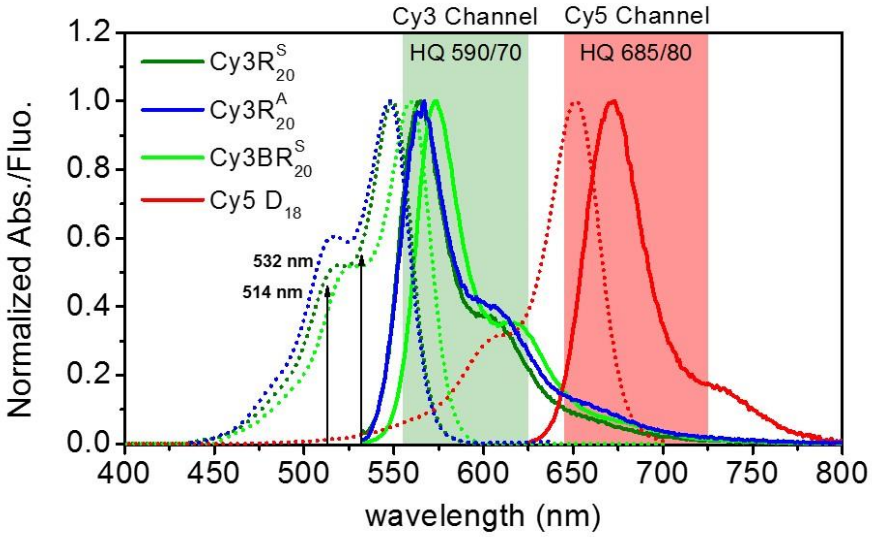

Figure 2.6. Cy3, Cy3B and Cy5 Spectral Discrimination. Absorbance (dotted line) and fluorescence (solid line) spectra of Cy3 (green) Cy3B (light green) and Cy5 (red) labeled oligonucleotides. Superimposed on the spectra are the bandpass profiles for the emission filters utilized for the Cy3 and Cy5 channels.

2.7.2 Revision of the Most Important Equations Used in FRET

The rate constant of energy transfer k_T was defined by Förster as shown in **equation 2.23** below. [39, 41 , 42] It depends on the spectral overlap integral between *donor* and *acceptor* dyes $J(\lambda)$, the fluorescence quantum yield of the donor in the absence of acceptor Φ_f^D, the donor lifetime in the absence of acceptor τ_d^D, the refractive index of the medium n, the Avogadro's number N_A, the geometric factor κ^2 which accounts for the relative dipole orientation between the donor and acceptor and the interfluorophore distance r. The Förster Radius R_0, defined as the distance r at which 50 percent of the energy is transferred to the acceptor, is described by **equation 2.24**. Combining **equations 2.23 and 2.24**, the rate of energy transfer may be written as shown in **equation 2.25**.

$$k_T = \frac{\Phi_f^D \kappa^2}{\tau_d^D r^6}\left(\frac{9000(ln10)}{128\pi^5 N_A n^4}\right)J(\lambda) \tag{2.23}$$

$$R_0 = \left(\Phi_f^D \kappa^2 \left(\frac{9000(ln10)}{128\pi^5 N_A n^4}\right)J(\lambda)\right)^{1/6} \tag{2.24}$$

$$k_T = \frac{1}{\tau_d^D}\left(\frac{R_0}{r}\right)^6 \tag{2.25}$$

The energy transfer efficiency E, defined as the fraction of the donor excitation that is transferred to the acceptor, is given by **equation 2.26**,[52] where k_r is the radiative decay rate constant and k_{nr} is the sum of all other non-radiative decay rates constants (excluding energy transfer). Several methods have been utilised to measure FRET Efficiency. It may be calculated from the donor emission intensity as shown in **equation 2.27**, where Φ_f^D and Φ_f^{DA} are the fluorescence quantum yields of the donor in the absence and presence of acceptor, respectively. Intensities (I^D and I^{DA}) or lifetimes (τ_d^D and τ_d^{DA}) can be used instead of quantum yield.

$$E = \frac{k_T}{k_T + k_r + k_{nr}} = \frac{1}{1+\left(\frac{r}{R_0}\right)^6} \tag{2.26}$$

$$E = 1 - \frac{\Phi_f^{DA}}{\Phi_f^D} = 1 - \frac{I^{DA}}{I^D} = 1 - \frac{\tau_d^{DA}}{\tau_d^D} \tag{2.27}$$

Provided that the acceptor is fluorescent, E may also be obtained using **equation 2.28** below, where I_D and I_A^{exp} are the background corrected experimental intensities of the donor and acceptor respectively.[53]

In order to obtain accurate values for E, corrections must be applied to account for crosstalk (leakage) of the donor into the acceptor channel, differences in the donor and acceptor quantum yields of fluorescence and differences in the detection efficiencies of the two channels (**Figure 2.7**).[48-49] In some cases, direct excitation of the acceptor I_A^{DE} can also be taken into account, especially when efficiency is low and direct excitation becomes an important part of the acceptor signal. In **equation 2.28**, βI_D corrects for the crosstalk of donor emission into the acceptor channel and I_A^{DE} for direct excitation of the acceptor. I_A is then the fully corrected acceptor intensity. The parameter γ as shown in **equation 2.29** accounts for the differences in the fluorescence quantum yield Φ_f and detection efficiency η of donor and acceptor channels.

$$E = \frac{I_A^{exp} - \beta I_D - I_A^{DE}}{I_A^{exp} - \beta I_D - I_A^{DE} + \gamma I_D} = \frac{I_A}{I_A + \gamma I_D} \tag{2.28}$$

$$\gamma = \frac{\eta_A}{\eta_D}\frac{\Phi_f^A}{\Phi_f^D} \tag{2.29}$$

Correction parameters β and γ can be calculated from single molecule intensity-time trajectories.[50, 52, 54-55] The correction factor γ is equivalent to $-\Delta I_A^{exp}/\Delta I_D$ when there is neither crosstalk from the donor to the acceptor channel nor direct excitation of the acceptor (see **Figure 2.7** and text therein), where ΔI_A^{exp} and ΔI_D are the acceptor and donor intensity changes, respectively when acceptor photobleaching occurs. β is determined according to I'_A/I'_D, where I'_A and I'_D are the intensities in the acceptor and donor channels respectively, corrected for background and recorded following acceptor photobleaching and prior to donor photobleaching.

The most frequently used single-molecule spectroscopy analysis based on FRET to monitor distance-conformational fluctuations uses the ratiometric method as an approximation to the real FRET efficiency. This analysis represents the ratio between the acceptor detected fluorescence and the total detected fluorescence (donor + acceptor). When intensities are neither corrected for background nor for crosstalk the result has been termed proximity factor P [56], proximity ratio P[57] PR[58] or relative proximity ratio E_{pr}[50]. When intensities are corrected for background and crosstalk it has been called apparent FRET efficiency E_{app}.[59-60] Recently, proximity ratio E_{pr} has been amply adopted with a new computation involved, where intensities are corrected for both background and crosstalk.[32, 61-62] In this work we have adopted E_{pr} in its new definition as the nomenclature of use. In this specific case, we have also corrected by direct excitation (**see equation 2.30**).

$$E_{pr} = \frac{I_A^{exp} - \beta I_D - I_A^{DE}}{I_A^{exp} - \beta I_D - I_A^{DE} + I_D} = \frac{I_A}{I_A + I_D} \tag{2.30}$$

In utilizing the above equation to calculate FRET efficiency E, it is assumed that $\eta_D \Phi_f^D = \eta_A \Phi_f^A$. This method provides an apparent value for E as recognized in the published literature.

2.7.3 Extracting Changes in the Fluorescence Quantum Yield from FRET Traces

In single molecule experiments, depending on the power of the excitation source, a fluorescent dye may usually undergo several excitation cycles per second and therefore it is convenient to focus on the quanta of energy absorbed, transferred, lost as heat or emitted per second. In the case of absorption and emission processes, those quanta of energy are called photons. For convenience

we will discuss the rates (v) of the processes to differentiate them from the rate constants (k) (k_r for radiative and k_{nr} for non-radiative processes). These new rates (v) may change over the course of the experiment as they will depend on the flux of photons from the excitation source (laser excitation power for the donor and energy transfer rate for the acceptor).

The excitation rate v_{ex} is the number of times a molecule is excited per unit time. The radiative decay rates v_r^D and v_r^A are the number of times the excited donor and acceptor respectively, emit a photon per unit time. Non-radiative decay rates v_{nr}^D and v_{nr}^A are the number of times the excited donor and acceptor respectively deactivate the excited state through non-radiative processes, excluding energy transfer. Finally, v_T is the number of times the donor can transfer a quantum of energy to the acceptor per unit time (**see Figure 2.1**)

A kinetic balance may be obtained from all the processes that populate and depopulate the excited state. The rate of excitation of the donor is equal to the sum of the rates for all the processes that depopulate the excited state of the donor. In the absence of an acceptor, the excited state is depopulated by radiative (emission of a photon) and non-radiative processes (all other paths) as shown by **equation 2.31**, where $I_{ex}(t)$ and σ_D are the excitation flux of photons (s^{-1} cm^{-2}) and the absorption cross section on the donor (cm^2) respectively.

$$I_{ex}(t)\sigma_D = v_{ex}^D = v_{nr}^D + v_r^D \tag{2.31}$$

The fluorescence quantum yield of the donor can be written as:

$$\Phi_f^D = \frac{k_r^D}{k_{nr}^D + k_r^D} = \frac{v_r^D}{v_{nr}^D + v_r^D} \tag{2.32}$$

In the presence of an acceptor, a new deactivation process involving energy transfer to the acceptor dye is added to the excited donor, therefore the new balance is:

$$v_{ex}^D = v_{nr}^D + v_r^D + v_T \tag{2.33}$$

As shown in **equation 2.9**, only a fraction of the energy transferred from the donor to the acceptor will be converted into photons, this fraction is given by the quantum yield of fluorescence of the acceptor dye.

$$\Phi_f^A = v_r^A / v_T \tag{2.34}$$

Replacing **equations 2.34 and 2.32** in **2.33** will yield **equation 2.35**. This equation is valid independently of the rate v_T of energy transfer.

$$v_{ex}^D = \frac{v_r^D}{\Phi_f^D} + \frac{v_r^A}{\Phi_f^A} \tag{2.35}$$

In order to convert v_r^D to rates of photon detection for the acceptor ($I_A(t)$) and donor ($I_D(t)$), it is necessary to correct for a detection efficiency factor (η) accounting for the collection efficiency of the objective, losses due to reflection at multiple interfaces and quantum detection efficiency of the detector utilized. Then $v_r^D = I_D(t)/\eta_D$ and $v_r^A = I_A(t)/\eta_A$. Replacing in **equation 2.35**, we obtain **equation 2.36**. Multiplying **equation 2.36** by $\eta_A \Phi_f^A$ and using the definition of γ in **equation 2.29** will lead to **equation 2.37**.

$$v_{ex}^D = \frac{I_D(t)}{\eta_D \Phi_f^D} + \frac{I_A(t)}{\eta_A \Phi_f^A} \tag{2.36}$$

$$v_{ex}^D \eta_A \Phi_f^A = \frac{\eta_A \Phi_f^A}{\eta_D \Phi_f^D} I_D(t) + I_A(t) = \gamma I_D(t) + I_A(t) \tag{2.37}$$

Armed with **equation 2.37**, the fluorescence quantum yield of the donor can be written in terms of the initial fluorescence quantum yield of the donor and a factor D accounting for fluctuations in Φ_f^D over time (**equation 2.38**. Replacing **equation 2.38** in **2.37** yield **equation 2.39**.

$$\Phi_f^D = D\Phi_f^{D_0} \tag{2.38}$$

$$v_{ex}^D \eta_A \Phi_f^A = \frac{\eta_A \Phi_f^A}{\eta_D D \Phi_f^{D_0}} I_D(t) + I_A(t) = \frac{\gamma_0}{D} I_D(t) + I_A(t) \tag{2.39}$$

Note that γ_0 is defined as a fixed initial parameter and it does not depend on variations of the fluorescence quantum yield of the donor. If the rate of the donor excitation v_{ex}^D, detection efficiency η_A and fluorescence quantum yield of the acceptor Φ_f^A remain constant, the left side of

equation 17 is a constant, and then the right side of the **equation 2.39** should also remain constant. Using an initial value of $D = D_0 = 1$, an initial condition can be calculated as:

$$\left(v_{ex}^{D}\eta_A\Phi_f^A\right)_0 = X_0 = \gamma_0 I_{D_0} + I_{A_0} \tag{2.40}$$

As discussed above X_0 will remain constant over the course of the experiment, provided that $\Delta\left(v_{ex}^{D}\eta_A\Phi_f^A\right) = 0$. **Equation 2.39 and 2.40** can then be combined to yield:

$$\gamma_0 I_{D_0} + I_{A_0} = X_0 = \frac{\gamma_0}{D} I_D(t) + I_A(t) \tag{2.41}$$

Rearranging equation 2.41, the factor D by which the fluorescence quantum yield of the donor is varied, can be calculated as:

$$D = \frac{I_D(t)\gamma_0}{\gamma_0 I_{D_0} + I_{A_0} - I_A(t)} = \frac{I_D(t)\gamma_0}{X_0 - I_A(t)} \tag{2.42}$$

Similarly, an equation to track changes in the fluorescence quantum yield of the acceptor, assuming that Φ_f^D is constant, can be derived from **equation 2.36** where $\Phi_f^A = A\Phi_f^{A_0}$.

$$v_{ex}^{D}\eta_D\Phi_f^D = I_D(t) + \frac{\eta_D\Phi_f^D}{\eta_A A\Phi_f^{A_0}} I_A(t) \tag{2.43}$$

Using **equation 2.29**, **equation 2.43** can be reduced to:

$$v_{ex}^{D}\eta_D\Phi_f^D = I_D(t) + \frac{1}{A\gamma_0} I_A(t) \tag{2.44}$$

Using an initial value of $A = 1$, the initial condition can be calculated as:

$$(v_{ex}^{D}\eta_D\Phi_f^D)_0 = Y_0 = I_{D_0} + \frac{1}{\gamma_0} I_{A_0} \tag{2.45}$$

Rearranging **equations 2.44 and 2.45**, the factor A by which the fluorescence quantum yield of the acceptor is varied, can be calculated as:

$$A = \frac{I_A(t)}{\gamma_0(Y_0 - I_D(t))} \tag{2.46}$$

2.7.4 Determination of γ from SMF Experiments Considering Donor-acceptor Cross-talk and Direct Excitation of the Acceptor

The parameter γ is typically determined following photobleaching of the acceptor, where the experimentally observed anticorrelated changes in the donor and acceptor signals, ΔI_D^{exp} and ΔI_A^{exp}, respectively, are measured and used in the calculation, according to **equation 2.47** (see also **Fig. 2.7**). This equation assumes that the recorded changes are purely due to deactivation of FRET energy transfer following photodestruction of the acceptor chromophore, where quanta not delivered to and emitted in the acceptor channel are in turn available for emission from the donor channel.

$$\gamma = -\frac{\Delta I_A^{exp}}{\Delta I_D^{exp}} \tag{2.47}$$

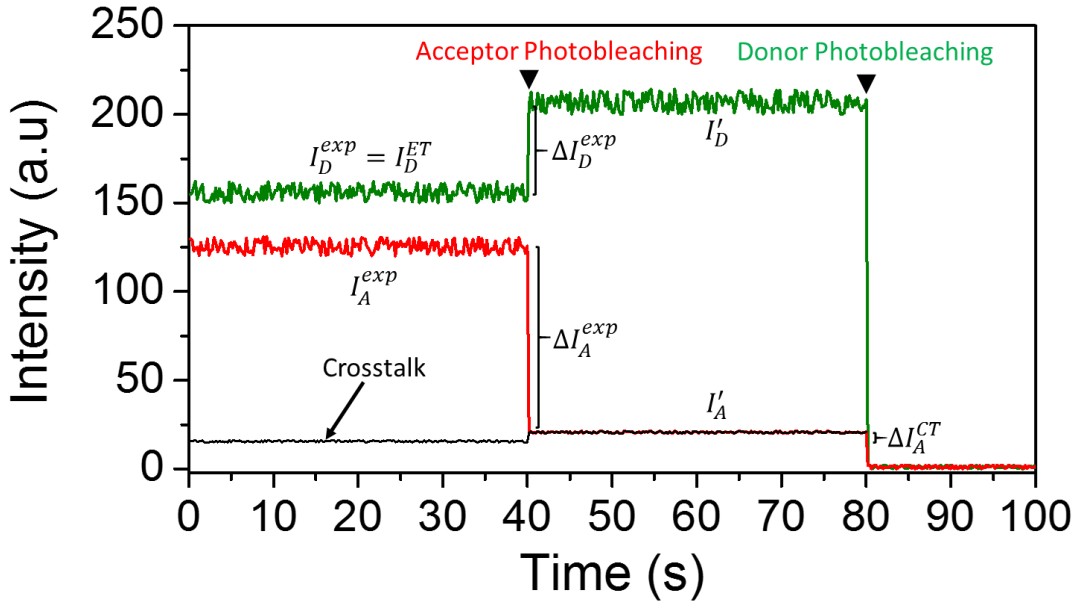

Figure 2.7. Measurement of γ from the Donor and Acceptor Intensity-time Trajectories. Representation of traces for a donor-acceptor pair where γ can be calculated upon the anti-correlated change in acceptor (red) and donor (green) intensity when the acceptor photobleaches. Acceptor and donor photobleaching are indicated with inverted triangles ▼. The black trace represents an imaginary trace for the leakage and its respective change after a donor change in intensity. ($\beta = 0.1, \gamma = 2.16$)

The experimental change in the donor channel, ΔI_D^{exp}, is purely the result of the deactivation of emissive losses from the donor that takes place via energy transfer from the donor to the acceptor channel ΔI_D^{ET}. This deactivation upon acceptor photobleaching results in an increase in intensity

(**equation 2.48**). In turn, the intensity drop in the acceptor channel, ΔI_A^{exp}, may contain elements from donor-acceptor cross-talk as well as from the direct excitation of the acceptor, not considered in **equation 2.47**. The experimentally observed change in the acceptor signal will then be given by **equation 2.49**, where ΔI_A^{ET} accounts for energy transfer from the donor dye to the acceptor dye via dipole-dipole interaction and where a parameter ΔI_A^{CT} is introduced accounting for donor cross-talk into the acceptor channel. A second parameter ΔI_A^{DE} is introduced to account for direct excitation of the acceptor by the laser line. The parameter γ is then given by **equation 2.50**.

$$\Delta I_D^{exp} = \Delta I_D^{ET} \tag{2.48}$$

$$\Delta I_A^{exp} = \Delta I_A^{ET} + \Delta I_A^{CT} + \Delta I_A^{DE} \tag{2.49}$$

$$\gamma = -\frac{\Delta I_A^{ET}}{\Delta I_D^{ET}} = -\frac{\Delta I_A^{ET}}{\Delta I_D^{exp}} \tag{2.50}$$

Utilizing **equations 2.48 and 2.49**, the experimental change in the acceptor channel over the donor channel can be written as shown below in **equation 2.51**. It may be appreciated that the first term on the right side of **equation 2.51** corresponds to $-\gamma$. In turn, the second and third term may be computed. Specifically, one may show that the change in cross talk signal in the acceptor channel ΔI_A^{CT} upon acceptor photobleaching is directly proportional to the simultaneous increase in donor signal ΔI_D^{exp} upon acceptor photobleaching, where the proportionality constant is β, see **equation 2.52** and also **equation 2.28** and text therein. Then, the second term on the right side of **equation 2.51** is equal to β.

The third term to the right may be calculated from a simple consideration based on the absorption cross section values for the donor σ_D and acceptor σ_A dyes at the donor excitation wavelength, **see equation 2.53**. Specifically, the emission arising upon direct excitation of the acceptor (constant throughout the experiment in as far as Φ_f^A remains constant) I_A^{DE} should be proportional to that arising upon direct excitation of the donor. The latter is given by I_D', see **Figure 2.7**. The proportionality constant is given by the correction factor γ due to fluorescence quantum yield and detection efficiencies of both dyes, and the correction factor for differences in cross section for both dyes, $\sigma_A/\sigma_D = \varepsilon_A/\varepsilon_D$, where ε_D and ε_A are the extinction coefficients at the excitation wavelength of the experiment. In turn, one may show that following acceptor photobleaching, the

change in intensity from direct excitation is equal to the intensity arising from direct excitation $\Delta I_A^{DE} = -I_A^{DE}$

$$\frac{\Delta I_A^{exp}}{\Delta I_D^{exp}} = \frac{\Delta I_A^{ET}}{\Delta I_D^{exp}} + \frac{\Delta I_A^{CT}}{\Delta I_D^{exp}} + \frac{\Delta I_A^{DE}}{\Delta I_D^{exp}} \tag{2.51}$$

$$\Delta I_A^{CT} = \beta \Delta I_D^{exp} \tag{2.52}$$

$$\Delta I_A^{DE} = -I_A^{DE} = -I_D' \, \gamma \frac{\sigma_A}{\sigma_D} = -I_D' \, \gamma \frac{\varepsilon_A}{\varepsilon_D} \tag{2.53}$$

Replacing **equations 2.50, 2.52 and 2.53** in **equation 2.51** gives:

$$\frac{\Delta I_A^{exp}}{\Delta I_D^{exp}} = -\gamma + \beta - \gamma \frac{I_D'}{\Delta I_D^{exp}} \frac{\varepsilon_A}{\varepsilon_D} \tag{2.54}$$

Rearranging for γ, we obtain the desired equation to determine γ following acceptor photobleaching.

$$\gamma = \frac{-\frac{\Delta I_A^{exp}}{\Delta I_D^{exp}} + \beta}{1 + \frac{I_D'}{\Delta I_D^{exp}} \frac{\varepsilon_A}{\varepsilon_D}} \tag{2.55}$$

2.7.5 Apparent FRET Efficiency Correction due to Crosstalk and Direct Excitation of the Acceptor

In order to obtain proximity ratio E_{pr} as defined in **section 2.6.2**, the background subtracted intensity of the acceptor I_A^{exp} must be corrected for both donor-acceptor crosstalk and direct excitation of the acceptor. Corrections require subtracting the contribution from both those phenomena (I_A^{CT} and I_A^{DE}) to the experimental intensity recorded in the acceptor channel I_A^{exp}. The acceptor intensity due to energy transfer I_A^{ET} will then be given by **equation 2.56**. The contribution from cross-talk can be expressed as βI_D^{exp} (see also **equation 2.52**). The contribution due to direct excitation of the acceptor can be calculated according to **equation 2.53**. Replacing those values in **equation 2.56** yields **equation 2.57**.

$$I_A^{ET} = I_A^{exp} - I_A^{CT} - I_A^{DE} \tag{2.56}$$

$$I_A^{ET} = I_A^{exp} - \beta I_D^{exp} - I_D' \, \gamma \frac{\varepsilon_A}{\varepsilon_D} \tag{2.57}$$

The parameter β may be calculated experimentally from single molecule trajectories after photobleaching of the acceptor and prior to photobleaching of the donor as described in the literature.[50, 52, 54-55] I_A^{DE} can be calculated from each trajectory using a combination of **equations 2.54 and 2.55**, as shown in **equation 2.58**

$$I_A^{DE} = I_D' \gamma \frac{\varepsilon_A}{\varepsilon_D} = I_D' \frac{\varepsilon_A}{\varepsilon_D} \left(\frac{-\frac{\Delta I_A^{exp}}{\Delta I_D^{exp}} + \beta}{1 + \frac{I_D' \varepsilon_A}{\Delta I_D^{exp} \varepsilon_D}} \right) \tag{2.58}$$

It is now possible to define E_{pr} as shown in **equation 2.59**, where I_D^{exp} and I_A^{exp} are the experimental donor and acceptor intensities, respectively.

$$E_{pr} = \frac{I_A^{ET}}{I_D^{ET} + I_A^{ET}} = \frac{I_A^{exp} - I_A^{CT} - I_A^{DE}}{I_D^{exp} + I_A^{exp} - I_A^{CT} - I_A^{DE}} \tag{2.59}$$

Alternatively, and for cases where donor photobleaches first, I_A^{DE} can be calculated according to **equations 2.60-2.63** using the known γ. Here **equation 2.60** may be directly inferred from **equation 2.41**.

$$I_D^{exp} + \frac{I_A^{ET}}{\gamma} = I_D' \tag{2.60}$$

Combining **equations 2.53 and 2.60** gives:

$$I_A^{DE} = \left(\gamma I_D^{exp} + I_A^{ET} \right) \frac{\varepsilon_A}{\varepsilon_D} \tag{2.61}$$

Combining **equations 2.57 and 2.61** gives:

$$I_A^{DE} = \left(\gamma I_D^{exp} + I_A^{exp} - \beta I_D^{exp} - I_A^{DE} \right) \frac{\varepsilon_A}{\varepsilon_D} \tag{2.62}$$

Reorganizing **equation 2.62** for I_A^{DE} and using $f = (1 + \varepsilon_D/\varepsilon_A)^{-1}$ results in a new expression for I_A^{DE}, **equation 2.63**.

$$I_A^{DE} = f\left((\gamma - \beta) I_D^{exp} + I_A^{exp} \right) \tag{2.63}$$

2.7.6 Distribution of E_{pr} Values Recorded from smFRET TIRF Experiments after Correction for Crosstalk and before Correction for Direct Excitation of the Acceptor

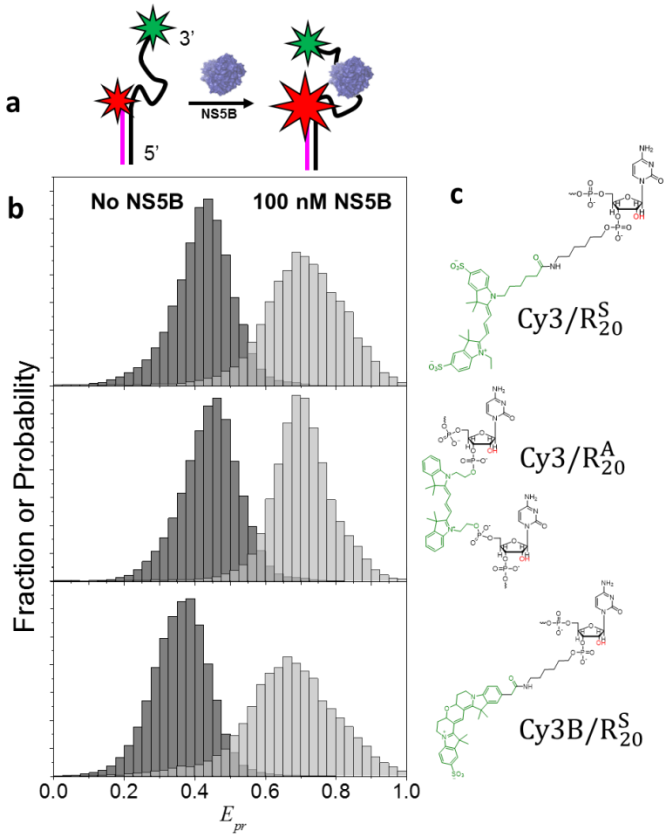

Figure 2.8. Distribution of E_{pr} Values Recorded from smFRET TIRF Experiments Before Direct Acceptor Excitation Corrections. a. Cartoon illustrating a DNA/RNA duplex before (left) and after (right) HCV-NS5B binding. **b.** Uncorrected ensemble histograms of single-molecule E_{pr} values for DNA/RNA duplexes before (left) and after (right) HCV-NS5B binding**. c.** Chemical structures of the linkers utilized to couple the donor (either Cy3 or Cy3B) in $Cy3B/R_{20}^{S}$, $Cy3/R_{20}^{A}$ and $Cy3/R_{20}^{S}$.

2.7.7 Correction Parameters Utilized to Correct Single-Molecule Data

Table 2.3. Correction Parameters

dye pair/R_n^X	Crosstalk (β)	Gamma (γ)	$\varepsilon_D/\varepsilon_A$ (532nm)
$\mathbf{Cy3-Cy5/R_{20}^S}$ [a]	0.09 ± 0.04 (74)	2.6 ± 0.6 (52)	86823/6723
$\mathbf{Cy3-Cy5/R_{20}^A}$ [b]	0.08 ± 0.02 (225)	1.3 ± 0.3 (127)	97893/6723
$\mathbf{Cy3B-Cy5/R_{20}^S}$ [c]	0.08 ± 0.02 (105)	0.37 ± 0.04 (57)	77586/6723
$\mathbf{Cy3-ATTO647N/R_{26}^A}$ [b]	-	2.6 ± 0.4 (94)	97893/4500

Superscript letters indicate the structure of the dye in **Figure 2.5.** Parenthesis indicate the number of trajectories utilized.

2.7.8 smPIFE TIRF Trajectories of Cy3/R^A_{20} in the Presence of 100 nM NS5B

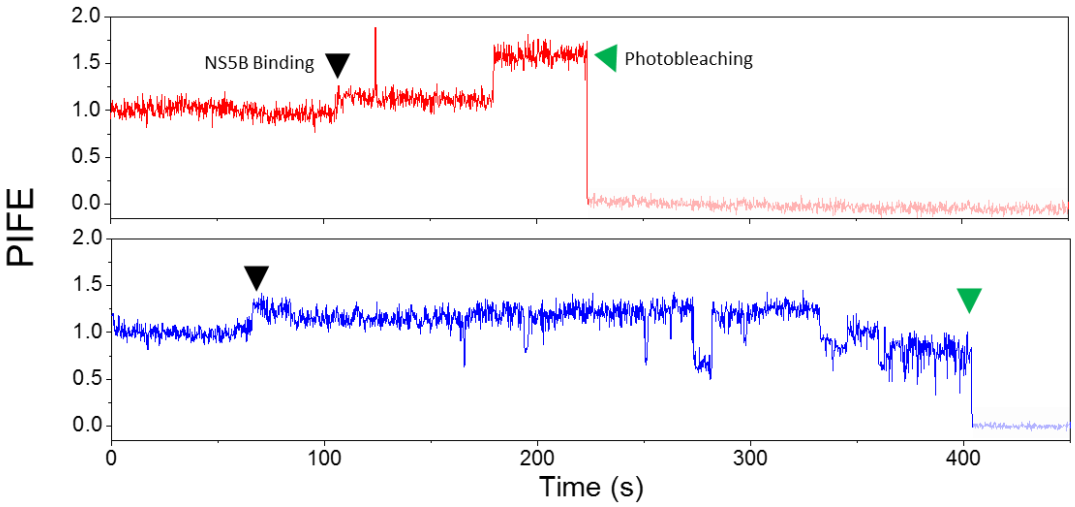

Figure 2.9. smPIFE Trajectories of Cy3/R^A_{20} when Flowing 100 nM NS5B. Normalized trajectories representing different Cy3 photophysical behaviours (associated to different binding modes) upon NS5B binding to $Cy3/R_{20}^A$. The red trace displays an enhancement-only trajectory. The blue trace shows a trajectory where enhancement and quenching of Cy3 are both recorded in the presence of NS5B.

2.8 References

1. Joo, C.; Balci, H.; Ishitsuka, Y.; Buranachai, C.; Ha, T., Advances in Single-Molecule Fluorescence Methods for Molecular Biology. *Annual Review of Biochemistry* **2008,** *77* (1), 51-76.
2. Moerner, W. E.; Orrit, M., Illuminating Single Molecules in Condensed Matter. *Science* **1999,** *283*, 1670-1676.
3. Weiss, S., Fluorescence Spectroscopy of Single Biomolecules. *Science* **1999,** *283*, 1676-1683.
4. Ha, T., Single-Molecule Fluorescence Resonance Energy Transfer. *Methods* **2001,** *25* (1), 78-86.
5. Roy, R.; Hohng, S.; Ha, T., A practical guide to single-molecule FRET. *Nat Meth* **2008,** *5* (6), 507-516.
6. Stryer, L.; Haugland, R. P., Energy Transfer: A Spectroscopic Ruler. *Proceedings of the National Academy of Sciences, USA* **1967,** *58*, 719-726.
7. Förster, T., *Delocalized Excitation and Excitation Transfer*. Academic Press Inc, New York: 1965; Vol. 3, p 93-137.
8. Hwang, H.; Kim, H.; Myong, S., Protein Induced Fluorescence Enhancement as a Single Molecule Assay with Short Distance Sensitivity. *Proceedings of the National Academy of Sciences, USA* **2011,** *108*, 7414-7418.
9. Hwang, H.; Myong, S., Protein Induced Fluorescence Enhancement (PIFE) for Probing Protein-nucleic Acid Interactions. *Chemical Society Reviews* **2014,** *43*, 1221-1229.
10. Luo, G.; Wang, M.; Konigsberg, W. H.; Xie, X. S., Single-Molecule and Ensemble Fluorescence Assays for a Functionally Important Conformational Change in T7 DNA Polymerase. *Proceedings of the National Academy of Sciences, USA* **2007,** *104*, 12610-12615.
11. Myong, S.; Cui, S.; Cornish, P. V.; Kirchhofer, A.; Gack, M. U.; Jung, J. U.; Hopfner, K.-P.; Ha, T., Cytosolic Viral Sensor RIG-I Is a 5'-Triphosphate–Dependent Translocase on Double-Stranded RNA. *Science* **2009,** *323*, 1070-1074.
12. Park, J.; Myong, S.; Niedziela-Majka, A.; Lee, K. S.; Yu, J.; Lohman, T. M.; Ha, T., PcrA Helicase Dismantles RecA Filaments by Reeling in DNA in Uniform Steps. *Cell* **2010,** *142*, 544-555.
13. Qiu, Y.; Myong, S., Chapter Two - Single-Molecule Imaging With One Color Fluorescence. In *Methods in Enzymology*, Maria, S.; Yann, R. C., Eds. Academic Press: 2016; Vol. Volume 581, pp 33-51.
14. Sanborn, M. E.; Connolly, B. K.; Gurunathan, K.; Levitus, M., Fluorescence Properties and Photophysics of the Sulfoindocyanine Cy3 Linked Covalently to DNA. *The Journal of Physical Chemistry B* **2007,** *111* (37), 11064-11074.
15. Stennett, E. M. S.; Ciuba, M. A.; Lin, S.; Levitus, M., Demystifying PIFE: The Photophysics Behind the Protein-Induced Fluorescence Enhancement Phenomenon in Cy3. *J. Phys. Chem. Lett.* **2015**, 1819-1823.
16. Aramendia, P. F.; Negri, R. M.; Roman, E. S., Temperature Dependence of Fluorescence and Photoisomerization in Symmetric Carbocyanines.Influence of Medium Viscosity and Molecular Structure. *Journal of Physical Chemistry* **1994,** *98* (12), 3165-3173.

17. Jia, K.; Wan, Y.; Xia, A.; Li, S.; Gong, F.; Yang, G., Characterization of Photoinduced Isomerization and Intersystem Crossing of the Cyanine Dye Cy3. *Journal of Physical Chemistry A* **2007,** *111*, 1593-1597.
18. Chibisov, A. K.; Zakharova, G. V.; Goerner, H.; Sogulyaev, Y. A.; Mushkalo, I. L.; Tolmachev, A. I., Photorelaxation Processes in Covalently Linked Indocarbocyanine and Thiacarbocyanine Dyes. *J. Phys. Chem* **1995,** *99*, 886-893.
19. Stennett, E. M. S.; Ma, N.; van der Vaart, A.; Levitus, M., Photophysical and Dynamical Properties of Doubly Linked Cy3–DNA Constructs. *Journal of Physical Chemistry B* **2014,** *118*, 152-163.
20. Spiriti, J.; Binder, J. K.; Levitus, M.; van der Vaart, A., Cy3-DNA Stacking Interactions Strongly Depend on the Identity of the Terminal Basepair. *Biophysical Journal* **2011,** *100*, 1049-1057.
21. Kozlov, A. G.; Lohman, T. M., Stopped-Flow Studies of the Kinetics of Single-Stranded DNA Binding and Wrapping around the Escherichia coli SSB Tetramer. *Biochemistry* **2002,** *41*, 6032-6044.
22. Kozlov, A. G.; Lohman, T. M., Kinetic Mechanism of Direct Transfer of Escherichia coli SSB Tetramers between Single-Stranded DNA Molecules. *Biochemistry* **2002,** *41*, 11611-11627.
23. Lucius, A. L.; Jason Wong, C.; Lohman, T. M., Fluorescence Stopped-flow Studies of Single Turnover Kinetics of E. coli RecBCD Helicase-catalyzed DNA Unwinding. *Journal of Molecular Biology* **2004,** *339*, 731-750.
24. Sreenivasan, R.; Heitkamp, S.; Chhabra, M.; Saecker, R.; Lingeman, E.; Poulos, M.; McCaslin, D.; Capp, M. W.; Artsimovitch, I.; Record, M. T., Fluorescence Resonance Energy Transfer Characterization of DNA Wrapping in Closed and Open Escherichia coli RNA Polymerase−λPR Promoter Complexes. *Biochemistry* **2016,** *55*, 2174-2186.
25. Nguyen, B.; Sokoloski, J.; Galletto, R.; Elson, E. L.; Wold, M. S.; Lohman, T. M., Diffusion of Human Replication Protein A Along Single-Stranded DNA. *Journal of Molecular Biology* **2014,** *426*, 3246-3261.
26. Sokoloski, J. E.; Kozlov, A. G.; Galletto, R.; Lohman, T. M., Chemo-Mechanical Pushing of Proteins Along Single-Stranded DNA. *Proceedings of the National Academy of Sciences, USA* **2016,** *113*, 6194-6199.
27. Craggs, T. D.; Hutton, R. D.; Brenlla, A.; White, M. F.; Penedo, J. C., Single-Molecule Characterization of Fen1 and Fen1/PCNA Complexes Acting on Flap Substrates. *Nucleic Acids Research* **2014,** *42*, 1857-1872.
28. Karam, P.; Powdrill, M. H.; Liu, H.-W.; Vasquez, C.; Mah, W.; Bernatchez, J.; Götte, M.; Cosa, G., Dynamics of Hepatitis C Virus (HCV) RNA-dependent RNA Polymerase NS5B in Complex with RNA. *Journal of Biological Chemistry* **2014,** *289*, 14399-14411.
29. Ablenas, C. J.; Liu, H.-W.; Shkriabai, N.; Kvaratskhelia, M.; Cosa, G.; Götte, M., Dynamic Interconversions of HCV Helicase Binding Modes on the Nucleic Acid Substrate. *ACS Infectious Diseases* **2017,** *3* (1), 99-109.
30. Morten, M. J.; Peregrina, J. R.; Figueira-Gonzalez, M.; Ackermann, K.; Bode, B. E.; White, M. F.; Penedo, J. C., Binding Dynamics of a Monomeric SSB Protein to DNA: a Single-Molecule Multi-Process Approach. *Nucleic Acids Research* **2015**.
31. Lerner, E.; Ploetz, E.; Hohlbein, J.; Cordes, T.; Weiss, S., A Quantitative Theoretical Framework For Protein-Induced Fluorescence Enhancement–Förster-Type Resonance Energy Transfer (PIFE-FRET). *Journal of Physical Chemistry B* **2016,** *120*, 6401-6410.

32. Ploetz, E.; Lerner, E.; Husada, F.; Roelfs, M.; Chung, S.; Hohlbein, J.; Weiss, S.; Cordes, T., Förster Resonance Energy Transfer and Protein-Induced Fluorescence Enhancement as Synergetic Multi-Scale Molecular Rulers. *Scientific Reports* **2016,** *6*, 33257.
33. Kapanidis, A. N.; Lee, N. K.; Laurence, T. A.; Doose, S.; Margeat, E.; Weiss, S., Fluorescence-Aided Molecule Sorting: Analysis of Structure and Interactions by Alternating-Laser Excitation of Single Molecules. *Proceedings of the National Academy of Sciences, USA* **2004,** *101*, 8936-8941.
34. Cooper, M.; Ebner, A.; Briggs, M.; Burrows, M.; Gardner, N.; Richardson, R.; West, R., Cy3B™: Improving the Performance of Cyanine Dyes. *Journal of Fluorescence* **2004,** *14*, 145-150.
35. Cosa, G.; Harbron, E. J.; Zeng, Y.; Liu, H.-W.; O'Connor, D. B.; Eta-Hosokawa, C.; Musier-Forsyth, K.; Barbara, P. F., Secondary Structure and Secondary Structure Dynamics of DNA Hairpins Complexed with HIV-1 NC Protein. *Biophysical Journal* **2004,** *87*, 2759-2767.
36. Cao, J.; Wu, T.; Hu, C.; Liu, T.; Sun, W.; Fan, J.; Peng, X., The Nature of the Different Environmental Sensitivity of Symmetrical and Unsymmetrical Cyanine Dyes: An Experimental and Theoretical Study. *Physical Chemistry Chemical Physics* **2012,** *14*, 13702-13708.
37. Krumova, K.; Oleynik, P.; Karam, P.; Cosa, G., Phenol-Based Lipophilic Fluorescent Antioxidant Indicators: A Rational Approach. *Journal of Organic Chemistry* **2009,** *74*, 3641-3651.
38. Texier, I.; Goutayer, M.; Da Silva, A.; Guyon, L.; Djaker, N.; Josserand, V.; Neumann, E.; Bibette, J.; Vinet, F., Cyanine-Loaded Lipid Nanoparticles for Improved In Vivo Fluorescence Imaging. *Journal of Biomedical Optics* **2009,** *14*, 054005.
39. Lakowicz, J. R., *Principles of Fluorescence Spectroscopy*. 3 ed.; Springer: 2006; Vol. 2, p 954.
40. Turro, N. J.; Ramamurthy, V.; Scaiano, J. C., *Principles of Molecular Photochemistry: An Introduction*. University science books: 2009.
41. Förster, T., Zwischenmolekulare Energiewanderung und Fluoreszenz (Intermolecular Energy Migration and Fluorescence). *Annalen der Physik* **1948,** *437*, 55-75. Translated by RS Knox, Department of Physics and Astronomy, University of Rochester, Rochester, NY 14627.
42. Braslavsky, S. E.; Fron, E.; Rodriguez, H. B.; Roman, E. S.; Scholes, G. D.; Schweitzer, G.; Valeur, B.; Wirz, J., Pitfalls and Limitations in the Practical Use of Forster's Theory of Resonance Energy Transfer. *Photochem. Photobiol. Sci.* **2008,** *7*, 1444-1448.
43. Gilbert, A.; Baggott, J. E., *Essentials of Molecular Photochemistry*. Blackwell Scientific Publications: Oxford; Boston, 1991.
44. Marko, R. A.; Liu, H.-W.; Ablenas, C. J.; Ehteshami, M.; Götte, M.; Cosa, G., Binding Kinetics and Affinities of Heterodimeric versus Homodimeric HIV-1 Reverse Transcriptase on DNA–DNA Substrates at the Single-Molecule Level. *Journal of Physical Chemistry B* **2013,** *117*, 4560-4567.
45. Behrens, S. E.; Tomei, L.; De Francesco, R., Identification and Properties of the RNA-Dependent RNA Polymerase of Hepatitis C Virus. *EMBO Journal* **1996,** *15*, 12-22.
46. Bressanelli, S.; Tomei, L.; Roussel, A.; Incitti, I.; Vitale, R. L.; Mathieu, M.; De Francesco, R.; Rey, F. A., Crystal Structure of the RNA-Dependent RNA Polymerase of Hepatitis C Virus. *Proceedings of the National Academy of Sciences, USA* **1999,** *96*, 13034-13039.

47. Ago, H.; Adachi, T.; Yoshida, A.; Yamamoto, M.; Habuka, N.; Yatsunami, K.; Miyano, M., Crystal Structure of the RNA-Dependent RNA Polymerase of Hepatitis C Virus. *Structure* **1999,** *7*, 1417-1426.
48. Dahan, M.; Deniz, A. A.; Ha, T.; Chemla, D. S.; Schultz, P. G.; Weiss, S., Ratiometric Measurement and Identification of Single Diffusing Molecules. *Chemical Physics* **1999,** *247*, 85-106.
49. Deniz, A. A.; Dahan, M.; Grunwell, J. R.; Ha, T.; Faulhaber, A. E.; Chemla, D. S.; Weiss, S.; Schultz, P. G., Single-Pair Fluorescence Resonance Energy Transfer on Freely Diffusing Molecules: Observation of Förster Distance Dependence and Subpopulations. *Proceedings of the National Academy of Sciences, USA* **1999,** *96*, 3670-3675.
50. McCann, J. J.; Choi, U. B.; Zheng, L.; Weninger, K.; Bowen, M. E., Optimizing Methods to Recover Absolute FRET Efficiency from Immobilized Single Molecules. *Biophysical Journal 99*, 961-970.
51. Eggeling, C.; Ringemann, C.; Medda, R.; Schwarzmann, G.; Sandhoff, K.; Polyakova, S.; Belov, V. N.; Hein, B.; von Middendorff, C.; Schonle, A.; Hell, S. W., Direct observation of the nanoscale dynamics of membrane lipids in a living cell. *Nature* **2009,** *457*, 1159-1162.
52. Ha, T.; Ting, A. Y.; Liang, J.; Chemla, D. S.; Schultz, P. G.; Weiss, S.; Deniz, A. A., Temporal fluctuations of fluorescence resonance energy transfer between two dyes conjugated to a single protein. *Chemical Physics* **1999,** *247*, 107-118.
53. Sabanayagam, C. R.; Eid, J. S.; Meller, A., Using fluorescence resonance energy transfer to measure distances along individual DNA molecules: Corrections due to nonideal transfer. *Journal of Chemical Physics* **2005,** *122*, 061103.
54. Ha, T.; Ting, A. Y.; Liang, J.; Caldwell, W. B.; Deniz, A. A.; Chemla, D. S.; Schultz, P. G.; Weiss, S., Single-molecule fluorescence spectroscopy of enzyme conformational dynamics and cleavage mechanism. *Proceedings of the National Academy of Sciences, USA* **1999,** *96*, 893-898.
55. Sabanayagam, C. R.; Eid, J. S.; Meller, A., High-throughput scanning confocal microscope for single molecule analysis. *Applied Physics Letters* **2004,** *84*, 1216-1218.
56. Ha, T.; Zhuang, X.; Kim, H. D.; Orr, J. W.; Williamson, J. R.; Chu, S., Ligand-induced conformational changes observed in single RNA molecules. *Proceedings of the National Academy of Sciences, USA* **1999,** *96*, 9077-9082.
57. Ying, L.; Wallace, M. I.; Balasubramanian, S.; Klenerman, D., Ratiometric Analysis of Single-Molecule Fluorescence Resonance Energy Transfer Using Logical Combinations of Threshold Criteria: A Study of 12-mer DNA. *Journal of physical chemistry B* **2000,** *104*, 5171-5178.
58. Nir, E.; Michalet, X.; Hamadani, K. M.; Laurence, T. A.; Neuhauser, D.; Kovchegov, Y.; Weiss, S., Shot-Noise Limited Single-Molecule FRET Histograms: Comparison between Theory and Experiments†. *Journal of physical chemistry B* **2006,** *110*, 22103-22124.
59. Roy, R.; Hohng, S.; Ha, T., A Practical Guide to Single-Molecule FRET. *Nat. Meth* **2008,** *5*, 507-516.
60. Shirude, P. S.; Balasubramanian, S., Single molecule conformational analysis of DNA G-quadruplexes. *Biochimie* **2008,** *90*, 1197-1206.
61. Hohlbein, J.; Craggs, T. D.; Cordes, T., Alternating-laser excitation: single-molecule FRET and beyond. *Chemical Society Reviews* **2014,** *43*, 1156-1171.

62. Lee, N. K.; Kapanidis, A. N.; Wang, Y.; Michalet, X.; Mukhopadhyay, J.; Ebright, R. H.; Weiss, S., Accurate FRET Measurements within Single Diffusing Biomolecules Using Alternating-Laser Excitation. *Biophysical Journal* **2005,** *88* (4), 2939-2953.

3 Unifying Mechanism for Thiol Induced Photoswitching and Photostability of Cyanine Dyes

Gidi, Y.; Payne, L.; Glembockyte, V.; Michie, M.; Schnermann, M. J.; Cosa, G., *Manuscript submitted*

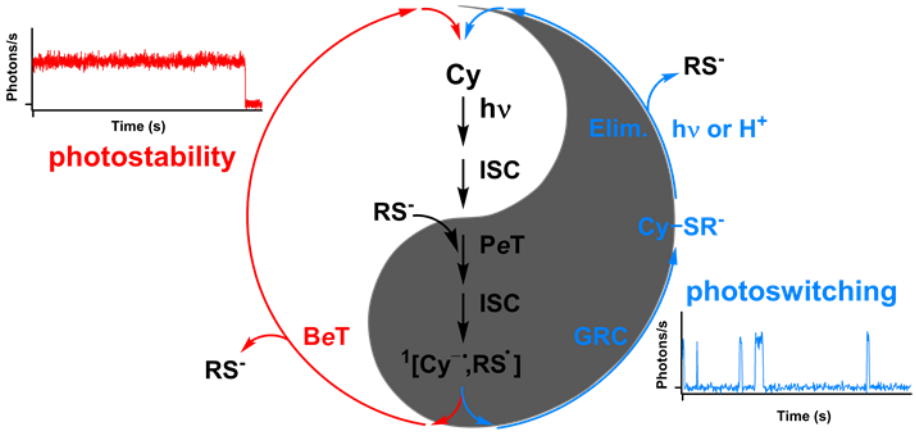

3.1 Preface

In **chapter 1,** we summarized the main photochemical and photophysical pathways involved in the photostabilization of fluorophores in SMF imaging. Among suitable fluorophores for SMF, cyanines (including Cy3, Cy3B, and Cy5) are the most widely utilized as they exhibit desired properties including photostability but also photoswitching in the presence of thiols. While the photostabilization pathway of cyanines in the presence of thiols has been previously studied, the mechanistic underpinnings of the photochemical reaction allowing photoswitching in Cy5 remains to be elucidated. In **chapter 3** we report the photoswitching mechanism of cyanine dyes as well as the mechanistic relationship between photoswitching and photostability in the presence of thiols for this key class of dyes most popular in single molecule studies.

3.2 Abstract

Cyanines (Cy3, Cy5, Cy3B) are the most utilized dyes for single molecule fluorescence and localization-based super-resolution imaging. These modalities exploit cyanines' versatile photochemical behavior with thiols. A mechanism reconciling seemingly divergent results and enabling control over cyanine photoreactivity is however missing. Utilizing single molecule fluorescence, transient-absorption spectroscopy and DFT modelling, herein we show that photoinduced electron transfer (P*e*T) from a thiolate to Cy in their triplet excited state, followed by triplet-to-singlet intersystem crossing in the nascent geminate radical pair, are crucial steps. Next, a bifurcation occurs, yielding either back electron transfer and regeneration of ground state Cy, required for photostabilization, or Cy-thiol adduct formation, necessary for super-resolution microscopy. Cy regeneration *via* photoinduced thiol-elimination is favored by adduct absorption spectra broadening. Elimination is also shown to occur through an acid-catalyzed reaction. Overall, our work provides a roadmap for designing fluorophores, photoswitching agents, and triplet excited state quenchers for single molecule and super-resolution imaging.

3.3 Introduction

Single molecule fluorescence (SMF) and related super-resolution single molecule localization microscopy (SMLM[1-3]) imaging methodologies are becoming transformative tools in biology, chemistry, and physics. Relying on monitoring single fluorophores over time, key to successful SMF experiments are high signal intensities and extended survival times. While conventional SMF techniques hinge on good signal stability, in turn, SMLM techniques require dyes to reversibly transition to dark transient states in photochemical reactions (photoswitching) to restrict the number of active fluorophores in the illumination field in a given imaging cycle to achieve super-resolution. Notably, given the opposing constraints for conventional SMF *vs* SMLM imaging, cyanine (Cy) dyes are *par excellence* the dyes utilized for all modalities, when combined with an oxygen scavenger and β-mercaptoethanol (β-ME). Here Cy3 and its rigid analog Cy3B showed extended survival times and good signal stability with β-ME (see **Fig. 3.1a** for structures). In stark contrast, the photoswitching of Cy5 – later shown to extend to structurally related dyes Cy5.5,[4] Cy7,[4] as well as Alexa Fluor 647[4-7] and 750,[7] - in the presence β-ME provided a timely system,

over a decade ago now,[3] to achieve the required on-off switching for the development of single molecule localization microscopy. Photoswitching in the presence of β-ME has not been observed however with Cy3, Cy3B and the structurally rigid analog of Cy5, Cy5B,[8] (see **Fig. 3.2a-b** for Cy5 vs Cy5B SMF trajectories acquired with β-ME).

The ability to control and optimize conventional SMF and SMLM imaging by judiciously steering the photoreaction pathway of cyanine dyes rests on the dichotomy between photostabilization *vs* photoswitching activities arising from β-ME. Missing is the molecular understanding reconciling seemingly divergent results on the photochemistry of cyanine dyes. (**Fig. 3.1b-d**). Such a mechanism should account for the enhanced brightness and extended survival time conveyed by β-ME, and the competing – photochemical[5, 9] and thermally[10] reversible - formation of a non-emissive photoproduct (formally a thiolate addition to the iminium ion rendering a Cy-SR adduct as shown by mass spectrometry studies,[10] **Fig. 3.1e**).

Herein we provide a unified mechanism on Cy-dye photochemistry that rationalizes several key SMF observations. Utilizing single molecule fluorescence microscopy, steady-state fluorescence, and transient absorption spectroscopy (laser flash photolysis, LFP), on Cy5 and Cy5B and employing density functional theory (DFT) modelling on various Cy dyes, we show that photoinduced electron transfer (P*e*T) from a thiolate to the Cy dye triplet excited state generates a geminate radical pair (GRP), a crucial intermediate to achieving Cy photoswitching and extended survival time (see **Fig. 3.1d**).

Thiyl radical assisted triplet-to-singlet intersystem crossing (ISC) in the newly formed GRP proves key to both photostabilizing (extended survival time) and photoswitching, ensuring geminate radicals can react before escaping from the solvent cage. Bifurcation between photostabilization and photoswitching results from competition between i) back electron transfer (B*e*T), central to enhanced signal stability and extended survival times, and ii) radical combination, yielding a non-emissive Cy-thiol adduct, accounting for photoswitching to a non-emissive state, key to super-resolution imaging. Importantly, the newly formed Cy-thiol adduct has a vanishingly small yet non-zero absorption cross section which, under the high excitation conditions operating in SMLM imaging, results in absorption of a photon, uncaging of the iminium ion upon thiolate β-elimination, and restoration of emission. Notably, thiol elimination is shown here to also proceed thermally *via* an acid catalyzed process (see **Fig. 3.1e**). Accordingly, the lifetime of the Cy-thiol

adduct (dark state) may be tuned by combination of the excitation rate (depending on laser intensity and wavelength applied) and pH, where longer lifetimes are achieved at higher pH and lower, red-shifted, photon fluxes. In turn, the duration of the on time is controlled by the excitation rate and determined primarily by the interplay of redox potentials of photoexcited Cy dye and thiolates, and by the probability of the GRP to undergo a back electron-transfer versus a geminate radical combination (GRC).

In general, our mechanistic studies set the stage to engineer better chromophores and imaging cocktails toward improved brightness, extended survival times, signal stability, and controlled photoswitching/on-off cycling for SMF and super-resolution SMLM imaging.

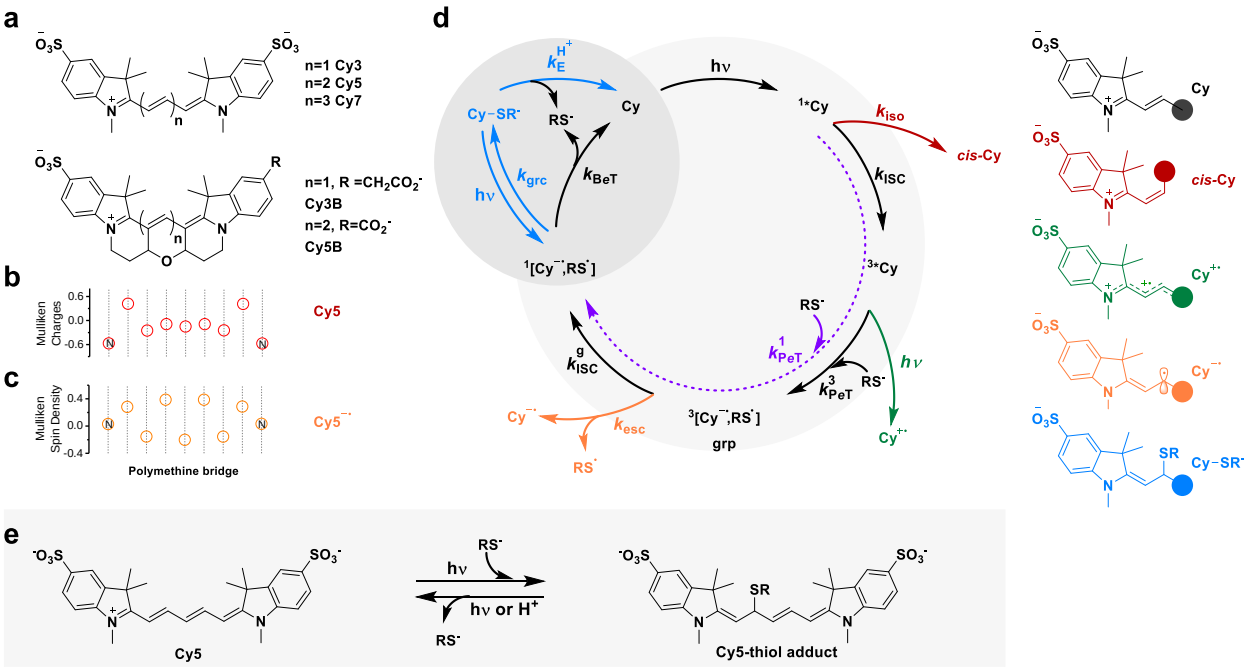

Figure 3.1. Structure and photoswitching mechanism of cyanine dyes. a. Structures. **b.** Mulliken charges and **c.** Mulliken spin density for ground state and one-electron reduced cyanines respectively (exemplified with Cy5). **d)** Proposed photoswitching mechanism of cyanines (Cy) in the presence of thiolates (RS^-), illustrating relevant photophysical and photochemical processes leading to extended survival time. Rate constants for intersystem crossing k_{ISC}, forward photoinduced electron transfer (P*e*T) in the excited triplet state k^3_{PeT}, intersystem crossing in the geminate radical pair k^g_{ISC}, and back electron transfer k_{BeT}, are listed along a circular pathway regenerating Cy dyes and resulting in extended photostability (light gray background). A detour following ISC in the geminate radical pair in blue reflects formation of a Cy5-SR^- adduct upon

geminate radical combination in competition with back electron transfer. Formation of the adduct is followed by either photoinduced $k_E^{h\nu}$ and/or thermal elimination ($k_E^{H^+}$) and regeneration of Cy. (dark gray circular background). The geminate radical pair in the singlet manifold is formed directly, in parallel, following P*e*T quenching of the excited singlet state by thiolate (k_{PeT}^1), see dashed line in violet. Competing photoprocesses include: in red, the formation of the nonfluorescent *cis*-Cy construct (k_{ISO}); in green, the oxidation *via* photoionization to generate $Cy^{+\bullet}$ (hυ, note that oxidation may also happen in the presence of an electron acceptor *via* P*e*T, not shown); in orange radical escape to yield $Cy^{-\bullet}$ and $RS^{\bullet}$ (k_{esc}) **e)** Cy5 structure before and after a photoinduced thiolate addition as proposed by Dempsey *et al.*[10]

3.4 Results and Discussion

3.4.1 Dark-state genesis from the triplet manifold

The choice of β-ME as a photostabilizing agent in SMF imaging is traced back to the first SMF experiments and was based on its reducing power,[11] and initially understood to rely on its ability to scavenge oxidative species involved in photobleaching.[12] Ultimately, the enhanced photostability of cyanine dyes with β-ME arises from a P*e*T-based quenching of the excited triplet state of the dye to generate a GRP.[13-14] We have previously shown that the GRP is formed in the triplet manifold. From this state, a rapid, thiyl radical-assisted triplet-to-singlet ISC is the key photostabilizing pathway of β-ME,[14] allowing for quantitative B*e*T to take place as shown by Holzmeister *et al.*[13] Here, the rapid spin relaxation dynamics in the thiyl radical, resulting from spin-orbit coupling, allow for otherwise spin-forbidden reactions in the GRP (*e.g.* B*e*T in photostabilization) to outcompete the otherwise prevalent radical escape from the solvent cage (**Fig. 3.1d**).[14]

The nature of the Cy5 photogenerated reversible dark-state with β-ME and the origin of this photochemical reaction garnered much attention. Product studies have shown that it formally arises from the β-addition of thiolate to the iminium ion in Cy5,[10] though its genesis remains elusive. We hypothesized that, upon P*e*T from β-ME to Cy5 in its excited triplet state, followed by triplet-to-singlet ISC in the newly formed GRP, geminate radical combination gives rise to the Cy-thiol dark adduct, in direct competition with B*e*T. Radical combination is consistent with the observed β-addition product reported, given the high electron spin density for photoreduced Cy5 at this position (see **Fig. 3.1c**).

To confirm that photoswitching is a triplet mediated process in Cy5, we monitored the intensity-time profile of the dye at the single molecule level. Solutions were prepared bearing increasing concentrations of potassium iodide to catalyze Cy5 excited singlet to triplet intersystem crossing[15] *via* the heavy atom effect.[16] Studies on surface-immobilized Cy5-ssDNA were performed by total internal reflection fluorescence (TIRF) microscopy (**Fig. 3.2a**).[17] Intensity-time trajectories were obtained under oxygen-depleted conditions, *via* enzymatic scavenging, in the presence of 143 mM β-ME. The duration of the on and off time intervals for every single molecule under a given set of conditions were recorded (**Fig. 3.2b**) and next combined in a histogram to establish average on and off times (τ_{on} and τ_{off}, respectively, **Fig. 3.2c**). Consistent with our hypothesis, we observed a linear correlation between the rate at which Cy5 reaches the off state ($v_{off} = 1/\tau_{on}$) and iodide concentration (see **Fig. 3.2d-e**), supporting the involvement of the triplet state in Cy5 photoswitching as initially proposed by Bates *et al*.[9] We also observed a linear correlation between the average number of photons per on interval and its average duration τ_{on} further supporting a triplet mediated dark state formation, **Fig. 3.2f**. By plotting $v_{off}^{I^-} = v_{off}^{o}$ (the ratio of the switching rates in the presence and absence of iodide) vs [I^-] one may also retrieve the value $k_{ISC}^{cat} = k_{ISC}^{o}$ where k_{ISC}^{cat} is the rate constant of catalyzed ISC of Cy5 by iodide, and k_{ISC}^{o} is the intrinsic intersystem crossing rate constant of Cy5, see **Eq. 3.1** below, **Fig 3.2e**, and **section 3.5.7**. The value of 227 ± 14 M^{-1} we calculated for $k_{ISC}^{cat} = k_{ISC}^{o}$ is within an order of magnitude of that previously reported based on fluorescence correlation studies, 125 ± 65 M^{-1} (corrected by the kinetic salt effect, **see section 3.5.7**),[16] further supporting a triplet-mediated dark state formation.

$$\frac{<\tau_{on}>^{0}}{<\tau_{on}>^{I^-}} = \frac{v_{off}^{I^-}}{v_{off}^{0}} = 1 + \frac{k_{ISC}^{cat}}{k_{ISC}^{o}}[I^-] \qquad (3.1)$$

Importantly, the singlet excited state of Cy5 can also give rise directly to the dark state adduct upon P*e*T from the thiolate to the singlet excited state, as shown in Fig. 1d (dashed line). Thus, while the fleeting lifetime of the excited singlet state (τ~1x10^{-9} s)[18] makes it an elusive intermediate to trap experimentally compared to the triplet excited state (τ~2x10^{-4} s), it is generated at a much higher frequency (quantum yield for triplet generation $\phi_{ISC} \sim 10^{-3}$). We have estimated that, under typical SMLM experimental conditions (no oxygen, β-ME 143 mM and pH=8), the rate of thiolates yielding an adduct from the singlet excited state is either smaller or on the same order of magnitude than that for the triplet (**see section 3.5.6**).

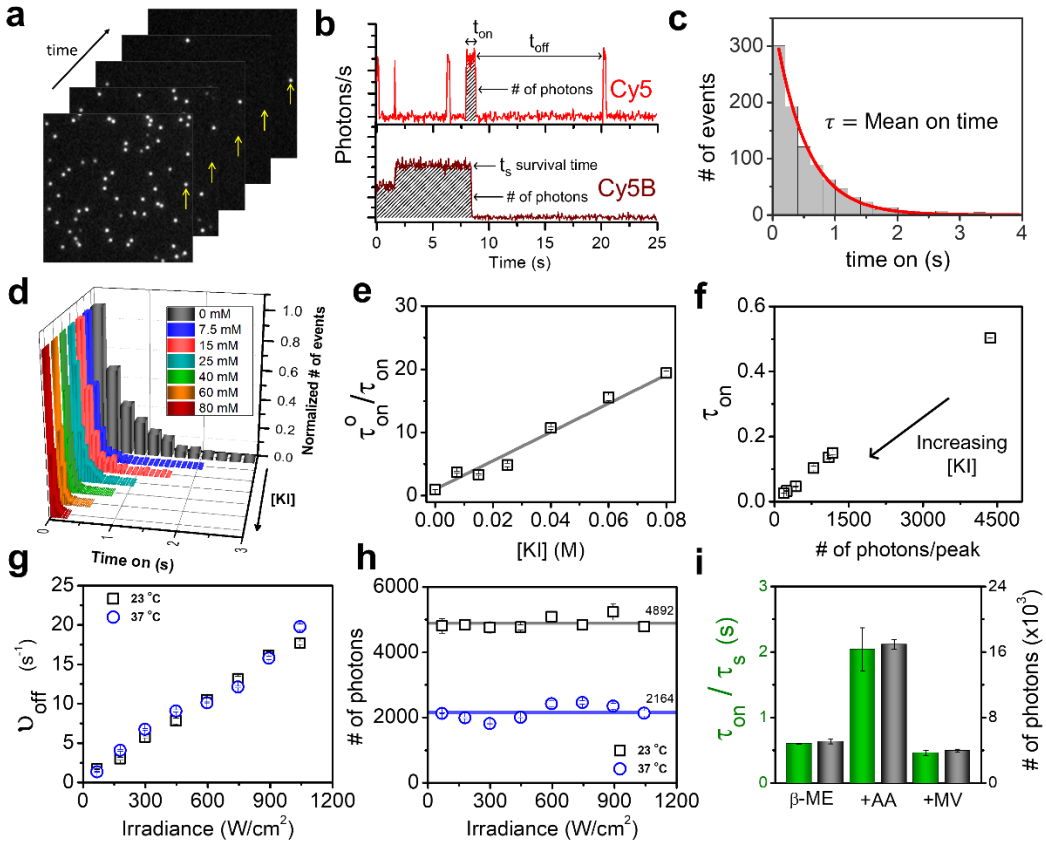

Figure 3.2. Assignment of triplet state of Cy5 in the genesis of the dark state *via* SMF studies. **a.** Widefield images *vs* time depicting fluorescent single molecules studied, arrows point to a single molecule switching from on to off and back to on states. **b.** Intensity-time single molecule trajectories of surface immobilized ssDNA bearing Cy5 (top) and Cy5B (bottom) under oxygen-depleted conditions with 143 mM β-ME. Time intervals until photobleaching (Cy5B) and where intensity is either on, or off (Cy5) are established. **c.** Histograms showing number of events *vs* time "on" are next constructed to extract the average time on of Cy5 by fitting an exponential decay function (similar histograms were constructed to extract the average number of photons and survival times). **d.** Histograms showing "on" time for Cy5 as a function of [KI]. **e.** Linear dependence between iodide concentration $[I^-]$ and $\upsilon_{off}/\upsilon^o_{off} = \tau^o_{on}/\tau_{on}$ (the ratio of the switching rates in the presence and absence of iodide) as anticipated by **Equation 3.1**. **f.** Linear correlation between the average time on τ_{on} and the average number of photons per on event. **g.** Linear correlation between υ_{off} vs excitation power at room temperature and 37° C. **h.** Average number of photons per "on" event as a function of excitation power showing a constant average number of photons is obtained. A decrease in the average number of detected photons is consistent with an increased probability of photoisomerization for Cy5 at higher temperatures.[19] **i.** Average on time (green) and average number of photons per "on" event (grey) for Cy5 with β-ME alone or supplemented with either ascorbic acid (AA) or methyl viologen (MV^{2+}). When supplemented with 1 mM MV^{2+}, Cy5 undergoes a single irreversible transition to a dark state.

In support of our hypothesis on the triplet mediated genesis of Cy5 dark-state, we were able to rule out various transient intermediates as possible non-emissive states, given their short lifetimes. We also ruled out alternative pathways that may account for formation of the dark-state photoproduct Cy5-SR adduct. Accordingly, transient absorption spectroscopy[20] studies on Cy5 yielded relatively short – microsecond to millisecond timescale – lifetimes for its *cis* photoisomer (*cis*-Cy5), one electron oxidized form (radical cation $Cy5^{+\bullet}$) and one electron reduced form (radical anion $Cy5^{-\bullet}$) (**Fig. 3.3** and **Table 3.1**, see also SI (**section 3.5.1-c**) for details). Given their short – sub-millisecond – lifetimes, and their spectral properties, the above transient species may not account for the long-lived (seconds) dark state of Cy5. Along the same lines, we note that transient absorption studies with Cy5B, the locked analog of Cy5 which is unable to undergo photoswitching,[8] showed transient species with lifetimes on the same order of magnitude as those of Cy5. The fact that the transient species of Cy5B show similar lifetimes as those to Cy5 and that Cy5B is unable to undergo photoswitching (see **Fig. 3.2b** for a representative trajectory with β-ME) further supports the hypothesis that none of these transient species account for the dark-state.

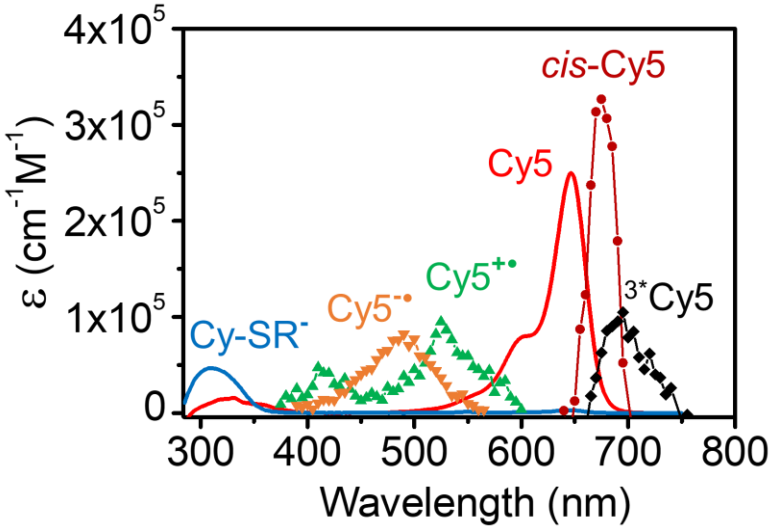

Figure 3.3. Absorption spectra for various transient species of Cy5. Absorption spectra of Cy5 and related transient species such as *cis* photoisomer, triplet excited state, photooxidized $Cy^{+\bullet}$, photoreduced $Cy^{-\bullet}$, and the dark state of Cy5 (β-ME-Cy5 adduct, $Cy5\text{-}SR^-$). The $Cy5\text{-}SR^-$ adduct was isolated upon irradiating Cy5 with a 100 mW defocused laser (638 nm) in a 450 mM Na_2CO_3 (pH=11) solution containing 430 mM of β-ME.

Table 3.1. Lifetimes and spectral properties for the transient species of Cy5 and Cy5B.

	$\tau\ (\mu s)$		$\lambda_{max}(nm)$	$\varepsilon\ (cm^{-1}M^{-1})$
Species	Cy5	Cy5B	Cy5	Cy5
cis-Cy	196 ± 5	n/a	675	326000
^{3*}Cy	209 ± 19	172 ± 24	695	105000
$Cy5^{+\bullet}$	440 ± 10	206 ± 6	525	95000
$Cy^{-\bullet}$	853 ± 7	1042 ± 15	490	82000
Cy-SR^-	$>10^6$	n/a	311	47000

We additionally ruled out a nucleophilic attack to the Cy5 radical cation ($Cy5^{+\bullet}$) by β-ME in its anionic form as a possible way to generate the Cy-thiol adduct. The Cy5 radical cation could form upon the absorption of two photons (**Fig. 3.1d**, green arrow, see **Fig. 3.10**): in this case, the rate v_{off} would scale with the square of the excitation intensity. In contrast, we have found that v_{off} scales linearly with the excitation intensity and is temperature independent, consistent with a one-photon process (**Fig. 3.2g**). The Cy5 radical cation can also be photochemically generated in the presence of the electron acceptor methyl viologen (MV^{2+}) (**Fig. 3.1d**, green arrow). Upon addition of MV^{2+} in the presence of β-ME, the Cy5 dye underwent irreversible photobleaching yielding ~4000 photons on average before degradation, less than the average ~5000 photons collected on the on-periods in photoswitching experiments (no MV^{2+}, **Fig. 3.2i**). Moreover, the average number of photons per on event was independent of the excitation rate (**Fig. 3.2h),** further supporting our proposed mechanism, as the number of times the triplet excited state is reached depends on the number of excitations rather then the excitation frequency. The decrease in the average number of photons at higher temperature (**Fig. 3.2h**) can be explained by the increased rate of isomerization of cyanines.[19]

Consistent with our hypothesis of a triplet state genesis for the Cy5-thiol adduct, SMF studies on addition of a competing triplet quencher (1 mM ascorbic acid) showed a decreasing rate for Cy5 switching off, as previously shown by Dempsey *et al*.[10] Importantly, addition of ascorbic acid thus increased the average number of photons per switching event by nearly 3-fold (~16000 vs ~5000, **Fig. 3.2i**), providing a strategy toward increasing image resolution.

3.4.2 Photoinduced and acid catalyzed restoration of the fluorescent state

Photoswitching of Cy5 requires fine tuning of the rate at which Cy5 recovers (v_{on}) from the newly formed Cy5-thiol adduct. Notably, uncaging of the thiolate moiety and restoration of the chromophore was previously reported to take place through indirect illumination of a closely lying, orange-emitting fluorophore (Cy3).[9] Direct illumination at relatively short wavelengths, namely 337 nm and 405 nm or even 532 nm was also shown to elicit thiolate uncaging.[5] Both findings present a major conundrum as to how the Cy5-thiol adduct, reported to have an absorption peak at 310 nm,[5, 10] may undergo photoinduced reactions at wavelengths where no absorption is detected.

We speculated that the observed photoinduced uncaging may result from spectral broadening of the electronic transition of the 310 nm peaked Cy5-thiol adduct absorption.[21] Inhomogeneous broadening of electronic transitions is associated with the thermal motion of solvent molecules in solution and generates a Gaussian distribution of energies for the 0-0 transition. Broadening of the electronic spectra resulting in a non-zero probability of excitation, combined with the high illumination intensities typically utilized in single molecule experiments, we reasoned, allows the transition of Cy5-SR to an excited electronic state from which uncaging of Cy5-SR is energetically favorable.

To test our hypothesis, we calculated the rate at which Cy5 recovers ($v_{on} = 1/\tau_{off}$) at different laser excitation wavelength and power conditions by building the distribution of off times t_{off} - the times to Cy5 recovery - from single molecule intensity-time trajectories of surface immobilized ssDNA bearing Cy5 under conditions favorable to thiol adduct formation (oxygen-depleted and presence of β-ME). The data were acquired in a two-color scheme, exciting with the "uncaging" wavelength while simultaneously exciting at 647 nm at a constant power to record the Cy5 emission intensity over time (**Fig. 3.4a**). The data revealed a linear dependence of the rate of Cy5 recovery v_{on} with laser power upon either 405, 488 or 561 nm irradiation, consistent with a one-photon process (*vs* a quadratic dependence that would be expected for a biphotonic process), in agreement with an electronic transition allowed by spectral broadening. Markedly shallower slopes (decreasing sensitivity to excitation power) were recorded with increasing wavelengths. Notably, even excitation at 647 nm resulted in uncaging of the Cy5-thiol adduct albeit the dependence of v_{on} with power was much shallower than for 561 nm, see **Fig. 3.4a**.

Consistent with our spectral broadening hypothesis, we obtained an action spectrum for the thiolate photoinduced uncaging, showing a tailing dependence with the wavenumber that can be approximated with a Gaussian function, see **Fig. 3.4b**. The action spectrum consisted of the product $\varepsilon_{(\lambda)}\Phi_u$, and was obtained from the derivative of the on rate v_{on} versus the illumination power P (dv_{on}/dP), where λ is the excitation wavelength (in nm), $\varepsilon_{(\lambda)}$ is the extinction coefficient (in M^{-1} cm^{-1}) units as a function of wavenumber, and Φ_u is the quantum yield of uncaging, independent of λ (**see section 3.5.8**). Related, the indirect uncaging of the Cy5-thiol adduct *via* a closely lying blue-shifted, *i.e.* Cy3, fluorophore would also tap on the broadened absorption spectrum *via* a combination of Förster and Dexter energy transfer mechanisms between the blue-shifted fluorophore and Cy5-SR, where the blue-shifted emitter can act as an antenna to assist the recovery of the fluorescent form of Cy5, allowing to decrease the illumination intensity by over a 1,000 fold when Cy3 is positioned at distances closer than 1 nm.[9] Whether direct or indirect, we postulate that photoinduced uncaging of the thiol involves homolytic cleavage to regenerate a geminate radical pair whose likelihood to undergo back electron transfer highly outcompetes the probability of reassociation ($k_{BeT}/k_{GRC} \sim 10^3$, see **section 3.5.10** for details on estimation).

Single molecule uncaging studies on Cy5-thiol adducts as a function of power and wavelength exposed a most insightful piece of the puzzle behind Cy5 photoswitching, namely that thiolate dissociation and restoration of Cy5 takes place in a parallel thermal (dark) reaction. This was manifested by a non-zero intercept in the linear dependence of the rate of recovery of Cy5 (v_{on}) as a function of excitation power (at 647 nm excitation), where the intercept (rate at zero excitation power) reports the thermal rate of recovery. Comparing the intercept of v_{on} as function of the 647 nm irradiance at both 23 and 37 °C and at pH 8.0, we found a minimal change in the intercept (0.010 ± 0.001 s^{-1} *vs* 0.011 ± 0.001 s^{-1}), indicative of a very low activation energy process for the thiol uncaging, see **Fig. 3.4c**.

The rate of thermal uncaging, recorded as described above *via* single molecule studies on the distribution of τ_{off} values was observed to increase with decreasing ionic strength at pH 8.0 as revealed by an increase on the intercept with no change in the slope for the correlation of v_{on} with power (0.020 ± 0.002 s^{-1}), see **Fig. 3.4c**. Given that the net charge of Cy5-SR is negative (two sulfonate groups (-2)), the observed kinetic salt effect points to a rate limiting step in thiolate uncaging involving a bimolecular reaction with a positive charge, which we assign to a protonation

of the adduct to activate the leaving group. Consistent with an acid catalyzed restoration of the emissive state (**Fig. 3.4d**), we found a linear relationship of $log(v_{on})$ versus pH. Here, a slope of one additionally reports on the molecularity of the chemical reaction. Notably, the acid catalyzed uncaging observation we report herein reconciles the ability to isolate the thiol adduct at high pH for characterization (e.g. pH 11 in our studies, 10.5 in product studies previously reported[10]), with the inability to do so when experiments are conducted at low pH. A high pH is thus not only required to increase the thiolate concentration, the rate of P*e*T and of the ensuing adduct formation, but it additionally results in a slower rate of thiol uncaging. Based on the linear correlation of pH vs $log(v_{on})$ one may estimate that while the uncaging rate is ~0.1 Ms^{-1} at pH 8 where most studies are reported, it is roughly 2.5 orders of magnitude slower at 2.5 pH units higher where product studies were reported.[10] The data underscore the tremendous sensitivity to pH, and highlights opportunities to switching, for the Cy5-thiol adduct.

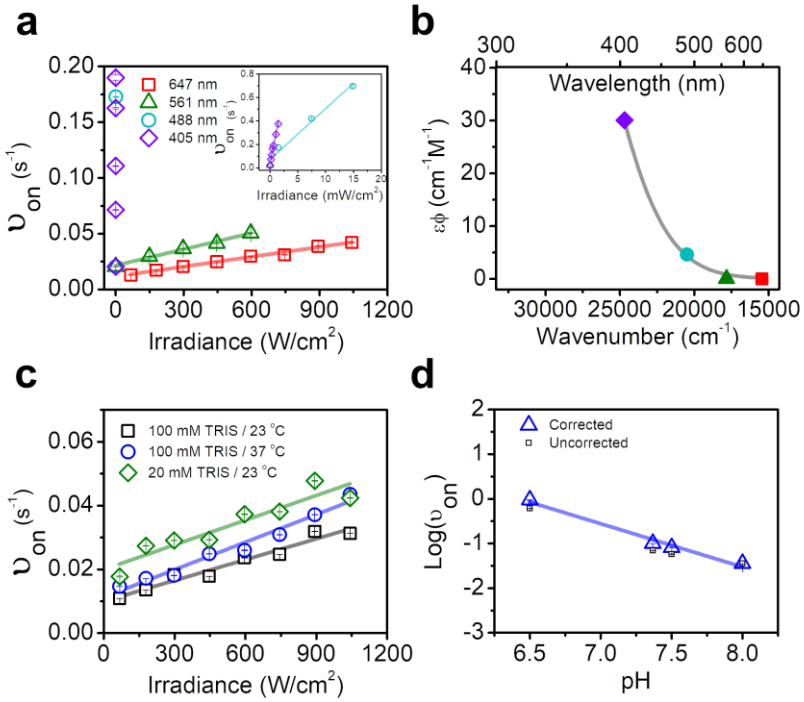

Figure 3.4. Single molecule mechanistic studies on photoinduced and acid catalyzed restoration of Cy5 fluorescence. a. Linear correlations of $\boldsymbol{v_{on}}$ as a function of the irradiance at 647 nm (red squares). Additionally, a two-color scheme was used to monitor $\boldsymbol{v_{on}}$ when exciting with different "uncaging" laser wavelengths (405, 488, and 561 nm) while simultaneously exciting at 647 nm at a constant power (298 W/cm^2). b. Action spectrum based on the sensitivity of $\boldsymbol{v_{on}}$ to excitation power. c. Kinetic salt and temperature effects on the rate of elimination monitored as a

function of the irradiance of a 647 nm wavelength laser. d. Correlation of $\boldsymbol{log(v_{on})}$ vs pH monitored at 647 nm (298 W/cm^2) supports an acid catalyzed/proton assisted thiol elimination.

Importantly, when performing single-molecule analyses on v_{on}, we have found that the distributions of "times off" are better adjusted through a biexponential function, uncovering an additional dark state in minor proportion (see **section 3.5.11**). We propose that a GRC can alternatively proceed through the C_1 of Cy5. The electron spin density for photoreduced Cy5 at this position is in fact not significantly lower than that at C_3 (see **Fig. 3.1c**). Ground state nucleophilic attacks on cyanines have been reported to proceed *via* the most electrophilic C_1[22-23] (see **figure 3.1c** for Milliken charges in the ground state). Adducts at this position show a red-shifted (~370 nm) absorption spectrum (see **figure 3.14 in section 3.5.12)**. Consistent with the hypothesis of an adduct with a red-shifted absorbing spectrum, we have found that the v_{on} of the minor component is ~10x more sensitive to a 647 nm light when compared to the dark state in major proportion. Regardless, note that for all the analysis reported in this work, we have used the major component (≥ 95%) of the distribution.

3.4.3 Energy landscape from DFT calculations

The mechanistic insight gained through our SMF and LFP experimental work with Cy5 and Cy5B illustrates key elementary reactions at play in Cy brightness, enhanced photon budget, signal stability, and photoswitching. Brightness is largely dictated by the ability or lack thereof to undergo relaxation in the excited state and *trans-cis* photoinduced isomerization (a mechanism available for Cy3 and Cy5 but not for Cy3B and Cy5B). On the other hand, for enhanced photon budget, signal stability, and photoswitching, ISC followed by P*e*T with thiolate is of paramount importance. Here, escape from the newly formed GRP is considered negligible based on rapid ISC in the GRP, and two photon ionization or photoinduced oxidation from the triplet excited state are also considered very minor pathways – albeit accounting ultimately for the fluorophore photobleaching with exceedingly low probabilities. Accordingly, the fates for all cyanines, will be dictated by whether they may undergo P*e*T with thiolates, and if so whether:

i. rapid regeneration of the ground state upon back electron transfer (B*e*T) takes place to continue the excitation/emission cycle yielding stable signals and enhanced photon budget (**Fig. 3.1d**, light gray background);

ii. GRC outcompetes, bringing the Cy dye to a non-emissive thiol adduct wherefrom it may be regenerated either photochemically or thermally (**Fig. 3.1d**, dark gray background)

DFT modelling on the different stages of relevance, namely P*e*T, B*e*T, and elimination (E), show that in all cases the reactions are energetically favorable (**Fig. 3.5** and **Table 3.2,** see also sections **3.5.1-d and 3.5.9**). The different behaviours observed for the cyanines are thus dictated by the kinetics of the competing pathways, through their activation energies.

We computed the activation energies for P*e*T and B*e*T from DFT-determined energy values, within the theoretical framework of Marcus theory of electron transfer, (see **Table 3.2** and sections **3.5.1-d and 3.5.9**). Our calculations show that the activation energies for P*e*T follow the trend Cy3<Cy5<Cy3B<Cy5B, consistent with the electron transfer rate constants obtained *via* transient absorption studies (see **Fig. 3.5** and **Table 3.2**).

Experimental values and theoretical estimates for k_{PeT} are consistent with the high photostability of Cy3 in the presence of β-ME and the lower photostability found for Cy3B, Cy5, and Cy5B.[8, 24] In turn, the low k_{PeT} value found for ^{3}*Cy5B/β-ME explains both the non-blinking property of Cy5B reported herein and elsewhere, and its low photostability as both processes require the initial formation of a GRP. As to why Cy3B and Cy3 do not show thiol adducts given that they readily undergo P*e*T, we posit that the answer lies in a combination of competition between B*e*T and GRC. However, we notice short lived dark states when exciting Cy3 with β-ME that are absent in e.g. studies conducted with Trolox and may well point to an elusive Cy3-thiol adduct. Geminate-radical combinations typically proceed with a minimum energetic barrier, which is expected to be larger for a rigidified structure (Cy3B and Cy5B) as compared to a more flexible structure (Cy3 and the less sterically hindered Cy5, respectively) as steric clashing may result upon addition and sp^2 to sp^3 hybridization change. In general, the formation of the adduct will be mostly modulated by the activation energy of the B*e*T process acting as a manifold. A higher activation energy for B*e*T will favor the GRC process, with the thiol acting as a photoswitching agent. In turn, a lower B*e*T activation energy will favor the restoration of the cyanine to its singlet ground state, enhancing

overall fluorophore survival time and photon budget. The combination of these two effects enables not only the photoswitching, but also the enhanced total photon budget required for super-resolution imaging.

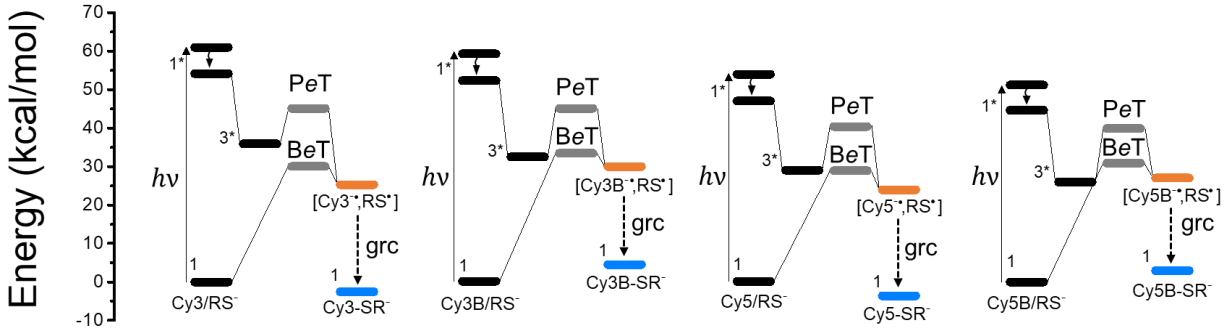

Figure 3.5. Energy landscape for Cy dye photoreactions. Energy of Cy/β-ME pairs and the computed transition states (grey) for the photoinduced electron transfer (P*e*T) and back electron transfer (B*e*T).

Table 3.2 Rate constants for photoinduced electron transfer to Cy dyes by β-ME, and estimated transition state energies for forward and back electron transfer.

Dye/β-ME	$\boldsymbol{k_{PeT}}$ ($s^{-1}M^{-1}$)	$\Delta \boldsymbol{E}^{\neq}_{\boldsymbol{PeT}}$ (kcal/mol)	$\Delta \boldsymbol{E}^{\neq}_{\boldsymbol{BeT}}$ (kcal/mol)
Cy3	$3.39 \pm 0.24 \times 10^{8}$	9.17	4.73
Cy3B	$1.55 \pm 0.16 \times 10^{7}$	12.60	3.50
Cy5	$9.89 \pm 0.80 \times 10^{7}$	11.39	5.01
Cy5B	$1.23 \pm 0.14 \times 10^{6}$	13.90	3.93

3.5 Conclusions

Herein, we provide a unified mechanistic framework highlighting the principles that dictate the photoswitching susceptibility of cyanines in the presence of thiols and their close relationship to the mechanism governing the photostabilizing properties of thiols.

The detailed understanding of the thiolate-induced photoswitching of cyanine dyes provides a roadmap for the design of fluorophores, photoswitching agents, and triplet quenchers with desired characteristics, and a set of guidelines toward a better photochemical control over currently used dye/thiol pairs, including photoswitching rates and enhanced photon budgets. Accordingly, thiolates are required in all instances given the thiyl radical's ability to rapidly undergo spin flipping *via* spin orbit coupling. Thiolates characterized by lower oxidation potential than serendipitously discovered β-ME are required to accelerate P*e*T and ensure a rapid exit along the "virtuous" photostabilizing cycle in **Fig 3.1d** if the triplet state is reached. This is particularly critical for Cy5B, which holds the promise to be a highly bright, stable-signal red-emissive fluorophore for SMF which currently lacks its efficient photostabilizing compound. In addition to lower oxidation potentials, thiolates are desired to have a low nucleophilic character if extended survival times and stable signals are needed for conventional SMF such as SMF FRET,[25-26] protein/nucleic acid induced fluorescence enhancement (PIFE,[27-28] and NAIFE,[29-30] respectively), or in PIFE-FRET combination.[31-33] In turn, a thiyl radical able to undergo GRC, would be sought after if photoswitching toward super-resolution SMLM is desired. In the latter context, we note that given the pH dependence in elimination of thiolate from the Cy-SR^- adduct, imaging under varying pH conditions such as those encountered in cellular systems may render critically different levels of turnovers and on/off duration periods based on the organelle where photoswitching is taking place. Importantly, photoswitching may be sensitive to different protein environments surrounding a Cy dye, as proximal basic residues may catalyze elimination. Also, electron donors such as tyrosine or cysteine residues may affect the triplet lifetimes and their availability toward adduct formation. Furthermore, in these types of environments, molecular crowding may prevent thiol encounter.

The diversity of possibilities for thiolate entrapment and uncaging offers both opportunities and challenges toward optimizing the off-time duration toward SMLM, and the SMF performance of

Cy fluorophores in the presence of thiols. More generally, it highlights the tremendous potential toward steering the photochemistry of cyanine dyes, and their iminium ion moiety, *via* P*e*T toward activation of nucleophilic attack in catalysis,[34-35] and toward photoinduced and thermal uncaging in biology. We thus note that catalyzed ISC in Cy dyes *via* heavy atom effect either intermolecularly or intramolecularly may open an avenue toward their facile integration in new applications that require efficient photochemical yields.

3.6 Supplementary information

3.6.1 Materials and Methods

3.6.1.1 Materials

1 M Tris-HCl buffer (pH=8), Sodium Hydroxide, Premium Cover Glass slides (25x25-1) and Acetone (HPLC grade) were purchased from Fischer Scientific. 5 M NaCl stock solution was purchased from Life Technologies (Ambion brand). Dimethyl sulfoxide (anhydrous, ≥99.9), Potassium iodide, D-(+)-Glucose, L-ascorbic acid, and β-mercaptoethanol were purchased from Sigma-Aldrich. Methyl viologen hydrate and glycerol (for molecular biology) were purchased from Acros Organics. Water (molecular biology grade) was acquired from Thermo Scientific HyClone (South Logan, UT). Sulphuric acid, sodium bicarbonate, and hydrogen peroxide were purchased from ACP Chemicals. Silicon mold, press fit tubing connectors and polycarbonate imaging chambers (Hybriwell) were purchased from Grace Bio-Labs, Inc. **Polymers.** Poly(ethylene glycol) polymers in the form of Silane (mPEG-Silane, MW 5000) as well as its biotinylated versions (Biotin-PEG-Silane, MW 5000) were purchased from Laysan Bio Inc. **Dyes.** Sulfo-Cyanine5 carboxylic acid was purchased from Abcam. Sulfo-Cy3 NHS ester was purchased from Lumiprobe. Cy3B mono NHS ester was purchased from GE Healthcare. Cy5B carboxylic acid and the Cy5B NHS ester (used to conjugate to DNA) were synthesised as previously described.[8] (**see Fig. 3.8**) **Nucleic acids.** Cy3 and Cy3B biotinylated DNA 18-mer (/5Dye_N/ACC-TCG-CGA-CCG-TCG-CCA/3Bio/) were purchased from Integrated DNA Technologies IDT. Cy5B biotinylated DNA 18mer was custom prepared by IDT from Cy5B NHS ester provided by us. Cy5-tagged biotinylated DNA 18-mer ((Cyanine 5) (C6-NH) ACC-TCG-CGA-CCG-TCG-CCA (BiotinBB)) was purchased from Trilink Biotechnologies (**see Fig. 3.7**). All stock solutions of potassium iodide, ascorbic acid, methyl viologen, and β-mercaptoethanol

were prepared freshly and the latter three were filtered through a 220 nm syringe filter before use in single-molecule fluorescence imaging and laser flash photolysis experiments. **Proteins.** Unlabeled streptavidin (S888) was purchased from (Thermo Fisher Scientific, Invitrogen). Glucose oxidase (from *Aspergillus niger*, type VII, G2133) and catalase C30 (from bovine liver, C30) were purchased from Sigma-Aldrich.

3.6.1.2 Single-molecule fluorescence imaging

3.6.1.2.1 Single Molecule Sample Preparation and surface immobilization.

Glass coverslips were initially cleaned and then passivated in one step utilizing PEG-Silane as previously described.[17] Before image acquisition, the surface was incubated with 15 μL of 0.2 mg/mL streptavidin solution for 10 min. The unbound streptavidin was washed away with imaging buffer (50 mM NaCl, 100 mM TRIS buffer pH 8). Following streptavidin incubation, a fluorophore-tagged biotinylated ssDNA 18-mer was immobilized on PEG-coated glass coverslips *via* biotin-streptavidin interactions upon incubating a 200 pM solution of the oligonucleotide. Unbound duplexes were flushed out with additional imaging buffer.

3.6.1.2.2 Anti-fading solution.

Experiments were run in the presence of an oxygen scavenger solution consisting of β-mercaptoethanol (143 mM), D-(+)-glucose (0.8% w/v), glucose oxidase (165 units/mL), and catalase C30 (2170 units/mL). The first image was acquired 10 min after introducing the oxygen removal system to allow the equilibration of the oxygen concentration in the chamber. Solutions contained 100 mM in Tris buffer pH 8 and 50 mM in NaCl. Additional reagents such as KI, L-ascorbic acid (AA), and methyl viologen (MV) were added when necessary. Experiments were conducted at room temperature (23 °C) unless otherwise specified.

3.6.1.2.3 TIRF Microscopy.

Fluorescence imaging was carried out using an inverted Nikon Eclipse Ti microscope equipped with the perfect focus system (PFS) implementing an objective-type TIRF configuration with a Nikon TIRF illuminator and an oil-immersion objective (CFI SR Apo TIRF 100× oil immersion objective lens, numerical aperture (NA) 1.49). The effective pixel size was 160 nm. With these settings, four lasers were used for excitation (Agilent MLC400B Monolithic Laser Combiner): 405, 488, 561, and 647 nm. The laser beam was passed through a multiband cleanup filter

(ZET405/488/561/647x, Chroma Technology) and coupled into the microscope objective using a multiband beam splitter ZT405/488/561/647rpc (Chroma Technology). Fluorescence light was spectrally filtered with an emission filter ZET405/488/561/647m (Chroma Technology). For Cy5 and Cy5B imaging, an additional emission filter ET705/72m (Chroma Technology) was used.

The camera was controlled using Micro-Manager Software (Micro-Manager 1.4.13, San Francisco, CA, USA), capturing 16-bit 512 x 512 pixel images with an exposure time of 20-200 ms. All movies were recorded onto a 512 x 512 pixel region of a back-illuminated electron-multiplying charge-coupled device (EMCCD) camera (iXon X3 DU-897-CS0-#BV, Andor Technology). The microscope was controlled using the software NIS element from Nikon.

3.6.1.2.4 Image and data analysis.

We observed typically ~400-800 spots over one field of view (~82^2 μm^2). Fluorescence intensity time trajectories of individual molecules were extracted from the videos using an algorithm written in MATLAB (MathWorks) defining a square region around the centers of the spots captured. The total number of photons detected for each molecule before photobleaching was calculated as the multiplication of the average intensity (photons/s) and the survival time corresponding to the molecule analyzed. The arbitrary intensity recorded by the EMCCD camera was converted to photons using the calibrated curve for the electron multiplication and the analog-to-digital conversion gain settings used during acquisition. For the blinking analysis we developed an algorithm in MATLAB (MathWorks) to analyse on and off dwell times as well as to count the number of photons. On dwell times were found by performing a thresholding analysis. A gaussian profile was fitted to the background intensity to find the standard deviation (σ). Signals above 5σ were considered as on states.

3.6.1.3 Laser flash photolysis studies

Experiments were conducted using a laser flash photolysis setup (Luzchem). A Nd:YAG (Continuum Surelite CLII-10, 10 Hz, 450 mJ at 1064 nm) laser was used for excitation at a wavelength of 532 nm. 20 mJ laser pulses were used with a pulse width of 6 ns. A 150 W Xe lamp was used as the monitoring light source. The detector consisted of a photomultiplier tube (PMT) connected to a digital oscilloscope (Tektronix TDS2012). All data was collected *via* the commercially available LFP 7.0 software (Luzchem). Samples contained the described dye at a concentration of approximately 5 µM in aqueous buffer (20 mM TRIS pH 8, 50 mM NaCl) with

specified concentrations of potassium iodide, β-mercaptoethanol, ascorbic acid, and/or methyl viologen. All samples were prepared freshly in 10 x 10 mm quartz cells using enzymatic scavenger to deplete oxygen as degassing with argon gas provided poorer depletion conditions. A minimum of 10 laser shots were averaged to obtain the temporal evolution of ΔOD for the various transient species monitored. In turn, a minimum of 5 laser shots were averaged per wavelength interval for obtaining the transient absorption spectra. The time per division recorded by the detector was varied from 1 μs to 1 ms on a sample-to-sample basis to optimize signal to noise and temporal resolution. ΔOD vs time traces were fitted using OriginPro 8.5 to obtain transient lifetimes.

3.6.1.3.1 Determination of electron transfer rate constants (k_{PeT})

Rate constants for the photoinduced electron transfer (k_{PeT}) to the triplet excited states of Cy5 and Cy5B by β-ME were determined by plotting the rate of triplet decay k_T vs the concentration of thiolate, $[RS^-]$, utilizing **Eq. 3.2**. The rate of triplet decay was obtained as the inverse of the triplet lifetime at a given $[RS^-]$ as shown in **Eq. 3.3**. k_o is defined as the triplet decay rate constant in the absence of a triplet quencher (**Eq. 3.4**). $[RS^-]$ was calculated using the Henderson-Hasselbach equation (pKa β-ME = 9.6)[36] for pH=8.

$$k_T = k_o + k_{PeT}[RS^-] \tag{3.2}$$

$$k_T = \frac{1}{\tau_T} \tag{3.3}$$

$$k_o = \frac{1}{\tau_T^o} \tag{3.4}$$

3.6.1.3.2 Generation of Cy5 and Cy5B transient species

To generate the desired transient species from Cy5, different environmental conditions were used. The photoisomer *cis*-Cy5 was observed upon direct photoexcitation of Cy5. To promote intersystem crossing and facilitate the observation of ^{3}*Cy5, 50 mM of KI was added to the buffer solution. Additionally, KI was added to generate $Cy5^{+\bullet}$ and $Cy5^{-\bullet}$, which can be generated from the triplet species by oxidation and reduction *via* P*e*T. $Cy5^{+\bullet}$ was generated by adding 1 mM of methyl viologen (MV^{2+}) as it can oxidize ^{3}*$Cy5^+$. Similarly, 1 mM of ascorbic acid (AA) was used to reduce ^{3}*Cy5 to $Cy5^{-\bullet}$. The same methodologies were utilized in studies with Cy5B.

3.6.1.3.3 Spectral characterization of Cy5 and Cy5B transient species

Previous studies have found *cis*-Cy5 to absorb modestly near 690 nm,[37] however, ^{3}*Cy5 is also known to absorb in this region. To discriminate between the absorption of these two species, spectra with and without 50 mM KI were recorded and compared. It was found that only ^{3}*Cy5 absorbs at 710 nm, hence this wavelength provides a clear window where to perform mechanistic studies on ^{3}*Cy5. In the presence of MV^{2+} (1 mM), a strong transient absorption band peaking at 525 nm was recorded and assigned to $Cy5^{+\bullet}$. Lifetime measurements of $Cy5^{+\bullet}$ were accordingly conducted at this wavelength. This species was found to be generated occasionally in the absence of oxidizing agents, due to biphotonic photoionization, as confirmed by a quadratic dependence of ΔOD at 525 nm on the laser excitation power (**Figure 3.9)**. $Cy5B^{+\bullet}$ was similarly located at 530 nm. With AA (1 mM) in solution, the absorption peak of $Cy5^{-\bullet}$ appeared near 490 nm. This wavelength was selected for subsequent lifetime measurements to monitor the evolution of $Cy5^{-\bullet}$. Similarly, $Cy5B^{-\bullet}$ transient absorption band was observed to peak at 515 nm. We expect very low interference using methyl viologen (MV^{2+}) and ascorbic acid (AA). Given their spectra and their low absorption coefficients at the relevant wavelengths, we expect the contribution of $MV^{+\bullet}$ and $AA^{-\bullet}$ to be negligible at the wavelengths monitored.[38-39]

3.6.1.3.4 Deconvolution of absorption spectra of Cy5 transient species

To obtain the transient absorption spectrum for each transient species of Cy5, solutions were prepared according to the conditions listed in **Table 3.3**. Spectra were acquired at 5 nm increments from 500-800 nm for *cis*-Cy5 and ^{3}*Cy5 and from 300-800 nm for $Cy5^{+\bullet}$ and $Cy5^{-\bullet}$. To estimate the extinction coefficient for the various transients we used the value of Cy5 at 645 nm ($\varepsilon_{645} = 2.5 \times 10^5$ $M^{-1}cm^{-1}$).[40] We assumed that none of the transient species of interest absorbed significantly at 645 nm, as the ΔOD values of all spectra produced a negative mirror image of the Cy5 absorption spectrum in this region. We also assumed that bleaching of the ground state resulted in 100% conversion to the desired species. Deconvolution of each species proceeded as follows:

***cis*-Cy5.** To study this transient, the GODCAT system was not included to allow oxygen quenching of any ^{3}*Cy5 formed as ^{3}*Cy5 absorption overlaps that of the *cis*-Cy5 spectrum. Preliminary studies of this transient showed that small amounts of $Cy5^{+\bullet}$ were generated (either from reaction with molecular oxygen or by two-photon absorption by Cy5). In turn, $Cy5^{+\bullet}$ partially interferes with the bleaching band of Cy5, complicating the analysis. In order to avoid recording

the presence of $Cy5^{+\bullet}$, 1 mM ascorbic acid was added to the solution to quench $Cy5^{+\bullet}$. In order to estimate the transient spectrum, the Cy5 absorption band was inverted and scaled to match that of the bleaching of ^{3}*Cy5. The scaled inverted band was then subtracted from the ^{3}*Cy5 spectrum, generating a new spectrum showing only the absorption of the *cis*-Cy5 species. The *cis*-Cy5 transient absorption band was then divided by the scaling factor used to match the Cy5 spectrum to the transient bleaching band. This operation yielded the molar extinction coefficient for *cis*-Cy5 relative to Cy5.

^{3}*Cy5. In order to minimize the formation of *cis*-Cy5, as its transient absorption overlaps that of ^{3}*Cy5 spectrum, experiments were carried out in glycerol 90% v/v given that an increased viscosity significantly decreases *cis*-Cy5 formation. The different solvent properties caused a 5 nm red-shift which was corrected before doing further analysis. 50 mM KI was included to catalyze intersystem crossing. GODCAT was included in the solution to prevent quenching by molecular oxygen. As described above, the bleached band accounting for the Cy5 absorption spectrum was used to generate the ^{3}*Cy5 absorption spectrum as well as to estimate its molar extinction coefficient.

$Cy5^{+\bullet}$. Herein, 50 mM KI and 1 mM MV^{2+} were included in the solution, where MV^{2+} promoted oxidation of the generated ^{3}*Cy5 species. Additionally, GODCAT was added to prevent ^{3}*Cy5 quenching by molecular oxygen. The transient spectrum recorded included contributions from a Cy5 bleaching band (negative ΔOD) and formation of the corresponding *cis*-Cy5, and $Cy5^{+\bullet}$ absorption (positive ΔOD). The inverted Cy5 absorption spectrum was adjusted to the ΔOD corresponding to Cy5 bleaching band at 645 nm (under the assumption that neither *cis*-Cy5 nor $Cy5^{+\bullet}$ absorb significantly there). The obtained spectrum corresponds to the sum of absorption of $Cy5^{+\bullet}$ and *cis*-Cy5. Next, the previously obtained isolated *cis*-Cy5 spectrum was scaled and fitted to the positive ΔOD values near 690 nm and subtracted from the obtained spectrum. The spectrum thus obtained corresponds to $Cy5^{+\bullet}$ absorption band.

$Cy5^{-\bullet}$. Herein, 50 mM KI and 1 mM AA^- were included for this acquisition, where the latter promoted reduction of the generated ^{3}*Cy5 species. Additionally, GODCAT was added to prevent ^{3}*Cy5 quenching by molecular oxygen. Here, ΔOD included contributions from Cy5 bleaching band (negative ΔOD) and the corresponding cis-Cy5, and $Cy5^{-\bullet}$ absorption (positive ΔOD). The analysis performed to obtain absorption band of $Cy5^{-\bullet}$ was similar to that reported for $Cy5^{+\bullet}$.

Table 3.3. Summary of experimental conditions utilized to generate and study transient species of Cy5 *via* laser flash photolysis.

Species	Solvent/Buffer	GODCAT	[KI] 50 mM	[AA^-] 1 mM	[MV^{2+}] 1 mM
cis-Cy5	Water/T50			✔	
^{3*}Cy5	Glycerol 90%/ T50		✔		
$Cy5^{+\bullet}$	Water/T50	✔	✔		✔
$Cy5^{-\bullet}$	Water/T50	✔	✔	✔	

It should be noted that all absorption spectra and molar extinction coefficients for the possible transient species formed from Cy5 are approximations. The resolution of all LFP spectra was set to 5 nm to optimize time restraints on data acquisition (given that the pH of the sample changes over time due to the formation of gluconic acid) and to avoid photobleaching of the fluorophore. Importantly, error is anticipated for the tails of all peaks as the transient species were formed in small quantities and are very weakly absorbent beyond their optimal wavelength.

3.6.1.4 Computational methods

Quantum chemical calculations were performed using the Gaussian 16W package (Version. 1.1 and revision A.03).[41] GaussView 6.0.16 package was used as graphical user interface. Dye structures were modelled as shown in **Fig. 3.8**

The molecular geometries in the ground state (S_0) were optimized *via* spin-restricted DFT calculations using the B3LYP functional and the 6-31G(d) basis set. The spin-unrestricted formalism was used in geometry optimization of the radicals. Vibrational frequency calculations were subsequently carried out to confirm that all the optimized structures correspond to the minima on the potential energy surfaces (i.e. no imaginary frequencies). The molecular geometries of the lowest triplet excited state (T_1) were initially optimized via spin-unrestricted DFT calculations (ground state) and next optimized using the time-dependent DFT (TD-DFT) formalism with the same functional and basis set of B3LYP/6-31G(d). The molecular geometries in the first singlet excited state (S_1) were optimized using the time-dependent DFT (TD-DFT) formalism with the same functional and basis set of B3LYP/6-31G(d). Single-point energy calculations were carried

out in all cases. All calculations were performed in water phase, modeled by the polarizable continuum model (PCM) with the integral equation formalism variant (IEFPCM). Vertical electronic transitions were obtained using non-equilibrium solvation and performed *via* a two-steps job: first, a single point energy calculation was performed on the initial state, specifying noneq=write in the PCM input section to store the information about non-equilibrium solvation based on the initial state. Second, the actual state-specific calculation is performed reading the non-equilibrium solvation information, using noneq=read, and specifying the checkpoint file from the first step.

3.6.1.4.1 Electron transfer calculations within the framework of Marcus theory of electron transfer

In Marcus theory of electron transfer,[42-44] the rate constant for electron transfer k_{eT} is given by **Eq. 3.5** where the Gibbs free energy of activation, $\Delta G_{eT}^{\ddagger}$, is related to the Gibbs free energy of electron transfer ΔG_{eT}^{o} and the reorganization energy λ according to **Eq. 3.6**.

$$k_{eT} = Ae^{\frac{-\Delta G_{eT}^{\ddagger}}{RT}} \tag{3.5}$$

$$\Delta G_{eT}^{\ddagger} = \frac{\left(\Delta G_{eT}^{o}+\lambda\right)^{2}}{4\lambda} \tag{3.6}$$

The reorganization energy λ is expressed as the sum of two components, the internal (λ_i) and solvent (λ_s) reorganization energy **Eq. 3.7**.

$$\lambda = \lambda_i + \lambda_s = \lambda_D + \lambda_A \tag{3.7}$$

$$\lambda_D = [E(D^+/D) - E(D^+/D^+)] \tag{3.8}$$

$$\lambda_A = \left[E\left(A^-/^{3*}A\right) - E(A^-/A^-)\right] \tag{3.9}$$

We have used the Buda method to calculate λ.[45] In this strategy, using density functional theory and continuum solvation models, the internal and solvent (also known as inner- and outer-sphere) contributions are not separated, but rather, they were computed as a sole parameter.

Given that the reorganization energy λ can be expressed as the sum of the donor (λ_D) and acceptor (λ_A) reorganization energies (**Eq. 3.7**), we have treated the thiolate donor (D) and the cyanine acceptor (A) separately (**Eqs. 3.8-3.9**). Here, $E(a/b)$ represents the energy of state "a" calculated at the optimized geometry of "b". The term "$^{3*}A$" denotes the cyanine in the triplet excited state.

3.6.2 Chemical Structures of Cyanine Dyes

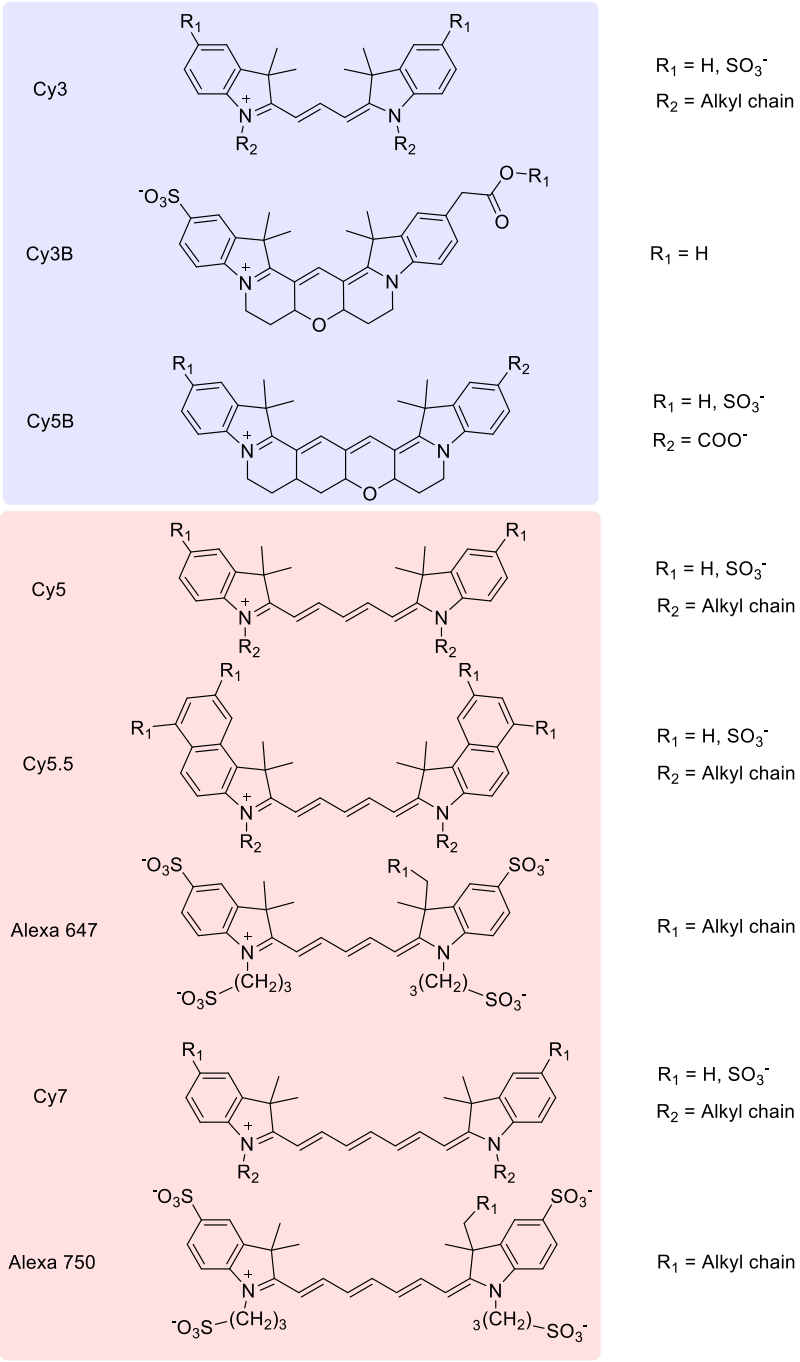

Figure 3.6. Cyanine chemical structures related to Cy5. Generic chemical structures of Cy3, Cy3B,[46] Cy5B,[8] Cy5, Cy5.5, Alexa 647,[47] Cy7, and Alexa 750.[47] R_1 and R_2 groups have been included due to structural differences observed from suppliers, however, other variations may be found. Inside the pale blue background are shown the cyanines with none or negligible photoswitching behaviour in the presence of thiols. Inside the pale red background are shown the cyanines able to undergo effective photoswitching behaviour in the presence of thiols.

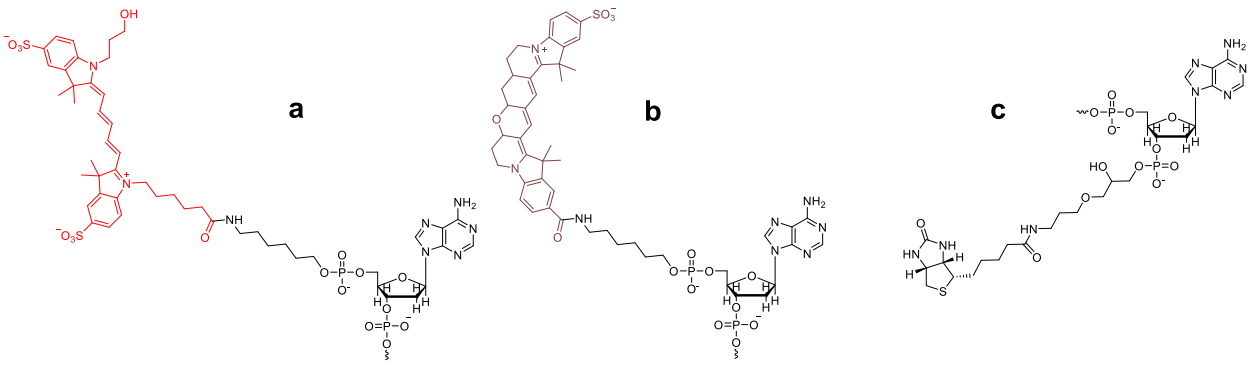

Figure 3.7. Dyes and modifications utilized. Chemical structure of the various dye and biotin conjugates utilized, Cy5 and Cy5B appear in red. Conjugate (a) and (b) correspond to Cy5 and Cy5B conjugates at the 5' end of the DNA strand respectively. Structure (c) shows the biotin conjugation at the 3' end of the DNA strand.

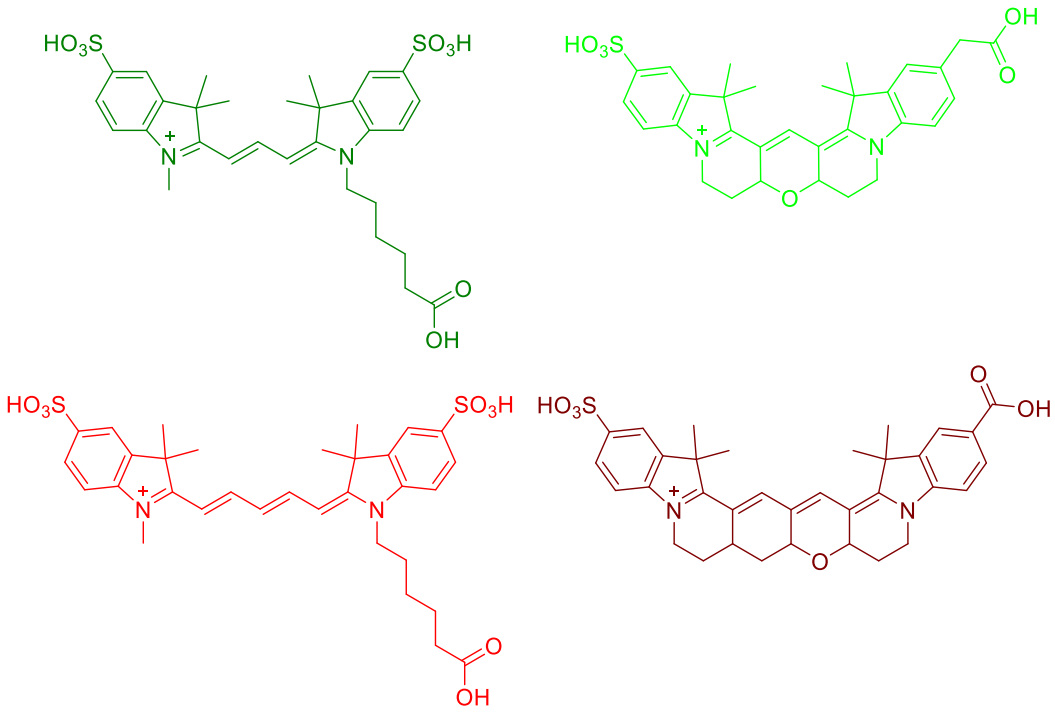

Figure 3.8. Chemical structures of cyanine dyes utilized for LPF and DFT calculation studies. Top left Cy3, top right Cy3B, bottom left Cy5, Bottom right Cy5B.

3.6.3 Geminate Back Electron-transfer Studies for Cy5 /β-ME Pair.

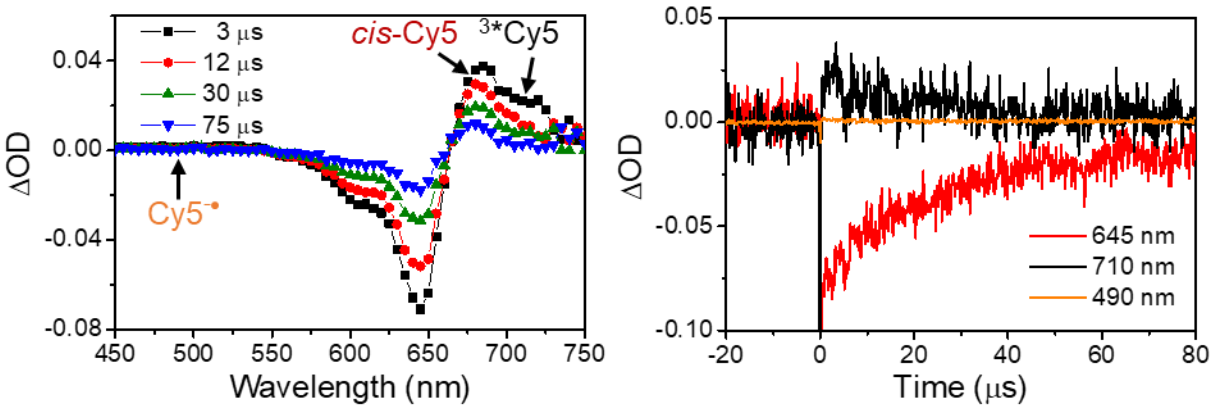

Figure 3.9. Geminate back electron-transfer examination. Transient absorption spectra (left panel) and temporal evolution of ΔOD traces recorded at 490, 645, and 710 nm (right panel) of Cy5 recorded in aqueous buffered solution (Tris 20 mM, 50 mM NaCl, pH 8) containing ~5 μM Cy5, 50 mM KI, and 14.3 mM β-ME. After excitation, immediate triplet state formation (enhanced by KI) can be followed at 710 nm. Upon β-ME quenching, via P*e*T, the triplet state completely decays while the ground state of Cy5 is recovered (645 nm). The band corresponding to a region where $Cy5^{-\bullet}$ is expected to absorb (490 nm, see also Fig. 2a) remains unchanged, supporting an efficient geminate B*e*T allowed by a rapid ISC in the newly formed geminate radical pair. Incomplete recovery of the ground state (at 75 μs) is explained due to presence of the long lived (~200 μs) *cis* isomer.

3.6.4 Photoinduced Formation of the Radical Cation Cy5+•

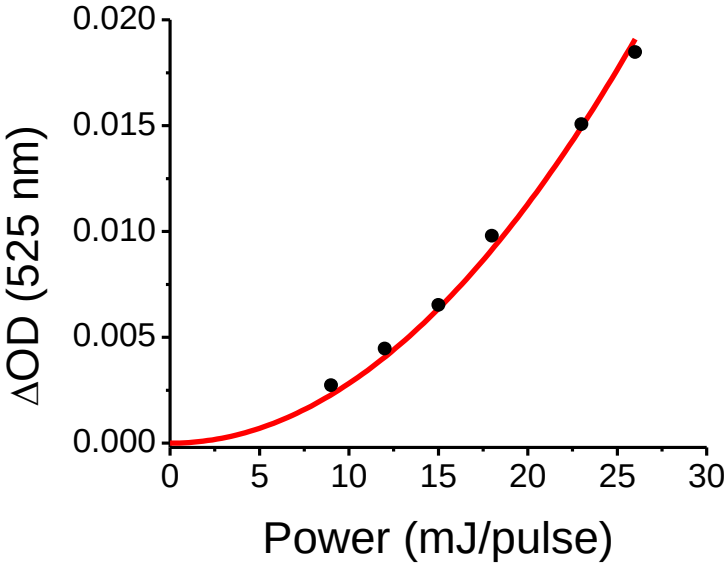

Figure 3.10. Quadratic dependence of photoinduced formation of radical cation $Cy5^{+\bullet}$. Maximum ΔOD (10 shots averaged) recorded at 525 nm as a function of the laser excitation power (532 nm). Transient absorption decays were recorded in aqueous buffered solution (Tris 20 mM, 50 mM NaCl, pH 8) containing ~5 μM Cy5. After excitation, immediate radical formation can be followed at 525 nm. Rather than linear, a quadradic dependence of ΔOD as a function of power was found ($\Delta OD = 2.82 \pm 0.05 \times 10^{-5} P^2$), consistent with a biphotonic process.

3.6.5 Rate of Photoinduced Electron-transfer from β-ME to the Singlet Excited State of Cy5

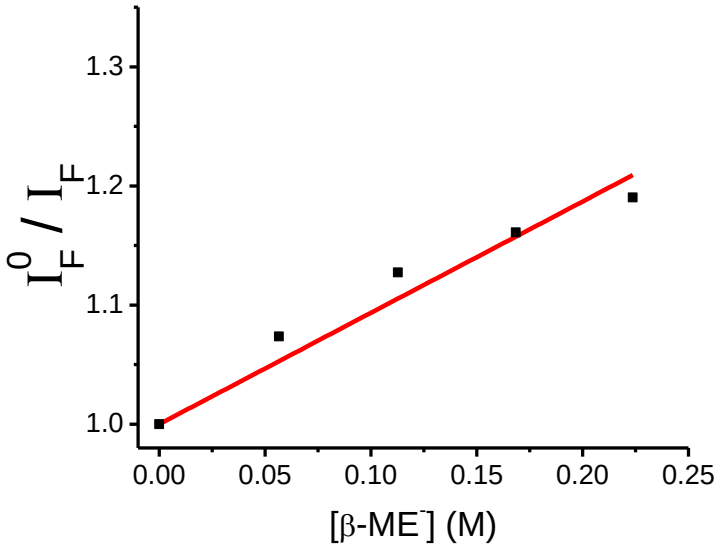

Figure 3.11. Stern-Volmer plot of fluorescence quenching of Cy5 with β-ME. Emission spectra of Cy5 (~3 μM) were recorded on 500 mM Na_2CO_3, pH=11 with increasing concentrations of β-ME. Emission scans were recorded by exciting at 610 nm and recording fluorescence in the 620-800nm. Fluorescence intensities $\boldsymbol{I_F}$ were computed by integrating the spectrum (corrected by background and changes in absorption at 610 nm). The Stern-Volver plot equation is given by: $\boldsymbol{I_F^0/I_F = 1 + k_{PeT}^s \tau_s [\beta ME^-]}$, where $\boldsymbol{I_F^0}$ and $\boldsymbol{I_F}$ are the fluorescence intensities in the absence and presence of β-ME. Here, the slope reports on the product of the photoinduced electron transfer rate constant $\boldsymbol{k_{PeT}^s}$, and the fluorescence lifetime $\boldsymbol{\tau_s}$. A linear regression yield $\boldsymbol{k_{PeT}^s \tau_s = 0.93 \pm 0.06\ M^{-1}}$. Utilizing the reported fluorescence lifetime of Cy5 $\boldsymbol{\tau_S = 0.92\ x10^{-9}\ s}$,[18] we obtain that the photoinduced electron transfer rate constant of the singlet excited state of Cy5 is: $\boldsymbol{k_{PeT}^s = 1 \times 10^9\ M^{-1} s^{-1}}$.

3.6.6 Probability of intercepting singlet vs triplet excited states

The rate of intercepting the triplet excited state by a quencher Q (v_i^T) is given by the product of its rate of generation v_g^T and its quantum yield of quenching ϕ_{PeT}^T ($v_i^T = v_g^T \phi_{PeT}^T$). A similar equation can be written for the quenching of the singlet excited state ($v_i^S = v_g^S \phi_{PeT}^S$). Combination of these two equations allows the estimation of the relative rate of interception of the two species (i.e. singlet and triplet) (**Eq. 3.10**). The rate of triplet excited state generation can be written in terms of the rate of generation of the singlet excited state and the quantum yield of ISC ϕ_{ISC}, using that $v_g^T = \phi_{ISC} v_g^S$.

$$\frac{v_i^T}{v_i^S} = \frac{v_g^T \phi_{PeT}^T}{v_g^S \phi_{PeT}^S} = \phi_{ISC} \frac{\phi_{PeT}^T}{\phi_{PeT}^S} \tag{3.10}$$

In turn, ϕ_{ISC} can be written in terms of the ISC rate constant k_{ISC} and the fluorescence lifetime of the fluorophore τ_S as in **Eq. 3.11**.

$$\phi_{ISC} = k_{ISC}\, \tau_S \tag{3.11}$$

The quantum yield of quenching of the triplet state ϕ_{PeT}^T can be written in terms of the photoinduced electron transfer rate constant k_{PeT}^T, the quencher concentration $[Q]$, and the triplet lifetime of the fluorophore τ_T, **Eq. 3.12.** A similar equation can be written for the quantum yield f quenching of the singlet excited state ϕ_{PeT}^S. **Eq. 3.13**.

$$\phi_{PeT}^T = \frac{k_{PeT}^T [Q]}{\tau_T^{-1} + k_{PeT}^T [Q]} \tag{3.12}$$

$$\phi_{PeT}^S = \frac{k_{PeT}^S [Q]}{\tau_S^{-1} + k_{PeT}^S [Q]} \tag{3.13}$$

All the values required have been taken from the literature or determined in this study: $k_{ISC} = 0.83 \times 10^6\ s^{-1}$,[16] $k_{PeT}^T = 9.9 \times 10^7\ s^{-1} M^{-1}$ (see **table 3.2**), $\tau_S = 0.92 \times 10^{-9}\ s$,[18] $\tau_T = 2.09 \times 10^{-4}\ s$ (see **table 3.1**), and $k_{PeT}^S = 1 \times 10^9\ M^{-1} s^{-1}$ (see **figure 3.11**). Additionally, $[Q] = [RS^-] = 3.5 \times 10^{-3}\ M$ was calculated using a total β-ME concentration of 143 mM and the Henderson-Hasselbach equation (pKa (β-ME) = 9.6)[36] for pH=8. Using **equations 3.11, 3.12, and 3.13** as well as the above reported values, we obtain $\phi_{ISC} = 0.71 \times 10^{-3}$, $\phi_{PeT}^T = 0.986$, $\phi_{PeT}^S = 3.21 \times 10^{-3}$. Using the above quantum yields in **equation 3.11** we obtain that $v_i^T / v_i^S = 0.22$.

3.6.7 Effect of KI on the average on time <τ_{on}> of Cy5

A model where the triplet state is a necessary intermediate to reach the nonfluorescent dark state can be written as:

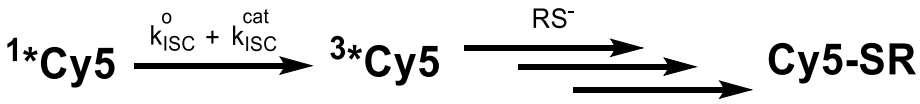

Figure 3.12. Proposed mechanism involving the triplet excited state of Cy5 as an intermediate.

v_{off}^{o} can be defined as the rate at which Cy5 switches from the fluorescent on state to the nonfluorescent off state in the absence of KI and is given by **Eq. 3.14** where $< \tau_{on} >^{o}$ is the average time Cy5 remains in the fluorescent state.

$$v_{off}^{o} = \frac{1}{<\tau_{on}>^{o}} = v_g^S \phi_{ISC}^{o} \phi_d \tag{3.14}$$

As shown in **Eq. 3.14**, v_{off}^{o} can be written in terms of the rate of singlet generation v_g^S (or excitation rate in s^{-1}), ϕ_{ISC}^{0} the quantum yield of intersystem crossing in the absence of an ISC catalyst like I^-, and ϕ_d the quantum yield of dark state formation from the triplet excited state. In the presence of a quencher such as KI (denoted by Q), **Eq. 3.14** can be rewritten as:

$$v_{off}^{Q} = \frac{1}{<\tau_{on}>^{Q}} = v_g^S \phi_{ISC}^{Q} \phi_d \tag{3.15}$$

The ratio $v_{off}^{Q} / v_{off}^{o}$ shown in **equation 3.16** can be simplified by assuming that the rate of singlet generation remains constant and the probability of forming the dark state once the triplet state is formed is not affected by the presence of an ISC catalyst such as I^-. As a result, $v_{off}^{Q} / v_{off}^{o}$ only depends on the quantum yield of intersystem crossing in the absence and presence of an ISC catalyst, ϕ_{ISC}^{o} (defined in **Eq. 3.11** as $\phi_{ISC}^{o} = k_{ISC}^{o} \tau_S$) and $\phi_{ISC}^{Q} = k_{ISC}^{o} \tau_S + k_{ISC}^{cat}[Q] \tau_S$ (under the assumption that $k_{ISC}^{cat}[Q] \ll \tau_S^{-1}$).

$$\frac{v_{off}^{Q}}{v_{off}^{o}} = \frac{v_g^S \phi_{ISC}^{Q} \phi_d}{v_g^S \phi_{ISC}^{o} \phi_d} = \frac{\phi_{ISC}^{Q}}{\phi_{ISC}^{o}} = \frac{k_{ISC}^{o} \tau_S + k_{ISC}^{cat}[Q] \tau_S}{k_{ISC}^{o} \tau_S} \tag{3.16}$$

Equation 3.16 can be simplified and re-written as:

$$\frac{v_{off}^{Q}}{v_{off}^{o}} = \frac{k_{ISC}^{o} + k_{ISC}^{cat}[Q]}{k_{ISC}^{o}} = 1 + \frac{k_{ISC}^{cat}}{k_{ISC}^{o}}[Q] \tag{3.17}$$

The rate constant of catalyzed ISC k_{ISC}^{cat} of Cy5 by KI as well as the rate constant of the intrinsic intersystem crossing k_{ISC}^{o} of Cy5 has been previously determined by the Schwille group.[16]

Reported values in pure water are: $k_{ISC}^{o} = (0.83 \pm 0.42) \times 10^{6} s^{-1}$ and $k_{ISC}^{cat} = (4.2 \pm 0.4) \times 10^{7} M^{-1} s^{-1}$ (where the error has been calculated using the reported data). Therefore, for the proposed model, the slope of $v_{off}^{Q} / v_{off}^{o}$ vs $[KI]$ is expected to yield a value for $k_{ISC}^{cat} / k_{ISC}^{o} = 51 \pm 26\ M^{-1}$ in pure water.

Given that the net charge of Cy5 is negative (-1) (two sulfonate groups (-2) plus the iminium ion moiety (+1)), the quenching rate by iodide ion (-1) will be enhanced in the presence of electrolytes due to the kinetic salt effect.[48] Accordingly, the reported k_{ISC}^{cat} has been corrected utilizing **Eq. 3.18**, where 1.018 is a constant that related to the solvent (water) and temperature (298 K), k and k_o are the rate constants at ionic strength I and at infinite dilute concentration $I = 0.$, respectively. z_A and z_B are the ionic charges of reactants A and B. The ionic strength I was calculated using **Eq. 3.19**.

$$Log(k/k_o) = 1.018 z_A z_B \sqrt{I} \tag{3.18}$$

$$I = \frac{1}{2} \sum c_i z_i^2 \tag{3.19}$$

k_{ISC}^{cat} was estimated to be $k_{ISC}^{cat} = (1.0 \pm 0.1) \times 10^{8} M^{-1} s^{-1}$. Therefore, for the proposed model, the slope of $v_{off}^{Q} / v_{off}^{o}$ vs $[KI]$ is expected to be: $k_{ISC}^{cat} / k_{ISC}^{o} = 125 \pm 65\ M^{-1}$ in 0.1 M Tris buffer and 0.05 M in NaCl at pH=8.

3.6.8 Action Spectrum of Cy5 at Long Wavelengths (Visible Range)

The absorption cross section of a fluorophore σ (cm^2) at a given wavelength can be expressed as the ratio of the excitation rate v_{ex} (s^{-1}) and the excitation photon flux I_{ex} (s^{-1} cm^{-2}) (**Eq. 3.20**). Utilizing $\sigma\,(\mathrm{cm}^2) = \varepsilon \times 3.82 \times 10^{-21}$,[49] (with ε in $M^{-1}cm^{-1}$), a relationship between the extinction coefficient and the ratio v_{ex}/I_{ex} can be expressed (**Eq. 3.20**).

$$\sigma = \frac{v_{ex}}{I_{ex}} = 3.82 \times 10^{-21}\varepsilon \tag{3.20}$$

Laser intensities *P* are usually reported in W/cm^2. It is then convenient to express **Eq. 3.20** in terms of *P* rather than I_{ex}. The relationship of *P* and I_{ex} is shown in **Eq. 3.21**, where λ is the excitation wavelength used in nanometer units.

$$I_{ex} = 5.03 \times 10^{15} P\lambda \tag{3.21}$$

We can additionally write that $v_{ex}\Phi_u = v_{on}$, where Φ_u is the quantum yield of uncaging. Additionally, combining **Eqs. 3.20 and 3.21**, we obtain:

$$\frac{v_{on}}{P} = 1.92 \times 10^{-5}\lambda\Phi_u\varepsilon \tag{3.22}$$

The absorption coefficients can be estimated by performing a power dependence of the v_{on} vs *P*. The slope of this plot will report on $1.92 \times 10^{-5}\lambda\Phi_u\varepsilon$. Deviations in **Eq. 3.22** may arise from the fact that the actual laser excitation sensed by the adduct may be lower than the measured value (due to scattering and evanescence field).

3.6.9 Energy Landscape for Cy Reactions via DFT Calculations

Table 3.4. **Cyanine energies for singlet and triplet excited states relative to their ground state.** DFT/PCM energies were obtained through single point energy calculations.

Dye	**^{1}Cy (Relaxed)** ΔE^o **(*kcal/mol*)**	**^{1*}Cy (Vertical)** ΔE^o **(*kcal/mol*)**	**^{1*}Cy (Relaxed)** ΔE^o **(*kcal/mol*)**	**^{3*}Cy (Relaxed)** ΔE^o **(*kcal/mol*)**
Cy3	0	61.01	54.19	35.92
Cy3B	0	59.13	52.17	32.33
Cy5	0	53.93	46.99	28.94
Cy5B	0	51.21	44.64	26.00

Table 3.5. **Calculated forward electron transfer energy parameters within the framework of Marcus theory of electron transfer.** DFT/PCM calculated reorganization energies λ and ΔE^o_{eT} for the P*e*T half-reaction, performing single point energy calculations.

P*e*T / half reaction	**λ (*kcal/mol*)**	**ΔE^o_{eT} (*kcal/mol*)**
^{3*}Cy3 → Cy3$^{-\bullet}$	18.34	-113.85
^{3*}Cy3B → Cy3B$^{-\bullet}$	17.78	-105.75
^{3*}Cy5 → Cy5$^{-\bullet}$	17.73	-108.32
^{3*}Cy5B → Cy5B$^{-\bullet}$	16.00	-102.23
(β-ME) RS^{-} → RS$^{-\bullet}$	37.60	103.21

Table 3.6. Calculated back electron transfer energy parameters within the framework of Marcus theory of electron transfer. DFT/PCM calculated reorganization energies λ and ΔE^{o}_{BeT} for the B*e*T half-reaction, performing single point energy calculations.

B*e*T / half reaction	λ (*kcal/mol*)	ΔE^{o}_{BeT} (*kcal/mol*)
$Cy3^{-\bullet} \rightarrow Cy3$	20.40	77.94
$Cy3B^{-\bullet} \rightarrow Cy3B$	20.23	73.42
$Cy5^{-\bullet} \rightarrow Cy5$	19.77	79.38
$Cy5B^{-\bullet} \rightarrow Cy5B$	18.77	76.22
(β-ME) $RS^{\bullet} \rightarrow RS^{-}$	38.14	-103.21

Table 3.7. **DFT/PCM calculated energy for P*e*T, associated reorganization energies λ, and activation energy $\Delta E^{\ddagger}_{PeT}$. λ and ΔE^{o}_{PeT} were calculated as the arithmetic sum of the half reactions. $\Delta G^{\ddagger}_{eT}$ was calculated using Marcus theory of electron transfer (Eq. 3.6).**

P*e*T / full reaction	λ (*kcal/mol*)	ΔE^{o}_{PeT} (*kcal/mol*)	$\Delta E^{\ddagger}_{PeT}$ (*kcal/mol*)
$^{3*}Cy3 + RS^{-} \rightarrow Cy3^{-\bullet} + RS^{\bullet}$	55.95	-10.64	9.17
$^{3*}Cy3B + RS^{-} \rightarrow Cy3B^{-\bullet} + RS^{\bullet}$	55.38	-2.54	12.60
$^{3*}Cy5 + RS^{-} \rightarrow Cy5^{-\bullet} + RS^{\bullet}$	55.33	-5.11	11.39
$^{3*}Cy5B + RS^{-} \rightarrow Cy5B^{-\bullet} + RS^{\bullet}$	53.60	0.99	13.90

Table 3.8. DFT/PCM calculated energy for B*e*T, associated reorganization energies λ, and activation energy $\Delta E^{\ddagger}_{PeT}$. λ and ΔE^{o}_{BeT} were calculated as the arithmetic sum of the half reactions. $\Delta E^{\ddagger}_{BeT}$ was calculated using Marcus theory of electron transfer (Eq. 3.6).

B*e*T / full reaction	λ (*kcal/mol*)	ΔE^{o}_{BeT} (*kcal/mol*)	$\Delta E^{\ddagger}_{BeT}$ (*kcal/mol*)
$Cy3^{-\bullet} + RS^{\bullet} \rightarrow Cy3 + RS^{-}$	58.54	-25.28	4.73
$Cy3B^{-\bullet} + RS^{\bullet} \rightarrow Cy3B + RS^{-}$	58.37	-29.79	3.50
$Cy5^{-\bullet} + RS^{\bullet} \rightarrow Cy5 + RS^{-}$	57.90	-23.83	5.01
$Cy5B^{-\bullet} + RS^{\bullet} \rightarrow Cy5B + RS^{-}$	56.90	-26.99	3.93

Given that for all cases $\lambda > |\Delta E^{o}_{eT}|$, we conclude that we are in the Marcus 'normal region".

3.6.10 Estimation of the Ratio of Back Electron-transfer and Geminate Radical Combination

The number of excitations before reaching the dark state (N_{ex}) is given by **equation 3.23**, where P^S_{adduct} and P^T_{adduct} are the probability of forming the Cy5/β-ME adduct from the singlet and triplet excited state, respectively. ϕ_{ISC}, ϕ_{PeT}, and ϕ_{GRC} are the quantum yields of intersystem crossing, photoinduced electron transfer, and geminate radical combination, respectively.

$$N_{ex} = \frac{1}{P^S_{adduct}+P^T_{adduct}} = \frac{1}{\phi^S_{PeT}\,\phi_{GRC}+\phi_{ISC}\phi^T_{PeT}\,\phi_{GRC}} = \frac{1}{\phi_{GRC}(\phi^S_{PeT}+\phi^T_{PeT}\phi_{ISC})} \quad (3.23)$$

The total number of detected photons (N_{ph}) can be written in terms of the number of excitations (N_{ex}), the fluorescence quantum yield (ϕ_f), and the detection efficiency of the microscope setup (ϕ_d) (**Eq. 3.24**). The quantum yield of geminate radical combination is defined in terms of the geminate radical combination rate constant (k_{GRC}) and the back electron-transfer rate constant (k_{BeT}) (**Eq. 3.25**).

$$N_{ph} = N_{ex}\phi_f\phi_d \quad (3.24)$$

$$\phi_{GRC} = \frac{k_{GRC}}{k_{GRC}+k_{BeT}} \quad (3.25)$$

Replacing **Eqs. 3.24** and **3.25** in **Eq. 3.23** and rearranging provides an expression for the ratio of the back electron-transfer and geminate radical combination rate constants (k_{BeT}/k_{GRC}).

$$\frac{k_{BeT}}{k_{GRC}} = N_{ph}\frac{\phi^S_{PeT}+\phi^T_{PeT}\phi_{ISC}}{\phi_f\phi_d} \text{-1} \quad (3.26)$$

Utilizing the values on **section 3.5.6** and that $N_{ph} = 4892$ (**see figure 3.2**), $\phi_f = 0.2$,[40] and assuming a detection efficiency $\phi_d = 0.1$, we have obtained that $k_{BeT}/k_{GRC} = 955$

3.6.11 A second dark state

We have plotted the cumulative distribution function $cdf(t)$ (**equation 3.27**), where the sum of the amplitudes $\alpha_1 + \alpha_2 = 1$. The fractional contributions f_1 and f_2 have been calculated as shown in **Eq. 3.28**.

$$P(t) = 1 - \left(\alpha_1 e^{-\frac{t}{\tau_1}} + \alpha_2 e^{-\frac{t}{\tau_2}}\right) \tag{3.27}$$

$$f_1 = \frac{\alpha_1\tau_1}{\alpha_1\tau_1+\alpha_2\tau_2} = 1 - f_2 \tag{3.28}$$

Rates $v_{on(1)} = 1/\tau_1$ (slow) and $v_{on(2)} = 1/\tau_2$ (fast) were calculated using the values shown in **Table 3.9** and plotted against the Irradiance (I) as shown in **Figure 3.13b**.

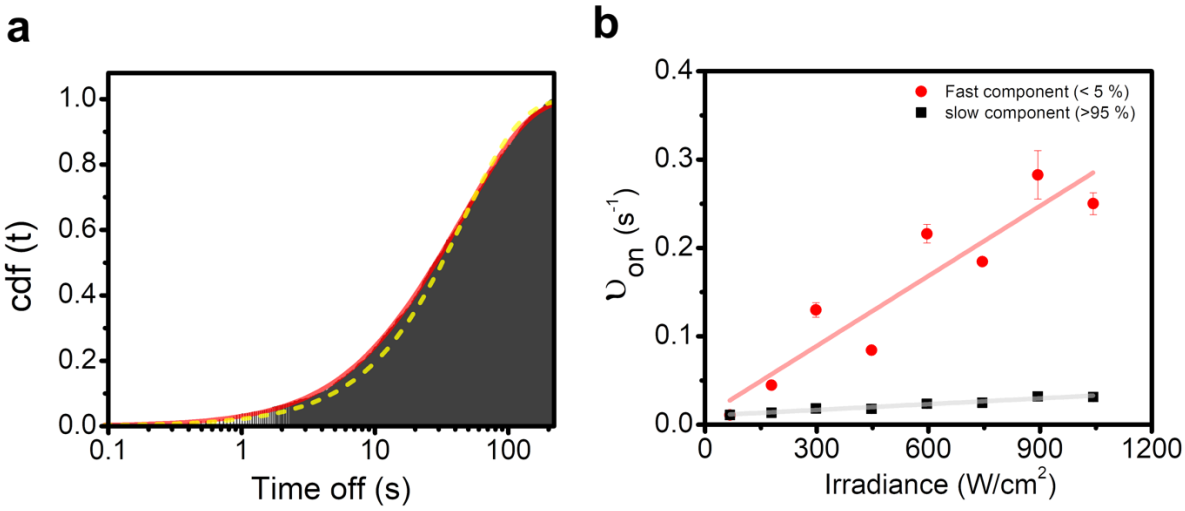

Figure 3.13. Biexponential decay fitting analysis**. (a)** Mono-exponential (green dashed line) versus bi-exponential (red solid line) fitting of the cumulative distribution function (taken at 447 W/cm^2). **(b)** Linear correlations of $v_{on(1)}$ (black squares) and $v_{on(2)}$ (red circles) as a function of the irradiance (I) at 647 nm. Linear fittings are $v_{on(1)} = 2.2 \pm 0.2\, x10^{-5}\, x\, I + 0.010 \pm 0.001$, and $v_{on(2)} = 2.6 \pm 0.4\, x10^{-4}\, x\, I + 0.01 \pm 0.03$. All experiments were recorded in aqueous buffered solution (Tris 100 mM, 50 mM NaCl, pH 8) under oxygen depleted conditions.

Table 3.9. Biexponential fitting parameters obtained as a function of the irradiance, using a 647 nm laser for excitation.

Irradiance (W/cm^2)	α_1	τ_1 (s)	α_2	τ_2 (s)	f_1	f_2
67	1	92.35 ± 0.05	-	-	-	-
179	0.877	73.94 ± 0.12	0.123	22.36 ± 0.45	0.959	0.041
298	0.938	54.41 ± 0.09	0.062	7.70 ± 0.49	0.991	0.009
447	0.804	56.16 ± 0.12	0.196	11.87 ± 0.22	0.951	0.049
596	0.929	42.37 ± 0.05	0.071	4.63 ± 0.23	0.992	0.008
745	0.920	40.48 ± 0.03	0.080	5.42 ± 0.14	0.988	0.012
894	0.971	31.37 ± 0.03	0.029	3.54 ± 0.34	0.997	0.003
1043	0.942	31.98 ± 0.03	0.058	4.00 ± 0.20	0.992	0.008

3.6.12 Hydrogenation of Cy5 with sodium borohydride

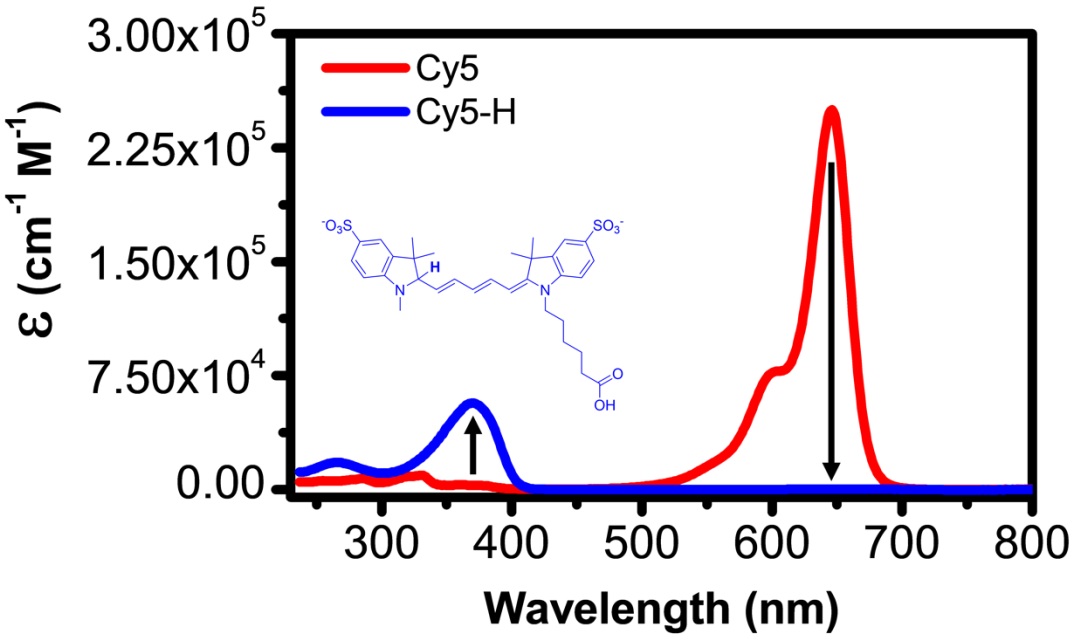

Figure 3.14. Absorption spectra and structure of hydrogenated Cy5. The hydrogenated Cy5 was generated by adding $NaBH_4$ (1 mM) to a solution of ~2 μM of Cy5 in 1x PBS buffer. Cy5-H was found to have an absorption maximum at 370 nm ($\boldsymbol{\varepsilon_{370} = 57.000}$).

3.7 References

1. Betzig, E.; Patterson, G. H.; Sougrat, R.; Lindwasser, O. W.; Olenych, S.; Bonifacino, J. S.; Davidson, M. W.; Lippincott-Schwartz, J.; Hess, H. F., Imaging Intracellular Fluorescent Proteins at Nanometer Resolution. *Science* **2006,** *313* (5793), 1642-1645.
2. Hess, S. T.; Girirajan, T. P. K.; Mason, M. D., Ultra-High Resolution Imaging by Fluorescence Photoactivation Localization Microscopy. *Biophysical Journal* **2006,** *91* (11), 4258-4272.
3. Rust, M. J.; Bates, M.; Zhuang, X., Sub-diffraction-limit imaging by stochastic optical reconstruction microscopy (STORM). *Nature Methods* **2006,** *3*, 793.
4. Bates, M.; Huang, B.; Dempsey, G. T.; Zhuang, X., Multicolor Super-Resolution Imaging with Photo-Switchable Fluorescent Probes. *Science* **2007,** *317* (5845), 1749-1753.
5. Heilemann, M.; Margeat, E.; Kasper, R.; Sauer, M.; Tinnefeld, P., Carbocyanine Dyes as Efficient Reversible Single-Molecule Optical Switch. *Journal of the American Chemical Society* **2005,** *127* (11), 3801-3806.
6. Heilemann, M.; van de Linde, S.; Schuttpelz, M.; Kasper, R.; Seefeldt, B.; Mukherjee, A.; Tinnefeld, P.; Sauer, M., Subdiffraction-resolution fluorescence imaging with conventional fluorescent probes. *Angewandte Chemie (International ed. in English)* **2008,** *47* (33), 6172-6.
7. Baddeley, D.; Crossman, D.; Rossberger, S.; Cheyne, J. E.; Montgomery, J. M.; Jayasinghe, I. D.; Cremer, C.; Cannell, M. B.; Soeller, C., 4D Super-Resolution Microscopy with Conventional Fluorophores and Single Wavelength Excitation in Optically Thick Cells and Tissues. *PLOS ONE* **2011,** *6* (5), e20645.
8. Michie, M. S.; Gotz, R.; Franke, C.; Bowler, M.; Kumari, N.; Magidson, V.; Levitus, M.; Loncarek, J.; Sauer, M.; Schnermann, M. J., Cyanine Conformational Restraint in the Far-Red Range. *J Am Chem Soc* **2017,** *139* (36), 12406-12409.
9. Bates, M.; Blosser, T. R.; Zhuang, X., Short-range spectroscopic ruler based on a single-molecule optical switch. *Phys Rev Lett* **2005,** *94* (10), 108101.
10. Dempsey, G. T.; Bates, M.; Kowtoniuk, W. E.; Liu, D. R.; Tsien, R. Y.; Zhuang, X., Photoswitching Mechanism of Cyanine Dyes. *Journal of the American Chemical Society* **2009,** *131* (51), 18192-18193.
11. Harada, Y.; Sakurada, K.; Aoki, T.; Thomas, D. D.; Yanagida, T., Mechanochemical coupling in actomyosin energy transduction studied by in vitro movement assay. *Journal of Molecular Biology* **1990,** *216* (1), 49-68.
12. Nie, S.; Chiu, D.; Zare, R., Probing individual molecules with confocal fluorescence microscopy. *Science* **1994,** *266* (5187), 1018-1021.
13. Holzmeister, P.; Gietl, A.; Tinnefeld, P., Geminate recombination as a photoprotection mechanism for fluorescent dyes. *Angewandte Chemie (International ed. in English)* **2014,** *53* (22), 5685-8.
14. Glembockyte, V.; Cosa, G., Redox-Based Photostabilizing Agents in Fluorescence Imaging: The Hidden Role of Intersystem Crossing in Geminate Radical Ion Pairs. *Journal of the American Chemical Society* **2017,** *139* (37), 13227-13233.
15. Kasha, M., Collisional Perturbation of Spin-Orbital Coupling and the Mechanism of Fluorescence Quenching. A Visual Demonstration of the Perturbation. *The Journal of Chemical Physics* **1952,** *20* (1), 71-74.

16. Widengren, J.; Schwille, P., Characterization of Photoinduced Isomerization and Back-Isomerization of the Cyanine Dye Cy5 by Fluorescence Correlation Spectroscopy. *The Journal of Physical Chemistry A* **2000,** *104* (27), 6416-6428.
17. Gidi, Y.; Bayram, S.; Ablenas, C. J.; Blum, A. S.; Cosa, G., Efficient One-Step PEG-Silane Passivation of Glass Surfaces for Single-Molecule Fluorescence Studies. *ACS Applied Materials & Interfaces* **2018,** *10* (46), 39505-39511.
18. Zheng, Q.; Jockusch, S.; Zhou, Z.; Blanchard, S. C., The Contribution of Reactive Oxygen Species to the Photobleaching of Organic Fluorophores. *Photochemistry and Photobiology* **2014,** *90* (2), 448-454.
19. Aramendia, P. F.; Negri, R. M.; Roman, E. S., Temperature Dependence of Fluorescence and Photoisomerization in Symmetric Carbocyanines.Influence of Medium Viscosity and Molecular Structure. *The Journal of Physical Chemistry* **1994,** *98* (12), 3165-3173.
20. Cosa, G.; Scalano, J. C., Laser Techniques in the Study of Drug Photochemistry¶. *Photochemistry and Photobiology* **2004,** *80* (2), 159-174.
21. Nemkovich, N. A.; Rubinov, A. N.; Tomin, V. I., Inhomogeneous Broadening of Electronic Spectra of Dye Molecules in Solutions. In *Topics in Fluorescence Spectroscopy: Principles*, Lakowicz, J. R., Ed. Springer US: Boston, MA, 2002; pp 367-428.
22. Kundu, K.; Knight, S. F.; Willett, N.; Lee, S.; Taylor, W. R.; Murthy, N., Hydrocyanines: A Class of Fluorescent Sensors That Can Image Reactive Oxygen Species in Cell Culture, Tissue, and In Vivo. *Angewandte Chemie International Edition* **2009,** *48* (2), 299-303.
23. Briks, Y. L. Y. Y. L., Hydrogenated derivatives of cyanine dyes. *Zh. Org. Khim.* **1990,** *26* (12), 2591-2600.
24. Glembockyte, V.; Lin, J.; Cosa, G., Improving the Photostability of Red- and Green-Emissive Single-Molecule Fluorophores via Ni2+ Mediated Excited Triplet-State Quenching. *The Journal of Physical Chemistry B* **2016,** *120* (46), 11923-11929.
25. Roy, R.; Hohng, S.; Ha, T., A practical guide to single-molecule FRET. *Nature Methods* **2008,** *5*, 507.
26. Rasnik, I.; McKinney, S. A.; Ha, T., Nonblinking and long-lasting single-molecule fluorescence imaging. *Nature Methods* **2006,** *3* (11), 891-893.
27. Hwang, H.; Kim, H.; Myong, S., Protein induced fluorescence enhancement as a single molecule assay with short distance sensitivity. *Proceedings of the National Academy of Sciences* **2011,** *108* (18), 7414-7418.
28. Hwang, H.; Myong, S., Protein induced fluorescence enhancement (PIFE) for probing protein–nucleic acid interactions. *Chemical Society Reviews* **2014,** *43* (4), 1221-1229.
29. Steffen, F. D.; Sigel, R. K. O.; Börner, R., An atomistic view on carbocyanine photophysics in the realm of RNA. *Physical Chemistry Chemical Physics* **2016,** *18* (42), 29045-29055.
30. Morten, M. J.; Lopez, S. G.; Steinmark, I E.; Rafferty, A.; Magennis, S. W., Stacking-induced fluorescence increase reveals allosteric interactions through DNA. *Nucleic Acids Research* **2018,** *46* (21), 11618-11626.
31. Gidi, Y.; Götte, M.; Cosa, G., Conformational Changes Spanning Angstroms to Nanometers via a Combined Protein-Induced Fluorescence Enhancement–Förster Resonance Energy Transfer Method. *The Journal of Physical Chemistry B* **2017,** *121* (9), 2039-2048.
32. Ploetz, E.; Lerner, E.; Husada, F.; Roelfs, M.; Chung, S.; Hohlbein, J.; Weiss, S.; Cordes, T., Förster resonance energy transfer and protein-induced fluorescence enhancement as synergetic multi-scale molecular rulers. *Scientific Reports* **2016,** *6*, 33257.

33. Lerner, E.; Ploetz, E.; Hohlbein, J.; Cordes, T.; Weiss, S., A Quantitative Theoretical Framework For Protein-Induced Fluorescence Enhancement–Förster-Type Resonance Energy Transfer (PIFE-FRET). *The Journal of Physical Chemistry B* **2016,** *120* (26), 6401-6410.
34. Silvi, M.; Verrier, C.; Rey, Y. P.; Buzzetti, L.; Melchiorre, P., Visible-light excitation of iminium ions enables the enantioselective catalytic β-alkylation of enals. *Nature Chemistry* **2017,** *9*, 868.
35. Arceo, E.; Jurberg, I. D.; Álvarez-Fernández, A.; Melchiorre, P., Photochemical activity of a key donor–acceptor complex can drive stereoselective catalytic α-alkylation of aldehydes. *Nature Chemistry* **2013,** *5*, 750.
36. Jencks, W. P.; Salvesen, K., Equilibrium deuterium isotope effects on the ionization of thiol acids. *Journal of the American Chemical Society* **1971,** *93* (18), 4433-4436.
37. Huang, Z.; Ji, D.; Wang, S.; Xia, A.; Koberling, F.; Patting, M.; Erdmann, R., Spectral Identification of Specific Photophysics of Cy5 by Means of Ensemble and Single Molecule Measurements. *The Journal of Physical Chemistry A* **2006,** *110* (1), 45-50.
38. Watanabe, T.; Honda, K., Measurement of the extinction coefficient of the methyl viologen cation radical and the efficiency of its formation by semiconductor photocatalysis. *The Journal of Physical Chemistry* **1982,** *86* (14), 2617-2619.
39. Bielski, B. H. J.; Comstock, D. A.; Bowen, R. A., Ascorbic acid free radicals. I. Pulse radiolysis study of optical absorption and kinetic properties. *Journal of the American Chemical Society* **1971,** *93* (22), 5624-5629.
40. Mujumdar, R. B.; Ernst, L. A.; Mujumdar, S. R.; Lewis, C. J.; Waggoner, A. S., Cyanine dye labeling reagents: Sulfoindocyanine succinimidyl esters. *Bioconjugate Chemistry* **1993,** *4* (2), 105-111.
41. Frisch, M. J.; Trucks, G. W.; Schlegel, H. B.; Scuseria, G. E.; Robb, M. A.; Cheeseman, J. R.; Scalmani, G.; Barone, V.; Petersson, G. A.; Nakatsuji, H.; Li, X.; Caricato, M.; Marenich, A. V.; Bloino, J.; Janesko, B. G.; Gomperts, R.; Mennucci, B.; Hratchian, H. P.; Ortiz, J. V.; Izmaylov, A. F.; Sonnenberg, J. L.; Williams; Ding, F.; Lipparini, F.; Egidi, F.; Goings, J.; Peng, B.; Petrone, A.; Henderson, T.; Ranasinghe, D.; Zakrzewski, V. G.; Gao, J.; Rega, N.; Zheng, G.; Liang, W.; Hada, M.; Ehara, M.; Toyota, K.; Fukuda, R.; Hasegawa, J.; Ishida, M.; Nakajima, T.; Honda, Y.; Kitao, O.; Nakai, H.; Vreven, T.; Throssell, K.; Montgomery Jr., J. A.; Peralta, J. E.; Ogliaro, F.; Bearpark, M. J.; Heyd, J. J.; Brothers, E. N.; Kudin, K. N.; Staroverov, V. N.; Keith, T. A.; Kobayashi, R.; Normand, J.; Raghavachari, K.; Rendell, A. P.; Burant, J. C.; Iyengar, S. S.; Tomasi, J.; Cossi, M.; Millam, J. M.; Klene, M.; Adamo, C.; Cammi, R.; Ochterski, J. W.; Martin, R. L.; Morokuma, K.; Farkas, O.; Foresman, J. B.; Fox, D. J. *Gaussian 16 Rev. A.03*, Wallingford, CT, 2016.
42. Marcus, R. A., Electron Transfer Reactions in Chemistry: Theory and Experiment (Nobel Lecture). *Angewandte Chemie International Edition in English* **1993,** *32* (8), 1111-1121.
43. CLOSS, G. L.; MILLER, J. R., Intramolecular Long-Distance Electron Transfer in Organic Molecules. *Science* **1988,** *240* (4851), 440-447.
44. Turro, N. J.; Ramamurthy, V.; Scaiano, J. C., *Modern molecular photochemistry of organic molecules*. University Science Books: Sausalito, Calif., 2010.
45. Buda, M., On calculating reorganization energies for electrochemical reactions using density functional theory and continuum solvation models. *Electrochimica Acta* **2013,** *113*, 536-549.

46. Cooper, M.; Ebner, A.; Briggs, M.; Burrows, M.; Gardner, N.; Richardson, R.; West, R., Cy3B™: Improving the Performance of Cyanine Dyes. *Journal of Fluorescence* **2004,** *14* (2), 145-150.
47. Vaughan, J. C.; Dempsey, G. T.; Sun, E.; Zhuang, X., Phosphine Quenching of Cyanine Dyes as a Versatile Tool for Fluorescence Microscopy. *Journal of the American Chemical Society* **2013,** *135* (4), 1197-1200.
48. La Mer, V. K., Reaction Velocity in Ionic Systems. *Chemical Reviews* **1932,** *10* (1), 179-212.
49. Lakowicz, J. R., *Principles of fluorescence spectroscopy*. 3rd ed. ed.; Springer: New York, 2006.

4 Efficient One-Step PEG-Silane Passivation of Glass Surfaces for Single-Molecule Fluorescence Studies

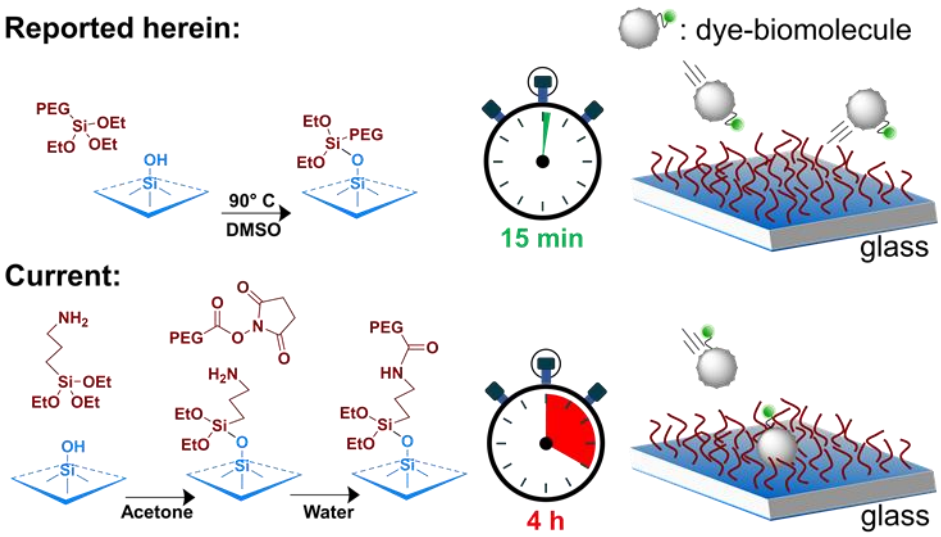

4.1 Preface

In **chapter 1** we discussed the importance of surfaces in SMF techniques. In particular, we highlighted the fact that surface passivation to prevent non-specific binding is of paramount importance to maximize the signal to noise ratio. Surface passivation using PEG grafted onto glass through a two-step process has been (until now) the most commonly used method in SMF studies. This protocol suffers from high variability from slide to slide and batch to batch and requires incubations lasting several hours, hampering the efficiency of this process. In **chapter 4**, we describe an efficient protocol (15 min) that provides a simple, cost-effective, and environmentally benign approach toward rendering glass surfaces for single-molecule studies with improved passivation.

4.2 Abstract

Surface passivation to inhibit nonspecific interactions is a key requirement for in vitro single-molecule fluorescent studies. Although the standard passivation methods involve the covalent attachment of poly(ethylene glycol) (PEG) in two steps preferably over quartz surfaces, this protocol and improvements thereon require extensive labor and chemicals. Herein, we report an efficient one-step surface grafting of PEG-silane that yields enhanced passivation, as evidenced by reduced nonspecific interactions, over the conventional method at a minimal time and reagent cost and on glass surfaces. Our method is rooted in a mechanistic understanding of the silane reaction with the silanol groups on the glass surface. Single-molecule fluorescence studies with fluorescently tagged proteins and DNA on PEG-silane-functionalized glass surfaces validate the enhanced performance of the method. Combined with atomic force microscopy surface characterization, our study further illustrates that few remaining pinhole defects, plausibly from defects on the glass, on PEG-silane glass-coated surfaces account for the minimal background, where typically no more than one molecule is nonspecifically attached in a given diffraction-limited spot on the surface.

4.3 Introduction

Single-molecule fluorescence (SMF) microscopy studies have been used to elucidate an increasing number of fundamental biological questions, involving cellular structures[1] and bionanomachines.[2-4] SMF studies are also instrumental toward understanding the physical, chemical, morphological, and dynamic properties of nanomaterials, such as DNA-based nanostructures,[5-6] supramolecular fibers,[7] metal nanocatalysts,[8] quantum dots,[9-10] and nanoantennas.[11] In a typical surface-based SMF study, fluorescently tagged biomolecules/nanostructures are attached specifically to a surface by exploiting strong noncovalent interactions, usually in the form of biotin–streptavidin (STV) interactions.[12] By using total internal reflection fluorescence (TIRF) microscopy, the fluorescent signal of hundreds of individual molecules can be simultaneously recorded over time, where from rich structural and dynamic information may be retrieved. SMF has thus enabled visualizing intermediates in systems where synchronization, necessary for bulk studies, is not amenable. SMF has also unraveled heterogeneous behavior otherwise hidden in ensemble measurements.

Key to the success of SMF experiments is minimizing/eliminating nonspecific binding of fluorescent substrates to the surface to minimize undesired background, while retaining biomolecule viability.[13] Reducing nonspecific interactions is particularly necessary when two- or multiple-body interactions, such as those present in protein–DNA complexes, are studied, where typical affinity constants require the use of substrate concentrations in the tens to hundreds of nanomolar. Here, fouling of the surface is detrimental to the experiment as it increases the fluorescent background and the effective concentrations of substrates.

The standard surface passivation method applied in SMF studies involves covalent attachment of poly(ethylene glycol) (PEG) to the surface in a two-step process.[14-16] This method has shown ample advantages over the originally proposed bovine serum albumin (BSA) surface coating,[17] among others, as the latter is prone to interact with small hydrophobic molecules, including untagged fluorophores.[18] The two-step PEG attachment initially requires surface functionalization with amine groups, achieved by employing (3-aminopropyl)triethoxysilane (APTES) that binds via silane chemistry. A second step involves grafting of a succinimidyl valerate PEG molecule (mPEG-SVA, typically 5000 Da) via N-hydroxysuccinimide ester–amino reaction. Several improvements to this method have been proposed, including (i) a protocol describing a second PEGylation round using a shorter mPEG-SVA polymer (333 Da) leading to a ∼3-fold decrease in the amount of nonspecific adsorption of Cy3-tethered protein (Cy3-Rep),[19] (ii) PEG deposition performed in cloud-point conditions to reduce the size of the PEG globule so as to form a denser PEG layer, followed by blocking unreacted amines with acetyl groups,[20] (iii) treatment of the surface with Tween 20 (T20), a nonionic detergent, to improve the performance of a PEG–polysiloxane[21] and PEG[22]-treated surfaces. An extension involves use of T20 on hydrophobic silane-treated quartz surfaces in combination with biotinylated-BSA,[23] showing what is to date, to the best of our knowledge, the best performance reported. A problem with T20 surfaces, however, is that fluorescent impurities and short single-stranded DNA (ssDNA) labeled with ATTO647N can bind to and diffuse along this surface, presumably due to incorporation into the surfactant layer.[23] Thus, T20 is expected to be unsuitable for lipophilic dyes such as BODIPYs and non-sulfonated cyanines, as well as for membrane-associated proteins that may potentially bind to a T20 surface.

Herein, we report an efficient passivation protocol relying on a one-step surface grafting of PEG-silane (PEG-Si(OEt)$_3$, PEG-sil) to the silanol groups on the glass coverslip surface.[24-31] The glass passivation performance of the new method is on par with that of the recently reported quartz passivation via BSA-T20 hybrid,[23] vide supra. Key advantages of our method involve its speed, low cost, robustness, sustainability, and the lack of undesired detergent–biomolecule interactions or solubilization of small organic molecules on T20 and/or BSA. SMF and atomic force microscopy (AFM) imaging further illustrate that nonspecific binding may be associated with the existence of pinhole defects in the PEG film, where mostly individual molecules, rather than clusters, are found to nonspecifically bind to the surface. Importantly, by carefully selecting reaction conditions, our method avoids lengthy incubation periods in organic solvents in the presence of catalysts, as previously reported.[24-31] We also reduce by over an order of magnitude the time required for PEG surface functionalization compared to the standard two-step process (∼15 min vs over 4 h). Furthermore, our reactions use a minimal amount of dimethyl sulfoxide (DMSO) and no chemical reagents, such as APTES. Our work ultimately provides a simple, cost-effective, and environmentally benign approach suitable for use in biological settings, toward rendering glass surfaces for single-molecule studies with improved passivation.

4.4 Results and Discussion

Our proposed passivation method is rooted in a mechanistic understanding of the PEG-silane grafting reaction with the glass surface. This reaction requires alcohol condensation between the unhydrolyzed PEG-Si(OEt)$_3$ and silanol groups at the glass coverslip surface that occurs via nucleophilic attack (S_N2) of a deprotonated silanol on the PEG-silane to form the siloxane group (Eq. 1 in Figure 4.1).[32] For the yield to be optimal, however, hydrolysis of PEG-Si(OEt)$_3$ in the presence of water (Eq. 2) must be avoided, as the newly generated PEG-silanol group (PEG-Si(OEt)$_2$OH) can then react with starting material, leading to depletion of reactant and generation of crosslinked structures in solution (Eq. 3). We identified the high boiling point polar aprotic solvent DMSO as the ideal solvent to use. Compared to polar protic solvents, DMSO minimizes the stabilization of the deprotonated silanol thus increasing its nucleophilic reactivity. DMSO may be easily obtained in anhydrous conditions, thus precluding reactions shown in Eqs 2 and 3 from

taking place. The high boiling point of DMSO further enables conducting the reaction in Eq. 1 at high temperature (90 °C) reducing the reaction time and rendering the use of catalysts unnecessary.

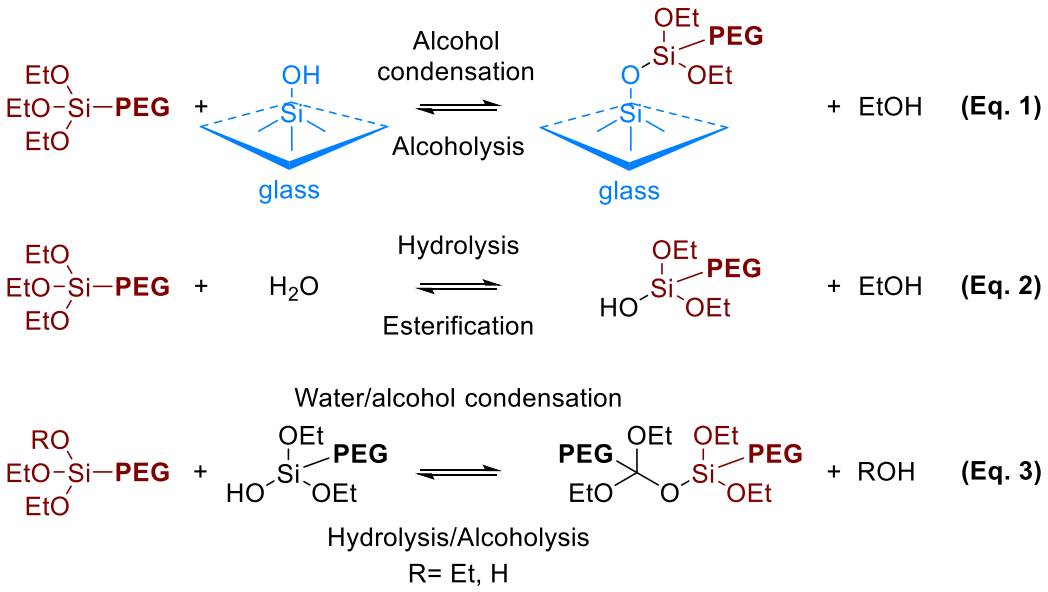

Figure 4.1. PEG-silane grafting reaction (Eq. 1) and competing hydrolysis reactions with water (Eq. 2) or newly generated PEG-silanol (Eq. 3). Glass surface passivation initially required cleaning, etching, and drying, and then attaching the PEG-silane. To clean the coverslip and also maximize the number of silanol groups exposed, we performed a piranha solution cleaning (90 min) followed by a mild etching using NaOH (0.5 M for 30 min). Soaking the slides in dry acetone prior to attaching PEG-silane was crucial to remove any water molecules adsorbed at the glass/air interface due to the hygroscopic nature of glass surfaces.[33] Given our extremely dry winter conditions, we had observed better surfaces in the winter season, which made us realize how critical this step is. Any residual water would elicit the premature hydrolysis of the PEG-$Si(OEt)_3$ (Eq. 2). To further ensure water-free conditions, we used a Petri dish containing desiccant as a reactor to avoid moisture before and during the reaction (**Figure 4.2**). PEG-silane grafting was then performed on the dry coverslips preheated for 5 min at 90 °C followed by incubation with a solution of PEG-silane in anhydrous DMSO for 15 min.

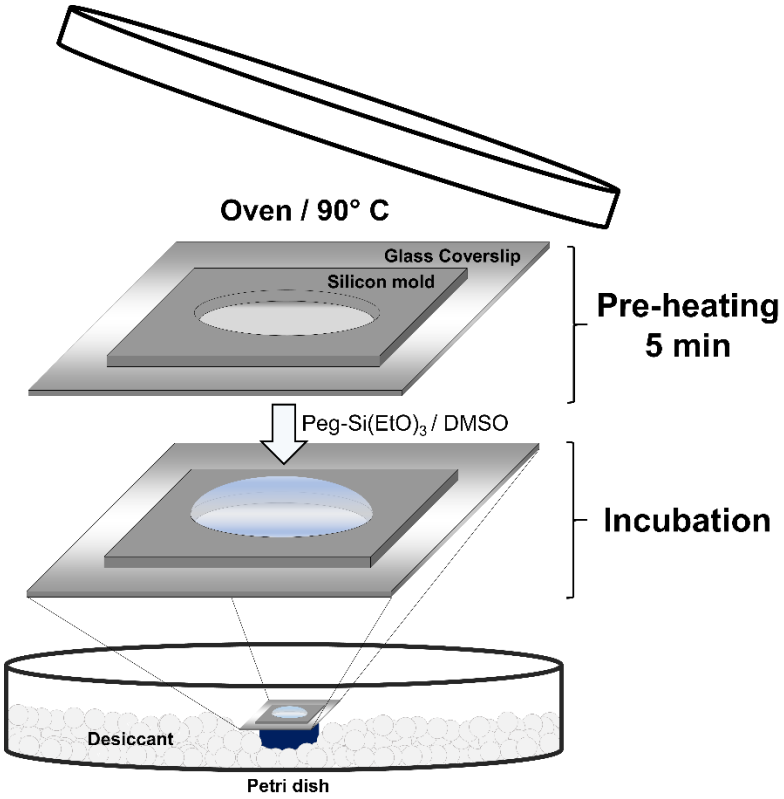

Figure 4.2. Scheme of the reaction chamber and PEGylation process. A Petri dish was used as a reaction chamber to perform the preheating of the glass coverslip and the PEG-silane incubation. To ensure water-free conditions, calcium sulfate was added to the Petri dish. The reaction was performed in a typical laboratory oven at 90 °C.

To benchmark the quality of PEG-silane-treated surfaces, we utilized an imaging experiment where nonspecific adsorption of a (nonbiotinylated) Cy3-tagged single-stranded DNA was monitored in the form of units of fluorescent spots within a 50 × 50 μm^2 sample area. A 100 nM solution of the ssDNA was incubated for 5 min, and then washed with a buffer solution of 50 mM NaCl and 20 mM TRIS, with a pH of 8.0 (T50). No antifading buffer was used herein. Imaging was conducted in a TIRF microscope with a 100× magnification objective utilizing an electron-multiplying charge-coupled device (EMCCD) camera upon exciting the sample with a 561 nm output (25 mW) diode laser.

To optimize conditions in terms of minimizing the number of nonspecifically bound fluorescently tagged biomolecules, we examined various PEG-silane incubation times (1–30 min) at a constant concentration of 15% w/w in DMSO. We also examined various PEG-silane concentrations (1.5–50% w/w) incubating for a constant time of 15 min, **see Figure 4.3a and b**, respectively. Optimal

passivation conditions were obtained upon incubating surfaces with 15–25% w/w PEG-silane for 15 min. Only a marginal improvement was obtained when using concentrations higher than 25% w/w, and this occurred at the expense of easily dissolving the PEG and readily removing it once the incubation period is over. In turn, if incubating for more than 15 min, a highly viscous solution with some precipitates was observed due to DMSO evaporation, thus preventing removal of excess solution. Although a second PEGylation round was also attempted, only a marginal improvement was obtained. Presumably because water used to remove the excess solution from the first PEGylation round increased the hydrolysis rate of newly added PEG-silane, competing with its grafting (condensation), **see Figure 4.3a**. We have chosen to use only one incubation for further characterization and comparisons with the PEG-SVA method. However, applications that require an increased level of passivation can take advantage of a second PEGylation.

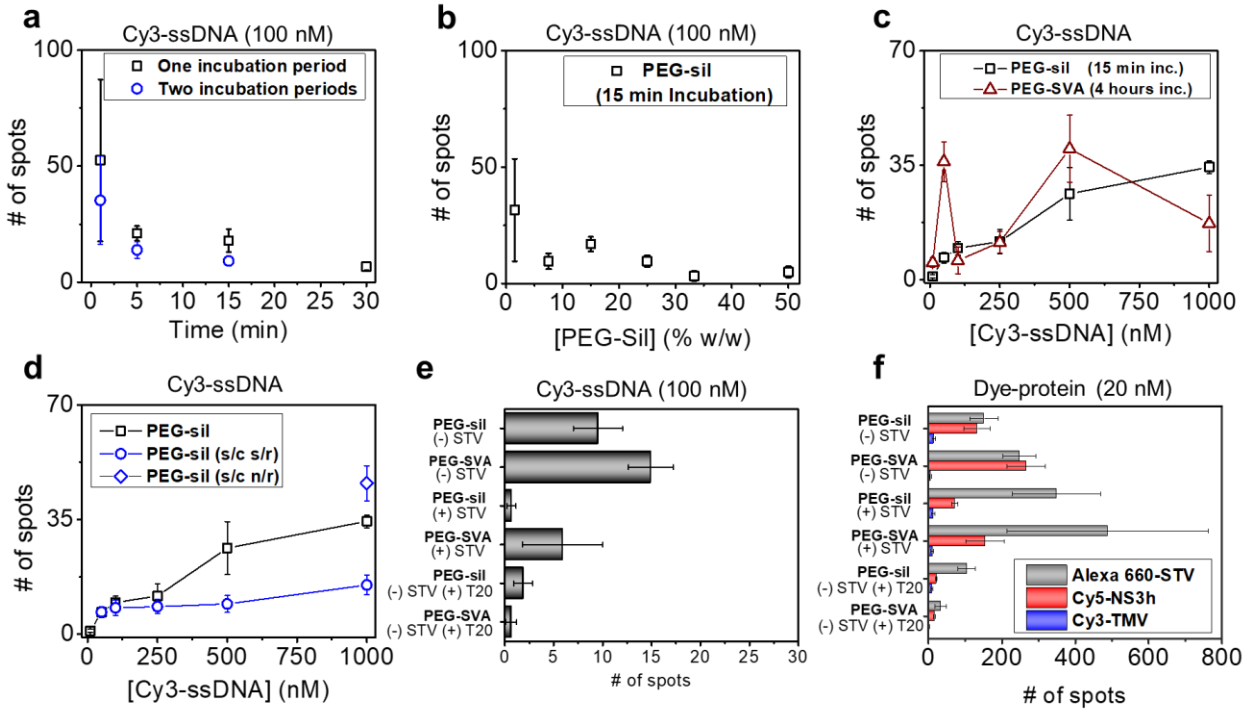

Figure 4.3. Quality tests of PEGylated surfaces utilizing labeled DNA and proteins. Nonspecific binding spots found at different (a) PEG-sil incubation time and (b) PEG-sil concentrations. (c) Performance comparison of PEG-SVA and PEG-sil-coated surfaces with increasing concentrations of Cy3-labeled ssDNA (44mer). (d) Surface performances when using different coverslips (d/c) each time (black squares) compared to using the same coverslip (s/c) and same region (s/r) (blue circles). The blue diamond corresponds to a new (unbleached) region of the same coverslip. (e) Nonspecific binding spots found on PEG-sil and PEG-SVA-coated surfaces after incubation of Cy3-labeled ssDNA (100 nM) on: nonbiotinylated surfaces, nonbiotinylated

surfaces + 10 min incubation of 200 nM STV, and nonbiotinylated surfaces + 5 min incubation of a T50 buffer solution containing 1% T20. (f) Nonspecific binding spots found on PEG-sil- and PEG-SVA-coated surfaces after incubation of Streptavidin (STV-Alexa 660), the hepatitis C virus nonstructural protein 3 helicase domain (NS3h-Cy5) and the capsid protein of the tobacco mosaic virus (TMV-Cy3) on: nonbiotinylated surfaces, nonbiotinylated surfaces + 10 min incubation of 200 nM nonlabeled STV, and nonbiotinylated surfaces + 5 min incubation of a T50 buffer solution containing 1% T20. The number of surface spots was normalized to an area of 2500 μm2. Error bars represent the standard deviation of the number of spots counted from nine different images.

We next compared surfaces prepared with our method against surfaces prepared via the standard two-step PEG attachment. In all these experiments, new coverslips were imaged at every new DNA-labeled concentration, where nine images, on areas sufficiently spread apart (200 μm) to avoid premature photobleaching, were recorded for each condition. Similar results were obtained for PEG-silane vs PEG-SVA surfaces in terms of the number of spots recorded with increasing concentrations of Cy3-tagged ssDNA, **see Figure 4.3c**. Importantly, Cy3-ssDNA spot counts on PEG-SVA were significantly lower in our hands, compared to those reported by others employing these same conditions (albeit we used newly opened acetone ~0.3% in water content; acetone being a hygroscopic solvent it may easily increase its water content over time/extended use).[22-23] Also worth noting, PEG-SVA surfaces showed high variability in our hands with no clear trend with increasing concentrations and larger standard deviations. In contrast, for PEG-silane surfaces the average number of spots regularly increased with increasing Cy3-ssDNA concentration up to 1 μM.

To elucidate the nature of the nonspecific binding between the biomolecules and the surface, we performed both single-molecule intensity and single-molecule photobleaching analysis. We also conducted AFM imaging of the surface. By computing the fluorescent spot intensity distribution and counting the photobleaching steps for each trajectory, we retrieved the number of molecules nonspecifically bound per fluorescent spot. Analysis of the intensity-time trajectories showed in most cases, (81%), a single photobleaching step, indicating that the spots arise from single Cy3-ssDNA molecules binding to the surface rather than clusters of DNA collapsing/forming over it, **Figure 4.4a and b**. Histograms of the initial single spot intensity were additionally obtained upon incubating samples with 100 nM or 1 μM Cy3-ssDNA on PEG-sil-passivated surfaces, which show that single fluorophores are the dominant species accounting for the emission from the spots, as

can be deduced by comparing with the histogram of a control sample consisting of ssDNA specifically bound to the PEG surface via biotin–streptavidin interactions (1% PEG-biotin was used, and streptavidin was incubated prior to the DNA in this control experiment), **see Figure 4.4c**.

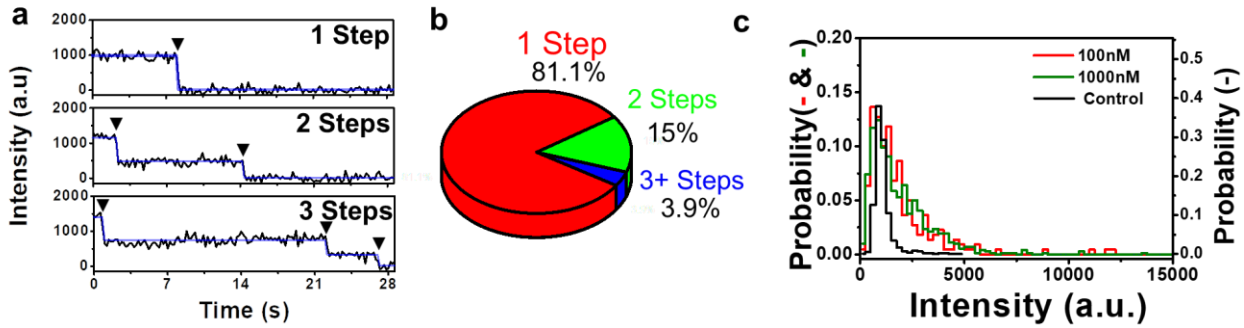

Figure 4.4. Quantitative analysis of nonspecific binding for Cy3-DNA. (a) Representative photobleaching trajectories for one-, two-, and three-step photobleaching events (b) Pie chart showing the distribution of photobleaching steps after incubating 1000 nM of Cy3-DNA. (c) Intensity histogram for specifically attached DNA molecules (black) and nonspecifically bound molecules after incubating 100 nM (red) and 1000 nM (green) of Cy3-DNA.

The intensity histogram shows, however, a tailing consistent with two or three fluorophores/spot. Taken together, the number of photobleaching steps and the intensity histogram analysis illustrate that spots arise mostly from single fluorophores yet we may not rule out small clusters of no more than two or three molecules, where single-step photobleaching would result from efficient energy transfer within chromophores in a single spot. Turning next our attention to AFM studies, this revealed the presence of pits in the glass surface appearing as depressions >5 nm in diameter. These depressions were observed on the glass surface before (**Figure 4.5c**) and after piranha treatment (**Figure 4.5d**). Following NaOH etching, the surface became more ragged, increasing the surface roughness (**Figure 4.5b**), yet the depressions were still observable (**Figure 4.5e**). Functionalization with PEG-silane reduced the apparent size of the depressions but did not eliminate them (**Figure 4.5f**). Comparable results were observed upon APTES treatment followed by PEG-SVA treatment, **see Figure 4.5e**. The surface density of these pinhole defects/depressions was, however, significantly greater than that of fluorescent spots, indicating that should these defects allow for nonspecific interactions, their affinity for DNA must be very low. When focusing our attention to the surface roughness of PEG-SVA (5000 Da)-coated surface, no significant

change was observed when comparing to the untreated surface (**Figure 4.5b,e,g**), consistent with previously reported values.[34] Similar results were obtained with the newly reported method using PEG-sil (5000 Da) (**Figure 4.5b,e,f**).

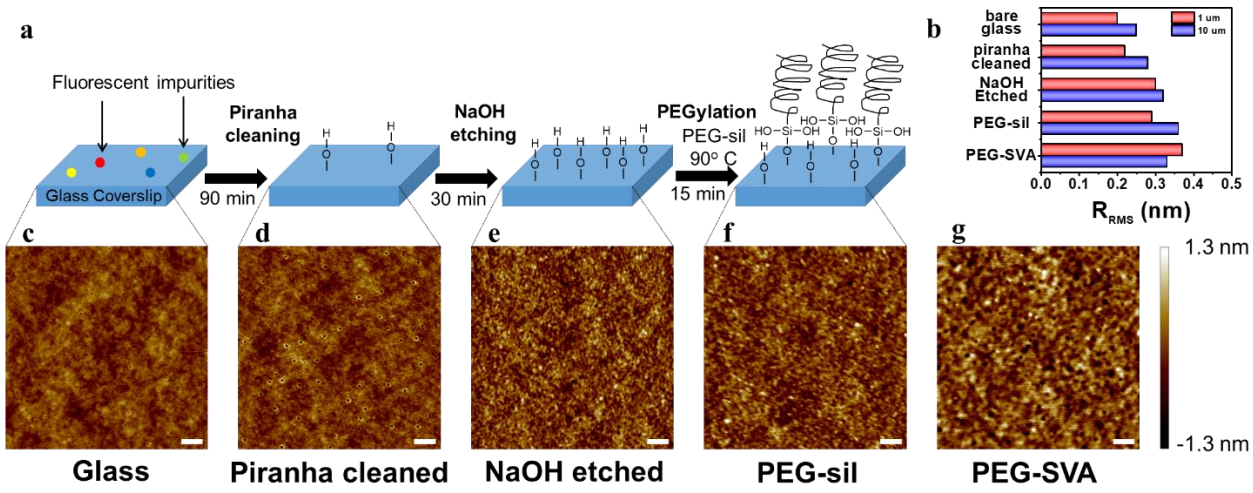

Figure 4.5. Surface Functionalization and AFM Imaging. (a) Schematic procedure for surface functionalization using PEG-sil. (b) Roughness of surfaces at different stages and areas (1 and 100 μm^2). Atomic Force Microscopy images (1 μm^2) of dry surfaces for (c) bare glass, (d) piranha cleaned surface, (e) NaOH (0.5 M) etched surface, PEGylated surface using (f) PEG-sil and (g) PEG-SVA. Scale bars are 100 nm.

Regarding the strength of the nonspecific interactions, experiments involving photobleaching, followed by additional Cy3-ssDNA incubation revealed the appearance of new fluorescent spots that did not localize with the previous ones, **see Figures 4.5 and 4.6**. These results showed that nonspecifically bound Cy3-ssDNA is strongly bound and thus may not be displaced from the surface. Sacrificial ssDNA thus filled surface defects preventing the addition of fresh material in a new cycle. The experiment additionally showed that a collection of sites of decreasing affinity for Cy3-ssDNA existed on the surface, where lower affinity sites were only developed at increasing (e.g., 1 μM) Cy3-ssDNA concentrations. Similar results were found when PEG-SVA was utilized (**see Figures 4.7 and 4.8**).

We subsequently explored whether nonspecific interactions may be minimized/supressed upon preincubating surfaces with either streptavidin (200 nM for 10 min) or Tween 20 (1%, 5 min) following a first PEG treatment to cover the pinhole defects on the surface. Initially exposing either

the PEG-silane or PEG-SVA surface to the above led to decreased nonspecific binding of Cy3-ssDNA (**Figure 4.3e**; note that the surfaces lacked biotin-PEG in these experiments, also note that as previously stated the DNA strand in Cy3-ssDNA is nonbiotinylated). This is consistent with previous studies with T20 showing that it can decrease the degree of nonspecific binding of DNA.[21-22] We note that T20 performed slightly better for the conventional PEG-SVA method than for the PEG-silane method.

To investigate the versatility of the newly prepared surface, we next extended the nonspecific binding tests to three fluorescently tagged proteins available in our laboratory, each utilized at a 20 nM final concentration. These included (i) streptavidin tagged with Alexa 660 (STV-Alexa 660), (ii) the hepatitis C virus nonstructural protein 3 helicase domain tagged with Cy5 (NS3h-Cy5), and (iii) the capsid protein of the tobacco mosaic virus tagged with Cy3 (TMV-Cy3). In all experiments, surfaces were prepared containing no PEG-biotin. PEG-silane surfaces performed better than conventional PEG-SVA for STV-Alexa 660 and NS3h-Cy5, whereas for TMV both methods showed a similar performance with very little nonspecific binding (**Figure 4.3f**). Given that most single-molecule experiments rely on biotin–streptavidin interaction to anchor biomolecules to the surface, we next tested the effect that 10 min preincubation of 200 nM streptavidin solution has on the passivation efficiency when TMV-Cy3, NS3h-Cy5, and STV-Alexa 660 are flowed in. Preincubation with unlabeled streptavidin was detrimental to surface quality for NS3h-Cy5 and STV-Alexa 660, presumably due to protein–protein interactions, yet it had no negative effect with TMV-Cy3. When T20 was tested as a prefilling agent it was found to decrease the nonspecific binding to the surface for the labeled proteins. However, the improvement was marginal in the case of TMV that already had low nonspecific binding.

These results suggest that the pinhole defects found on the glass surface are mainly hydrophobic, lacking silanol groups to anchor PEG-sil or APTES. When comparing proteins vs DNA, it was found that proteins are more prone to nonspecifically bind to the surface as proteins often have hydrophobic moieties on their surface (**see Figure 4.9** for a hydrophobic surface analysis).[35] We found no significant differences on surface hydrophobicity between the proteins utilized on this study. We also found that a protein with a low isoelectric point, such as TMV (pI = 3.4),[36] can minimize the interaction with the surface compared to NS3h (pI = 6.4, calculated from the amino acid sequence using ExPASy)[37] and STV (pI = 6.8–7.5, Thermo Fisher Scientific). This hypothesis

is further supported by the fact that T20, a detergent that can form self-assembled monolayers on hydrophobic surfaces, can minimize the nonspecific binding of NS3h and STV. On the other hand, T20 has a marginal effect on the nonspecific binding of TMV or DNA.

4.5 Conclusions

In our experience, we have found that a limiting factor in SMF studies is the availability of high-quality passivated surfaces, generated in a reproducible fashion. The work we described herein mitigates the reproducibility issues by simplifying the protocol and providing a controlled atmosphere on the most critical step. This protocol enables an efficient surface passivation and requires minimal availability of dedicated chemistry infrastructure insofar, as acetone and DMSO are the only organic solvents utilized. Our method delivered similar or better performance when compared to the PEG-SVA two-step functionalization typically used in SMF studies. Our work provides a cost-effective and environmentally benign approach toward rendering glass surfaces for single-molecule studies with improved surface passivation.

4.6 Materials and Methods

4.6.1 Surface Cleaning and Mild Etching

The coverslip cleaning procedure combines previously reported strategies. A detailed procedure can be found in the Supporting Information. Briefly, coverslips were soaked in piranha solution (25% H_2O_2 and 75% concentrated H_2SO_4) and sonicated for 90 min, followed by several water (Milli-Q) rinsing cycles (5×). Then, coverslips were soaked with a 0.5 M solution of NaOH and sonicated for 30 min, followed by several water (Milli-Q) rinsing cycles (5×). To ensure that the surface to be passivated is water free, the slides were then soaked in high-performance liquid chromatography grade acetone for 5 min while sonicating and dried with N_2.

4.6.2 Preparation of the PEG-Coated Surface

To prevent nonspecific adsorption of biomolecules onto the glass surface, coverslips were functionalized prior to use with poly(ethylene glycol) silane, MW 5000 (mPEG-sil). For experiments requiring sample immobilization, 99:1 ratio w/w of PEG-sil/biotin-PEG-sil was used.

A 25% (w/w) mixture of PEG-sil/DMSO (anhydrous) was incubated at 90 °C for 15 min. The excess PEG was rinsed with water, and the coverslips were dried under a N_2 stream. Imaging chambers (~8 μL) were constructed by pressing a polycarbonate film with an adhesive gasket onto a PEG-coated coverslip. Before image acquisition (and when necessary), the surface was incubated with 12 μL of 0.2 mg/mL (~200 nM) streptavidin solution for 10 min. The unbound streptavidin was washed away twice with 50 μL of T50 imaging buffer (50 mM NaCl, 20 mM TRIS buffer pH 8.0). All experiments were conducted at room temperature (23 °C).

4.6.3 Nonspecific Binding Tests

Surfaces with an area of ~81^2 μm^2 were imaged for 30 s at a frame rate of 33.3 Hz (30 ms). The fluorescent spots were counted, and the values normalized to an area of (50 μm^2) (for comparison) at varying concentrations of labeled biomolecules (proteins or nucleic acids). Labeled DNA and proteins were incubated for 5 min, then the chamber was washed twice with 50 μL T50 buffer. Nine regions forming a square and spaced out by 200 μm were imaged. The average surface spot counts were used to quantify the level of nonspecific binding.

4.6.4 TIRF Microscopy and Image Analysis

Fluorescence imaging was carried out using an inverted Nikon Eclipse Ti microscope equipped with the perfect focus system implementing an objective-type TIRF configuration with a Nikon TIRF illuminator and an oil-immersion objective (CFI SR Apo TIRF 100× oil immersion objective lens, numerical aperture 1.49). The effective pixel size was 160 nm. With these settings, two lasers were used for excitation (Agilent MLC400B Monolithic Laser Combiner): 561 nm (25 mW, measured out of the objective) and 647 nm (25 mW, measured out of the objective). For Cy3 imaging, the laser beam was passed through a multiband cleanup filter (ZET405/488/561/647x, Chroma Technology) and coupled into the microscope objective using a multiband beam splitter (ZT405/488/561/640rpc, Chroma Technology). Fluorescence light was spectrally filtered with a (ET600/50m, Chroma Technology) emission filter. For Cy5 and Alexa 660 imaging, the emission was spectrally filtered with a (ET705/72 m, Chroma Technology) emission filter. All movies were recorded onto a 512 × 512 pixel region of a back-illuminated electron-multiplying charge-coupled device (EMCCD) camera (iXon X3 DU-897-CS0-#BV, Andor Technology).

The camera was controlled using Micro-Manager Software (Micro-Manager 1.4.13, San Francisco, CA). Fluorescence intensity-time trajectories of individual molecules were extracted from the videos using a self-written algorithm in Matlab. To avoid premature photobleaching of fluorescent spots, we started laser excitation after image acquisition.

4.6.5 AFM Imaging

For AFM, Silicon lever and tip-ACTA probes (*k*: 37 N/m, frequency: 300 KHz and ROC: 6 nm) from AppNano were used. AFM data acquisition was done in Tapping Mode in air using a multimode AFM equipped with NSIIIa controller and extender (Digital Instruments, Santa Barbara, CA).

4.7 Supplementary Information

4.7.1 Materials

1M Tris-HCl buffer (pH=8), Sodium Hydroxide, Premium Cover Glass slides (25x25-1) and Acetone (HPLC grade) were purchased from Fisher. 5 M NaCl stock solution was purchased from Life Technologies (Ambion brand). Dimethyl sulfoxide (anhydrous, ≥99.9) and Tween 20 (molecular biology) were purchased from Sigma-Aldrich. Water (molecular biology grade) and Sodium Bicarbonate 7.5% solution were acquired from Thermo Scientific HyClone (South Logan, UT). VectabondTM was purchased from Vector Laboratories (Burlington, ON). Sulphuric acid and Hydrogen Peroxide were purchased from ACP Chemicals. Silicon mold, Press fit tubing connectors and polycarbonate imaging chambers (Hybriwell) were purchased from Grace Bio-Labs, Inc. **Polymers.** Poly(ethylene glycol) polymers in the form of succinimidyl valerate (mPEG-SVA, MW 5000) and Silane (mPEG-Silane, MW 5000) as well as their biotinylated versions (Biotin-PEG-SVA, MW 5000) and (Biotin-PEG-Silane, MW 5000) were purchased from Laysan Bio Inc. **Nucleic acids.** Cy3-tagged DNA 44mer (TGG-CGA-CGG-TCG-CGA-GGT-AAT-TAT-AAC-GGT-TTC-CTT-TTC-TCT-CC[.AmC6][Cyanine3]) was purchased from Trilink Biotechnologies. Biotinilated DNA 18mer (ACC-TCG-CGA-CCG-TCG-CCA/3Bio/) was purchased from Integrated DNA Technologies IDT. **Proteins.** Unlabeled (S888) and labeled

(S21377, Alexa Fluor™ 660 conjugate) Streptavidin were purchased from (Thermofisher Scientific, Invitrogen).

4.7.2 Surface Cleaning

Surface cleaning before surface passivation is a key step as it removes organic impurities that can not only block the attachment of PEG-sil but can also be fluorescent. We have initially cleaned the surface by incubating glass coverslips in piranha (**Figure 4.5a**) for 90 minutes while sonicating, maintaining the bath temperature between 20 and 30 °C. **Figures 4.5c and d** show AFM Images of bare glass and piranha cleaned surface respectively. Surface roughness R_{RMS} (root mean squared) measured for two different areas (1 and 100 μm^2) was slightly increased on this process (**Figure 4.5b**).

4.7.3 Surface Etching

Besides cleaning, piranha also hydroxylates the surface to a certain extent. These silanol groups are necessary to anchor PEG-sil therefore they need to be maximized. To increase the surface area and to maximize the surface density of silanol groups, a mild etching was performed by incubating the glass slides in a solution of 0.5 M of sodium hydroxide for 30 minutes while sonicating and maintaining the temperature between 20 and 30 °C. As shown in **Figures 4.5b and e** the surface roughness increases slightly after this treatment.

4.7.4 Ensuring Water Free Conditions

To avoid variabilities on the performance of this protocol due to water molecules adsorbed at the interface glass/air, we have soaked the slides in acetone (HPLC grade) while sonicating to ensure that the interface glass/air previous incubation is water free. Additionally, we have used a petri dish as a reactor to ensure a water free atmosphere during the reaction. The chamber contains calcium sulphate as desiccant as shown in **Figure 4.2**.

4.7.5 Detailed Protocol for cleaning and Surface Passivation

4.7.5.1 Surface Cleaning with Piranha

1- Using flat-tip tweezers, place five capillaries in each space of a Coplin Staining Jar (Wheaton® 900520).

2- Place eight glass coverslips in the slide holder making sure that one side of each coverslip is touching a capillary and the other side facing the bulk solution.

3- Wash the coverslips with Milli-Q water to remove any dust that can be in the coverslips and/or jar.

4- Under a chemical fume hood carefully mix cold (8 °C) H_2O_2 (30%) and H_2SO_4 in a 1:3 ratio (piranha solution).

5- Slightly shake the jar to homogenize the mixture (temperature will increase) and sonicate for 90 minutes.

6- Pour piranha solution into a bath containing a NaHCO3 solution to neutralize (bubbles will appear) and dispose appropriately.

7- Rinse the jar three times with Milli-Q water, add water again and sonicate for 5 minutes.

8- Remove the water and rinse again with Milli-Q water.

4.7.5.2 Mild NaOH Etching to Maximize the Surface Density of Silanol Groups

9- Add a 0.5 M solution of NaOH and sonicate for 30 min maintaining the temperature between 20 and 30°C.

10- Rinse the jar three times with Milli-Q water, add Milli-Q water again and sonicate for 5 minutes.

11- Remove the water and rinse again, this time using molecular biology grade water.

4.7.5.3 Removing water molecules adsorbed on the glass surface

12- Soak the coverslips on HPLC grade acetone four times and sonicate for 5 min.

13- Remove the acetone and rinse again with acetone.

4.7.5.4 Preparation of PEG-coated Surface

14- Dry the glass coverslip under a nitrogen stream.

15- Place a silicon mold on the exposed side of the coverslip. (The side that is not touching the capillary).

16- Prepare a 25% (w/w) solution of PEG-Silane in dry DMSO. PEG-Silane consist of a mixture of poly(ethylene glycol) silane, MW 5000 (mPEG-Sil-5000) and (biotin-PEG-Sil-5000) at a ratio of 99/1 (w/w)

17- Preheat the coverslip in a clean glass chamber at 90 °C for 5 min.

18- Add the freshly prepared solution in step 15 and wait 15 min.

19- Remove the silicon mold, wash with water (Molecular Biology) and dry under nitrogen stream.

20- Place an adhesive polycarbonate imaging chamber onto the PEG-coated coverslip.

21- Place 2 silicon tubing connectors (glued with double-sided tape) onto the predrilled holes.

4.7.6 Supplementary Figures

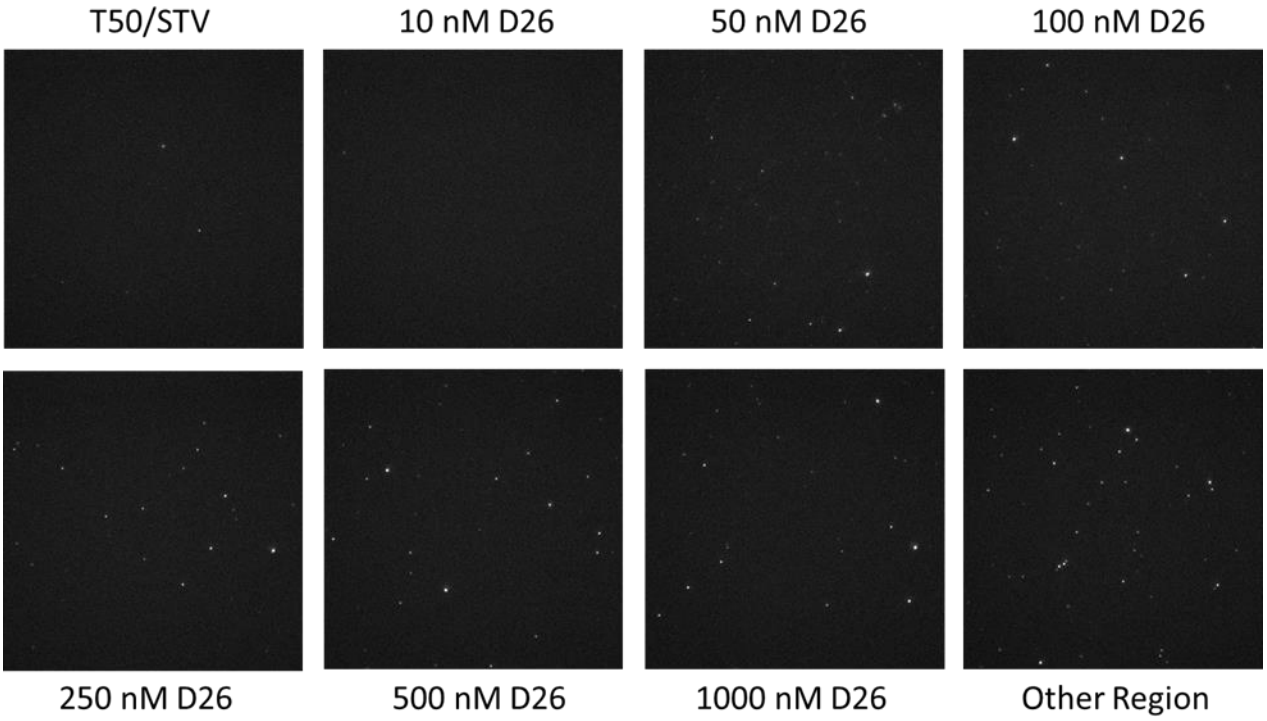

Figure 4.6. Set of Images of the Same Region After Several Incubation-Photobleaching Cycles for PEG-sil Treated Surfaces

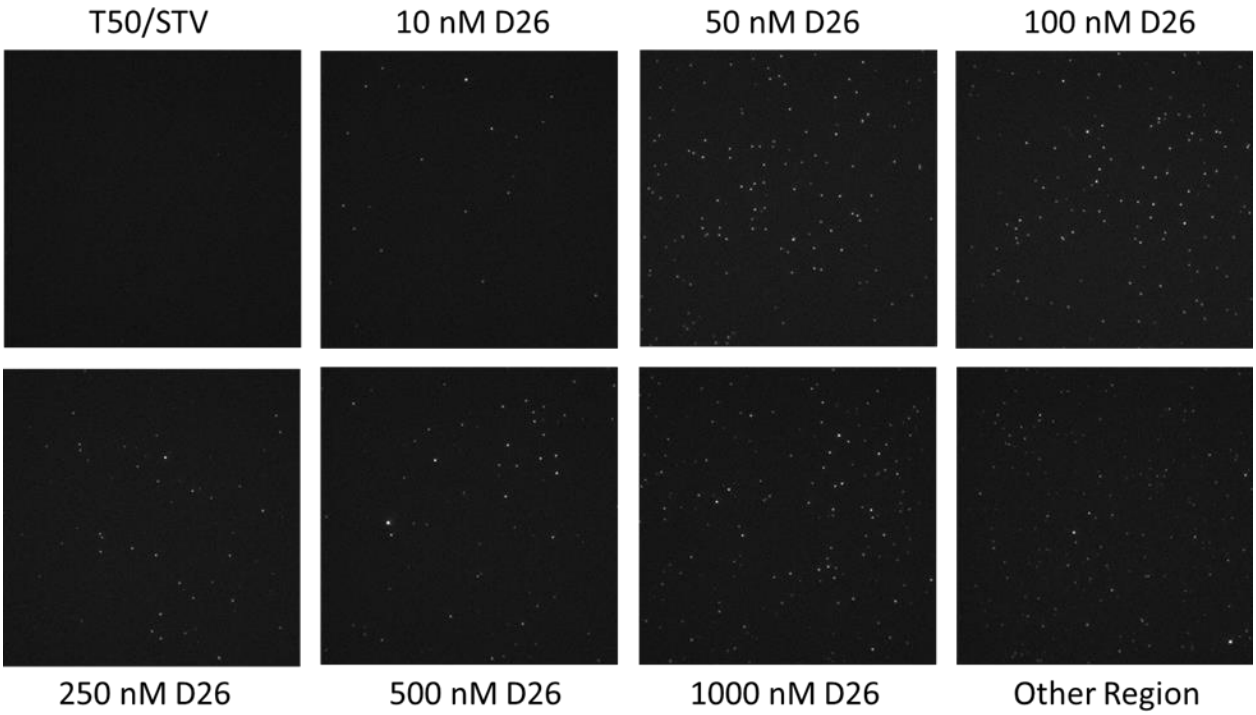

Figure 4.7. Set of Images of the Same Region After Several Incubation-Photobleaching Cycles for PEG-SVA Treated Surfaces

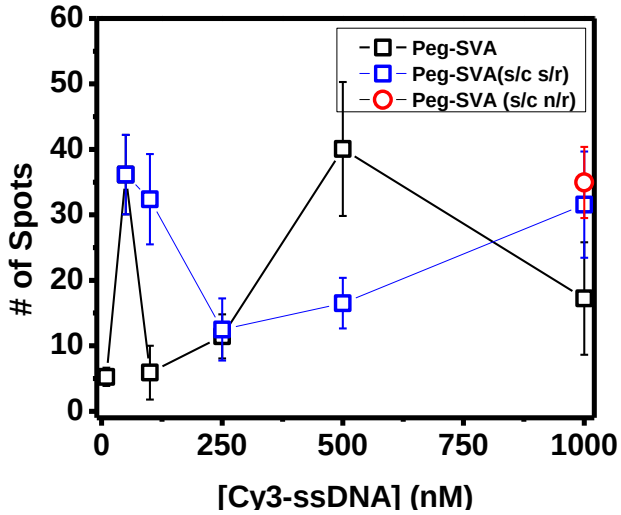

Figure 4.8. Comparison of PEG-SVA Surfaces Performance When Using Different Coverslips vs Using the Same Coverslip. Peg-SVA surfaces performance when using different coverslips (d/c) each time (black squares) compared to using the same coverslip (s/c) and same region (s/r) (blue squares). Red circle corresponds to a new (unbleached) region of the same coverslip.

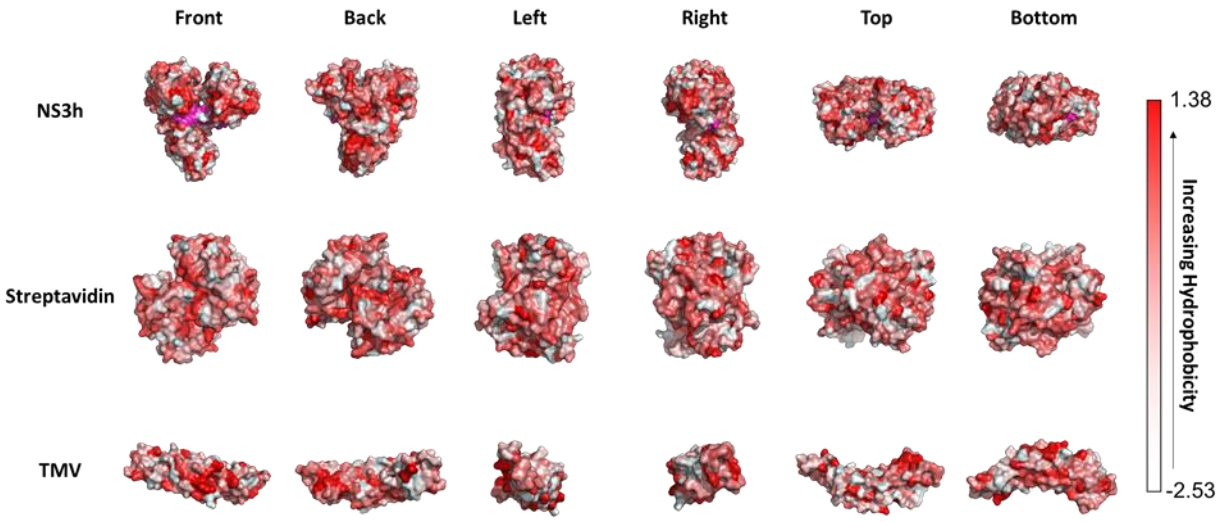

Figure 4.9. Hydrophobic Surface Analysis of NS3h, Streptavidin and TMV proteins. Several views of crystal structures obtained from the protein databank (PDB) of NS3h (PDB code 1A1V)[38], Streptavidin (PDB code 1SWB)[39], and TMV proteins (PDB code 1EI7)[40]. Structures were and displayed using pyMOL utilizing the normalized consensus hydrophobicity scale for aminoacids.[35]

4.7.7 Protocols for Protein expression and labeling

4.7.7.1 NS3h Purification and Fluorescent Labeling

HCV NS3h was expressed, purified, and fluorescently labeled as described previously.[41] Briefly, the coding sequence for HCV NS3h (genotype 1a) corresponding to amino acids 167−631 of NS3 was expressed in *Escherichia coli* BL21(DE3) cells with a C-terminal hexa-histidine tag. NS3h was purified from pelleted cells by a two-step nickel, heparin column purification. Purified protein concentrations were determined by absorbance at 280 nm on a NanoDrop 2000 (Thermo Scientific) using the calculated extinction coefficient of 48,205 M^{-1} cm^{-1}. For fluorescent labeling, NS3h was incubated with 1 mM TCEP before being buffer exchanged into labeling buffer (50 mM sodium phosphate, pH 7.0). Nine nanomoles of NS3h was reacted with an equimolar amount of Cy5-maleimide for 1 h at room temperature in a reaction volume of 100 µL. After quenching the reaction with 2 mM DTT, any remaining free dye was removed by buffer exchanging the labeled protein into 2× storage buffer (50 mM Tris, pH 7.9, and 200 mM NaCl) using a NAP-5 column (GE Healthcare Life Sciences). NS3h was then concentrated, and glycerol was added to a final concentration of 50% prior to storage at −20 °C. The concentration of dye in the labeled protein

solution was determined by the absorbance at 650 nm using a NanoDrop 2000 (Thermo Scientific) using an extinction coefficient of 250,000 M^{-1} cm^{-1} for Cy5. The labeling efficiency (1.39/1 D/P) was determined by dividing the Cy5 dye concentration by the protein concentration (correcting for the dye absorbance at 280 nm, see equation below) to give Cy5/NS3h.

4.7.7.2 S123C-TMVcp expression and purification

The procedure used for expression and purification of the S123C TMVCP is a modified version of that detailed by Francis et al.[42] Tuner (DE3)pLysS competent cells (Novagen, San Diego, CA) were transformed with the vector, plated on LB-agar and incubated at 37 °C overnight. A colony was removed from the plate and inserted into 50 mL of LB Broth containing 100 µg/mL ampicillin and placed in a shaker (250 rpm, 37°C) overnight. 1 mL of this overnight-grown culture was further grown in 25 mL of LB broth to an optical density (O.D.) of 0.5 at 600 nm. This culture was then entirely added to 1L of Terrific Broth (100 µg/mL ampicillin, 25 µg/mL chloramphenicol) and shaken (250 rpm, 37°C) until the colony scattering signal reached an O.D. of 0.6-0.8. Isopropyl β-D-1-thiogalactopyranoside (IPTG, ≥ 99%, Sigma-Aldrich) was added at this point to a final concentration of 30 µM. Cultures were grown for 24 hours at 30°C, harvested by centrifugation and stored at -80 °C. Cells from a 2 L batch were thawed, resuspended in 200 mL of 20 mM triethanolamine (TEA), 1 mM EDTA, pH 7.2 and lysed by sonicating at a 60% duty cycle at 70% amplitude. The resulting lysate was clarified by ultracentrifugation for 30 minutes at 11,000 rpm. The supernatant was warmed to RT then stirred while adding a saturated ammonium sulfate solution dropwise to a final concentration of 35% (v/v). The precipitate formed was isolated by ultracentrifugation for 30 minutes at 20,000 rpm then resuspended in 40 mL 20 mM TEA, 1 mM EDTA, pH 7. The solution was dialyzed overnight against the same buffer to remove residual ammonium sulfate and then diluted to 1 L in buffer before loading onto a DEAE Sepharose weak anion exchange column (GE Healthcare Life Sciences, Piscataway, NJ). The coat protein was eluted using a 0-300 mM NaCl in TEA gradient. Purity was confirmed by SDS-PAGE. 1 mM dithiothreitol (DTT) was added to the suspension and dialysis TEA buffers to prevent cysteine thiol oxidation.

4.7.7.3 Sulfo-Cy3 maleimide conjugation to S123C-TMVcp

S123C-TMVcp was dialyzed to pH 7.0 using $H_2PO_4^-$/$HPO4_4^{2-}$ phosphate buffer (IS 100 mM) and was then degassed under nitrogen for 30 minutes. Then, 100 molar excess of tris(2-chloroethyl) phosphate (TCEP) was added to prevent the oxidation of free thiols into di-sulfide bonds. The sample was then degassed for additional 30 minutes. Then 10 molar excess of the Sulfo-Cy3-maleimide (GE Healthcare) prepared in anhydrous DMF solution was added to a final % v/v of 5 to 10%. At pH 7, TMVcp assembles primarily into disks which makes the cysteines at the 123rd position well-accessible by the dye.[43] The reaction was then set to proceed at room temperature while thoroughly shaking it every two hours for at least 4 hours. The TMVcp conjugate was then stored in the dark at 2 to 8 °C overnight. Excess dye was removed using Zeba™ Spin size exclusion desalting columns, 7K MWCO, 0.5 mL (Thermo Fischer) followed by dialysis to a final pH of 8.2 against 50 mM phosphate buffer using Dry Spectra/Por® dialysis tubing (Standard regenerated cellulose membrane, SPECTRUM) of a nominal MWCO of 13 KDa to ensure a rigorous purification. At pH 8.2, TMV disassembles into its monomer units (MW 17.508 KDa). LC-ESI-MS was then used to verify the success of the conjugation. The molecular probe labeling efficiency (0.3/1 D/P) was determined from the measured absorbance spectrum of the TMV/Cy3 conjugate after correcting for the dye absorbance at 280 nm using the following relation:

$$\%\left[\frac{cy3}{TMV}\right] = \frac{0.092 \times A_{552}}{[A_{280} - (0.08 \times A_{552})]} \times 100$$

Where: $0.092 = \frac{\varepsilon_{TMV}^{280}{}_{M^{-1}cm^{-1}}}{\varepsilon_{cy3}^{552}{}_{M^{-1}cm^{-1}}}$.

4.8 References:

1. Sigal, Y. M.; Zhou, R.; Zhuang, X., Visualizing and discovering cellular structures with super-resolution microscopy. *Science* **2018,** *361* (6405), 880-887.
2. Joo, C.; Balci, H.; Ishitsuka, Y.; Buranachai, C.; Ha, T., Advances in Single-Molecule Fluorescence Methods for Molecular Biology. *Annual Review of Biochemistry* **2008,** *77* (1), 51-76.
3. Lee, S.-J.; Syed, S.; Enemark, E. J.; Schuck, S.; Stenlund, A.; Ha, T.; Joshua-Tor, L., Dynamic look at DNA unwinding by a replicative helicase. *Proceedings of the National Academy of Sciences of the United States of America* **2014,** *111* (9), E827-E835.
4. Abbondanzieri, E. A.; Bokinsky, G.; Rausch, J. W.; Zhang, J. X.; Le Grice, S. F. J.; Zhuang, X., Dynamic binding orientations direct activity of HIV reverse transcriptase. *Nature* **2008,** *453*, 184.
5. Hariri, A. A.; Hamblin, G. D.; Gidi, Y.; Sleiman, H. F.; Cosa, G., Stepwise growth of surface-grafted DNA nanotubes visualized at the single-molecule level. *Nature Chemistry* **2015,** *7*, 295.
6. Jungmann, R.; Steinhauer, C.; Scheible, M.; Kuzyk, A.; Tinnefeld, P.; Simmel, F. C., Single-Molecule Kinetics and Super-Resolution Microscopy by Fluorescence Imaging of Transient Binding on DNA Origami. *Nano Letters* **2010,** *10* (11), 4756-4761.
7. Albertazzi, L.; van der Zwaag, D.; Leenders, C. M. A.; Fitzner, R.; van der Hofstad, R. W.; Meijer, E. W., Probing Exchange Pathways in One-Dimensional Aggregates with Super-Resolution Microscopy. *Science* **2014,** *344* (6183), 491-495.
8. Zhou, X.; Andoy, N. M.; Liu, G.; Choudhary, E.; Han, K.-S.; Shen, H.; Chen, P., Quantitative super-resolution imaging uncovers reactivity patterns on single nanocatalysts. *Nature Nanotechnology* **2012,** *7*, 237.
9. Nirmal, M.; Dabbousi, B. O.; Bawendi, M. G.; Macklin, J. J.; Trautman, J. K.; Harris, T. D.; Brus, L. E., Fluorescence intermittency in single cadmium selenide nanocrystals. *Nature* **1996,** *383*, 802.
10. Empedocles, S. A.; Norris, D. J.; Bawendi, M. G., Photoluminescence Spectroscopy of Single CdSe Nanocrystallite Quantum Dots. *Physical Review Letters* **1996,** *77* (18), 3873-3876.
11. Acuna, G. P.; Möller, F. M.; Holzmeister, P.; Beater, S.; Lalkens, B.; Tinnefeld, P., Fluorescence Enhancement at Docking Sites of DNA-Directed Self-Assembled Nanoantennas. *Science* **2012,** *338* (6106), 506-510.
12. Ha, T., Single-Molecule Fluorescence Resonance Energy Transfer. *Methods* **2001,** *25* (1), 78-86.
13. Visnapuu, M.-L.; Duzdevich, D.; Greene, E. C., The importance of surfaces in single-molecule bioscience. *Molecular BioSystems* **2008,** *4* (5), 394-403.
14. Rasnik, I.; Myong, S.; Cheng, W.; Lohman, T. M.; Ha, T., DNA-binding Orientation and Domain Conformation of the E. coli Rep Helicase Monomer Bound to a Partial Duplex Junction: Single-molecule Studies of Fluorescently Labeled Enzymes. *Journal of Molecular Biology* **2004,** *336* (2), 395-408.
15. Ha, T.; Rasnik, I.; Cheng, W.; Babcock, H. P.; Gauss, G. H.; Lohman, T. M.; Chu, S., Initiation and re-initiation of DNA unwinding by the Escherichia coli Rep helicase. *Nature* **2002,** *419* (6907), 638-641.

16. Roy, R.; Hohng, S.; Ha, T., A practical guide to single-molecule FRET. *Nat Meth* **2008,** *5* (6), 507-516.
17. Jeyachandran, Y. L.; Mielczarski, J. A.; Mielczarski, E.; Rai, B., Efficiency of blocking of non-specific interaction of different proteins by BSA adsorbed on hydrophobic and hydrophilic surfaces. *Journal of Colloid and Interface Science* **2010,** *341* (1), 136-142.
18. Jameson, L. P.; Smith, N. W.; Annunziata, O.; Dzyuba, S. V., Interaction of BODIPY dyes with bovine serum albumin: a case study on the aggregation of a click-BODIPY dye. *Physical Chemistry Chemical Physics* **2016,** *18* (21), 14182-14185.
19. Chandradoss, S. D.; Haagsma, A. C.; Lee, Y. K.; Hwang, J.-H.; Nam, J.-M.; Joo, C., Surface Passivation for Single-molecule Protein Studies. *J. Vis. Exp.* **2014,** (86), e50549.
20. Zhang, Z.; Park, S. R.; Pertsinidis, A.; Revyakin, A., Cloud-point PEG Glass Surfaces for Imaging of Immobilized Single Molecules by Total-internal-reflection Microscopy. *Bio-protocol* **2016,** *6* (7).
21. Revyakin, A.; Zhang, Z.; Coleman, R. A.; Li, Y.; Inouye, C.; Lucas, J. K.; Park, S.-R.; Chu, S.; Tjian, R., Transcription initiation by human RNA polymerase II visualized at single-molecule resolution. *Genes & Development* **2012,** *26* (15), 1691-1702.
22. Hai, P.; Yifan, X.; Meng, Q.; Yi, C.; Wei, W., A simple procedure to improve the surface passivation for single molecule fluorescence studies. *Physical Biology* **2015,** *12* (4), 045006.
23. Hua, B.; Han, K. Y.; Zhou, R.; Kim, H.; Shi, X.; Abeysirigunawardena, S. C.; Jain, A.; Singh, D.; Aggarwal, V.; Woodson, S. A.; Ha, T., An improved surface passivation method for single-molecule studies. *Nat Meth* **2014,** *11* (12), 1233-1236.
24. Cai, H.; Depoil, D.; Palma, M.; Sheetz, M. P.; Dustin, M. L.; Wind, S. J., Bifunctional nanoarrays for probing the immune response at the single-molecule level. *Journal of Vacuum Science & Technology B, Nanotechnology and Microelectronics: Materials, Processing, Measurement, and Phenomena* **2013,** *31* (6), 06F902.
25. Cai, H.; Wolfenson, H.; Depoil, D.; Dustin, M. L.; Sheetz, M. P.; Wind, S. J., Molecular Occupancy of Nanodot Arrays. *ACS Nano* **2016,** *10* (4), 4173-4183.
26. Schvartzman, M.; Palma, M.; Sable, J.; Abramson, J.; Hu, X.; Sheetz, M. P.; Wind, S. J., Nanolithographic Control of the Spatial Organization of Cellular Adhesion Receptors at the Single-Molecule Level. *Nano Letters* **2011,** *11* (3), 1306-1312.
27. Palma, M.; Abramson, J. J.; Gorodetsky, A. A.; Penzo, E.; Gonzalez, R. L.; Sheetz, M. P.; Nuckolls, C.; Hone, J.; Wind, S. J., Selective Biomolecular Nanoarrays for Parallel Single-Molecule Investigations. *Journal of the American Chemical Society* **2011,** *133* (20), 7656-7659.
28. Blümmel, J.; Perschmann, N.; Aydin, D.; Drinjakovic, J.; Surrey, T.; Lopez-Garcia, M.; Kessler, H.; Spatz, J. P., Protein repellent properties of covalently attached PEG coatings on nanostructured SiO2-based interfaces. *Biomaterials* **2007,** *28* (32), 4739-4747.
29. Chai, J.; Wong, L. S.; Giam, L.; Mirkin, C. A., Single-molecule protein arrays enabled by scanning probe block copolymer lithography. *Proceedings of the National Academy of Sciences* **2011,** *108* (49), 19521-19525.
30. Palma, M.; Abramson, J. J.; Gorodetsky, A. A.; Nuckolls, C.; Sheetz, M. P.; Wind, S. J.; Hone, J., Controlled Confinement of DNA at the Nanoscale: Nanofabrication and Surface Bio-Functionalization. In *DNA Nanotechnology: Methods and Protocols*, Zuccheri, G.; Samorì, B., Eds. Humana Press: Totowa, NJ, 2011; pp 169-185.

31. Cai, H.; Wind, S. J., Improved Glass Surface Passivation for Single-Molecule Nanoarrays. *Langmuir* **2016,** *32* (39), 10034-10041.
32. Grubb, W. T., A Rate Study of the Silanol Condensation Reaction at 25° in Alcoholic Solvents1. *Journal of the American Chemical Society* **1954,** *76* (13), 3408-3414.
33. Pike, R. G.; Hubbard, D., Physicochemical studies of the destructive alkali-aggregate reaction in concrete. *J. RES. NATL. BUR. STAN. Journal of Research of the National Bureau of Standards* **1957,** *59* (2), 127.
34. Heyes, C. D.; Kobitski, A. Y.; Amirgoulova, E. V.; Nienhaus, G. U., Biocompatible Surfaces for Specific Tethering of Individual Protein Molecules. *The Journal of Physical Chemistry B* **2004,** *108* (35), 13387-13394.
35. Eisenberg, D.; Schwarz, E.; Komaromy, M.; Wall, R., Analysis of membrane and surface protein sequences with the hydrophobic moment plot. *Journal of Molecular Biology* **1984,** *179* (1), 125-142.
36. Zaitlin, M. H. W. I., Tobacco mosaic virus (type strain). *CMI/AAB Description of Plant Viruses,* **1975,** *151*.
37. Gasteiger, E.; Hoogland, C.; Gattiker, A.; Duvaud, S. e.; Wilkins, M. R.; Appel, R. D.; Bairoch, A., Protein Identification and Analysis Tools on the ExPASy Server. In *The Proteomics Protocols Handbook*, Walker, J. M., Ed. Humana Press: Totowa, NJ, 2005; pp 571-607.
38. Kim, J. L.; Morgenstern, K. A.; Griffith, J. P.; Dwyer, M. D.; Thomson, J. A.; Murcko, M. A.; Lin, C.; Caron, P. R., Hepatitis C virus NS3 RNA helicase domain with a bound oligonucleotide: the crystal structure provides insights into the mode of unwinding. *Structure* **1998,** *6* (1), 89-100.
39. Stenkamp, R. E.; Trong, I. L.; Klumb, L.; Stayton, P. S.; Freitag, S., Structural studies of the streptavidin binding loop. *Protein Science* **1997,** *6* (6), 1157-1166.
40. Bhyravbhatla, B.; Watowich, S. J.; Caspar, D. L. D., Refined Atomic Model of the Four-Layer Aggregate of the Tobacco Mosaic Virus Coat Protein at 2.4-Å Resolution. *Biophysical Journal* **1998,** *74* (1), 604-615.
41. Ablenas, C. J.; Liu, H.-W.; Shkriabai, N.; Kvaratskhelia, M.; Cosa, G.; Götte, M., Dynamic Interconversions of HCV Helicase Binding Modes on the Nucleic Acid Substrate. *ACS Infectious Diseases* **2017,** *3* (1), 99-109.
42. Dedeo, M. T.; Duderstadt, K. E.; Berger, J. M.; Francis, M. B., Nanoscale Protein Assemblies from a Circular Permutant of the Tobacco Mosaic Virus. *Nano Letters* **2010,** *10* (1), 181-186.
43. Klug, A., The tobacco mosaic virus particle: structure and assembly. *Philosophical Transactions of the Royal Society of London. Series B: Biological Sciences* **1999,** *354* (1383), 531-535.

5 Binding and Sliding Dynamics Preceding *de novo* RNA Replication by the Hepatitis C Virus Polymerase: Hunting the 3'

Gidi, Y.; Robert, A.; Tordo, A.; Götte, M.; Cosa, G., *Manuscript in preparation*

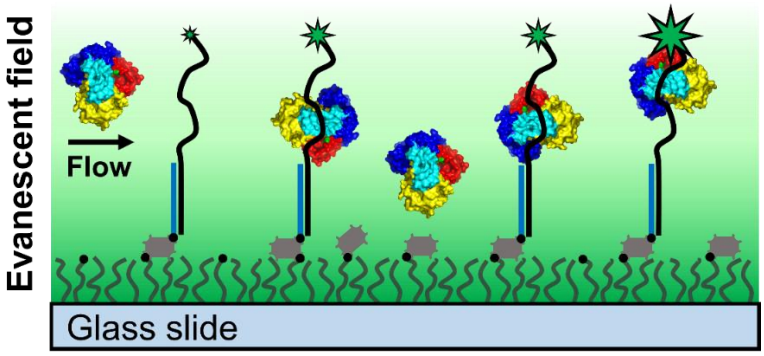

5.1 Preface

In **chapter 1** we described the power of single molecule fluorescence techniques to study heterogeneous and unsynchronized systems, revealing unique information otherwise hidden in long-established ensemble measurements. In particular, we highlighted the importance of SMF techniques to study protein-oligonucleotide interactions. In **chapter 5** we utilize a single molecule assay to study relevant biomolecular mechanisms related to the replication machinery of the Hepatitis C virus (HCV). Specifically, we develop an smPIFE assay to study the non-structural 5B polymerase of HCV, which has the ability to initiate synthesis *de novo* through a primer independent mechanism. Here, we report studies on NS5B binding, sliding, and searching for the 3' of its single stranded RNA substrate. Our studies are centered on the dynamic processes allowing this protein to locate the 3'-terminus of the RNA template. Application of this technique has expanded our understanding of key mechanistic aspects of NS5B-RNA complexes preceding *de novo* initiation, including RNA binding/unbinding and sliding. This methodology has allowed us to also study the effect of a divalent ion such as Mg^{2+} on the stability and dynamics of NS5B and its RNA substrate.

5.2 Abstract

The hepatitis C virus (HCV) non-structural protein 5B (NS5B) polymerase catalyses the conversion of the (+) single-stranded RNA genome of HCV into double-stranded RNA. In vitro studies have shown that this task can be performed through both a primer-dependent and a remarkable primer-independent mechanism. However, the general dynamics and the mechanism by which this enzyme locates the 3′-terminus of the RNA template to initiate synthesis *de novo* remains elusive. Here we performed single molecule fluorescence studies based on protein induced fluorescence enhancement (PIFE), that report on NS5B binding, sliding and search for the 3' of its ssRNA substrate. Our results suggest that, NS5B can exist in a fully open conformation in solution. Additionally, dwell time analysis of single molecule fluorescence trajectories is consistent with two binding modes for NS5B, an unstable one resulting in rapid dissociation, and a stable one characterized by a longer residence time on the substrate. We associate these bindings to an unproductive and a productive orientation respectively. Addition of divalent Mg^{2+} cations increases the mobility of NS5B along its RNA substrate while simultaneously decreasing its residence time to a few seconds, leading to binary PIFE trajectories showing multiple on (bound) and off (unbound) segments. Therefore, presumably several attempts are necessary before NS5B form a productive complex to initiate the synthesis of the complementary strand. The presence of NTPs and GpG primer have minor effects on NS5B-RNA dynamics.

5.3 Introduction

Viruses within the *Flaviviridae* family, including West Nile (WNV), Dengue (DENV), Zika (ZIKV), Yellow Fever (YFV), Japanese Encephalitis (JEV), Bovine Viral Diarrhea (BVDV), and Hepatis C (HCV), represent a major health threat and economic challenge. Accordingly, there is considerable ongoing activity to develop antiviral drugs for these viruses. Polymerases constitute an important target to inhibit viral replication since not only they play a key role in the viral replication cycle, but also show a high degree of conservation within the *Flaviviridae* family.[1]

HCV and its non-structural protein 5B (NS5B) polymerase provide an ideal model to study the *Flaviviridae* family of viruses. HCV exemplifies one of the major successes of modern medicine in the treatment of viral diseases, with recently developed drugs achieving over 95% success rates

in treatment.[2] Among these new drugs, Sofosbuvir,[3] a clinically approved direct-acting antiviral (DAA) in the form of a nucleotide analogue inhibitor targeting the active site of NS5B, has been recently reported to also inhibit ZIKV[4] and DENV[5] replication. As such, the working mechanism of NS5B can be used as an archetype to study the replication of newly emerging viruses within the *Flaviviridae* family.

NS5B, an RNA-dependent RNA-polymerase (RdRp), resembles a right hand containing finger, palm, and thumb subdomains, similar to other polymerases (**Figure 5.1b**).[6-8] It was initially shown that, due to extensive interactions between the fingers and thumb subdomains, NS5B can fully encircle the active site. This "closed" conformation would require NS5B to thread over the RNA strand to localize the active site. Subsequent studies showed that NS5B can be crystalized in two different states, revealing a structure with a more open conformation.[9] In ensuing studies, it was shown that NS5B can initiate *de novo* synthesis on circularized RNA templates, suggesting that NS5B can undergo transitions to a fully "open" conformation before template recognition.[10] The catalytic activity of NS5B is mediated by two metal ions (either Mg^{2+} or Mn^{2+}) in the active site. These metal ions are bound to two conserved aspartic acid residues in the catalytic site of NS5B and are essential for the nucleotidyl transfer reaction through the "two-metal-ion" mechanism.[11] Both Mg^{2+} and Mn^{2+} can support RNA synthesis, however, it has been shown that RNA synthesis is increased by 4-20 fold in the presence of Mn^{2+},[12-13] Furthermore, Mn^{2+} is preferred for *de novo* initiation.[14-15]

Remarkably, NS5B has the ability of initiating synthesis *de novo* through a primer-independent mechanism (**Figure 5.1a**).[13, 15-17] Notably, this function is shared by other polymerases of the *Flaviviridae* family such as DENV,[18] BVDV,[19] and ZIKV.[20] How these enzymes locate the 3′-terminus of the RNA template, however, remains an unsolved question. Previous reports have shown that *de novo* synthesis is favoured under certain conditions. After NS5B locates the 3' target, *de novo* RNA synthesis is initiated with the positioning of a single nucleotide, complementary to the nucleotide in the 3' position of the template. Initiation from pyrimidine bases shows much higher activity than from purine bases (with C being more active than U).[13, 15, 17, 21-22] Furthermore, several studies have shown that high concentrations of the initiating nucleotide, GTP or ATP, are required to allow *de novo* initiation.[13-15, 19, 22] More recently, it has been shown that high concentrations of NTPs corresponding to the first three incorporated

nucleotides are needed for efficient *de novo* RNA synthesis.[23] On a possible related note, NS5B has been observed to have a surface binding site specific for GTP lying at about 30 Å from the catalytic site, next to the region of interaction between fingertips and thumb.[24]

While the precise mechanism of *de novo* initiation remains unknown, the presence of the first di- and tri-nucleotides has been suggested to play a key role. The first reaction product during *de novo* initiation is a dinucleotide which can dissociate from the polymerase/template complex in a process known as abortive initiation,[21] leading to an accumulation of di- and tri-nucleotides that can be used in a next round by NS5B to efficiently initiate RNA replication.[25] Furthermore, exogenously added di- or tri-nucleotides can abolish the need for high concentration of the initiating nucleotides.[23]

Although rich structural information about NS5B and the interaction with its RNA substrate is available, [6-9, 26-27] the intrinsic dynamic interaction of NS5B/RNA and the effect of divalent metal ions (Mg^{2+} or Mn^{2+}), and NTPs, remains poorly understood, hampering a better mechanistic understanding of NS5B polymerization. Here, we developed and applied a single molecule protein induced fluorescence enhancement (smPIFE)[28-30] assay to study the binding and sliding dynamics of NS5B polymerase on a single-stranded RNA (ssRNA) substrate. Single molecule fluorescence techniques provide unique spatiotemporal resolution and allow for the study of heterogeneous and unsynchronized events.[31] We explored the effect of Mg^{2+}, NTPs, and GpG primer on the protein-ssRNA interaction dynamics. Our studies suggest that NS5B can transiently bind RNA in two orientations, characterized by short (fraction of a second) vs permanent (within our observation window) binding under monovalent ions. PIFE data indicates that NS5B does not bind preferentially to the 3′-terminus of an ssRNA but rather randomly. Taken together, our findings suggest that NS5B exists in an open conformation before template recognition. Single molecule intensity time profiles additionally show that NS5B affinity for and dynamic activity with ssRNA is modulated by the presence of magnesium ions. Thus, Mg^{2+} dramatically decreased the affinity of NS5B to its ssRNA substrate, and simultaneously, Mg^{2+} enhanced the rate at which NS5B scans its ssRNA template. We posit then that Mg^{2+} may assist NS5B towards the efficient localization of its 3’ terminus target. Surprisingly, the presence of NTPs showed a limited effect on the dynamics of NS5B-RNA.

Overall, our work not only unravels new insights on the working mechanism of NS5B, but additionally provides new associated methods for the rapid screening of potential antiviral drugs toward viral polymerases relying on synthesis *de novo*.

5.4 Results and Discussion

5.4.1 Single-molecule PIFE assay interrogates the dynamic interaction of NS5B–ssRNA

In order to better understand how NS5B interacts with its ssRNA substrate, we designed a single molecule assay to localize the relative position of NS5B with respect to the 3' terminus of an ssRNA by using smPIFE,[28-29] a methodology that is well suited to probing dynamic interactions between proteins and nucleic acids.[32] A Cy3 fluorophore was specifically attached to the 3' end of an ssRNA to serve as PIFE reporter (**Fig. 5.5**). Given that NS5B can accommodate 7-8 bases of nucleic acid within its template-binding cleft,[33] we utilized a Cy3-tagged 38-nucleotide (nt) RNA strand. This strand is attached to the surface *via* hybridization to an 18-nt DNA strand bearing a biotin moiety at the 3' position, leaving a 20-base overhang (**See Figure 5.1c and Fig. 5.5**). This length enables examining simultaneously on the binding and sliding of NS5B, where we note that the conjugation to the 3' end of the RNA does not inhibit NS5B synthesis *de novo*.[34] DNA/RNA duplexes were surface-immobilized *via* biotin-streptavidin interactions in previously passivated glass surfaces (**Fig. 5.1d**).[35] DNA/RNA duplexes were initially immersed in a microchamber containing a buffer solution and a photostabilizing cocktail (**See material and methods, section 5.5.1**). Next, an identical solution, however, now including the wild type NS5B was flowed into the chamber.

The fluorescence of individual surface immobilized substrates was monitored using total internal reflection fluorescence (TIRF) microscopy upon 561 nm laser excitation. Using this method, we observed the binding and sliding of freely diffusing NS5B in real time, reported in the form of a sudden increase and gradual changes, respectively, in the fluorescence signal intensity collected from Cy3 (**Fig. 5.1e**). Here, as the protein approaches the 3' end, the fluorescence of Cy3 increases. The fluorescence enhancement then provided information on the binding and sliding of NS5B as well as its proximity to the 3' end. The sudden drop in the fluorescence signal to background levels signaled photobleaching of the Cy3 fluorophore. The observed normalized fluorescence value

(PIFE value) thus allowed us to monitor changes in the enzyme position relative to the 3' of the ssRNA overhang.

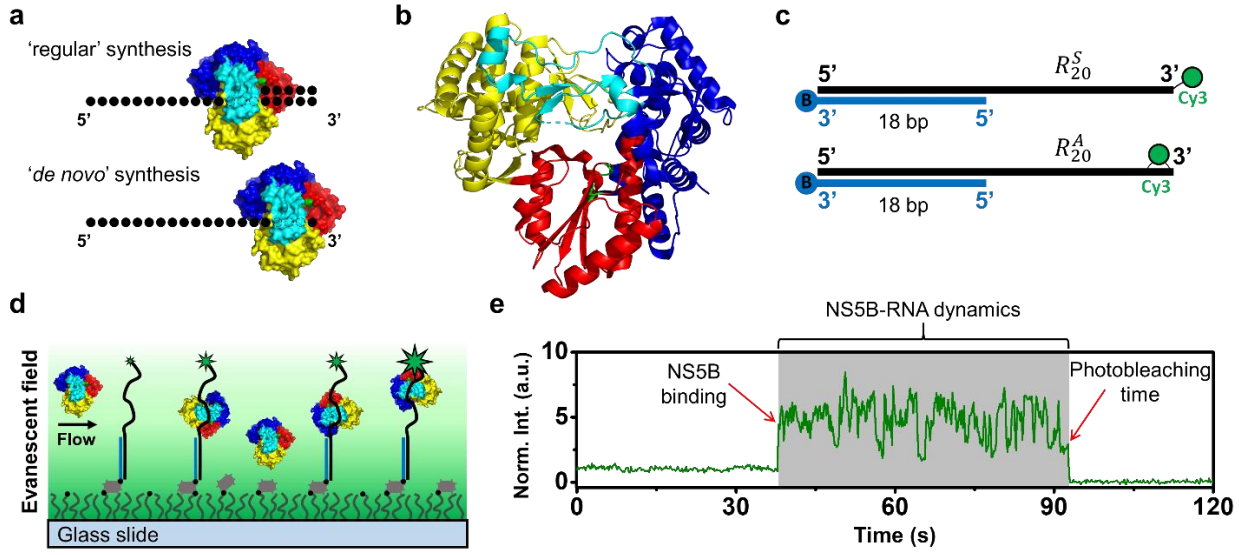

Figure 5.1. smPIFE assay reporting on the proximity of NS5B to the 3' end of a ssRNA. (a) Regular (primer dependent) RNA synthesis *vs de novo* (primer independent) RNA synthesis. (b) Crystal structure of HCV NS5B polymerase from genotype 1b (isolate Con1) (PDB: 3FQL)[26] highlighting the palm (red), fingers (blue), and thumb (yellow) subdomains. Two loops interconnecting the finger and palm subdomains are shown in cyan and the two metal binding aspartate residues are shown in green to highlight the catalytic site.[6] (c) DNA/RNA duplexes utilized in this study. 18 base-pair DNA:RNA hybrid duplex region with 3' RNA overhang, DNA and RNA strands are represented in blue and black, respectively, with biotin conjugation represented as B. RNA templates used in our studies are simplified as (R_n^X), where n denotes the length of the 3' overhang and x specifies the dye functionalization strategy (A for amidite and S for succinimide); the Cy3 position is displayed as a stem when a succinimide-C6 linker is used and as a hook when an internal Cy3 amidite is employed. (d) Schematic illustration of the smPIFE assay in an evanescent excitation field. Cy3 labeled DNA/RNA duplexes as shown in (c) were surface immobilized on a glass slide *via* biotin-streptavidin interactions (the size of the stars indicates the relative fluorescence of Cy3 depending on NS5B proximity). (e) Normalized fluorescence-time trajectory highlighting NS5B binding, NS5B-RNA dynamics, and Cy3 photobleaching.

In order to calibrate smPIFE in terms of the intensity enhancement dynamic range, we conducted a series of bulk and single molecule studies with two different constructs, (**Figure 5.1c**).[34] RNA templates used in our studies (R_n^X), thus were prepared bearing two different functionalization strategies, amidite (R_n^A) and succinimide (R_n^S) where n denotes the length of the 3' overhang. We have previously shown that R_{20}^S and R_{20}^A templates possess different fluorescence emission quantum yields (Φ_f) (0.09 and 0.15, respectively), therefore, different enhancements were expected upon NS5B binding.[36] By comparing the Φ_f of free Cy3 in water (0.04), and in glycerol (0.43, where photoisomerization is completely supressed (**See section 5.5.3**)) and the Φ_f of Cy3 bound to RNA in R_{20}^S and R_{20}^A, we established that the maximum enhancement of free Cy3 under optimal conditions is 10-fold. However, due to the initial higher Φ_f of Cy3 when tagged to the RNA templates utilized herein, we expected maximum enhancements of 2.9- and 4.8-fold for R_{20}^A and R_{20}^S, respectively. We additionally calibrated Cy3 enhancement in the presence of the divalent cation Mg^{2+}, previously reported to increase the Φ_f of Cy3 when attached to oligonucleotides.[37] Single molecule as well as ensemble measurements show that Mg^{2+} increased the Φ_f of Cy3 by 1.7- and 1.4-fold for R_{20}^A and R_{20}^S , respectively (**see section 5.5.3**). As such, the expected maximum Φ_f enhancements of Cy3 for R_{20}^A and R_{20}^S were 1.6- and 3.3-fold, respectively, in the presence of Mg^{2+}. Accordingly, we chose to work with R_{20}^S as it provided the largest dynamic range, where the difference of 4.8-fold vs 3.3-in Cy3 maximum enhancements expected in the absence and presence of Mg^{2+} should be considered in comparing smPIFE results with NS5B.

We first examined the binding of NS5B to the 20 base ssRNA overhang in the DNA/RNA duplex construct (R_{20}^S) in the absence of Mg^{2+} ions (Hepes 10 mM, 20 mM NaCl, pH 7.3). When NS5B was added to the microchamber, we observed that in some cases NS5B transiently interacted with R_{20}^S before becoming permanently bound (until dye photobleaching was recorded) (**Figure 5.2a**). The short interaction is evidenced by brief spikes in the fluorescence intensity. We hypothesize that the positively charged binding site of NS5B can accommodate a negatively charged ssRNA in two possible orientations (**Figure 5.2c**), the one necessary for productive RNA transcription and a second unstable binding mode where the protein is flipped 180 degrees over the template. Here, and due to the specificity of the contact groups of NS5B and RNA, we propose that only one orientation will result in stable binding. Under this assumption, the probability distribution (P_n) of the number of unstable bindings (n) recorded in a given trajectory before a stable binding occurs

can be expressed as $P_n = P_s \times (P_u)^n$, where P_s and P_u are the probabilities of stable and unstable binding, respectively. On the basis of a collision encounter, probabilities may *a priori* be assumed equal, i.e., 0.5. A histogram showing the expected probability P_n *vs* the number of unstable bindings (n) before NS5B forms a permanent complex with R_{20}^S (**Figure 5.2b, red histogram**) is consistent with the experimentally observed probability distribution (**Figure 5.2b, grey histogram**), supporting the hypothesis of two contact modes leading to binding (stable and unstable).

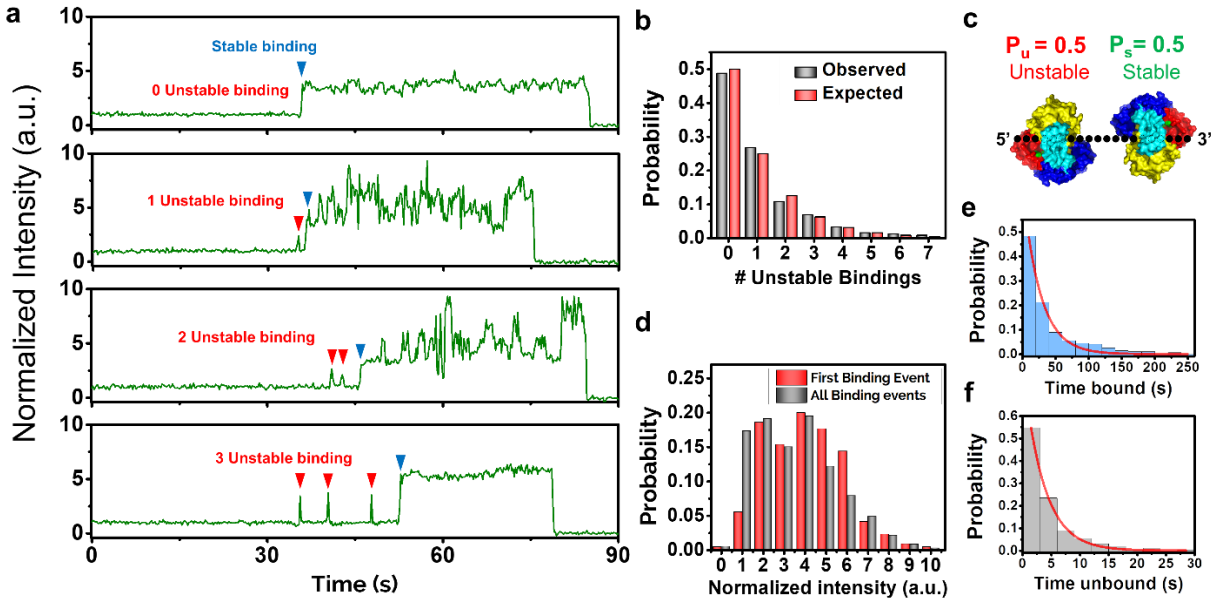

Figure 5.2. NS5B binding dynamics in the absence of Mg^{2+} ions. (a) Single molecule fluorescence trajectories showing zero, one, two, and three unstable bindings before NS5B stably binds to a ssRNA strand. (b) Observed (grey) and expected (red) probability of the number of unstable binding events, before NS5B can stably binds to an ssRNA strand. The expected probability has been calculated assuming an equal probability of unstable and stable binding, P_u = 0.5 and P_s = 0.5, respectively. (c) Schematic representation of a stable and unstable binding of ssRNA by NS5B. (d) Histograms showing the distribution of the initial stable binding enhancement (red) *vs* the distribution of enhancements recorded for bound protein (grey). (e) Probability distribution of the bound times (t_b) showing a mono-exponential fitting to yield average bound time (τ_b). (f) Probability distribution of the unbound times (t_u) and its mono-exponential fitting to yield average unbound time (τ_u).

While polymerases are expected to rapidly diffuse along the backbone to find their target, under our experimental conditions with no Mg^{2+} and no NTPs, the sliding dynamics of NS5B were found to be slower than reported at >300 nt/s.[38] This is evidenced by slow changes in the PIFE signal that can be monitored within the time resolution (200 ms) of our smPIFE imaging experiments (**Figure 5.2a**).

In order to test if NS5B initially binds preferentially to the 3' terminus, we computed the distribution of enhancements immediately after stable protein binding. A broad distribution of enhancements was found as shown in **Figure 5.2d** (red histogram), consistent with binding at random positions along the ssRNA. This finding implies that NS5B must be in a fully opened conformation - rather than threading through the 3' end - before binding the ssRNA backbone. While we had hypothesized that once bound, NS5B can slide along the RNA backbone to find the 3', our results further showed that the distribution of NS5B is rather random, resulting in a range of PIFE values over time. Thus, upon comparing the distribution of enhancements recorded for bound protein (**Figure 5.2d, grey histogram**) with the histogram constructed solely from the enhancement value upon initial binding, we found both distributions to be similar. This suggests that under these experimental conditions NS5B can slide but cannot recognize the 3'terminus. Moreover, consistent with our previous report,[34] in the absence of Mg^{2+} ions, NS5B was observed to bind tightly (permanent binding) to its ssRNA substrate (**Figure 5.2a**). As such, kinetic information on average bound time (τ_b) under these conditions was limited by the photobleaching of the dye ($\tau_b \geq 26\ s$) (**Figure 5.2e and Table 5.1**). Here the dwell time between unstable bindings further allowed us to estimate the average unbound time (τ_u) under the protein experimental conditions we worked at ($\tau_u = 3.6\ s$) (**Figure 5.2f and Table 5.1**).

5.4.2 Mg^{2+} ions decrease the affinity while increasing the dynamism of NS5B and its RNA substrate

We subsequently studied the role that Mg^{2+} (5mM), necessary for the catalytic activity of NS5B, plays in modulating the affinity and dynamics of NS5B with regards to its RNA substrate. Upon addition of Mg^{2+}, the dissociation rate constant of the NS5B-RNA complex increased. Here, NS5B underwent repeated binding and unbinding events (**Figure 5.3a**). We studied the kinetics of the binding/unbinding process and found that the probability distribution of dwell times for the enzyme bound to its RNA substrate is better adjusted by a biexponential function. We have plotted

the cumulative distribution function as it allows to better separate the two contributions (**see Figure 5.3b and section 5.5.4**). Two average bound times (τ_b) were found, ($\tau_b^1 = 0.43$ s) and ($\tau_b^2 = 5.29$ s), with fractional contributions $f_1 = 0.54$ and $f_2 = 0.46$, respectively, suggesting, as also shown in the absence of Mg^{2+}, two modes of binding with equal probability but different stability. While the short component τ_b^1 remains unaffected when compared with solutions containing no Mg^{2+}, the long component τ_b^2 is largely shortened. When analyzing the unbound dwell times, the probability distribution is well adjusted by a monoexponential decay (**Figure 5.3c**). In the presence of 5 mM Mg^{2+} the average unbound time was ~3-fold larger than the one we recorded in the absence of Mg^{2+} ($\tau_u = 11.3\ s$) under otherwise identical conditions. The increase in τ_u can be attributed to a Mg^{2+}-induced compaction of the ssRNA strand that can inhibit proper ssRNA-NS5B contact.[39]

Notably, we found that for the longer binding events, the fluorescence enhancement (~3.3-fold) is unchanged during each binding event. Furthermore, the same enhancement is found for most of the binding events (**Figure 5.3a**). This is underscored in the sharper intensity enhancement distribution with NS5B when compared to the distribution encountered in the absence of Mg^{2+}, see **Figure 5.3d**. We interpret this observation as arising from a rapid sliding of NS5B along the backbone, beyond our time resolution. In this regime, single molecule trajectories would only show average enhancements on the Cy3 signal. In order to better understand the short *vs* long binding events, we have plotted separately the average enhancement per event for the short ($t_b < 1$ s) and long ($t_b \geq 1$ s) binding events (**Figure 5.3e**). The histogram of average intensity enhancements for the long binding events is centered around a sharp peak at ~3.3. On the other hand, the short binding events resulted in a broad distribution. The latter is consistent with NS5B binding at a random position and being unable to slide due to binding in an unstable orientation.

We note that the average enhancement of 3.3-fold found in the presence of Mg^{2+} corresponds to the maximum enhancement expected from our calibration experiments. This may, at first sight, seemingly contradict our interpretation of the data as a 3.3-fold enhancement would implicate a protein very close to the 3' end. However, some of the short binding events show enhancements larger than expected of up to 7-fold, pointing towards a Cy3 with a higher dynamic range than the expected from our calibration. This deviation from expected values is currently under investigation and two hypotheses are to be tested. First, the 561 nm laser beam, utilized in the current work,

excites the red edge of Cy3 absorption spectrum. Here a protein induced spectral red shift would increase the excitation rate of Cy3, effectively contributing with a second component (enhanced absorption, in addition to reduced isomerization) to the fluorescence enhancement. Preliminary results show that under the same experimental conditions, when a 532 nm laser beam is utilized, the PIFE recorded upon NS5B biding in the presence of Mg^{2+} is ~1.5-fold instead of 3.3-fold. A second hypothesis points toward a Cy3 with a fluorescence quantum yield higher than the one measured in glycerol. Cy3B, the locked analog of Cy3, has been reported to have a fluorescence quantum yield of 0.67,[40] higher than the 0.43 measured for Cy3 in glycerol.

The increased dissociation rate constant with Mg^{2+}, when compared to the permanent binding in the absence of Mg^{2+} ions, suggests that NSB5 can not support efficient *de novo* replication by itself *in vivo* as it would require multiple trials before it can firmly bind to the 3' of its RNA substrate. This implies that, for efficient *de novo* replication *in vivo*, NS5B may need other proteins to prevent RNA from escaping the replication complex. It has been previously reported that NS3 and its cofactor NS4A,[41] as well as NS5A[42] can form complexes with NS5B. Moreover, NS3[43] and NS5A[44-46] exhibit RNA binding activity, suggesting that they may play a role in stabilizing the NS5B-RNA complex.

Table 5.1. Average NS5B bound (τ_b) and unbound (τ_u) times recorded under different experimental conditions. All measurements were taken in solutions containing 10 mM Hepes buffer pH 7.3, and 20 mM NaCl. Additionally, when indicated, Mg^{2+} (5 mM), NTPs (20 μM UTP, 20 μM GTP, 20 μM CTP, and 400 μM ATP), and GpG primer (20 μM) were added. Errors have been obtained from the mono and bi exponential fitting functions.

Condition	$\tau_b^1\,(s)/\,f_1$	$\tau_b^2\,(s)/\,f_2$	$\tau_b^{av}\,(s)$	$\tau_u\,(s)$
(-) Mg^{2+}	~ 0.2/ ~ 0.5	[a]≥ 26.5 ± 1.7 / ~ 0.5	-	3.6 ± 0.1
(+) Mg^{2+}	0.43 ± 0.02 / 0.54	5.29 ± 0.06 / 0.46	2.4	11.3 ± 0.2
(+) Mg^{2+} (+) NTPs	0.40 ± 0.02 / 0.52	6.01 ± 0.08 / 0.48	3.1	12.3 ± 0.3
(+) Mg^{2+} (+) NTPs (+) GpG	0.48 ± 0.02 / 0.48	6.67 ± 0.05 / 0.52	3.7	7.7 ± 0.1

[a] The reported average lifetime value corresponds to photobleaching. Accordingly, dissociation takes as long or longer than photobleaching for the permanent binding observed.

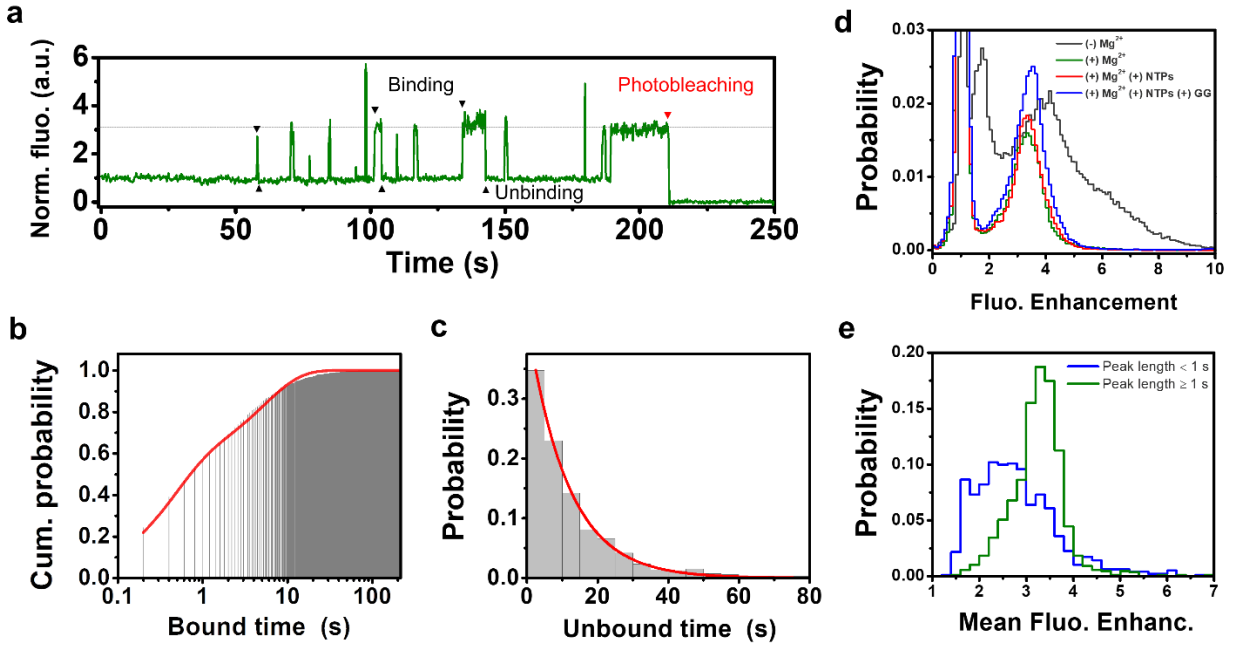

Figure 5.3. Effect of Mg^{2+} ions on the dynamics of NS5B and its RNA substrate. (a) Single molecule fluorescence trajectory showing repeated binding and unbinding events. (b) Cumulative probability distribution of the dwell bound times and its biexponential fitting function (red). (c) Probability distribution of the dwell unbound times and its monoexponential fitting function (red). (d) Histograms showing the distribution of the normalized fluorescence enhancements in the absence of Mg^{2+} (grey), with Mg^{2+} (green), with Mg^{2+} and NTPs with GTP at a higher concentration (red), with Mg^{2+}, NTPs and GpG primer (blue). (e) Histograms showing the distributions of the mean normalized fluorescence enhancements per peak in the presence of 5 mM of Mg^{2+}. Distribution have been separated according to their peak length. Blue and green distributions represent peaks with length times < 1 s and ≥1 s, respectively.

5.4.3 NTPs and GpG primer show minor effects on NS5B-RNA dynamics

In order to fulfill the necessary conditions to allow *de novo* initiation, we next studied the binding dynamics of NS5B and its RNA substrate in the presence of NTPs. Given that a high concentration of the initiating nucleotide (GTP in this case) is required for *de novo* synthesis. [13-15, 19, 22-23] GTP was utilized at a higher concentration (ATP, UTP, and CTP at 20 µM and GTP at 400 µM) in the presence of 5 mM of Mg^{2+}. Under these conditions, primer formation in a major proportion as well as primer extension in a minor extent are expected. Importantly, our smPIFE assay is not able to sensitively report on changes from single to double stranded oligonucleotides as the fluorescence of Cy3 in R_{20}^{S} is only increased by 1.14-fold when the single stranded overhang (20 bp) is hybridized to a fully complementary DNA sequence (**see section 5.5.3-d**). Therefore, the ability of our smPIFE assay to report on primer formation and primer extension will depend on the stability of the newly formed ternary complexes (template/primer/NS5B or template/complementary strand/NS5B, respectively).

We have found that the average bound and unbound times as well as PIFE distributions were not considerably affected when compared to experiments in the absence of NTPs but bearing 5 mM Mg^{2+} (**Table 5.1 and Figure 5.3e**). The modest increase in τ_b and τ_u we recorded is within the error of our measurements. Notably, primer formation followed by a rapid dissociation may be occurring without being detected.

A major difference between single molecule and ensemble regimes lies in the fact that surface-immobilized DNA/RNA duplexes are in extremely low concentrations (~pM). This amount is not enough to quickly build up a pool of primers that can be utilized by NS5B in a second round to undergo primer extension. In order to overcome this intrinsic difference between single molecule and bulk experimental conditions, we added exogenous GpG primers (20 µM). Under these conditions, average bound times were not considerably affected (**Table 5.1 and Figure 5.3e**), however, average unbound times were decreased from 13.3 s to 7.7 s. The cause of this change is currently under investigation.

Different factors may explain our inability to visualize the formation as well as the extension of a primer. It may be that both processes are rare events where many attempts by NS5B are required. In our smPIFE experiments, we are limited by the photobleaching time of the fluorophore (~60 s, pre-binding plus after binding average times). Additionally, visualization of primer formation and

extension is not feasible if the process is followed by a rapid dissociation. Future experiments including Mn^{2+} may reveal more insights on *de novo* synthesis as *de novo* synthesis performs more efficiently in the presence of Mn^{2+} when compared to Mg^{2+}. However, experiments utilizing Mn^{2+} may be very challenging as this divalent metal ion has been associated with Cy3 photobleaching.[47] Carefully optimized concentrations for this cofactor may provide a window to visualize primer extension before Cy3 photobleaching.

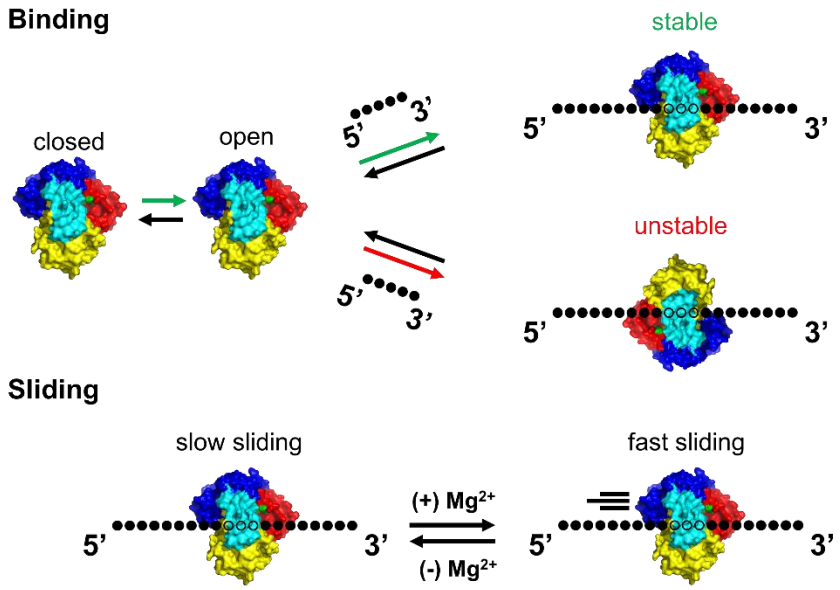

Figure 5.4. Dynamic mechanism of NS5B and RNA. (top) Binding mechanism of NS5B illustrating that an open NS5B in solution is required before binding to an ssRNA. The scheme also shows NS5B binding in two possible directions, an unstable and a stable mode. (bottom) Sliding speed of NS5B depending on the presence of divalent metal ions. While in the absence of Mg^{2+} NS5B can slowly slide (seconds timescale) along a ssRNA strand (bottom, left), in the presence of Mg^{2+}, NS5B can rapidly slide (beyond our detector time resolution, 200 ms) along an ssRNA backbone (bottom, right).

5.5 Conclusions

Herein we have described the dynamics of the early steps of *de novo* RNA synthesis catalyzed by the NS5B polymerase of HCV, including binding, sliding, and attachment to the 3'. We have found that, instead of threading, NS5B binds to the template at random positions, suggesting that, in solution, an open conformation must exist in equilibrium with the closed conformation previously

described by crystallographic studies (**Figure 5.4, top left**), consistent with NS5B activity on circular DNA. We have also found that NS5B can bind to its RNA template in two orientations. While one mode of binding is found to be unstable, the other mode forms a permanent complex in Mg^{2+} free solutions (**Figure 5.4, top right**).

Upon binding, NS5B can slowly slide along the ssRNA template in the absence of Mg^{2+} ions (**Figure 5.4, bottom left**). However, in the presence of Mg^{2+} ions NS5B can rapidly slide along the RNA backbone, beyond the resolution limit of our detector (**Figure 5.4, bottom right**). Addition of NTPs (with GTP in higher concentration) as well as GpG primer, has marginal effects in the dynamics of NS5B in terms of sliding and the ability to bind ssRNA.

Our smPIFE studies provide a window into the working mechanism of NS5B at the early steps of *de novo* synthesis and provide a strategy for the rapid screening of potential antiviral drugs interfering with the binding and sliding of related polymerases found within the *Flaviviridae* family.

5.6 Supplementary Information

5.6.1 Materials and Methods

5.6.1.1 Materials

5.6.1.1.1 Reagents

d-(+)-Glucose, glucose oxidase type VII from *Aspergillus niger* (G2133), β-mercaptoethanol, and Dimethyl sulfoxide (anhydrous, ≥99.9) were purchased from Sigma Aldrich. 1 M Tris–HCl buffer, pH 8.0; 1 M HEPES buffer, pH 7.3; Sodium Hydroxide; Premium Cover Glass slides (25x25-1), and Acetone (HPLC grade) were purchased from Fisher Scientific. NaCl solution (5 M), $MgCl_2$ (1 M), and Streptavidin (S888) were purchased from ThermoFisher Scientific, Invitrogen. GTP, ATP, UTP, and CTP solutions were purchased from ThermoFisher. Water (molecular biology grade) was acquired from Thermo Scientific HyClone (South Logan, UT). Sulphuric acid and Hydrogen Peroxide were purchased from ACP Chemicals. Poly(ethylene glycol) polymers in the form of silane (mPEG-Silane, MW 5000) as well as the biotinylated version (Biotin-PEG-Silane, MW 5000) were purchased from Laysan Bio Inc. Silicon mold, press fit tubing connectors and polycarbonate imaging chambers (Hybriwell) were purchased from Grace Bio-Labs, Inc.

5.6.1.1.2 Nucleic acids

Cy3-tagged RNA strands and GpG RNA dinucleotide were purchased from Trilink Biotechnologies, and biotin-tagged DNA strand was purchased from Integrated DNA Technologies (IDT). Listed below in **Table 5.2** are the sequences utilized in constructing the DNA/RNA duplexes in our study.

5.6.1.2 Single Molecule Fluorescence Imaging

5.6.1.2.1 Single molecule sample preparation and surface immobilization

Glass coverslips were initially cleaned and then passivated in one step utilizing PEG-Silane as previously described.[35] Before image acquisition, the surface was incubated with 15 μL of 0.2 mg/mL streptavidin solution for 10 min. The unbound streptavidin was washed away with imaging buffer (20 mM NaCl, 10 mM Hepes buffer, pH 7.3). Following streptavidin incubation, the DNA/RNA hybrid was immobilized on PEG-coated glass coverslips *via* biotin-streptavidin

interactions upon incubating a 200 pM solution of the annealed construct. Unbound constructs were flushed out with additional imaging buffer.

5.6.1.2.2 Anti-fading solution

Experiments were carried out in the presence of an oxygen scavenger solution consisting of β-mercaptoethanol (143 mM), D-(+)-glucose (0.8% w/v), and glucose oxidase (165 units/mL). The first image was acquired 10 min after introducing the oxygen removal system to allow the equilibration of the oxygen concentration in the chamber. Solutions were 10 mM in HEPES buffer pH 7.3 and 20 mM in NaCl with 100 nM NS5B when necessary. Additional reagents such as $MgCl_2$, NTPs, and GpG were added when necessary. Experiments were conducted at room temperature (23 °C) unless otherwise specified.

5.6.1.2.3 TIRF microscopy

Fluorescence imaging was carried out using an inverted Nikon Eclipse Ti microscope equipped with the perfect focus system (PFS) implementing an objective-type TIRF configuration with a Nikon TIRF illuminator and an oil-immersion objective (CFI SR Apo TIRF 100× oil immersion objective lens, numerical aperture (NA)=1.49). The effective pixel size was 160 nm. With these settings, a 561 nm laser was used for excitation (Agilent MLC400B Monolithic Laser Combiner). The laser beam was passed through a multiband cleanup filter ZET405/488/561/647x (Chroma Technology) and coupled into the microscope objective using a multiband beam splitter ZT405/488/561/647rpc (Chroma Technology). Fluorescence was spectrally filtered with two emission filters ZET405/488/561/647m and ET600/50m (Chroma Technology).

All movies were recorded onto a 512 x 512 pixel region of a back-illuminated electron-multiplying charge-coupled device (EMCCD) camera (iXon X3 DU-897-CS0-#BV, Andor Technology). The camera was controlled using Micro-Manager Software (Micro-Manager 1.4.13, San Francisco, CA, USA), capturing 16-bit 512 x 512 pixel images with an exposure time of 50-200 ms. The microscope was controlled using the software NIS element from Nikon.

5.6.1.2.4 Image and data analysis

We observed typically ~500-800 spots corresponding to single DNA-RNA duplexes over one field of view (~82^2 μm^2). We utilized a Matlab-based graphical user interphases to perform single molecule data analysis. Single molecule detection was based on an IDL script utilized by the Ha group, where diffraction-limited spots (DLSs) are mapped *via* threshold analysis and the clustered

DLSs are rejected. A second script was written and used to extract intensity-time single-molecule trajectories, where background correction was performed for each DLSs at every frame considering its local background. For the kinetic analysis, we developed a graphical user interphase in Matlab to analyse bound and unbound dwell times. Bound dwell times were found by performing a thresholding analysis. A Gaussian profile was fitted to the normalized intensity prior to NS5B binding to find the standard deviation (σ), where signals above 5σ were considered as bound states. Histograms of smPIFE values were constructed from the beginning of the first binding event to the end of the last binding event prior photobleaching of the donor dye. In this manner the region prior to protein arrival upon flowing is effectively rejected. All histograms were constructed using OriginPro 8.5 (OriginLab).

5.6.1.3 Steady-state and Time-resolved Studies

5.6.1.3.1 Steady-state absorption and fluorescence measurements

Absorbances were recorded using a HITACHI U-2800 UV–vis spectrophotometer. Emission scans were recorded using a PTI QuantaMaster 400 spectrofluorometer and the provided software. The fluorescence spectra were recorded using a 2 nm bandwidth excitation and emission slits. Fluorescence was recorded every 1 nm using a 0.2 s integration time. Emission spectra were corrected for wavelength-dependent variations in the detector sensitivity. The fluorescence quantum yield of Cy3 dye at room temperature was determined using PM605 in acetonitrile ($\Phi_f = 0.72$) as a standard.[48] The absorption and emission spectra of Cy3 when free and in the constructs of interest were measured in imaging buffer (10 mM in HEPES buffer pH 7.3 and 20 mM in NaCl) at different concentrations. Cy3 was also measured in glycerol solutions. The absorbance of all samples was kept below 0.05 at the excitation wavelength (514 nm). The integrated intensities versus absorbance were then plotted and fitted linearly. Relative fluorescence quantum yields for the unknown with respect to the standard were obtained according to well-established methods[49] by comparing the absorption and emission of the unknown and standard samples and correcting for the solvent refractive index of the solution of the unknown and standard.

5.6.1.3.2 Time-resolved fluorescence measurements

Fluorescence lifetime measurements were carried out using a Picoquant Fluotime 200 time-correlated single photon counting (TCSPC) setup employing a supercontinuum laser as the excitation source (WhiteLase SC-400-4, Fianium Beverly, MA). A center excitation wavelength of 514 nm was spectrally separated from the broadband emission by a computer-controlled acousto-optical tunable filter (AOTF, Fianium). Samples were excited at 514 nm and fluorescence lifetimes were recorded when monitoring at 580 nm. The excitation rate was 40 MHz, and the detection frequency was less than 400 kHz. Photons were collected at the magic angle. The fluorescence decay traces were fitted to exponential decay functions using FluoFit (Picoquant) software. The samples (200 µL in volume) contained 200 nM Cy3-tagged RNA constructs in imaging buffer in a small volume quartz cuvette (400 µL, 3 mm path length).

5.6.1.3.3 Transient absorption laser flash photolysis measurements

Experiments were conducted using a laser flash photolysis setup (Luzchem). The second harmonic of a Nd:YAG (Continuum Surelite CLII-10, 10 Hz, 450 mJ at 1064 nm) laser was used for excitation at a wavelength of 532 nm. 10 mJ laser pulses were used with a pulse width of 6 ns. A 150 W Xe lamp was used as the probe beam. The detector consisted of a photomultiplier tube (PMT) connected to a digital oscilloscope (Tektronix TDS2012). All data was collected *via* the commercially available LFP 7.0 software (Luzchem). Samples containing Cy3 at a concentration of approximately ~2 µM were prepared either in water or glycerol. All samples were prepared freshly in 10 x 10 mm quartz cells. A minimum of 10 laser shots were averaged to obtain the temporal evolution of ΔOD for the various transient species monitored. In turn, a minimum of 3 laser shots were averaged per wavelength interval for obtaining the transient absorption spectra. The time per division recorded by the detector was 2.5 µs (25 µs total). ΔOD *vs* time traces were fitted to monoexponential functions using OriginPro 8.5 to obtain transient lifetimes.

5.6.1.4 Preparation of RNA–DNA Duplexes

The RNA–DNA duplexes were annealed from biotinylated 18mers (ACC TCG CGA CCG TCG CCA-biotin) and dye/R_n^X sequences (**see Figure 5.5**). Oligonucleotides were purified through HPLC by the provider. To enable surface immobilization of the DNA/RNA duplex, the 3′ end of the DNA strand was attached to a biotin moiety. The duplexes were annealed by mixing 2.5 µm of both DNA and RNA strands in an annealing buffer (50 mM Tris–HCl, 50 mM NaCl, pH ~ 8.0)

and then incubating the mixture in a thermal cycler at 95 °C for 2 min and gradually (2 °C/min) cooling it to 25 °C. The duplex formation was confirmed using 10% native polyacrylamide gel electrophoresis.

5.6.2 Chemical structures and Oligonucleotides Sequences

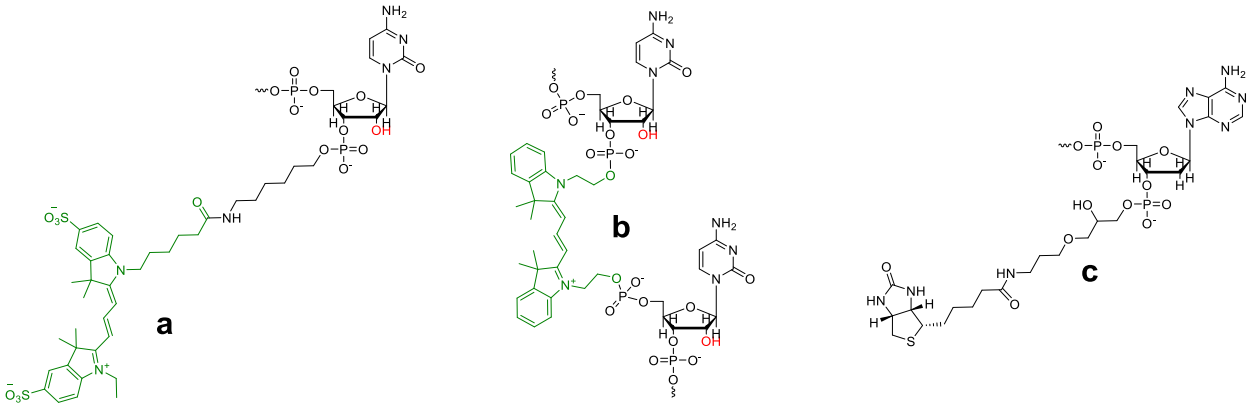

Figure 5.5. Dye and biotin modifications utilized. Chemical structure of the dye conjugates utilized, Cy3 appears in green. Conjugate (**a**) utilized in R_{20}^{S} is a cytidylate terminated 3' overhang with Cy3 tethered to the phosphate at position 3' of the ribose *via* a succinimide linker. Conjugate (**b**) utilized in R_{20}^{A} is an internal Cy3 tethered to the phosphate backbone (internal amidite). Structure (**c**) shows the biotin conjugation at the 3' end of the DNA strand.

Table 5.2. Sequences for all the oligomers used.

Name	Sequences (5'-3')
$\boldsymbol{Bio - D_{18}}$	**ACCTCGCGACCGTCGCCA** /3Bio/ (IDT)
$\boldsymbol{D_{20}}$	GGAGAGAAAAGGAAACCGTT (IDT)
$\boldsymbol{R_{20}^{S}}$	**UGGCGACGGUCGCGAGGU**AACGGUUUCCUUUUCUCUCC (C6-NH) (Cy3) (TriLink)
$\boldsymbol{R_{20}^{A}}$	**UGGCGACGGUCGCGAGGU**AACGGUUUCCUUUUCUCUC-(Cy3)-C (TriLink)

5.6.3 Test and calibration of Cy3 and Cy3-tagged RNA strands

5.6.3.1 Cy3 is unable to undergo photoisomerization in glycerol

In order to set the upper limit of the fluorescence quantum yield of Cy3 (i.e. when Cy3 is unable to undergo trans-cis isomerization in the excited state), we tested the use of glycerol as it provides a highly viscous environment (~1000 cp) compare to water (~1 cp). Transient absorption LFP studies showed that, in water, Cy3 can effectively undergo trans-cis photoisomerization **Figure 5.6 (panels a, b, and c)**. However, no photoisomerization is detected when glycerol is used as solvent **Figure 5.6 (panels d, e, and f)**. Upon excitation, the *cis*-Cy3 transient absorption spectra can be observed at ~568 nm. The depletion of the ground state of Cy3 can be observed as a negative band centered at ~548 nm. The temporal evolution of *cis*-Cy3 and Cy3 ground state can be followed at 568 and 548 nm, respectively. **Figure 5.6c** shows that as the *cis* form of Cy3 decays, the *trans* form is recovered. When glycerol is used as a solvent, a null transient absorption is obtained (**Figure 5.6e and f)** suggesting that the fluorescence quantum yield of Cy3 measured in glycerol can be used as the upper limit of PIFE.

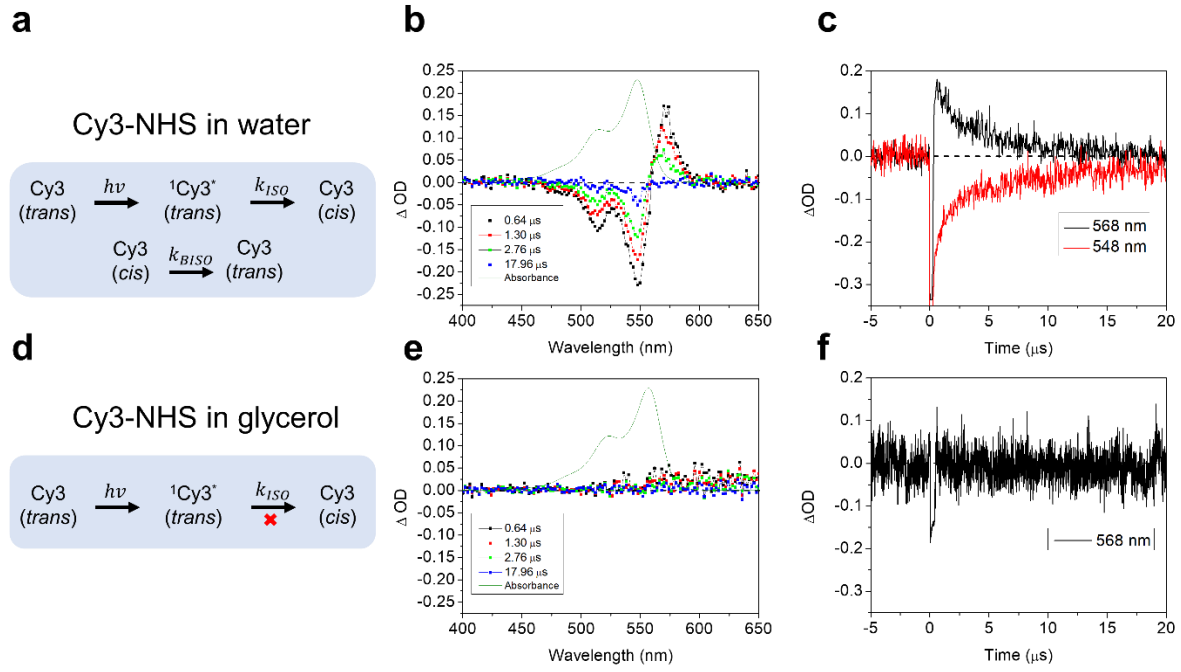

Figure 5.6. Mechanism of Cy3 photoisomerization (left panels), transient absorption spectra (middle panels), and temporal evolution of ΔOD traces recorded at 548 and 568 nm (right panels). LFP studies were performed in air-equilibrated solutions of water (top) and glycerol (bottom) containing ~2 µM of Cy3. After excitation in water, *cis* photoisomer can be observed formed within the laser pulse, where its decay profile may be followed at 568 nm (b, c). Over time,

concomitant with the decay of the *cis* form of Cy3 (τ = 3.7 ± 0.2 μs), the ground state of Cy3 is recovered (548 nm) (τ = 3.5 ± 0.2 μs). After excitation in glycerol, the formation of the *cis* photoisomer was not detected at 568 nm (e, f).

5.6.3.2 Solvent, labeling strategy, and magnesium effect on the photophysical properties of Cy3

In order to calibrate our system as well as to find the most sensitive Cy3-labeled oligonucleotide to be used in smPIFE studies, we studied the photophysical properties of Cy3 (fluorescence quantum yield Φ_f and fluorescence lifetime τ_f) under different conditions (**Figure 5.7**). Note that similar trends were found when measuring the fluorescence emission decay lifetimes τ_f (**Figure 5.7a**) and the fluorescence emission quantum yields Φ_f (**Figure 5.7b**. We thus focus the analysis on the values of Φ_f. The Φ_f values we recorded for Cy3 in aqueous solution (imaging buffer) and glycerol were 0.04 and 0.43, respectively. Accordingly, the maximum possible enhancement (dynamic range) of Cy3 in PIFE experiments is ~10-fold. However, it has been previously reported that the Φ_f of Cy3 is dependent on the oligonucleotide sequence utilized as well as on the strategy and position utilized to label the oligonucleotide.[36, 50] Therefore, we compared two labeled sequences (R_{20}^A and R_{20}^S) we previously utilized to study NS5B, for maximum sensitivity.[34] The Φ_f of Cy3 increased in both constructs when compared to free dye, however, the increase was larger for R_{20}^A compared to R_{20}^S (Φ_f = 0.15 and 0.09, respectively). Accordingly, under normal buffer conditions (absence of Mg^{2+} ions), the theoretical maximum enhancements for R_{20}^A and R_{20}^S are 2.9-fold and 4.8-fold, respectively. These results suggest that R_{20}^S is more sensitive than R_{20}^A for PIFE experiments.

We additionally tested the effect of magnesium ions on the photophysical properties of RNA bound Cy3. The Φ_f of Cy3 was increased in R_{20}^A by 1.7-fold and in R_{20}^S by 1.4-fold when these constructs are solubilized in imaging buffer containing 91 mM of Mg^{2+} ions. The theoretical maximum enhancements for R_{20}^A and R_{20}^S are thus decreased to values of 1.6-fold and 3.3-fold, respectively. These results underscore that R_{20}^S is more sensitive than R_A^{20} for PIFE experiments. Accordingly, smPIFE experiments in this study were carried out using the R_{20}^S strand.

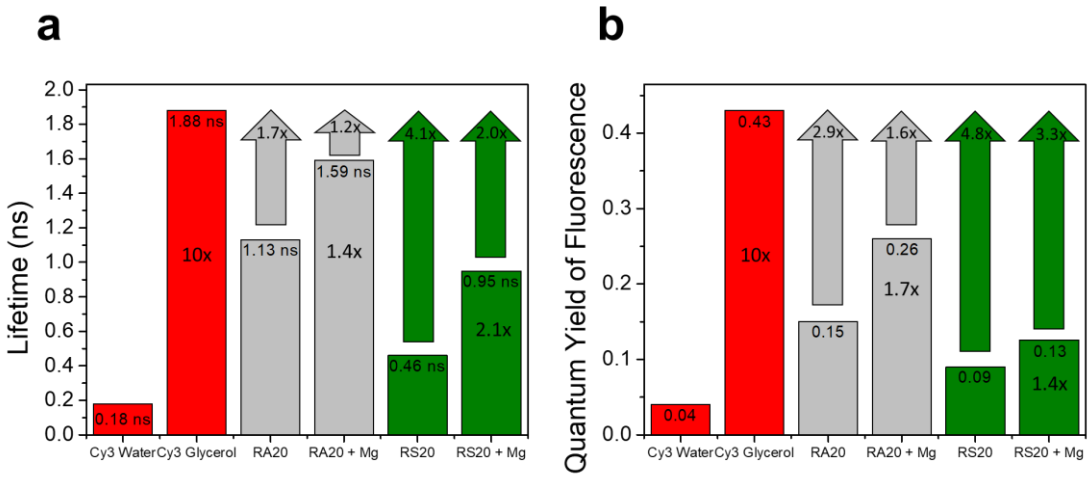

Figure 5.7. Cy3 calibration *via* lifetime and fluorescence quantum yield. Photophysical properties such as lifetimes (a) and fluorescence quantum yield of Cy3. Fluorescence measurements of Cy3 (free in solution) were performed in aqueous buffer and glycerol. The fluorescence of Cy3 on R_{20}^{A} and R_{20}^{S} strands was studied in buffer in the absence and presence of 91 mM of Mg^{2+} ions.

5.6.3.3 Magnesium effect on the fluorescence of Cy3 R_{20}^{S}

Bulk steady-state fluorescence experiments were performed to study the fluorescence enhancement of Cy3-R_{20}^{S} as a function of Mg^{2+} concentration (**Figure 5.8**). Single molecule enhancements (~1.4 under saturation conditions) are in agreement with ensemble studies, see **Figure 5.9**. The fluorescence of Cy3-R_{20}^{S} was initially monitored in buffer solution (Hepes 10 mM, pH 7.3, and NaCl 20 mM). The same buffer solution was flown in real time into the single molecule chamber, however, now supplemented with 10 mM Mg^{2+}.

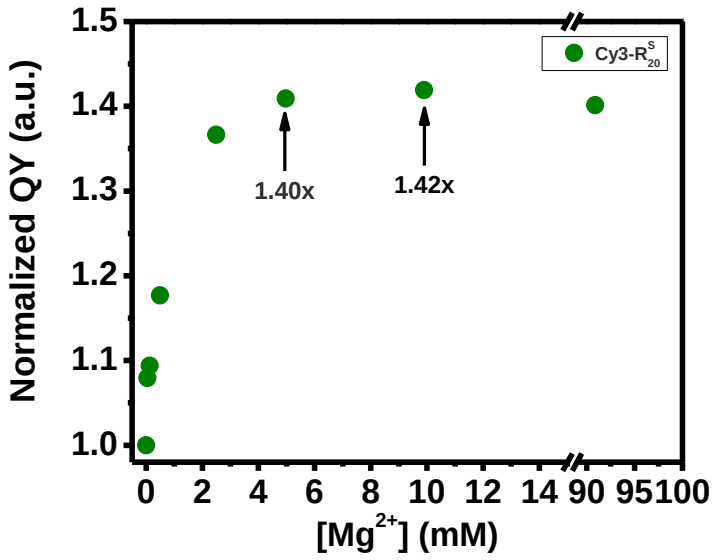

Figure 5.8. Mg^{2+}-induced fluorescence enhancement of Cy3-R_{20}^{S}visualized at the ensemble level. Aqueous solutions (Hepes 10 mM, pH 7.3, and NaCl 20 mM) containing different concentrations of Mg^{2+} up to 91 mM were used to monitor the fluorescence enhancement of Cy3-R_{20}^{S} induced by Mg^{2+} binding to ssRNA.

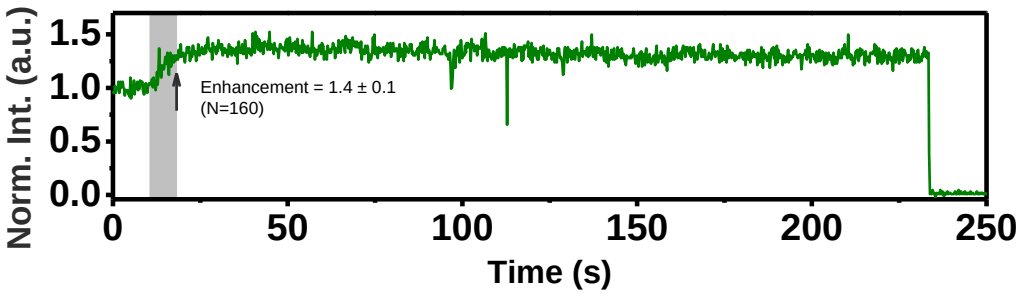

Figure 5.9. Mg^{2+}-induced fluorescence enhancement of Cy3-R_{20}^{S} visualized at the single molecule level. Cy3-R_{20}^{S} was initially immersed in buffer (Hepes 10 mM, pH 7.3, and NaCl 20 mM). Following initiation of the imaging experiment, the buffer solution now supplemented with 10 mM of Mg^{2+} was flown into the chamber at a rate of 10 µL/min to monitor the changes in fluorescence intensity of Cy3-R_{20}^{S}.

5.6.3.4 Hybridization of Cy3-R20S.

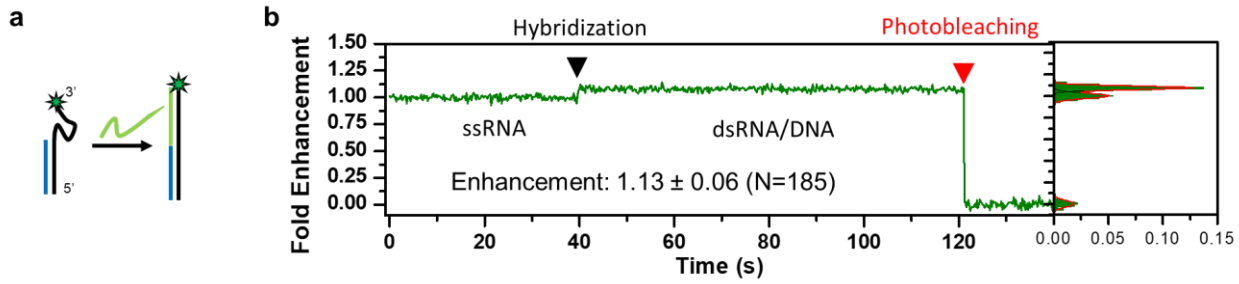

Figure 5.10. Full hybridization (20nt) of Cy3-R20S visualized at the single molecule level. (a) Scheme of the hybridization process. Strands in pink, black, and blue represent DNA, initially hybridized RNA, and initially non-hybridized RNA, respectively. (b) Single-molecule trajectory showing real-time hybridization and its enhancement.

5.6.4 Cumulative Distribution Function

We have found that the distribution of bound times is better adjusted through a biexponential function rather than a mono-exponential one. The normalized bi-exponential distribution $P(t)$ can be expressed as shown in **equation 5.1**. Here, $\alpha_1\tau_1 + \alpha_2\tau_2 = 1$ and the fractional contributions f_1 and f_2 can be calculated as shown in **equations 5.2 and 5.3**. The cumulative distribution function $cdf(t)$ (**equation 5.4**), can be derived by integrating **equation 5.1**. The cumulative distribution function is more convenient to use when average times are too different as it circumvents the problem of data binning.

$$P(t) = \alpha_1 e^{-\frac{t}{\tau_1}} + \alpha_2 e^{-\frac{t}{\tau_2}} \tag{5.1}$$

$$f_1 = \alpha_1\tau_1 \tag{5.2}$$

$$f_2 = \alpha_2\tau_2 \tag{5.3}$$

$$cdf(t) = 1 - \left(f_1 e^{-\frac{t}{\tau_1}} + f_2 e^{-\frac{t}{\tau_2}}\right) \tag{5.4}$$

5.7 References

1. Wu, J.; Liu, W.; Gong, P., A Structural Overview of RNA-Dependent RNA Polymerases from the Flaviviridae Family. *International Journal of Molecular Sciences* **2015,** *16* (6), 12943-12957.
2. Rice, C. M.; Saeed, M., Treatment triumphs. *Nature* **2014,** *510*, 43.
3. Bhatia, H.; Singh, H.; Grewal, N.; Natt, N., Sofosbuvir: A novel treatment option for chronic hepatitis C infection. *Journal of Pharmacology and Pharmacotherapeutics* **2014,** *5* (4), 278-284.
4. Sacramento, C. Q.; de Melo, G. R.; de Freitas, C. S.; Rocha, N.; Hoelz, L. V. B.; Miranda, M.; Fintelman-Rodrigues, N.; Marttorelli, A.; Ferreira, A. C.; Barbosa-Lima, G.; Abrantes, J. L.; Vieira, Y. R.; Bastos, M. M.; de Mello Volotão, E.; Nunes, E. P.; Tschoeke, D. A.; Leomil, L.; Loiola, E. C.; Trindade, P.; Rehen, S. K.; Bozza, F. A.; Bozza, P. T.; Boechat, N.; Thompson, F. L.; de Filippis, A. M. B.; Brüning, K.; Souza, T. M. L., The clinically approved antiviral drug sofosbuvir inhibits Zika virus replication. *Scientific Reports* **2017,** *7*, 40920.
5. Xu, H.-T.; Colby-Germinario, S. P.; Hassounah, S. A.; Fogarty, C.; Osman, N.; Palanisamy, N.; Han, Y.; Oliveira, M.; Quan, Y.; Wainberg, M. A., Evaluation of Sofosbuvir (β-D-2′-deoxy-2′-α-fluoro-2′-β-C-methyluridine) as an inhibitor of Dengue virus replication#. *Scientific Reports* **2017,** *7* (1), 6345.
6. Lesburg, C. A.; Cable, M. B.; Ferrari, E.; Hong, Z.; Mannarino, A. F.; Weber, P. C., Crystal structure of the RNA-dependent RNA polymerase from hepatitis C virus reveals a fully encircled active site. *Nature Structural Biology* **1999,** *6* (10), 937-943.
7. Bressanelli, S.; Tomei, L.; Roussel, A.; Incitti, I.; Vitale, R. L.; Mathieu, M.; De Francesco, R.; Rey, F. A., Crystal structure of the RNA-dependent RNA polymerase of hepatitis C virus. *Proceedings of the National Academy of Sciences* **1999,** *96* (23), 13034-13039.
8. Ago, H.; Adachi, T.; Yoshida, A.; Yamamoto, M.; Habuka, N.; Yatsunami, K.; Miyano, M., Crystal structure of the RNA-dependent RNA polymerase of hepatitis C virus. *Structure* **1999,** *7* (11), 1417-1426.
9. Biswal, B. K.; Cherney, M. M.; Wang, M.; Chan, L.; Yannopoulos, C. G.; Bilimoria, D.; Nicolas, O.; Bedard, J.; James, M. N. G., Crystal Structures of the RNA-dependent RNA Polymerase Genotype 2a of Hepatitis C Virus Reveal Two Conformations and Suggest Mechanisms of Inhibition by Non-nucleoside Inhibitors. *Journal of Biological Chemistry* **2005,** *280* (18), 18202-18210.
10. RANJITH-KUMAR, C. T.; KAO, C. C., Recombinant viral RdRps can initiate RNA synthesis from circular templates. *RNA* **2006,** *12* (2), 303-312.
11. Steitz, T. A., A mechanism for all polymerases. *Nature* **1998,** *391* (6664), 231-232.
12. Ferrari, E.; Wright-Minogue, J.; Fang, J. W. S.; Baroudy, B. M.; Lau, J. Y. N.; Hong, Z., Characterization of Soluble Hepatitis C Virus RNA-Dependent RNA Polymerase Expressed in Escherichia coli. *Journal of Virology* **1999,** *73* (2), 1649-1654.
13. Luo, G.; Hamatake, R. K.; Mathis, D. M.; Racela, J.; Rigat, K. L.; Lemm, J.; Colonno, R. J., De Novo Initiation of RNA Synthesis by the RNA-Dependent RNA Polymerase (NS5B) of Hepatitis C Virus. *Journal of Virology* **2000,** *74* (2), 851-863.
14. Ranjith-Kumar, C. T.; Kim, Y.-C.; Gutshall, L.; Silverman, C.; Khandekar, S.; Sarisky, R. T.; Kao, C. C., Mechanism of De Novo Initiation by the Hepatitis C Virus RNA-Dependent

RNA Polymerase: Role of Divalent Metals. *Journal of Virology* **2002,** *76* (24), 12513-12525.

15. Zhong, W.; Uss, A. S.; Ferrari, E.; Lau, J. Y. N.; Hong, Z., De Novo Initiation of RNA Synthesis by Hepatitis C Virus Nonstructural Protein 5B Polymerase. *Journal of Virology* **2000,** *74* (4), 2017-2022.
16. Oh, J.-W.; Ito, T.; Lai, M. M. C., A Recombinant Hepatitis C Virus RNA-Dependent RNA Polymerase Capable of Copying the Full-Length Viral RNA. *Journal of Virology* **1999,** *73* (9), 7694-7702.
17. Sun, X.-L.; Johnson, R. B.; Hockman, M. A.; Wang, Q. M., De Novo RNA Synthesis Catalyzed by HCV RNA-Dependent RNA Polymerase. *Biochemical and Biophysical Research Communications* **2000,** *268* (3), 798-803.
18. Ackermann, M.; Padmanabhan, R., De Novo Synthesis of RNA by the Dengue Virus RNA-dependent RNA Polymerase Exhibits Temperature Dependence at the Initiation but Not Elongation Phase. *Journal of Biological Chemistry* **2001,** *276* (43), 39926-39937.
19. Kao, C. C.; Del Vecchio, A. M.; Zhong, W., De NovoInitiation of RNA Synthesis by a Recombinant Flaviridae RNA-dependent RNA Polymerase. *Virology* **1999,** *253* (1), 1-7.
20. Calmels, C.; Ventura, M.; Aknin, C.; Métifiot, M.; Andreola, M.-L., De novo RNA synthesis catalyzed by the Zika Virus RNA polymerase domain. *Scientific Reports* **2017,** *7* (1), 2697.
21. Shim, J. H.; Larson, G.; Wu, J. Z.; Hong, Z., Selection of 3′-Template Bases and Initiating Nucleotides by Hepatitis C Virus NS5B RNA-Dependent RNA Polymerase. *Journal of Virology* **2002,** *76* (14), 7030-7039.
22. Kao, C. C.; Yang, X.; Kline, A.; Wang, Q. M.; Barket, D.; Heinz, B. A., Template Requirements for RNA Synthesis by a Recombinant Hepatitis C Virus RNA-Dependent RNA Polymerase. *Journal of Virology* **2000,** *74* (23), 11121-11128.
23. Ferrari, E.; He, Z.; Palermo, R. E.; Huang, H.-C., Hepatitis C Virus NS5B Polymerase Exhibits Distinct Nucleotide Requirements for Initiation and Elongation. *Journal of Biological Chemistry* **2008,** *283* (49), 33893-33901.
24. Bressanelli, S.; Tomei, L.; Rey, F. A.; De Francesco, R., Structural Analysis of the Hepatitis C Virus RNA Polymerase in Complex with Ribonucleotides. *Journal of Virology* **2002,** *76* (7), 3482-3492.
25. Zhong, W.; Ferrari, E.; Lesburg, C. A.; Maag, D.; Ghosh, S. K. B.; Cameron, C. E.; Lau, J. Y. N.; Hong, Z., Template/Primer Requirements and Single Nucleotide Incorporation by Hepatitis C Virus Nonstructural Protein 5B Polymerase. *Journal of Virology* **2000,** *74* (19), 9134-9143.
26. Hang, J. Q.; Yang, Y.; Harris, S. F.; Leveque, V.; Whittington, H. J.; Rajyaguru, S.; Ao-Ieong, G.; McCown, M. F.; Wong, A.; Giannetti, A. M.; Le Pogam, S.; Talamás, F.; Cammack, N.; Nájera, I.; Klumpp, K., Slow Binding Inhibition and Mechanism of Resistance of Non-nucleoside Polymerase Inhibitors of Hepatitis C Virus. *Journal of Biological Chemistry* **2009,** *284* (23), 15517-15529.
27. Appleby, T. C.; Perry, J. K.; Murakami, E.; Barauskas, O.; Feng, J.; Cho, A.; Fox, D.; Wetmore, D. R.; McGrath, M. E.; Ray, A. S.; Sofia, M. J.; Swaminathan, S.; Edwards, T. E., Structural basis for RNA replication by the hepatitis C virus polymerase. *Science* **2015,** *347* (6223), 771-775.

28. Hwang, H.; Kim, H.; Myong, S., Protein induced fluorescence enhancement as a single molecule assay with short distance sensitivity. *Proceedings of the National Academy of Sciences* **2011,** *108* (18), 7414-7418.
29. Hwang, H.; Myong, S., Protein induced fluorescence enhancement (PIFE) for probing protein-nucleic acid interactions. *Chemical Society Reviews* **2014,** *43* (4), 1221-1229.
30. Stennett, E. M. S.; Ciuba, M. A.; Lin, S.; Levitus, M., Demystifying PIFE: The Photophysics Behind the Protein-Induced Fluorescence Enhancement Phenomenon in Cy3. *The Journal of Physical Chemistry Letters* **2015,** *6* (10), 1819-1823.
31. Herbert, K. M.; Greenleaf, W. J.; Block, S. M., Single-Molecule Studies of RNA Polymerase: Motoring Along. *Annual Review of Biochemistry* **2008,** *77* (1), 149-176.
32. Ray, S.; Widom, J. R.; Walter, N. G., Life under the Microscope: Single-Molecule Fluorescence Highlights the RNA World. *Chemical Reviews* **2018**.
33. Deval, J.; D'Abramo, C. M.; Zhao, Z.; McCormick, S.; Coutsinos, D.; Hess, S.; Kvaratskhelia, M.; Götte, M., High Resolution Footprinting of the Hepatitis C Virus Polymerase NS5B in Complex with RNA. *Journal of Biological Chemistry* **2007,** *282* (23), 16907-16916.
34. Karam, P.; Powdrill, M. H.; Liu, H.-W.; Vasquez, C.; Mah, W.; Bernatchez, J.; Götte, M.; Cosa, G., Dynamics of Hepatitis C Virus (HCV) RNA-dependent RNA Polymerase NS5B in Complex with RNA. *Journal of Biological Chemistry* **2014,** *289* (20), 14399-14411.
35. Gidi, Y.; Bayram, S.; Ablenas, C. J.; Blum, A. S.; Cosa, G., Efficient One-Step PEG-Silane Passivation of Glass Surfaces for Single-Molecule Fluorescence Studies. *ACS Applied Materials & Interfaces* **2018,** *10* (46), 39505-39511.
36. Gidi, Y.; Götte, M.; Cosa, G., Conformational Changes Spanning Angstroms to Nanometers via a Combined Protein-Induced Fluorescence Enhancement–Förster Resonance Energy Transfer Method. *The Journal of Physical Chemistry B* **2017,** *121* (9), 2039-2048.
37. Steffen, F. D.; Sigel, R. K. O.; Börner, R., An atomistic view on carbocyanine photophysics in the realm of RNA. *Physical Chemistry Chemical Physics* **2016,** *18* (42), 29045-29055.
38. Gorman, J.; Greene, E. C., Visualizing one-dimensional diffusion of proteins along DNA. *Nature Structural &Amp; Molecular Biology* **2008,** *15*, 768.
39. Newby Lambert, M.; Vöcker, E.; Blumberg, S.; Redemann, S.; Gajraj, A.; Meiners, J.-C.; Walter, N. G., Mg2+-Induced Compaction of Single RNA Molecules Monitored by Tethered Particle Microscopy. *Biophysical Journal* **2006,** *90* (10), 3672-3685.
40. Cooper, M.; Ebner, A.; Briggs, M.; Burrows, M.; Gardner, N.; Richardson, R.; West, R., Cy3B™: Improving the Performance of Cyanine Dyes. *Journal of Fluorescence* **2004,** *14* (2), 145-150.
41. Ishido, S.; Fujita, T.; Hotta, H., Complex Formation of NS5B with NS3 and NS4A Proteins of Hepatitis C Virus. *Biochemical and Biophysical Research Communications* **1998,** *244* (1), 35-40.
42. Shirota, Y.; Luo, H.; Qin, W.; Kaneko, S.; Yamashita, T.; Kobayashi, K.; Murakami, S., Hepatitis C Virus (HCV) NS5A Binds RNA-dependent RNA Polymerase (RdRP) NS5B and Modulates RNA-dependent RNA Polymerase Activity. *Journal of Biological Chemistry* **2002,** *277* (13), 11149-11155.
43. Kwong, A. D.; Kim, J. L.; Lin, C., Structure and Function of Hepatitis C Virus NS3 Helicase. In *The Hepatitis C Viruses*, Hagedorn, C. H.; Rice, C. M., Eds. Springer Berlin Heidelberg: Berlin, Heidelberg, 2000; pp 171-196.

44. Foster, T. L.; Belyaeva, T.; Stonehouse, N. J.; Pearson, A. R.; Harris, M., All Three Domains of the Hepatitis C Virus Nonstructural NS5A Protein Contribute to RNA Binding. *Journal of Virology* **2010,** *84* (18), 9267-9277.
45. Huang, L.; Hwang, J.; Sharma, S. D.; Hargittai, M. R. S.; Chen, Y.; Arnold, J. J.; Raney, K. D.; Cameron, C. E., Hepatitis C Virus Nonstructural Protein 5A (NS5A) Is an RNA-binding Protein. *Journal of Biological Chemistry* **2005,** *280* (43), 36417-36428.
46. Hwang, J.; Huang, L.; Cordek, D. G.; Vaughan, R.; Reynolds, S. L.; Kihara, G.; Raney, K. D.; Kao, C. C.; Cameron, C. E., Hepatitis C Virus Nonstructural Protein 5A: Biochemical Characterization of a Novel Structural Class of RNA-Binding Proteins. *Journal of Virology* **2010,** *84* (24), 12480-12491.
47. Ciuba, M. A.; Levitus, M., Manganese-Induced Triplet Blinking and Photobleaching of Single Molecule Cyanine Dyes. *ChemPhysChem* **2013,** *14* (15), 3495-3502.
48. Krumova, K.; Oleynik, P.; Karam, P.; Cosa, G., Phenol-Based Lipophilic Fluorescent Antioxidant Indicators: A Rational Approach. *The Journal of Organic Chemistry* **2009,** *74* (10), 3641-3651.
49. Lakowicz, J., Principles of fluorescence spectroscopy, Joseph R. *Lakowicz, editor* **2006**.
50. Harvey, B. J.; Perez, C.; Levitus, M., DNA sequence-dependent enhancement of Cy3 fluorescence. *Photochemical & Photobiological Sciences* **2009,** *8* (8), 1105-1110.

6 Conclusions and Future Work

6.1 Conclusions

Single molecule fluorescence (SMF) microscopy techniques have allowed for the study of the dynamics and structure of the microscopic and nanoscopic world. SMF techniques allow unprecedented spatiotemporal resolution and are particularly powerful for the study of heterogeneous and unsynchronized systems, revealing unique information otherwise hidden in traditional ensemble measurements.

In this work we studied several mechanistic aspects related to single molecule fluorescence spectroscopy and its applications to biology. We started covering important **photophysical** processes associated to widely used single molecule techniques such as FRET and PIFE. We next continued with a **photochemical** study of cyanine dyes in the presence of thiol bearing compounds. We then explored improvements to the **surface chemistry** associated with the passivation of glass coverslips used in single molecule assays. Finally, we provided an example of how single molecule techniques allow us to extract relevant **biophysical** information of a bionanomachine involved in the viral replication of the Hepatitis C Virus (HCV).

In **Chapter 2**, through the evaluation of the probability of photophysical and photochemical competing pathways, we provided a theoretical framework establishing the compatibility of two single molecule techniques, smPIFE and FRET. We also studied how to quantify conformational changes in single molecule studies when both smPIFE and FRET processes are at play. In doing so, we demystified the idea that PIFE and FRET are incompatible techniques. We first demonstrated that through a ratiometric method FRET can be reliably measured in the presence of PIFE, or in the presence of any intensity fluctuation in the donor dye. Furthermore, we showed that changes in the fluorescence quantum yield of the donor (e.g. protein induced fluorescence enhancement) can be extracted in a FRET experiment. Thus, PIFE and FRET methods can be

combined, providing complementary information in a single experiment. A new method, intensity-FRET, was proposed to monitor conformational changes spanning from angstroms to nanometers. Unifying FRET and PIFE extends the molecular ruler in doubly labeled substrates to sub nanometer interaction studies. Our analysis shed light on the effects that protein or environmental effects can have on single molecule FRET studies. Using these analysis methods, it may be possible to revisit previously acquired data in order to retrieve PIFE results from existing single molecule donor-acceptor intensity trajectories recorded with Cy3 and ATTO647N dyes, a popular donor-acceptor pair used in single molecule FRET studies.

In **Chapter 3**, we reported a detailed understanding of the thiolate-induced photoswitching of cyanine dyes. This work provides a roadmap for the design of fluorophores, photoswitching agents, and triplet quenchers with desired characteristics in terms of enhanced photostability and controllable photoswitching. The photochemical mechanism we reported provides guidelines towards better photochemical control of currently used dye/thiol pairs, including photoswitching rates and enhanced photon budgets. Overall, by combining traditional bulk time-resolved transient studies and single molecule mechanistic studies, we were able to gain fundamental mechanistic insight. Our results present a fascinating picture of how seemingly minor/unimportant photochemical reactions become prominent at the high excitation rate conditions prevailing in single molecule studies.

In **Chapter 4**, we tackled a major hurdle in SMS techniques involving the reliability of passivated glass surfaces, where substrates are immobilized and studied. Such passivation is critical to minimize non-specific interactions. We provided a novel and efficient methodology relying on PEG-silane chemistry for the passivation of glass surfaces. The methodology is rooted in the mechanistic understanding of the silane reaction with the silanol groups on the glass surface. Single molecule fluorescence studies with fluorescently tagged proteins and DNA on PEG-silane functionalized glass surfaces were reported. We benchmarked our surfaces against the currently used method in most single molecule fluorescence studies which involves two-step aminosilanization followed by covalent tethering the PEG to the surface. Our results showed improved performance in terms of lower non-specific interactions, and excellent reproducibility. Additionally, key advantages of our method are speed (~15 minutes as compared to several hours for previous methods), robustness, sustainability, and lack of undesired detergent-biomolecule

interactions observed in what is to date the best reported surface, involving tween-20/BSA passivation. Our work ultimately provides a simple, cost-effective, and environmentally benign approach suitable for use in biological settings, towards rendering glass surfaces for single molecule/particle studies with superior surface passivation.

In **chapter 5** we reported an smPIFE platform to study the mechanism of the viral replication machinery of the Hepatitis C virus (HCV). The non-structural 5B (NS5B) polymerase of HCV has been reported to initiate synthesis *de novo* through a primer independent mechanism. The dynamic process of how this protein locates the 3'-terminus of the RNA template remains an unsolved question. Through smPIFE studies, we reported key aspects of the early steps of *the novo* synthesis such as NS5B binding to (and sliding along) its single stranded RNA substrate. Magnesium ions were found to modulate NS5B dynamic behaviour. In the absence of Mg^{2+} ions, upon binding, NS5B slowly slides along the ssRNA template. However, in the presence of Mg^{2+} ions NS5B can rapidly slide along the RNA backbone. Addition of NTPs as well as GpG primer, has a marginal effect in the dynamics of NS5B in terms of sliding and the ability to bind ssRNA. We noted that the smPIFE platform reported herein can be used as a strategy for the rapid screening of drugs designed to interfere with the binding and sliding of NS5B and related polymerases found within the *Flaviviridae* family.

Overall, the work reported in this thesis, through mechanistic analyses, provides new insights on most aspects of SMF techniques such as sample preparation (**chapter 4**), fluorescence signal control (**chapter 3**), and data analysis (**chapter 2**). Additionally, it provides an example of the power of SMS to study relevant biomolecular mechanisms such as the replication machinery of viruses.

6.2 Future work and Future Directions

6.2.1 A Methodology to Predict P*e*T Rate Constants of Potential Photostabilizers and Photoswitching Agents

In **chapter 3**, we established the unifying elements existing between the mechanisms underlying photostability and photoswitching of cyanine dyes in the presence of thiols. We found that an efficient P*e*T rate constant (k_{PeT}) is crucial for both photostability and photoswitching. In the quest for improved photostabilizers and photoswitching agents, however, a strategy to accurately predict k_{PeT} is still missing.

We propose a theoretical-empirical strategy to predict k_{PeT} computationally. On the one hand, experimental k_{PeT} can be measured via transient absorption laser flash photolysis (LFP) spectroscopy. On the other hand, activation energies of P*e*T ($\Delta G^{\neq}_{PeT}$) can be calculated using the Marcus theory of electron transfer (**see section 1.2.4.2**). Here, $\Delta G^{\neq}_{PeT}$ can be calculated from the Gibbs free energy of reaction for photoinduced electron transfer (ΔG^{o}_{PeT}) and the reorganization energy (λ) of P*e*T. ΔG^{o}_{PeT} and λ can in turn be computationally obtained via DFT calculations (**see section 3.6.1.4**). Experimental values for k_{PeT}, we reason, can be next correlated with $\Delta G^{\neq}_{PeT}$ for several dye-quencher pairs to obtain a calibration curve enabling gaging the protective role different triplet quenchers may play in ingle molecule fluorescence studies, based on the estimated rates of P*e*T. We propose to use 16 dye-quencher combinations based on the most utilized cyanines dyes (Cy3, Cy3B, Cy5, Cy5B) and P*e*T-based reducing agents (*n*-PG, AA, TX, and β-ME).

A second crucial step to both photostability and photoswitching is the efficient triplet to singlet ISC of the newly formed geminate radical pair (GRP). Here, the thiyl radical of β-ME is particularly efficient toward this purpose (**see chapter 3**).[1-2] Thus, we suggest that thiol-containing compounds, able to form thiyl radicals upon P*e*T, should be screened. We also suggest that the search should not only focus on enhanced k_{PeT} values, but also for low vapor pressure (reduced malodor) and lower pKa values (increased thiol acidity) ensuring there is a larger tendency toward dissociation for new thiol based compounds.

The proposed theoretical-empirical strategy to predict k_{PeT}, when applied to screen thiol-containing molecules, has the potential to identify better photostabilizers as well as photoswitching agents. We anticipate that improved photostabilizers and photoswitching agents will maximize the

photon budget and allow for a better control of photoswitching kinetics of dyes utilized in single-molecule fluorescence imaging.

6.2.2 A methodology to improving both the performance and shelf life of passivated surfaces

In **chapter 4**, we described an improved methodology to passivate glass surfaces utilizing PEG polymers. Our strategy offers in most of the cases decreased nonspecific binding, shorter preparation times, and reduced variability. However, we noticed that independently of the PEG-based methodology utilized to passivate the surfaces, inherent hydrophobic imperfections in the glass slides limit the performance of the surfaces. This is particularly important for single molecule studies requiring high concentrations of labelled substrates. In agreement with previous reports, we showed that incubation of solutions (1%) containing the detergent Tween 20 (T20), can further improve the quality of the surfaces, especially when working with proteins.[3-4]

A limitation of the methods involving PEG is the short shelf life of the passivated surface. Here, as we have observed, imperfections appearing as micron-sized cracks in the surface limit their shelf life to typically less than a week. We hypothesize that this is due to loss of the remaining solvent occluded in the polymer layer, which likely decreases the effective melting temperature of the polymer (PEG 5000, T_m ~ 60 °C).

We propose to use low molecular weights molecules as plasticizers to increase the shelf life of passivated surfaces. Here PEG molecules of lower molecular weight (for example PEG 400, T_m ~ 6 °C) may serve to this purpose. In this context, T20 may play a dual role, acting not only as an inhibitor of nonspecific binding but also as a plasticizer. The main challenge we foresee in testing plasticizers is that they must be water free.

6.2.3 Further Studies on the Replication Machinery of HCV and the *Flaviviridae* family

6.2.3.1 PIFE studies on NS5B in the presence of Manganese

In **chapter 5**, we provided new insights on the binding and sliding dynamics of NS5B and its RNA substrate via smPIFE. Under our working conditions (5 mM Mg^{2+}), we were not able to detect *de novo* initiation. It has been shown that RNA synthesis is increased by 4-20 fold in the presence of

Mn^{2+},[5-6] and that Mn^{2+} is preferred for *de novo* initiation.[7-8] We posit then that the addition of Mn^{2+} will allow us to visualize *de novo* initiation.

The addition of Mn^{2+} brings new challenges as it has been reported to induce blinking and photobleaching of Cy3.[9] We postulate that there may be a compromise when adding Mn^{2+}. This is, a concentration high enough to induce *de novo* synthesis while not inducing significant blinking and photobleaching.

6.2.3.2 I-FRET Assay with Enzymes from the HCV Family

In **chapter 2**, we provided a framework to combine two widely used single molecule techniques: smPIFE and smFRET. While in **chapter 5**, we studied the dynamics of NS5B binding to (and sliding along) its RNA substrate via smPIFE. Given that PIFE technique is generally insensitive to distances larger than ~3 nm, this technique only offers a limited range of protein visualization relative to the labeling site in the oligonucleotide. This short-range sensitivity range can hinder a proper analysis of a protein-oligonucleotide system. The intensity signal of a protein moving further form the oligonucleotide labeling site will not be distinguished from protein unbinding. Here a labeled protein could serve as a marker to differentiate these two events.

In order to obtain an extended description of the dynamics of protein-oligonucleotide interaction, we propose to study Cy5-labeled NS5B as well as other oligonucleotide binding proteins of the HCV family such as NS3h.[10-11] In collaboration with the Pezacki and Götte groups we have recently reported a site-specific strategy to effectively label NS3h, a strategy that can be extended to NS5B.[11] I-FRET may reveal new insights on the dynamic working mechanism of enzymes binding to oligonucleotides, specifically those requiring the tracking of changes in distances spanning from angstroms to nanometers.

6.2.4 Rapid screening of drugs targeting polymerases and helicases

We note that the smPIFE platform reported herein provides the scaffold for the development of assays with the potential to identify compounds that interfere with the dynamic behavior of viral polymerases and/or helicases in general. As such, we expect our findings to impact the study of other diseases beyond HCV.

After establishing the working mechanism of NS5B and other HCV-related RNA binding proteins, we propose extending the mechanistic studies to other viral proteins within the *Flaviviridae* family such as the Zika Virus (ZIKV). A similar single molecule platform can be used as a strategy for the rapid screening of drugs designed to interfere with the binding and sliding of the NS5B of the Zika Virus. The proposed strategy will greatly benefit from elements of automation in terms of surface immobilization and flowing of enzymes through a computer-controlled microfluidics system. Additionally, data analysis can be in part simplified by using an adapted version of a recently reported method for image correlation for high-throughput and rapid analysis of single molecule data, published in collaboration with the Wiseman group.[12] Here, drugs interfering with the binding and sliding of NS5B will render different dissociation and association rates as well as different fluorescent signal patterns arising from sliding.

6.2.5 Studies on PIFE fundamentals for a potentially improved technique

In **chapter 5**, we used a Cy3 fluorophore as reporter for the smPIFE assay. Prior to single molecule experiments, we calibrated the system via steady state ensemble fluorescence measurements. We found that the maximum fluorescence enhancement was expected to be ~3.3-fold. However, some binding events exhibited enhancements of up to 7-fold, suggesting that Cy3 bears a higher dynamic range than the one obtained from our calibration.

In order to elucidate this puzzling result, we propose two hypotheses to be tested:

1. ***A protein induced red-shift absorption spectrum.***

This hypothesis is based on preliminary results that show that when a 532 nm, instead of a 561 nm, laser beam is utilized, the average enhancement recorded upon NS5B binding in the presence of Mg^{2+} is ~1.5-fold instead of ~3.3-fold. A 561 nm laser beam excites the red edge of Cy3 absorption spectrum. As such, a protein induced red shift in the spectrum would increase the excitation rate of Cy3, effectively enhancing the fluorescence through an increase in its excitation rate.

2. ***The upper limit of fluorescence quantum yield of Cy3 is higher than in glycerol***

This hypothesis is based on the fact that Cy3B, the locked analog of Cy3, has been reported to have a fluorescence quantum yield of 0.67,[13] higher than the 0.43 measured for Cy3 in glycerol.

Then, it is possible that Cy3, in the absence of rotation, bears a fluorescence quantum yield higher than 0.43. We suggest measuring the fluorescence of Cy3 in vitrified solutions to verify if the fluorescence intensity can be further enhanced.

The additional enhancement of Cy3 can be explained by either of these hypotheses or possibly a combination of both. Further investigations on this serendipitous finding may offer the opportunity to increase the sensitivity of PIFE experiments. Systems containing proteins that produce low enhancements on Cy3 will certainly benefit from a PIFE technique with enhanced sensitivity.

6.3 Publications Resulting from the Thesis Work and Collaborations

Article 1 will be submitted. Article 2 has been submitted. Articles 3-4 were published as part of this thesis. Co-authored articles 5-9 were published during the thesis period but are not included in this thesis.

1. Gidi. Y.; Robert, A.; Tordo, A.; Götte. M.; Cosa. G.*; Binding and Sliding Dynamics Preceding *de novo* RNA Replication by the Hepatitis C Virus Polymerase: hunting the 3'. *To be submitted*

2. Gidi, Y.; Payne, L.; Glembockyte, V.; Michie, M.; Schnermann, M.; Cosa, G.*; Unifying Mechanism for Thiol Induced Photoswitching and Photostability of Cyanine Dyes. *Submitted*

3. Gidi, Y.; Bayram, S.; Ablenas C.; Blum A. S.; Cosa, G.*; Efficient One-step PEG-silane Passivation of Glass Surfaces for Single-molecule Fluorescence Studies. *ACS Appl. Mater. Interfaces.* **2018**, 10, 39505–39511. (DOI: 10.1021/acsami.8b15796)

4. Gidi. Y.; Götte. M.; Cosa. G.*; Conformational Changes Spanning Angstroms to Nanometers *via* a Combined Protein-Induced Fluorescence Enhancement–Förster Resonance Energy Transfer Method. *J. Phys. Chem. B.* **2017**, 121, 2039–2048. (DOI: 10.1021/acs.jpcb.6b11495)

5. Ablenas, C.; Gidi. Y.; Powdrill, M.; Ahmed, N.; Shaw, T.; Mesko, M.; Götte. M.; Cosa. G.*; Pezacki, J.*; Hepatitis C Virus Helicase Binding and Activity Monitored Through Site-Specific Labeling Using an Expanded Genetic Code. *ACS Infect. Dis*. **2019**, 5, 2118-2126. (DOI: 10.1021/acsinfecdis.9b00220)

6. Sehayek, S.; Gidi, Y.; Glembockyte, V.; Brandao, H.; Francois, P.; Cosa, G.; Wiseman, P. W.; A High-Throughput Image Correlation Method for Rapid Analysis of Fluorophore Photo-Blinking and Bleaching Rates. *ACS Nano.* **2019**, 13, 11955-11966. (DOI: 10.1021/acsnano.9b06033)

7. Glembockyte, V.; Wieneke, R.; Gatterdam, K.; Gidi, Y.; Tampé, R.; Cosa, G.*; TrisNTA Fluorophore as a Self-Healing Dye for Single-Molecule Fluorescence Imaging. *J. Am. Chem. Soc.* **2018**, 140, 11006–11012. (DOI: 10.1021/jacs.8b04681)

8. Rahbani, J. F.; Vengut-Climent, E.; Chidchob, P.; Gidi, Y.; Trinh, T.; Cosa, G.; Sleiman, H. F.*; DNA Nanotubes with Hydrophobic Environments: Toward New Platforms for Guest Encapsulation and Cellular Delivery. *Adv. Healthc. Mater*. **2018**, 7, 1701049. (DOI: 10.1002/adhm.201701049)

9. Hariri, A. A.; Hamblin, G. D.; Gidi, Y. Sleiman, H. F.*; Cosa, G.*; Stepwise growth of surface-grafted DNA nanotubes visualized at the single-molecule level. *Nat. Chem.* **2015**, 7, 295–300. (Journal Cover) (DOI: 10.1038/nchem.2184)

6.4 References

1. Glembockyte, V.; Cosa, G., Redox-Based Photostabilizing Agents in Fluorescence Imaging: The Hidden Role of Intersystem Crossing in Geminate Radical Ion Pairs. *Journal of the American Chemical Society* **2017,** *139* (37), 13227-13233.
2. Holzmeister, P.; Gietl, A.; Tinnefeld, P., Geminate recombination as a photoprotection mechanism for fluorescent dyes. *Angewandte Chemie (International ed. in English)* **2014,** *53* (22), 5685-8.
3. Gidi, Y.; Bayram, S.; Ablenas, C. J.; Blum, A. S.; Cosa, G., Efficient One-Step PEG-Silane Passivation of Glass Surfaces for Single-Molecule Fluorescence Studies. *ACS Applied Materials & Interfaces* **2018,** *10* (46), 39505-39511.
4. Hai, P.; Yifan, X.; Meng, Q.; Yi, C.; Wei, W., A simple procedure to improve the surface passivation for single molecule fluorescence studies. *Physical Biology* **2015,** *12* (4), 045006.
5. Ferrari, E.; Wright-Minogue, J.; Fang, J. W. S.; Baroudy, B. M.; Lau, J. Y. N.; Hong, Z., Characterization of Soluble Hepatitis C Virus RNA-Dependent RNA Polymerase Expressed in Escherichia coli. *Journal of Virology* **1999,** *73* (2), 1649-1654.
6. Luo, G.; Hamatake, R. K.; Mathis, D. M.; Racela, J.; Rigat, K. L.; Lemm, J.; Colonno, R. J., De Novo Initiation of RNA Synthesis by the RNA-Dependent RNA Polymerase (NS5B) of Hepatitis C Virus. *Journal of Virology* **2000,** *74* (2), 851-863.
7. Ranjith-Kumar, C. T.; Kim, Y.-C.; Gutshall, L.; Silverman, C.; Khandekar, S.; Sarisky, R. T.; Kao, C. C., Mechanism of De Novo Initiation by the Hepatitis C Virus RNA-Dependent RNA Polymerase: Role of Divalent Metals. *Journal of Virology* **2002,** *76* (24), 12513-12525.
8. Zhong, W.; Uss, A. S.; Ferrari, E.; Lau, J. Y. N.; Hong, Z., De Novo Initiation of RNA Synthesis by Hepatitis C Virus Nonstructural Protein 5B Polymerase. *Journal of Virology* **2000,** *74* (4), 2017-2022.
9. Ciuba, M. A.; Levitus, M., Manganese-Induced Triplet Blinking and Photobleaching of Single Molecule Cyanine Dyes. *ChemPhysChem* **2013,** *14* (15), 3495-3502.
10. Ablenas, C.; Liu, H.-W.; Shkriabai, N.; Kvaratskhelia, M.; Cosa, G.; Götte, M., Dynamic Interconversions of HCV Helicase Binding Modes on its Nucleic Acid Substrate. *ACS Infectious Diseases* **2016**.
11. Ablenas, C. J.; Gidi, Y.; Powdrill, M. H.; Ahmed, N.; Shaw, T. A.; Mesko, M.; Götte, M.; Cosa, G.; Pezacki, J. P., Hepatitis C Virus Helicase Binding Activity Monitored through Site-Specific Labeling Using an Expanded Genetic Code. *ACS Infectious Diseases* **2019**.
12. Sehayek, S.; Gidi, Y.; Glembockyte, V.; Brandão, H. B.; François, P.; Cosa, G.; Wiseman, P. W., A High-Throughput Image Correlation Method for Rapid Analysis of Fluorophore Photoblinking and Photobleaching Rates. *ACS Nano* **2019,** *13* (10), 11955-11966.
13. Cooper, M.; Ebner, A.; Briggs, M.; Burrows, M.; Gardner, N.; Richardson, R.; West, R., Cy3B™: Improving the Performance of Cyanine Dyes. *Journal of Fluorescence* **2004,** *14* (2), 145-150.